Effective Methods for Human-Robot-Environment Interaction by means of Haptic Robotics

Pholchai Chotiprayanakul

A thesis submitted for the fulfilment
for the degree of
DOCTOR OF PHILOSOPHY

Faculty of Engineering and Information Technology
University of Technology, Sydney

March 2012

Declaration of Authorship

I, Pholchai Chotiprayanakul, certify that the thesis titled, "Effective Methods for Human-Robot-Environment Interaction by means of Haptic Robotics" and the work presented in this thesis are my own. I confirm that:

- This work was done while in candidature for the degree of doctor of philosophy at the University of Technology, Sydney.
- This thesis has not previously been submitted for a degree or any other qualification at any other institution.
- The thesis is based on work done by myself and where I have consulted the published work of others, this is always clearly attributed.
- All information sources and literature used are indicated in the thesis.

Signed: Production Note:
Signature removed prior to publication.

Date: 21/03/12

Abstract

Industrial robots have been widely used to perform well-defined repetitive tasks in carefully constructed simple environments such as manufacturing factories. The futuristic vision of industrial robots is to operate in complex, unstructured and unknown (or partially known) environments, to assist human workers in undertaking hazardous tasks such as sandblasting in steel bridge maintenance. Autonomous operation of industrial robots in such environments is ideal, but semi-autonomous or manual operation with human interaction is a practical solution because it utilises human intelligence and experience combined with the power and accuracy of an industrial robot. To achieve the human interaction operation, there are several challenges that need to be addressed: environmental awareness, effective robot-environment interaction and human-robot interaction

This thesis aims to develop methodologies that enable natural and efficient Human-Robot-Environment Interaction (HREI) and apply them in a steel bridge maintenance robotic system. Three research issues are addressed: Robot-Environment-Interaction (REI), haptic device and robot interface and intuitive human-robot interaction.

To enable efficient robot-environment interaction, a potential field-based Virtual Force Field (VF^2) approach has been investigated. The VF^2 approach includes an Attractive Force (AF) method and a force control algorithm for robot motion control, and a 3D Virtual Force Field (3D-VF^2) method for real-time collision avoidance. Results obtained from simulation, experiments in a laboratory setup and field test have verified and validated these methods.

A haptic device-robot interface has been developed for providing intuitive human-robot interaction. Haptic devices are normally small compared to industrial robots. Thus, the workspace of a haptic device is much smaller than the workspace of a big industrial manipulator. A novel workspace mapping method, which includes drifting control, scaling control and edge motion control, has been investigated for mapping a small haptic workspace to the large workspace of manipulator with the aim of providing natural kinesthetic feedback to an operator and smooth control of robot operation. A haptic force control approach has also been studied for transferring the virtual contact force (between the robot and the environment) and the inertia of the manipulator to the operator's hand through a force feedback function.

Human factors have significant effect on the performance of haptic-based human-robot interaction. An eXtended Hand Movement (XHM) model for eye-guided hand movement has been investigated in this thesis with the aim of providing natural and comfortable interaction between a human operator and a robot, and improving the operational performance. The model has been studied for increasing the speed of the manipulator while maintaining the control accuracy. This model is applied into a robotic system and it has been verified by various experiments.

These theoretical methods and algorithms have been successfully implemented in a steel bridge maintenance robotic system, and tested in both laboratory and a bridge maintenance site located in Sydney.

Acknowledgements

I would like to thank my supervisor Professor Dikai Liu for his great effort and time to advise and assist me throughout my candidature years. I also would like to thank my co-supervisor Professor Gamini Dissanayake for his support through my study. Without they support this thesis would not have been possible.

I would like to thank all my friends and colleagues at the ARC Centre of Excellence for Autonomous Systems (CAS), especially DalongWang, Ngai Ming Kwok, and Stephen Webb for their helpful comments and support. Special thanks to Gavin Paul, who gave a lot of helpful suggestions on improving the thesis.

Thanks to everyone at the Department of Industrial Engineering at King Mongkut's Institute of Technology Ladkrabang, especially Associate Professor Pornsak Auttavanich, Assistant Professor Sunpasit Limnorarath, and Associate Professor Rattikorn Varakulsiripun for giving me the best opportunity of my life.

Thanks to my sponsor, Ministry of Science and Thai Government for the scholarship and the Office of the Civil Service Commission (OCSC) and the Office of Educational Affairs in Australia for look after me all years long of study.

Special thanks to my mum, my dad, and my family who have always supported and believed in me. Thanks to my wife "Sasima" and my daughter "Sasicha" for always be by my side and make me smile.

Table of Content

List of Figures

Nomenclature

General Formatting Style

$f(\ldots)$	A scalar valued function	
$\mathbf{f}(\ldots)$	A vector function	
$\boldsymbol{F}(\ldots)$	A matrix function	
$\{\ldots\}$	A set of …	
$[\ldots]^{\mathrm{T}}$	Transpose	
$\lvert\ldots\rvert$	Absolute value	
$\lVert\ldots\rVert$	Vector length	
$\mathrm{minmin}\{\ldots\}$	The objective function of two parameters minimization	
$\prod_{\cdots}^{\cdots}\cdots$	Product sign	
x	A scalar variable	- lower case and italic
X	A scalar variable	-upper case and italic
$\mathbf{x}$	A vector or a single-dimensional matrix	- lower case and bold
$\mathbf{X}$	A matrix or a set	- upper case and bold

$P(Z \leq a)$	Cumulative probability function
$P(Z \geq a)$	Complementary cumulative probability function
$P(b \leq Z \leq a)$	Cumulative point-to-point probability function

General Referencing with Subscript and Superscript

$^{\cdots}x_{\cdots}$ A scalar variable

- Front superscript is reference coordinate

- Rear subscript is transforming coordinate

${}^{\cdots}x_{\cdots\ \cdots}$ A scalar variable

- Front superscript is reference coordinate
- Rear first subscript is numerical index, customized abbreviation or description
- Rear second subscript is transforming coordinate

${}^{\cdots}\mathbf{X}_{\cdots}$ or ${}^{\cdots}\mathbf{x}_{\cdots}$ A matrix

- Front superscript is reference coordinate
- Rear subscript is transforming coordinate

${}^{\cdots}\mathbf{X}_{\cdots\ \cdots}$ or ${}^{\cdots}\mathbf{x}_{\cdots\ \cdots}$ A matrix

- Front superscript is reference coordinate
- Rear first subscript is numerical index, customized abbreviation or description
- Rear second subscript is transforming coordinate

$\mathbf{X}_{\cdots\ \cdots}$ A set (does not have front superscript)

- Rear first subscript is customized abbreviation or description
- Rear second subscript is index of set's member

Local and Global Variables

i,j	Index of a set or to refer to a count
x,y,z	Axes of Cartesian coordinate
$\Re^3$	3DOF Cartesian space
$\Re^6$	6DOF Cartesian space
$\Re_{\mathbf{q}}^7$	7DOF manipulator's joint space

Specific Symbol Usage

${}^{\cdots}\mathbf{T}_{\cdots}$	A homogeneous transformation matrix (4 by 4)
${}^{\cdots}\mathbf{R}_{\cdots}$	A rotation matrix (3 by 3)
${}^{\cdots}\mathbf{n}_{\cdots}$	A directional vector or a normal vector (3 by 1)
${}^{\cdots}\mathbf{p}_{\cdots}$	A position vector (3 by 1)
${}^{\cdots}\mathbf{P}_{\cdots}$	A configuration vector (6 by 1), a combination of $[{}^{\cdots}\mathbf{n}_{\cdots}, {}^{\cdots}\mathbf{p}_{\cdots}]$
n_x, n_y, n_z	components of ${}^{\cdots}\mathbf{n}_{\cdots}$
p_x, p_y, p_z	components of ${}^{\cdots}\mathbf{p}_{\cdots}$

$\mathbf{F}_{\ldots}$	A 6DOF spatial force
$\mathbf{f}_{\ldots}$	A 3DOF linear force, a component of$\mathbf{F}_{\ldots}$
$\boldsymbol{\sigma}_{\ldots}$	A 3DOF angular moment, a component of$\mathbf{F}_{\ldots}$
$f_{\ldots x}, f_{\ldots y}, f_{\ldots z}$	scalar components of $\mathbf{f}_{\ldots}$
$\sigma_{\ldots x}, \sigma_{\ldots y}, \sigma_{\ldots z}$	scalar components of$\boldsymbol{\sigma}_{\ldots}$

$\mathbf{q}$	A joint position matrix (7 by 1)
q_i	A position of joint i , a component in $\mathbf{q}$ - joint 1 to 6 are angle (degree) - joint 7 is length (m)

$\mathbf{I}$	Mass-inertia matrix of the robot links
$\boldsymbol{\beta}$	Damping coefficient matrix of the robot joints
$\boldsymbol{\kappa}$	Stiffness coefficient matrix of the robot joints

$\boldsymbol{\Gamma}$	A torque-force matrix defining in joint space (7 by 1)
τ_i	Joint torque-force of a joint i , a component in $\boldsymbol{\Gamma}$ - joint 1 to 6 are torque (N.m) - joint 7 is linear force (N)

$\boldsymbol{\Gamma}_{att}$	Attractive torque-force matrix
$\boldsymbol{\Gamma}_{rep_i}$	Repulsive torque-force matrix on a link in joint i coordinate

$^{0}\mathbf{P}_e$	Configuration of the end-effector of a manipulator
$^{0}\mathbf{n}_e$	A component of $^{0}\mathbf{P}_e$
$^{0}\mathbf{p}_e$	A component of $^{0}\mathbf{P}_e$
$^{0}\mathbf{P}_t$	Configuration of target/attractive point for the manipulator's end-effector
$^{0}\mathbf{n}_t$	A component of $^{0}\mathbf{P}_t$
$^{0}\mathbf{p}_t$	A component of $^{0}\mathbf{P}_t$
$\mathbf{F}_{att}$	A6DOF spatial attractive force for the manipulator's end-effector
$\mathbf{f}_{att}$	A 3DOF attractive force (linear force), a component of $\mathbf{F}_{att}$
$\boldsymbol{\sigma}_{att}$	A 3DOF attractive moment (angular moment), a component of $\mathbf{F}_{att}$
$f_{att\,x}, f_{atty}, f_{att\,z}$	components of $\mathbf{f}_{att}$
$\sigma_{att\,x},\sigma_{atty},\sigma_{att\,z}$	components of$\boldsymbol{\sigma}_{att}$
$K_{att\ 1}$	Coefficient of a linear attractive force's amplitude
$K_{att\ 2}$	Coefficient of an angular attractive moment's amplitude
ε_0	A small non-zero positive constant (in this research ε_0= 0.0001)
K_{as}	A constant for defining a transient state of the attractive force
δ_a	Attractive force function
$\mathbf{P}_{ob}$	Obstacle point cloud set
$^{0}\mathbf{p}_{ob\ i}$	The i^{th} member in the obstacle point cloud set
m	Number of points in the obstacle point cloud set
D_{min}	inner force field
D_{max}	outer force field
Er	distance between D_{min} and D_{max}
r_c	The radius of D_{min}
$^{0}\mathbf{p}1_i$	Ending point 1 of the centre line of a link in joint i coordinate

${}^{0}\mathbf{p}2_{i}$	Ending point 2 of the centre line of a link in joint *i* coordinate
${}^{0}\mathbf{p}3_{i}$	The nearest point on the centre line of a link on joint *i* coordinate
u	A parameter of a centre line of a link function for defining ${}^{0}\mathbf{p}3_{i}$
${}^{0}\mathbf{p}_{ob\,s}$	The point in the point cloud set that is the closest point to a manipulator link at ${}^{0}\mathbf{p}3_{i}$
ds_{s}	The shortest distance measured from ${}^{0}\mathbf{p}_{ob\,s}$ to ${}^{0}\mathbf{p}3_{i}$
d_{0}	The shortest distance from the point ${}^{0}\mathbf{p}_{ob\,s}$ to the surface of D_{min}

$\mathbf{F}_{rep_i}$	A spatial repulsive force on a link of a manipulator in joint *i* coordinate
$\mathbf{f}_{rep_i}$	A repulsive force on a link of a manipulator in joint *i* coordinate, a component of $\mathbf{F}_{rep_i}$
$f_{rep_{x_i}}, f_{rep_{y_i}}, f_{rep_{z_i}}$	components of $\mathbf{f}_{rep_i}$
δ_{r}	Repulsive force function
K_f	A coefficient of the amplitude of a repulsive force

$\mathbf{H}_{i}$	Force transformation matrix in joint *i* coordinate
${}^{0}\mathbf{p}_{f}$	Position vector of a force
$\mathbf{h}_{j}$	j^{th} component of $\mathbf{H}$
$\mathbf{L}_{i}$	Configuration matrix of joint *i* coordinate

${}^{\cdots}\mathbf{M}_{\cdots}$	A rotation skew-symmetric matrix (6 by 6)
$\mathrm{S}(\Delta\mathbf{p})$	A skew-symmetric matrix (3 by 3)
$\Delta\mathbf{p}$	A differential vector between ${}^{0}\mathbf{p}_{i}$ and ${}^{0}\mathbf{p}_{f}$
$\Delta p_{x}, \Delta p_{y}, \Delta p_{z}$	components of $\Delta\mathbf{p}$

$\mathbf{F}_{h}$	A haptic force
k_{vir}	Coefficient of virtual spring stiffness

${}^0\mathbf{p}_a$	Position vector of the haptic cursor on the world coordinate
${}^0\mathbf{p}_h$	Position vector of the haptic cursor on the haptic workspace coordinate
${}^0\mathbf{p}_w$	Position vector of the haptic workspace origin on the world coordinate
${}^0\dot{\mathbf{p}}_h$	Velocity vector of the haptic cursor on the haptic workspace coordinate
${}^0\dot{\mathbf{p}}_w$	Drifting velocity of the haptic workspace origin on the world coordinate

k_{sc}	Workspace scaling coefficient
$\dot{k}_{sc}$	Workspace scaling rate (first order differentiate)
k_{sp}	Positive scaling rate of scaling control
k_{sn}	Negative scaling rate of scaling control
k_{dp}	The positive drifting rate of drifting control
k_{em}	Drifting rate of edge motion control
v_{ht}	Haptic cursor speed threshold

k_e	Elasticity coefficient of a 3D-VF^2 (virtual skin)
μ_{cap}	Energy absorbability of a 3D-VF^2
μ_{in}	Potential energy from the attractive force

φ	Probability density
O_{acc}	Pointing accuracy
Z_{ac}	Coefficient of the pointing accuracy
σ	Standard deviation of robot end-effector in a pointing task
σ^2	Variance of robot end-effector in a pointing task
IP	Index of Performance

$\emptyset$	Path-track width
$\emptyset_{obj}$	Dimension of a task plane
$\emptyset_{scn}$	Dimension of a computer screen
d_v	A view distance between a camera screen and an object plane

α_v	A camera's field of view
G_e	A control display scale
G_h	A control movement scale
G_x	A control scale

MT	Hand movement time
a	Operator's start/stop movement time
b	Operator's hand movement speed

v_a	A haptic cursor speed from hand movement model
k_{pw}	Coefficient of power expense in haptic interface

Chapter 1 Introduction

1.1 Human-Robot-Environment Interaction: Research Challenges

Industrial manipulators (or industrial robots)have been widely used in manufacturing where they repeatedly perform pre-programmed routines and tasks in carefully defined environments. With advances in robotics science, systems and techniques, industrial manipulators have started to 'move' (with a mobile platform), to interact with unknown or partially known environments, to undertake tasks in hazardous environments and to assist people in daily living activities by augmenting human strength.

There are many challenges when applying an industrial manipulator, which is placed on a mobile platform, in an unstructured, complex and dynamic environment. The manipulator must have the ability to sense the surrounding environment, avoid collisions and perform various tasks that are not repeatable. Examples of applications and tasks include robotic sandblasting of a complex steel structure in steel bridge maintenance, surveillance and rescue with the use of a mobile manipulator with camera and other sensing equipment affixed, robotic painting of a large vessel and robotic cleaning of a large tank, robotic drilling in coalmining.

Autonomous operation of a mobile industrial manipulator in complex, dynamic and unknown/partially known environments is ideal but very difficult to achieve. One example is robotic steel bridge maintenance, where a mobile industrial manipulator conducts sandblasting (otherwise called grit-blasting) in complex steel bridge structures with girders, trusses, frames and box girders. Some areas in a steel bridge are difficult for a human operator to access. It is computationally expensive if a mobile industrial manipulator is applied in these areas and operated autonomously. Due to sandblasting, the steel bridge maintenance environment is normally very dusty which prevents the use of sensors during blasting. Therefore, for difficult to access areas, semi-autonomous operation or manual operation with human operator interaction is a practical solution, using human intelligence and experience combined with the power and accuracy of an industrial manipulator. Thus, Human-Robot-Environment Interaction (HREI) framework and enabling methodologies for human-robot interaction need to be developed.

When a human operator is required to be in the loop of robot manipulator operation, but is not allowed to go into the environment where the industrial manipulator is operating, remote-operation is the option. To effectively keep the human operator in the loop and to utilise human intelligence and knowledge, sensory feedback should be provided to the human operator. A haptic device can help a human operator to extend their kinesthetic sense (i.e. sense of touch) to the manipulator operation and the remote three-dimensional (3D) complex environment. To achieve effective and intuitive human-robot interaction by means of haptic robotics, many challenging research issues need to be addressed.

One challenge is environmental awareness, i.e. how the mobile robot manipulator senses the environment. Proximity sensor networks or tactile sensor networks that cover the entire manipulator can provide the means to detect obstacles which are in close range. Additionally, some types of proximity sensors are affected by the conditions in the environment; for example, airborne particles and dust will impede an infrared or sonar sensor, and capacitive sensors are interfered by electrical field when in proximity to high voltages [1]. Therefore, when a manipulator moves at high speeds or is inside a very dusty environment, the proximity sensor network may not be able to detect potential collisions. In order to predict possible collisions between a moving manipulator and obstacles/environment, a 3D map of the environment is essential. Hence, the surrounding environment of the manipulator must first be explored using sensors in order to generate a 3D map by efficient exploration and mapping methods.

After the map of an environment is built, how the mobile manipulator interacts with the environment is another challenge. Many path planning approaches can be used to enable a manipulator to operate in a simple environment [2][3] or in an open space [4] [5][6][7]. The available planning methods are not efficient enough for a manipulator with over 6 degrees of freedom (DOF) to interact quickly with a complex environment. Many researchers have been developing approaches for motion planning in the Cartesian coordinate-based operational space (*O-space*); examples include the potential field method [5][6][8] and the force field method [9][10]. However, for a multi-DOF mobile manipulator operating in a complex 3D environment, practical operational and environmental constraints (i.e. efficiency, speed and orientation) make motion planning increasingly difficult.

In order for the operator to 'feel' the environment and the operation of a robot manipulator in haptic-based human-robot interaction, three issues need to be studied: force reflection, haptic rendering, and workspace mapping. Force reflection transfers a (virtual) contact force, calculated on the distance between the robot manipulator and the environment or obstacles from a (virtual) contact point, to the handle of the haptic device using the kino-dynamic model of the manipulator. Haptic rendering concerns the way in which haptic force/feedback is generated. Virtual spring approach is an effective haptic rendering approach which can be applied to HREI. Workspace mapping is another challenge when a small haptic device is used to control a big industrial manipulator and simple haptic workspace scaling has been shown to be ineffective [11][12] when precise manipulator control is required. The workspace spanning approach [13] effectively expands the workspace for the haptic cursor. However, it is not directly applicable to the control of a mobile manipulator because the approach does not have a feature that can generate contact force between the manipulator and the virtual environment.

Human factors have significant effect on haptic-based interaction when a human is in the loop of robot control and this is another research challenge that needs to be addressed in HREI research. The major performance indicators in HREI are(1) the speed and accuracy of a movement made by the operator and the robot; and (2) the level of intuitive haptic force feedback. Uniform motion between the operator's hand

and the end-effector of the manipulator makes the interaction more natural. The latency caused by communication between the haptic device and the robot hinders the natural interface in haptic-based interaction. There is a direct relationship to a human cognition and human movement; thus, human factor models including Fitts's law and Steering law [14][15] are directly applicable to haptic-based human-robot interaction.

1.2 The Targeted Application

This research aims to address the challenges in HREI stated above, develop efficient methods for enabling effective HREI, and apply these methods in industrial applications. Examples of such industrial applications are shown in Figure 1.1.


(a) (b)

Figure 1.1 Examples of industrial applications in which operators can be replaced by a mobile robot manipulator to interact with complex environments in hazardous workplaces: (a) Sandblasting operation in steel bridge maintenance, (b) Vessel maintenance (from Broadbent's, Inc)

In this thesis, the industrial application targeted is robotic sandblasting in steel bridge maintenance. The paint on steel bridges gradually deteriorates due to weather, time and stresses on the bridge. Corrosion can cause major bridge failure; thus, steel bridges require regular maintenance. Stripping and repainting provides protection from rust and prolongs the lifespan of steel bridges, but manual stripping and repainting is hazardous for workers and can cause fatigue, injuries, and occupational illness. Steel bridges are often coated with lead-based paints and asbestos is sometimes present in the insulating base paints. The dust that becomes airborne due to the sandblasting process can thus contain highly toxic particles [16] which cause such diseases as asbestosis, silicosis and lead poisoning. Additionally, the equipment used in sandblasting is often heavy. The blasting abrasive is piped from a pressurised container (sandblasting pot) through the nozzle at high velocity, and a large reaction force is generated from the blast nozzle, so the blasting stream could cause serious injury or be fatal if it struck a human operator. Finally, although engineering drawings exist for most steel bridges, the information is not necessarily up-to-date, nor do they provide a detailed indication of the state of paint deterioration or the rusted surfaces.

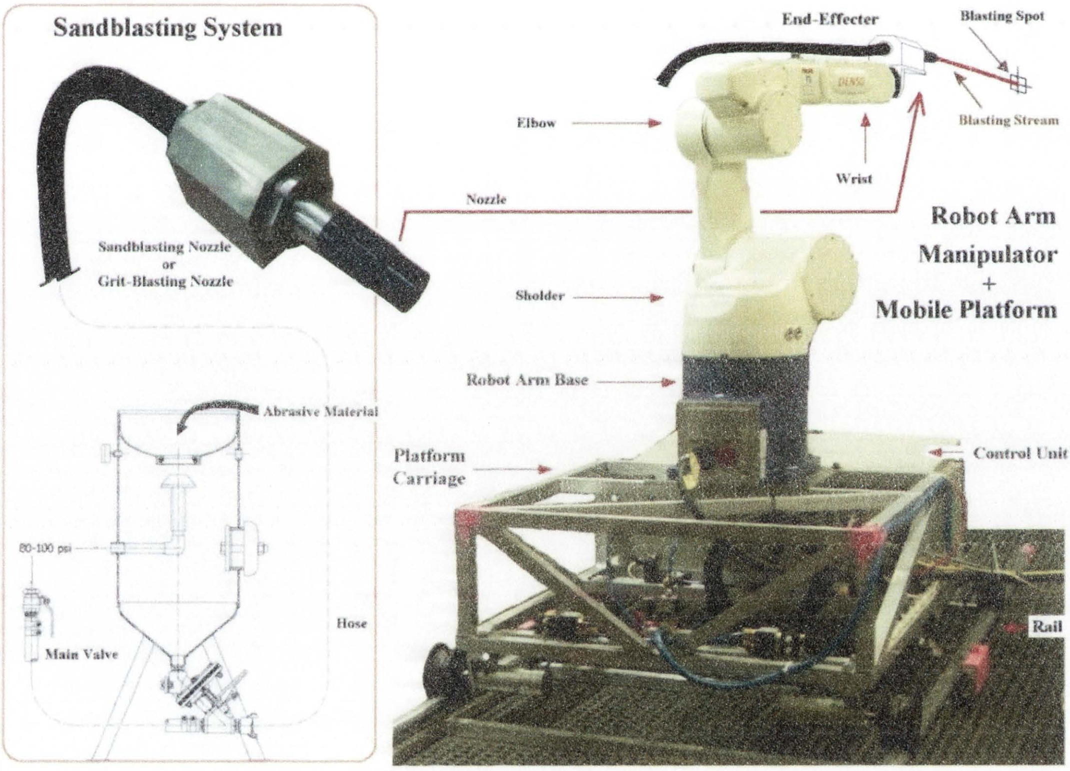

Figure 1.2 Prototype of the sandblasting robotic system

A large team at the University of Technology, Sydney (UTS) has been working the research project 'A Robotic System for Steel Bridge Maintenance' funded by the Australian Research Council (ARC) and the Roads and Traffic Authority of New South Wales (RTA). This project aims to develop a robotic system for complex steel bridge maintenance with the ultimate objectives of reducing human exposure to hazardous and dangerous debris (containing rust, paint particles, lead, asbestos and/or Chromium-6), relieving workers from labour intensive tasks, reducing costs associated with bridge maintenance and improving the safety of bridge maintenance operations. The current prototype sandblasting robotic system (Figure 1.2) developed by the team consists of a Denso® VM6083 industrial robot manipulator mounted on a rail-track mobile platform, a sandblasting nozzle affixed to the end-effector, a sensor package and a control system which includes all the modules developed to date. The manipulator is approximately 1.6 m tall when fully extended. The effective range of the blast stream from the nozzle tip to a blasting spot is from 100 mm to 500 mm. The mobile platform is wheel-driven along a track, and every time the mobile platform is moved the workspace surrounding the manipulator is changed. The robot must therefore be able to explore the new environment, build a new map, and plan its actions safely and efficiently.

Three operation modes have been developed for the sandblasting robotic system: an autonomous mode which allows the robotic system to autonomously explore a bridge maintenance environment, build a 3D map of the environment, plan the sandblasting path and motion of the manipulator, and conduct sandblasting; a manual operation mode; and a semi-autonomous operation mode which allows human operators to interact with the robot.

This thesis, as part of the research project, addresses the research challenges in HREI in the semi-autonomous and manual operation modes, and develops essential theoretical algorithms and methods for effective human-robot-environment interaction. Algorithms and methods are studied to make the robotic system easy to control and to interact. These algorithms and methods are generic and can be used for many other applications in which a mobile industrial manipulator is used in unstructured environments.

1.3 Scope

In a HREI system, interactions include robot-environment interaction and human-robot interaction (Figure 1.3). When a haptic device is applied to enable natural human-robot interaction, algorithms are required for the coordination of a haptic device with small workspace and an industrial manipulator with a large workspace. The scope of this research, therefore, is to develop methodologies that enable efficient human-robot-environment interaction, apply the developed algorithms and methods in a robotic steel bridge maintenance system, and conduct field testing and verification.

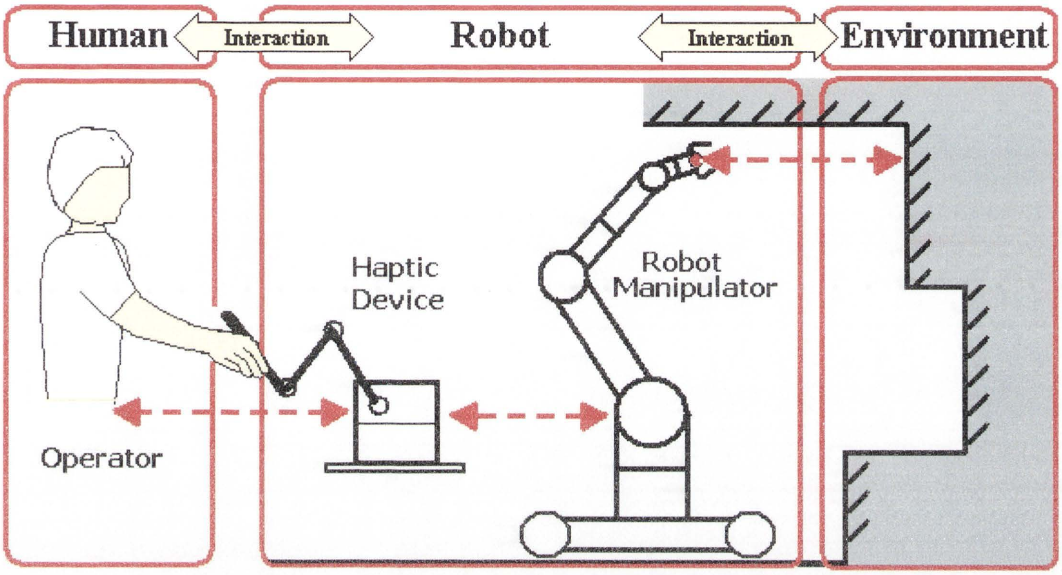

Figure 1.3 Human-Robot-Environment Interaction (HREI) diagram

1. Robot-environment interaction: In order to enable the safe and efficient interaction of a mobile industrial manipulator with a compact and complex 3D environment, environmental awareness and real-time motion planning and collision avoidance need to be addressed. Efficient algorithms for environmental exploration and robot collision-free motion planning are therefore investigated by taking into account the complexity of the environment, and the practical operational requirements/constraints such as efficiency, robot speed and tool orientation. A potential field-based Virtual Force Field (VF^2) approach has been investigated. The VF^2 approach includes an Attractive Force (AF) method and a force control algorithm for robot motion control, and a 3D Virtual Force Field (3D-VF^2) method for real-time collision avoidance. In this thesis, all tasks are pointing tasks, that is, the manipulator must position a projection point from the end effector, within the task constraints, onto a surface in the environment. Pointing tasks

generally must be completed in a specific order and must include both point-to-point and contour motions.

2. Haptic-robot interface: This interface creates a channel for an operator and a robot to perform collaborative tasks. The haptic-robot interface includes a workspace mapping method and haptic control approach. Haptic devices are normally small compared to industrial robots, thus the workspace of a haptic device is much smaller than the workspace of a big industrial manipulator. A novel workspace mapping method is investigated for mapping a small haptic workspace to the large workspace of manipulator with the aim of providing natural kinesthetic feedback to an operator. To reflect force and render the environment, a haptic force control approach transfers the contact force and inertia of the manipulator to the operator's hand through the force feedback function of the haptic device. The fidelity of force reflection and force rendering is affected by the communication latency between the master control system (operator and haptic device) and the slave system (manipulator). In this thesis the latency is very small because the master system and the slave system are assumed to be in close proximity.

3. Human-robot interaction: Human factors have a significant effect on the performance of haptic-based human-robot interaction. An extended hand movement model is investigated in this research with the aim of providing natural and comfortable interaction. The model is studied for increasing the speed of the manipulator while maintaining control accuracy. Various experiments are conducted to verify the human hand movement model.

1.4 Contributions

This research has made significant theoretic and practical contributions to research on Human-Robot Interaction (HRI). The theoretical contributions include novel algorithms and methods for enabling efficient HREI:

- A Virtual Force Field (VF^2) approach for efficient robot-environment interaction: including a Three-Dimensional Virtual Force Field (3D-VF^2) method for collision avoidance in a 3D complex environment and an Attractive Force (AF) method for motion planning.
- A haptic force generation method and a workspace mapping method for coordination of the operation of a haptic device and a robot.
- An eXtended Hand Movement (XHM) model for natural and intuitive human-robot interaction and a haptic Force-Speed Control (HFSC) method for operational performance improvement in human-robot interaction.
- The research outcomes have been implemented in a steel bridge maintenance robotic system and tested in both the laboratory and on a bridge maintenance site. A complete software component has been developed and used in the maintenance robotic system.

1.5 Publications

1.5.1 Conference Papers

1. P. Chotiprayanakul, D.K. Liu, D. Wang, and G. Dissanayake (2007), "A 3-dimensional force field method for robot collision avoidance in complex environments", *in Proceedings of the 24th International Symposium on Automation and Robotics in Construction* (ISARC 2007), 19-21 September 2007, Kochi, Kerala, India, pp. 139-145. **(Best student paper award)**
2. P. Chotiprayanakul and D.K. Liu (2009), "Workspace mapping and force control for small haptic device based robot teleoperation", *in Proceedings of 2009 IEEE International Conference on Information and Automation* (ICIA 2009), 22-25 June 2009, Zhuhai/Macau, China, pp. 1613-1618.
3. P. Chotiprayanakul, D. Wang, N.M. Kwok, and D.K. Liu (2008), "A Haptic base human robot interaction approach for robotic grit blasting", *in Proceedings of the 25th International Symposium on Automation and Robotics in Construction*(ISARC 2008), 26-29 June 2008, Vilnius, Lithuania, pp.148-154.

4. P. Chotiprayanakul, D.K. Liu, D. Wang, and G. Dissanayake (2007), "Collision-free trajectory planning for manipulators using virtual force based approach", *in Proceeding of the International Conference on Engineering, Applied Sciences, and Technology*(ICEAST 2007), November 21-23, 2007, Swissôtel Le Concorde, Bangkok, Thailand,4 pages.
5. P. Chotiprayanakul and D.K. Liu (2011), "Performance Improvement in Haptic-based Remote Operation of Sandblasting Robot by a Human Hand Movement Model", *in Proceeding of the 28th International Symposium on Automation and Robotics in Construction* (ISARC 2011), Seoul, South Korea, 29 June-2 July 2011. Part 2, pp 590-596
6. P. Chotiprayanakul and D.K. Liu (2011), "Effect of View Distance and Movement Scale on Haptic-based Teleoperation of Industrial Robots in Complex Environments", *in Proceeding of the 28th International Symposium on Automation and Robotics in Construction* (ISARC 2011), Seoul, South Korea, 29 June-2 July 2011. Part 2, pp 413-418

1.5.2 Journal Papers

1. P. Chotiprayanakul, D.K. Liu, and G. Dissanayake (2010), "Virtual Force Field Approach to Haptic-based Control for a Sandblasting Robot in Complex 3D Environments", revised and submitted again to *Automation in Construction*, in December 2011.

1.6 Thesis outline

Chapter 2 reviews HREI-related research, the current state-of-the-art, and the safety issues inherent in HREI. Robot-environment interaction, motion planning algorithms and collision avoidance methods for robotic manipulators are reviewed. Human-robot interaction and robot teleoperation are reviewed with a focus on haptic-based operation. Human factors in human computer interaction (HCI) are also reviewed for the purpose of research on human-robot interaction.

Chapter 3 describes robot-environment interaction and presents the Virtual Force Field (VF^2) approach, including a force control (FC) algorithm, an Attractive Force (AF) method, and the Three-Dimensional Virtual Force Field ($3D\text{-}VF^2$) algorithm. The AF method generates an attractive force to drive the manipulator to a target position and the $3D\text{-}VF^2$ method generates repulsive forces for collision avoidance. The attractive and repulsive forces are derived in *O-space* and the FC algorithm transforms these forces from *O-space* into joint space and then controls the motion of a robot manipulator. Several case studies are presented to validate these methods.

Chapter 4 presents the research on coordination of a haptic device (master device) and a mobile industrial robot (slave device), including a workspace mapping method and a haptic force generation method. Workspace mapping includes three key control methodologies: drifting control, scaling control, and edge motion control, which enable a small haptic device, with a relatively small workspace, to control a significantly larger manipulator. A virtual spring approach is used to generate haptic force on a haptic device. Occupancy voxel maps are used for reducing the computational time to an acceptable level so that real-time interaction is possible.

Chapter 5 presents an extended human hand movement model, the development of which is based upon human factors, for improving the performance of haptic-based human-robot interaction. The novel contributions to the extended human movement model are presented and experiments are performed to examine the parameters of the extended hand movement model. This model is then implemented in the haptic-based interaction system and is validated through experiments.

Chapter 6 summarises the research work and outcomes presented in this thesis. The limitations of the approaches presented are also discussed. Conclusions are then drawn with regards to this research and avenues for future work are proposed.

Appendices provide details of relevant methods which complement this thesis, along with technical information about the equipment used in this research.

Chapter 2 Literature Review

This chapter presents a literature review of Human-Robot-Environment Interaction (HREI) with a focus specifically on human-robot interaction by means of haptic robotics. Related work in the field of HREI includes physical Human-Robot Interaction (pHRI), robot-environment interaction, robot motion planning including collision avoidance, haptic-based teleoperation, and human factors and ergonomics. When a robotic manipulator (or an industrial robot) is placed in a complex 3D environment to perform a required movement, it must be able to avoid potential collisions with the environment and with itself (self-collision). Therefore, to enable robot-environment interaction (REI), a 3D map of the surrounding environment is needed so that safe plans can be made for a robot manipulator. For collision avoidance and motion planning, there is no obvious method/algorithm that is efficient enough to generate an effective trajectory for 6DOF robot arm in such complex environments with real-time control.

The most important issue in human-robot interaction (HRI) is safety. One way to address this issue is remote operation, which is particularly useful in applications such as sandblasting where it is not recommended that workers carry out their tasks inside a blasting environment for health and safety reasons. Interaction with a remote robot manipulator can be facilitated by using haptic devices that provide kinesthetic feedback, such that the operator can become aware of the operation of the robot and the proximity of the robot to the remote environment. Many haptic force reflection and rendering approaches for enabling high-fidelity have been studied; however, we found it difficult to find an approach that can be directly applied in this research and in the application of sandblasting in steel bridge maintenance. Furthermore, the effect of haptic feedback, provided by a haptic device on the operational performance of operators, needs to be studied through research on human factors. The study of human factors will result inefficient ways to improve the operational performance in haptic-based human-robot interaction.

This chapter is organized as follows: Section 2.1 presents the state-of-the-art HREI research. Section 2.2 introduces the motion planning and collision avoidance approaches applicable to multi-DOF robot manipulators. Section 2.3 reviews the important issues in HRI such as safe interaction, force control and safety standards. Section 2.4 reviews haptic-based teleoperation. Finally, Section 2.5 details the human factors in the context of interaction.

2.1 Human-Robot-Environment Interaction

There is a significant body of literature that describes the different aspects of HREI: social aspects, multi-modal human robot interaction, human-robot interaction architecture, and so on.

Research on human-robot interaction focuses on a contact (either physically or remotely) between a robot and a human operator in order to enable the performance of tasks. There are still many challenges that need to be addressed, such as safety and dependability [17], before robots can be deployed in interactions with humans. For a multiple DOF robot manipulator to perform tasks in a complex environment, it is insufficient to use only a force sensor and an interaction control algorithm [131]; rather, it is advantageous to maintain the operator in the control loop to take advantage of their intelligence and skills in high-level reasoning.

According to current safety standards related to industrial robot operation [18-23], human operators are not allowed to have physical contact with an industrial robot while the robot is performing a task. Remote operation or teleoperation is therefore the most acceptable alternative when the robot is applied to perform a non-repetitive task in a complex, dynamic, partially-known, hazardous environment. The availability of high-speed networks means that real-time teleoperation becomes possible. In order to facilitate comfortable remote operation, kinesthetic feedback to the operator can be provided by using haptic devices [24][25][26]. This haptic feedback helps the operator to control the robot manipulator operation safely in complex environments.

Haptic force feedback has been demonstrated to improve the performance (e.g., movement speed and positioning accuracy) of the remote operation of an industrial robot [27][28]. A haptic device falls into the category of a pointing device, other examples of which would be a computer mouse, touch pad, joystick, or game controller. The international standard applied to a pointing device is ISO 9241-9 which covers non-keyboard input devices and pointing devices (excluding voice input). ISO 9241-9 includes the usability, controllability, and conformability of pointing device usage [14][29]. The fundamental principle of the ISO 9241-9 standard is Fitts's Law and the Steering law of human hand movement [14][30][31]. These laws describe human hand movement models that are applicable to haptic devices. Although standards for pointing devices exist, there is no specific section in these standards which incorporates human factor models and addresses the effect of haptic force feedback on operational performance.

2.2 Robot-Environment Interaction

2.2.1 Environmental Awareness

Industrial robots are typically used in manufacturing environments to perform pre-programmed tasks such as painting, welding and to pick-and-place components. The environments are carefully defined and structured. In field robotics, where mobile industrial robots are deployed in an unstructured and dynamically changing environment, an up-to-date map is required, and a 3D map of an environment must be generated by using sensors, exploration and map building algorithms. However, the 3D map of an environment may be incomplete due to the complexity of the environment and the limitations of the exploration techniques used. Where the 3D map is only partially complete, further exploration and map improvement are required, or alternatively tactile sensor network or skin-type sensors may be used to improve the safety of robot operation.

2.2.1.1 Mapping a Complex 3D Environment

3D scanning sensors can generally provide information about the distance to surfaces in a surrounding environment, and the intensity of each scan ray which reflects back from the surrounding surfaces. In robotics literature, a 3D map of an environment [32][33][34] is generally represented as a point cloud (Figure 2.1) or as a surface mesh model [35]. The intensity of the reflected scan ray, which a 3D scanner can provide, has been shown to allow for classification of surface material-types [34][36][37].

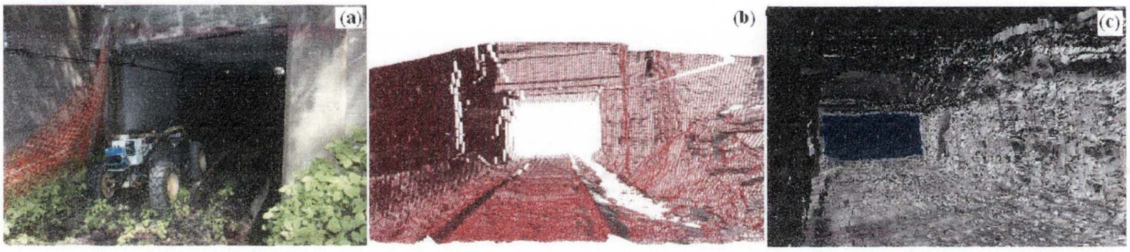

Figure 2.1 a) A mobile robot with 3D scanner, b) 3D local map of a mine corridor, c) 3D virtualisation of a volumetric mine map [32][33]

2.2.1.2 Tactile Sensors

Many sensors can be used for robot environmental awareness. A tactile sensor can be used in robotics to mimic the human sense of touch. There are two common types of tactile sensors: the pressure sensor (e.g., resistive sensor, piezo sensor, strain gauge sensor) and the proximity sensor (e.g., infrared sensor, ultrasonic sensor, capacitive sensor). Figure 2.2 shows examples of sensors. A resistive tactile sensor cell [38], which is made from an electrode board and a piece of conductive polymer, decreases its resistance between electrodes when the conductive polymer is pressed. Force sensing registers [39] are used for measuring touch force. Proximity-type sensors, such as capacitive sensors [40], have been tested in a manipulator-based system to detect the presence of surrounding objects. Capacitive sensors measure the change in electrical capacitance between the electrodes when the sensor is close to an object. Tactile sensors can be connected in an array matrix, and then used as a skin-type sensor that covers the links of a manipulator. Thus, the signal and location of the contact point could be used to improve the control strategy.

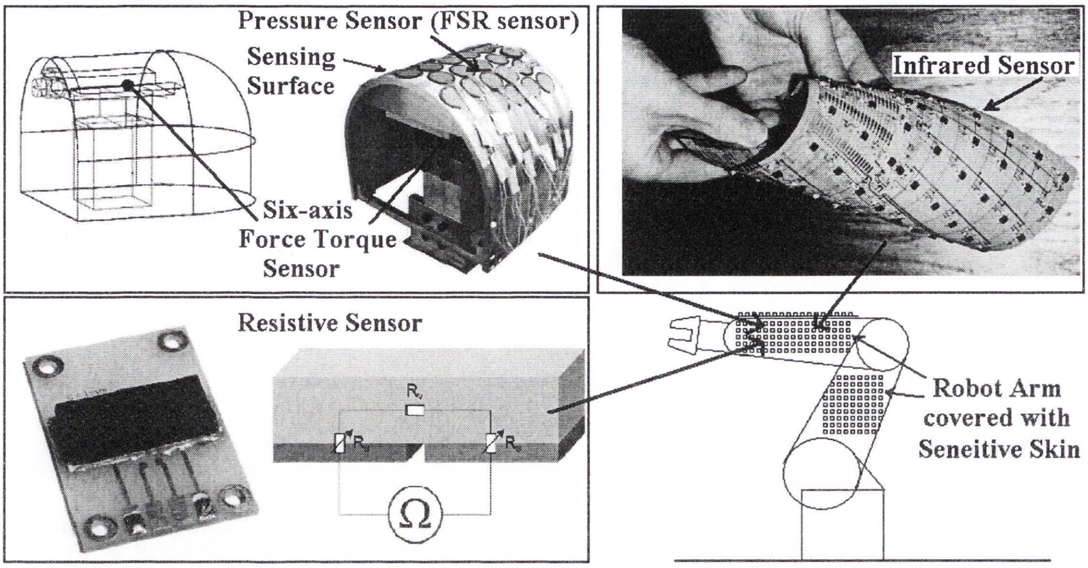

Figure 2.2 Manipulator covered skin-type sensors [38][39][41].

2.2.2 Collision-free Motion Planning

Industrial robots are designed to manipulate objects with high precision, repeatability and speed. Path and collision-free motion planning has been widely investigated and many algorithms have been developed. However, when a mobile robot manipulator is used in a compact and complex 3D environment for performing non-repeatable tasks, efficient on-line motion planning and collision avoidance are still challenging research issues.

2.2.2.1 Motion Planning in Configuration Space

Lozano-Perez proposed a motion planning approach in discrete Configuration Space (*C-space*) [2][3], which uses polyhedrons to represent the geometry of a robot manipulator and the geometry of a static environment($\mathcal{E}$) (Figure 2.3). A pose $\mathbf{q}$ of the manipulator is defined by angles of the joints $q_1\ q_2\ \ldots\ q_n$: $\mathbf{q} = [q_1\ q_2\ \ldots\ q_n]$.

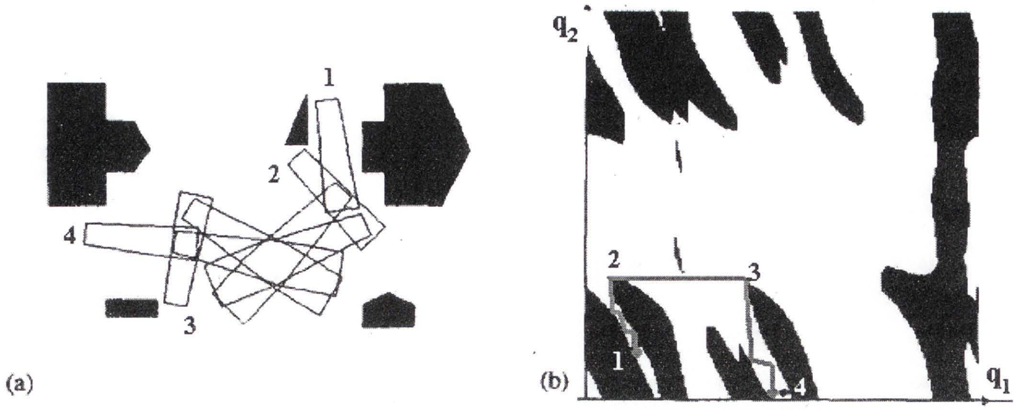

Figure 2.3 (a) Various intermediate configurations (b) Path found between start (1) and goal (4) configurations [3]

The geometry of a robot manipulator and the geometry of a static environment are used to generate a *C-space* map ($\mathcal{C}$) in the joint space ($\Re_q{}^n$) where n is the number of joints of a manipulator. In a *C-space* map, a manipulator pose is represented by a point. A motion planner is then used to plan a continuous motion through the free space($\mathcal{C}_f$). Thus, planning in *C-space* does not need to consider the physical properties of the manipulator.

2.2.2.2 Sampling-Based Planning Approaches

Sampling-based planning is a motion planning approach using a *C-space* map. A network of road fragments through *C-space* is generated for a manipulator or a mobile robot that covers the free-space ($\mathcal{C}_f$). A search is conducted through the connected network to determine the shortest motion path. An example of a sampling-based planning approach is the roadmap method [42]. This method generates a network of links by building a graph which connects all the vertices of the polygonal obstacles with the lines that do not cross the obstacles. However, the generation of the links can be easily trapped by bottle-necks created in the roadmap due to obstacles. To overcome this bottle-neck problem, Brooks [4] proposed an extension known as the freeway method. Brooks' freeway method finds obstacles that face each other and generates a freeway to passing between them. This path segment is a generalised cylinder. A freeway is an elongated piece of free-space that describes a path between obstacles. This freeway may be described as overlapping cones; it is essentially composed of straight lines with free-space on both sides, which could easily be inverted. A generalised cone is obtained by sweeping a two-dimensional cross section along a curve in space, called a spine, and deforming it according to a sweeping rule.

Figure 2.4 (a) shows the probabilistic roadmaps method [43][44], which is another popular way of building a roadmap in sampling-based planning. Nodes or links are randomly generated in the free-space ($\boldsymbol{C}_f$), and are linked to each other by lines that do not cross obstacles. This enables a roadmap network to be built. A search is then conducted to find the shortest path.

Figure 2.4 (b) shows a 2D example of the Rapidly-exploring Random Tree (RRT) method [46] which is used extensively for planning in high-dimensional space. The concept of the RRT is to incrementally construct links from the current node to the next random nodes like the branches of a tree. The node that is generated closest to the target will then be defined as the next node for generating new branches.

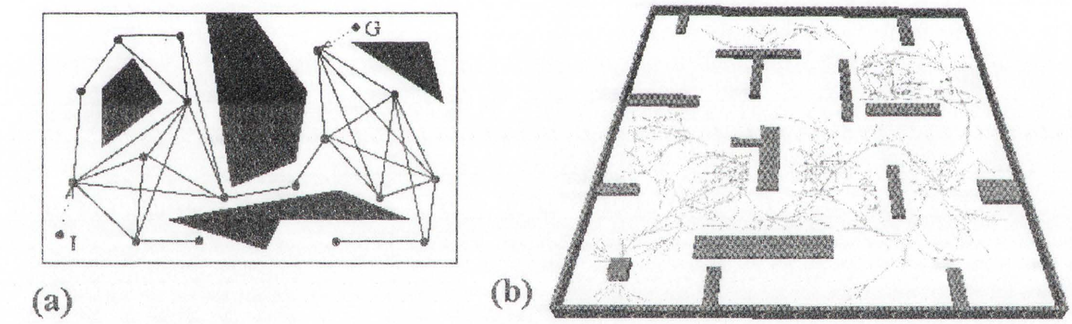

Figure 2.4 (a) Probabilistic roadmaps [43] [44], (b) RRT method [46]

2.2.2.3 Potential Field Method

The Potential Field (PF) method is widely used for collision-free motion planning in the Operational space (*O-space*): the Cartesian coordinate space. The PF method was first proposed by Khatib [5][6] for manipulators and mobile robots. Researchers have developed different methods based on the concept of PF [5][47]. In this method, a manipulator or mobile robot is attracted by a target point which is the minimum potential point on the field and it is repulsed by the high potential points which are closed to obstacles. A potential field [5] is represented as $U_{art}(x)$which includes the attractive potential field as $U_{x_d}(x)$ and the artificial potential field $U_o(x)$ as shown in Figure 2.5.

$$U_{art}(x) = U_{x_d}(x) + U_o(x) \tag{2.1}$$

$$U_{x_d}(x) = \frac{1}{2}k_p(x - x_d)^2 \tag{2.2}$$

$$U_o(x) = \begin{cases} \frac{1}{2}\eta\left(\frac{1}{\rho} - \frac{1}{\rho_0}\right)^2 & if\ \rho \leq \rho_0 \\ 0 & if\ \rho > \rho_0 \end{cases} \tag{2.3}$$

where x is the current position of the robot and x_d is the goal position and k_p is a position gain.ρ represents the shortest distance between the robot and an obstacle and ρ_0 denotes the influence distance of the potential field. η is a constant which determines the magnitude of the repulsive potential.

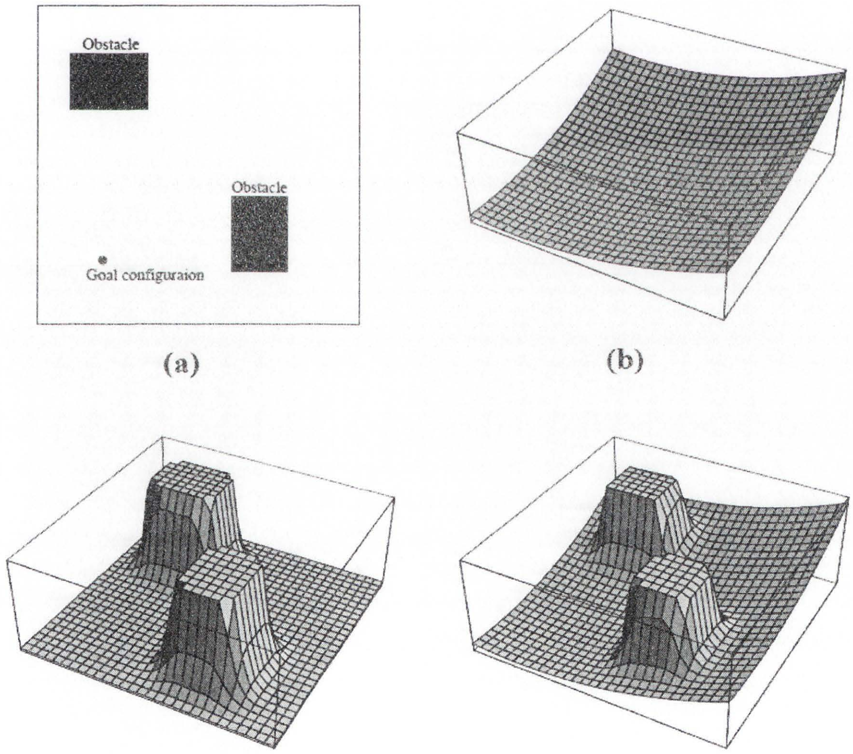

(a) (b)

(c) (d)

Figure 2.5 An example of a 2D potential field [5]:(a) Operational space of a robot, (b) Attractive potential field, (c) Artificial potential field, (d) Potential field

Based on the concept of PF, Juang [47][48] applied polyhedrons to represent a manipulator and a potential field method to dynamically control the manipulator. Lin and Chuang [49] used potential fields in a 3D workspace to generate a collision-free path by locally adjusting the robot configuration for the minimum potential. Xie [50] used spheres covering a robot and converted the repulsive forces to joint torques by inverse kinematics to find a collision-free trajectory. Inverse kinematics for force control can generate jerky movements to the robot at singularity poses. The PF method can also be applied to *C-space* planning. A manipulator that is represented as a vector **q** in *C-space* can be guided to the target point passing through a *C-space* map by using a potential field method [51].

2.2.2.4 Elastic Strip Method

Brock and Khatib [7] presented an elastic strip framework. The concept of the elastic strip is developed from the elastic band method [4] which supports a higher DOF mobile manipulator. The elastic strip is a combination of a pre-planned paths and motions that enables real-time collision avoidance.

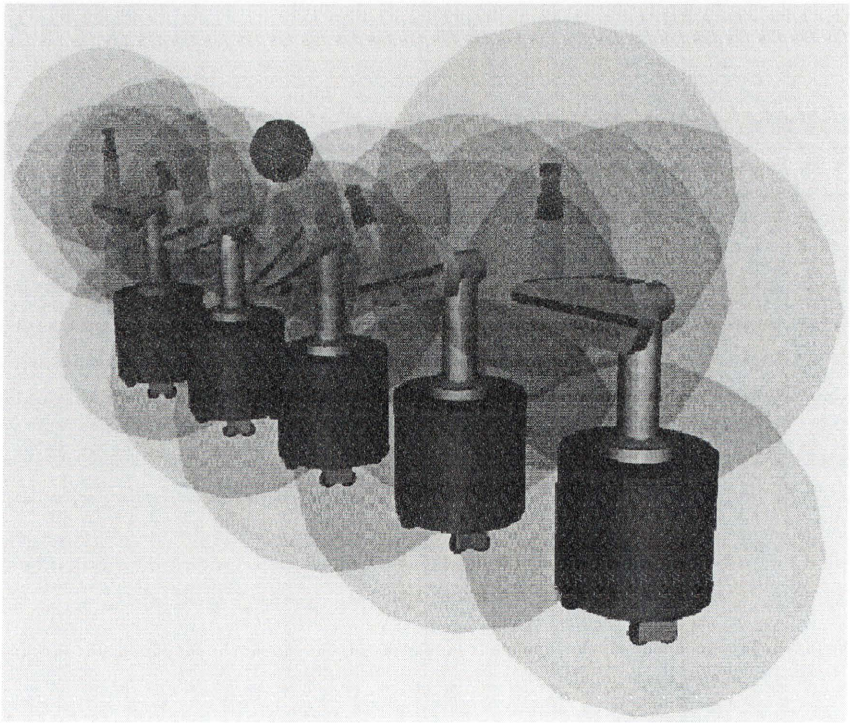

Figure 2.6 Elastic tunnel: configurations are selected from pre-planned path. The union of protective hulls of these configurations forms an elastic tunnel. [7]

A manipulator is covered by a virtual protective hull (Figure 2.6). The configuration of the protective hull is changed along the pre-planned path due to obstacles. During operation, the set of continuous protective hulls along a pre-planned path (i.e. elastic tunnels) will deform automatically depending on how the environment changes.

2.2.2.5 Weight Voxel Map Approach

Greenspan and Burtnyk [52][53] modelled a manipulator and obstacles with sets of spheres. By measuring the distances with a weighted voxel map, they demonstrated successful collision avoidance and on-line path planning in an open space (with few obstacles). However, the method still needs to be tested if it is to be used in compact and complex environments.

2.2.2.6 Optimal Pose Selection Method

A pose selection method [54][55] uses forward kinematics to generate a set of possible manipulator joint configurations. A search is then done on the set to find the optimal solution according to predefined constraint functions. This method is normally an offline and discrete pose selection method, and is not focused on online collision-free path planning. Applying this method for on-line motion planning is difficult, particularly if there are many obstacles located around the manipulator operating in a compact and complex environment.

2.3 Human-Robot Interaction

Human-Robot Interaction (HRI) research aims to enable a robot to interact with people either through direct and physical contact (physical interaction) or remote and indirect contact (e.g., gesture and verbal based interaction).HRI has attracted a lot attention from researchers. To achieve safe, intelligent and intuitive interaction there are still numerous research issues that need to be addressed.

2.3.1 Physical Human-Robot Interaction

In physical Human-Robot Interaction (pHRI), a human operator has physical contact with a robot. The robot responds to the human operator's intentions, which can be identified by sensors such as force sensors, cameras, and so on.

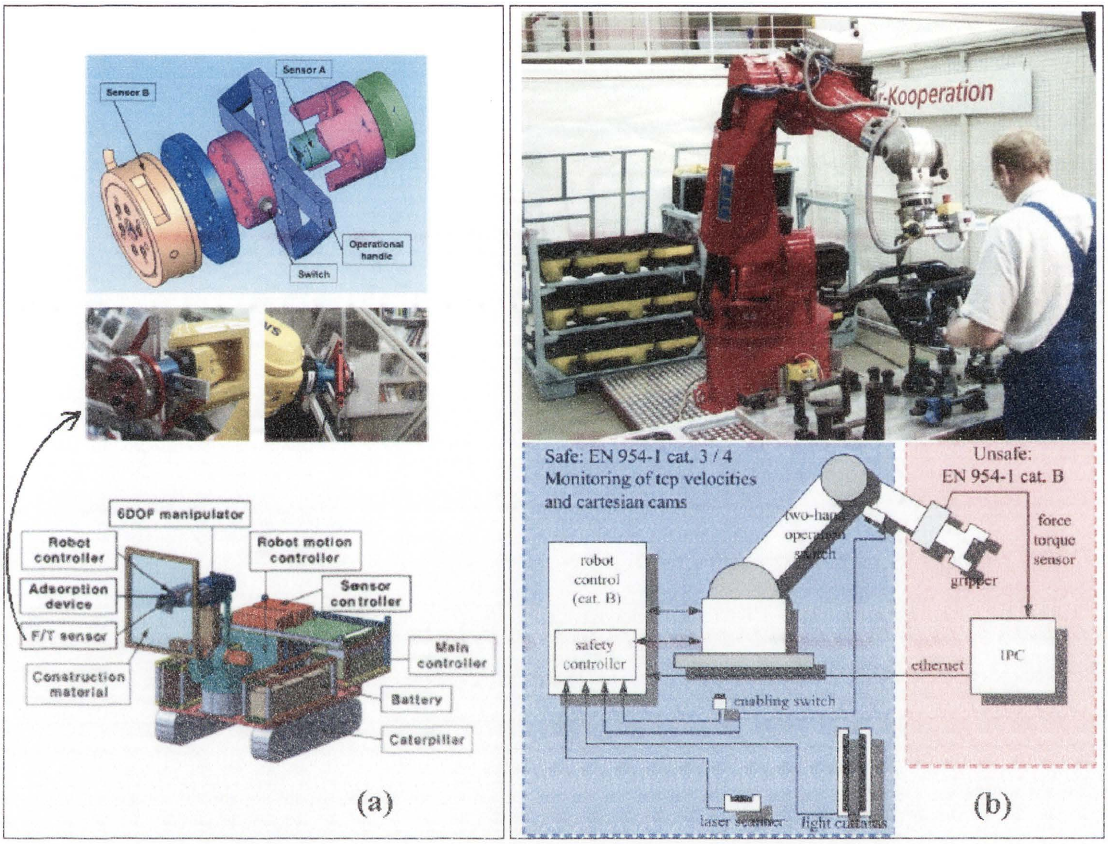

Figure 2.7 (a) System overview of multipurpose robot for installing construction materials [56][57], (b) System overview of PowerMate robot for gearbox assembly [58]

Fujisawa *et al.* [59] and Fukuda *et al.*[60] presented an assistant mobile manipulator for lifting and moving a heavy object. Two force sensors were used to weigh objects and to measure the pulling force of an operator. A 'ratio of intent' is then used to classify an operator's command in this research. Wu [61] designed a 12DOF force sensor to measure the interaction forces, and to determine the mass of a grasped object. Esteves [62] presented a motion planning algorithm for human and mobile manipulator cooperation in a slab lifting task. Kobayashi [63] presented a novel force estimation technique which was shown to work without a multi-DOF force sensor. For robots in construction, Lee [56][57] presented a Multipurpose Field Robot (MFR) for installing construction materials (Figure 2.7a) and a sophisticated motion planning algorithm for heavy material installation. In PowerMate [58] (Figure 2.7b), a 6DOF force sensor is used to control a manipulator in the assembly of an automotive rear gearbox. Recently, ABB launched two commercial programs called RobotWare Assembly FC and RobotWare Machining FC [64]. These programs interface with a 6DOF force sensor and the position controller of a manipulator to plan the motions of a manipulator performing assembly tasks.

2.3.2 Force Control Method

The force control method [65] has been studied for motion control of industrial robots. In this method, an external force, **F**, from an operator (e.g., a push or pull force) or a virtual force from an obstacle (e.g., a virtual repulsive force generated based on the distance of the robot from an obstacle)is converted to control signals for controlling the motion of a robot manipulator. Force control can be achieved by using the dynamic model of an industrial manipulator:

$$A(q)\ddot{q} + b(q,\dot{q}) + g(q) = \Gamma \tag{2.4}$$

where $b(q,\dot{q})$, $g(q)$, and Γrepresent the centripetal and Coriolis effects matrix, gravity torque vector, and generalised joint torque/force vector in joint space, respectively. $A(q)$ is the joint-space inertia matrix. q,$\dot{q}$,and $\ddot{q}$ are the joint angles, joint angular velocities, and joint angular accelerations of the manipulator, respectively. The transformation from a Cartesian force to a joint force is given by

$$\Gamma = \mathbf{J}^{\mathrm{T}}(q)\mathbf{F} \tag{2.5}$$

where $\mathbf{J}^{\mathrm{T}}$ is Jacobian transpose matrix of the manipulator. Therefore,

$$A(q)\ddot{q} + b(q,\dot{q}) + g(q) = \mathbf{J}^{\mathrm{T}}(q)\mathbf{F} \tag{2.6}$$

More details of the force control method are presented in [65][78][79].

2.3.3 Safety in HRI

2.3.3.1 Safety Standards in Robot Operation

Standards for safe robot operation [18-23] in factories and industrial environments that were established in the 1980s prohibited close contact between humans and operating robots. In order to enable safe pHRI these standards have been regularly updated, but human operators are still not allowed to be in the work envelope of an operating industrial robot when it is working. Some of the international standards which are used today include:

- ANSI/RIA R15.06-1999 Industrial Robots and Robot Systems - Safety Requirements (American National Standard)
- EN775:1993 Manipulating Industrial Robots-Safety (European Countries)
- ISO 10218-1:2006 Robots for Industrial Environments-Safety Requirements (International Organization for Standardization)
- AS2939:1987 Industrial Robot Systems-Safe Design and Usage (Australian Standard®)

2.3.3.1 HRI Safety Research

Safety is an important issue in HRI, particularly in physical interaction. Safety and dependability in HRI are discussed by Alami in [17]. In general, research on safe HRI has focused on both an active approach and a passive approach. The active approach aims to prevent an accident, and the passive approach seeks to minimise any possible loss due to an accident.

Some researchers have conducted research on an active approach to safe HRI. The Collaborative Advanced Robotics and Intelligent Systems (CARIS) Laboratory at the University of British Columbia in Canada has studied human robot interaction and its safety strategies based on human monitoring [80][81]. Kulic and Croft [9][82] estimated a level of danger for a motion plan by monitoring a user with robot vision. This research also used the physiological measurements (i.e. electromyography) to detect a user's level of anxiety and emotion [83].

Oberer [84] shows a simulation system of a crash test by swinging the arm of a manipulator into a dummy's torso, neck, or head (Figure 2.8). The simulation program Comau SMART NS16 [85] is the same program used in car crash simulation and severe injury index values are collected from simulation and analysis.

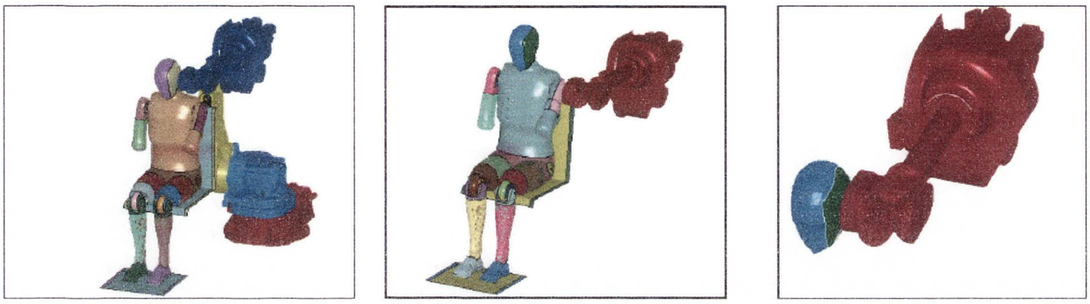

Figure 2.8 Robot-dummy crash simulation setups [84]

To facilitate safe interaction in physical HRI, lightweight manipulators have been developed to meet the Head Injury Criterion (HIC) [85]. Examples include the Kuka-DLR light weight robots, and the WAM robot from Barrett Technology Inc [86]. Research has also been conducted in new actuations [88] and flexible compliant joints[89].

2.4 Haptic-based interaction

Haptic technology has been developed in Human-Computer Interaction (HCI) that allows a user to explore a virtual world, and haptic devices have been applied to control robots remotely. A force feedback haptic device is used in this thesis to enable HREI. By providing an operator with kinesthetic perception using a haptic device, the operator is able to remotely control a robot more safely and accurately.

There are two main types of haptic devices providing force feedback: a parallel-mechanism (Stewart platform), and a serial-link mechanism [90][91]. The available haptic devices generally have a smaller workspace than a typical industrial robot manipulator; thus, workspace mapping algorithms are required. Workspace mapping should allow relatively small movements made by the operator's hand in the haptic workspace to control relatively large manipulator movements. Additionally, this mapping should not distort the kinesthetic feedback.

2.4.1 Haptic Force Reflection

A simple method for haptic force reflection is to use a haptic device which has the same configuration (i.e. type of mechanism) as a manipulator [92] (Figure 2.9), but they may not be the same size, i.e. the haptic device usually smaller than a manipulator. The haptic device will thus have the same pose as the robot. Once the robot is running close to an obstacle and stops, the haptic device will stop at the same pose. This simple method has been shown in some applications [94][95]; however, it can not be easily applied in a system in which the haptic device has different configuration from the manipulator.

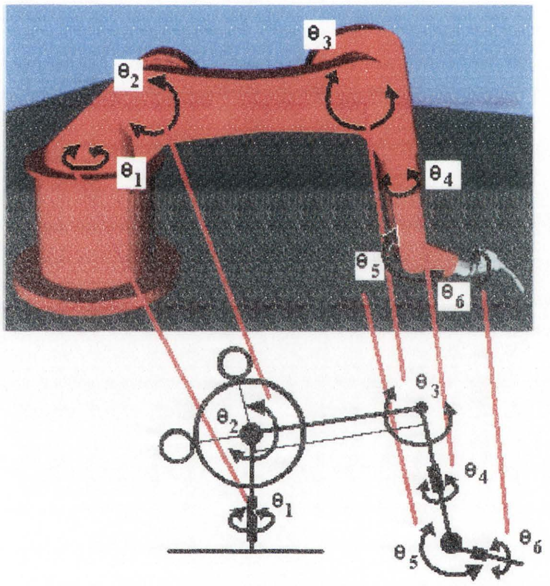

Figure 2.9 Haptic force reflection (rearranged figure from [92])

A virtual spring approach [96][24] is a popular haptic force reflection approach (Figure 2.10). The virtual spring [94][98][100][101] is used to enable a haptic cursor (avatar) to be virtually connected to the end-effector of a manipulator. A virtual tension force, generated by the virtual spring, can be considered to be the pulling force for a manipulator. This force is proportional to the distance between the haptic cursor and the virtual robot end-effector [94][100][101]. The virtual tension force is then translated to a haptic force by a haptic device, and is fed back to the operator's hand. In the case where 'contact' is required between the operator and the remote environment [26][58][102], sensors may be installed on the manipulator to enable objects in the surrounding environment to be sensed, and then transmitted to the operator by haptic feedback. A virtual touch approach [98] has been applied to haptic force rendering [34], where the sensor used was a 3D scanner.

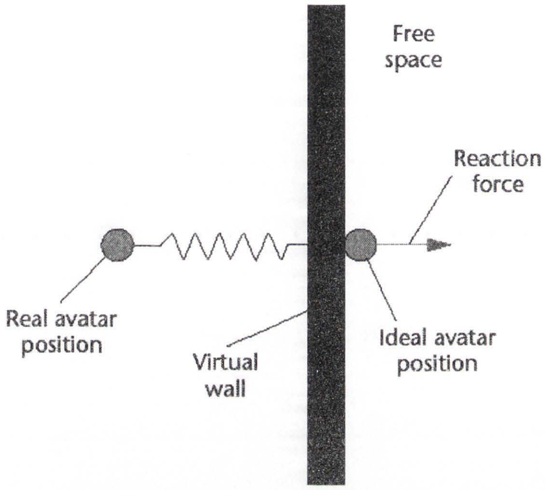

Figure 2.10 Virtual spring conceptual diagram [96]

2.4.2 Workspace Mapping

There are several different types of haptic devices with different sizes, payloads, degrees of freedom, resolutions and internal mechanisms. The workspace of a haptic device is normally smaller than the workspace of a robot manipulator. Building a large haptic device [103] or an exoskeleton device [104] that has a workspace which matches the workspace of an industrial robot manipulator is generally not an option. Therefore, in haptic-based teleoperation, a transformation that includes scaling, rotating and translating is required to 'map' a haptic device workspace and a robot manipulator workspace. However, workspace transformation affects the perception of a human operator, and the resolution and precision of haptic-based remote control [11]. Spanning a large workspace [13] has been shown to enable the haptic cursor to effectively reach a large workspace, but the operator may perform unnecessary movement when approaching a target; therefore, the spanning algorithm must be carefully formulated.

2.4.3 Computation Time and Time delay

Communication and computational time in haptic-based human-robot interaction and teleoperation are important considerations when a high-quality haptic force reflection is required. In order to provide high-fidelity feedback to a human [90][91], a feedback force with at least a 1kHz refresh rate is needed. Furthermore, the display refresh rate of the surveillance camera, the animation or the simulation should be more than 30 frames per second, and time delay should be lower than 50ms to avoid the latency effect.

Another important consideration is the operational performance which is indicated by transparency of a teleoperation system [95][105][106]. The transparency (Z) is given by the ratio of impedance of the master system - haptic device (Z_h=F_h/V_h) to the impedance of the slave system - manipulator (Z_e=F_e/V_e)[95]. F_h and V_h are the force and the speed of the haptic handle applied by the operator. F_e and V_e are the haptic force and the speed of the haptic cursor occurring when the haptic cursor contacts the environment. A model of the master-slave system with time delay is shown in Figure 2.11. Three significant factors that affect transparency are the computation time of the master system (T_h), the computation time of the slave system (T_e), and the communication delay time (T_d). These time factors are presented in Equation 2.11. For the ideal case (Z=1 or Z_e=Z_h) [106], time delay and computation times must be zero.

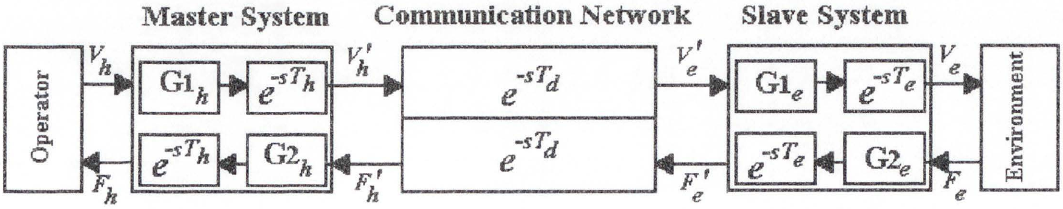

Figure 2.11 A model of the master-slave teleoperation system with computation time and communication delay time.

$$Z_e = \frac{F_e}{V_e} \tag{2.7}$$

$$Z_h = \frac{F_h}{V_h} \tag{2.8}$$

$$Z = \frac{Z_h}{Z_e} = \frac{F_h}{V_h}\frac{V_e}{F_e} \tag{2.9}$$

$$Z = G1_h G1_e G2_h G2_e e^{-s(2T_h+2T_e+2T_d)} \tag{2.10}$$

From the transparency function, Deng [107] analysed the stability of time-delay teleoperation systems. The results from [25][107][108] indicate that the stability of a time-delay teleoperation system is dependent on the time delay and force frequency generated by the master system.

2.5 Human Factors in Haptic Interface and Haptic-based Human-Robot Interaction

The study of human factors seeks to understand human psychomotor behaviour along with human capability. Psychomotor behaviour concerns the collaboration between the mind, eye, brain, and body. In computer interfacing, when a human looks at a target point and the current cursor position of the pointing device in a monitor, the brain receives information from the eyes and sends commands to the hand muscles to compensate for positional difference. A simple pointing task or Point-and-Click task is common when interfacing with a Graphic User Interface (GUI) and for a human interfacing with a robot in 2D and 3D environments. For HREI by means of haptic device, a haptic device is used to control the robot and to provide kinesthetic feedback to an operator. However, an operator still needs to locate the position of the robot with their eyes in a virtual map or virtual environment. The most popular model of human psychomotor behaviour is Fitts's law of human hand movement [14], which was first presented by P. M. Fitts in 1954. Fitts's law has been used to predict movement time and indicate the difficulty of using computer-input devices. This law has been mathematically formulated upon empirical evidence gathered from experiments which include a single dimension movement testing method and a circular testing method. In 1997, Accot and Zhai [31] presented a well-known extension to the Steering law of human hand movement. The Steering Law takes the geometry of the travelling path (i.e. a path width and a travelling distance) and hand movement into consideration.

Accot and Zhai derived an index of difficulty for Fitts's law in an integral form, which can be used to test movements along a 2D tunnel path. Accot-Zhai's Steering law[15][31][30] is now widely used to evaluate GUI design in computer applications, operating systems and computer-console games. The two most common design guidelines for software and hardware interaction are ISO 9241-920:2009-3: Ergonomic of Human System Interaction for Tactile and Haptic Hardware and Software Interaction, and ISO 9241-9: Virtual Display Terminals (VDTs) - requirements of non-keyboard input device [29].

Teleoperation is usually conducted through multi-level workspaces that need coordinate transformations to map the workspace of the operator and the workspace of the robot agent. A coordinate transformation, which is also known as a workspace transformation, includes scaling, zooming, rotating, translating, mirroring, and other irregular transformations. The transformation might affect an operator's performance in terms of their accuracy and control ability. The distance between the observing camera and the operational space causes jitter [117], i.e. cursor vibration due to the instability of human hand movement and the resolution of an input device (e.g., haptic device). A low-pass filter is often applied to reduce the jitter effect, but this solution can magnify the latency effect [117]. The scaling and zooming effect was investigated by researchers such as Accot and Zhai [30] in 2001, Guiard and Lafon [118] in 2004, and Casiez [12] in 2008. Their research showed the effect of Control-Movement (CM) scaling and Control-Display (CD) scaling on the movement time for pointing tasks. In 2009, Munoz and Casals proposed an adaptive multi-space transformation for improving the human-robot interface [11], which showed the relationship between the workspace and the accuracy of a manipulator when teleoperated by a joystick.

2.5.1 Fitts's Law

According to Fitts's law [14], human psychomotor behaviour is formulated as a human hand movement model for a pointing task. The human hand movement model is useful when describing tasks such as hand-writing and computer interaction in a virtual 3D environment. The movement time (*MT*) of a point-to-point task, disregarding the trajectory, is a function of the geometry of a task and the characteristics of the movement exhibited by an operator. The geometry of a task, which includes the size of the target (ϕ) and the travel distance (s) (examples are shown in Figure 2.12), indicate the difficulty of the task.

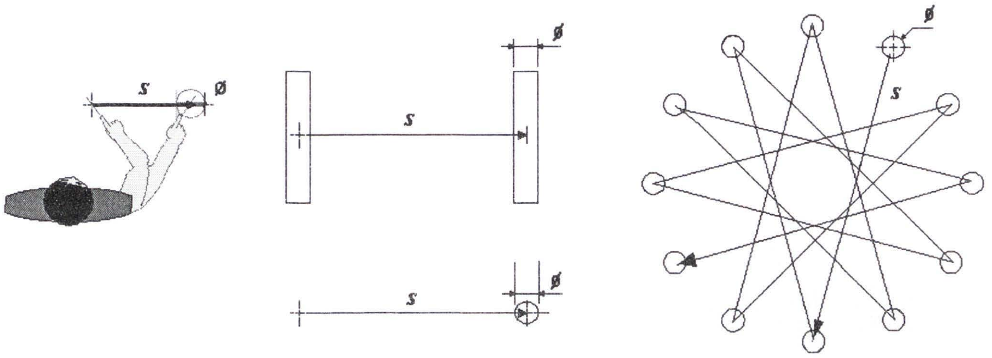

Figure 2.12 Common target patterns for performance testing of pointing tasks by Fitts's law

$$MT = a + b\,ID \tag{2.11}$$

$$ID = \log_2\left(\frac{s}{\emptyset} + 1\right) \tag{2.12}$$

Where a is the start/stop time, b is the inherent speed of the operator hand movement, and ID is index of difficulty (a function of the geometry of the task).

2.5.2 Steering Law

In Steering law [31][15], a 2D contour path is created by moving a target along a desired path (s) in n steps, where every step moves ds. The path width of the contour isϕ. Therefore, the Fitts's law equation has been modified by [31][15] and presented as

$$MT = \lim_{ds\to 0}\left(\sum_{i=0}^{n}\left(a + b\,\log_2\left(\frac{ds_i}{\emptyset} + 1\right)\right)\right) \tag{2.13}$$

$$MT = a + b\int lim_{ds\to 0}\left(log_2\left(\frac{ds}{\emptyset} + 1\right)\right) \tag{2.14}$$

$$ID = b\int lim_{ds\to 0}\left(log_2\left(\frac{ds}{\emptyset} + 1\right)\right) \tag{2.15}$$

If x=ds/ϕ, $\lim_{x\to 0}\frac{(\ln(x+1))}{x} = 1$, the Fitts's law equation becomes,

$$ID = \frac{b}{\ln 2} \int \frac{ds}{\emptyset} \tag{2.16}$$

Let $\frac{b}{\ln 2}$ be represented by b' and then the equation of human movement in Steering law is given by

$$MT = a + \acute{b} \int \frac{ds}{\emptyset} \tag{2.17}$$

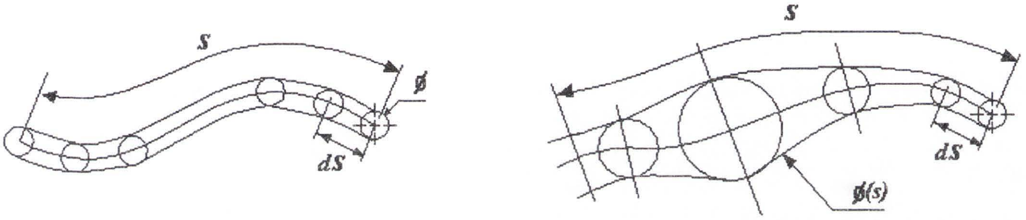

(a) (b)

Figure 2.13 (a) Path width does not change, (b) Path width changes with path length

If the width of a path ϕ is a function of the path length (s) (Figure 2.13b), the Steering law is given by

$$MT = a + \acute{b} \int \frac{ds}{\emptyset(s)} \tag{2.18}$$

However, if the width of a path ϕdoes not change (Figure 2.13a), the Steering law is given by

$$MT = a + \acute{b} \left(\frac{s}{\emptyset}\right) \tag{2.19}$$

2.5.3 Control-Movement Scale and Control-Display Scale

When an operator performs a task using visual feedback or a virtual environment, as shown in Figure 2.14, the length of a path and the target size are closely related to the difficulty of the task (*ID*). In order to show the task space (i.e. where the task is performed) at an optimal size for the operation, the dimension of the task space can be scaled up or down by a control-display scale (CD gain: G_e) according to Casiez's work

[12].The CD gain (G_e) from [30] can be used to scale the target size (ϕ)to a perceived target size (ϕ_e).

$$G_e = \frac{s_e}{s} = \frac{\emptyset_e}{\emptyset} \tag{2.20}$$

A control-movement scale (CM gain: G_h) is used to represent the relationship between a task distance (s) and a hand moving distance (s_h) [12][30].

$$G_h = \frac{s_h}{s} = \frac{\emptyset_h}{\emptyset} \tag{2.21}$$

For computer-based operation, both CM scale and CD scale are used to scale the task space (s and ϕ) to the operational space (s_h and ϕ_e).

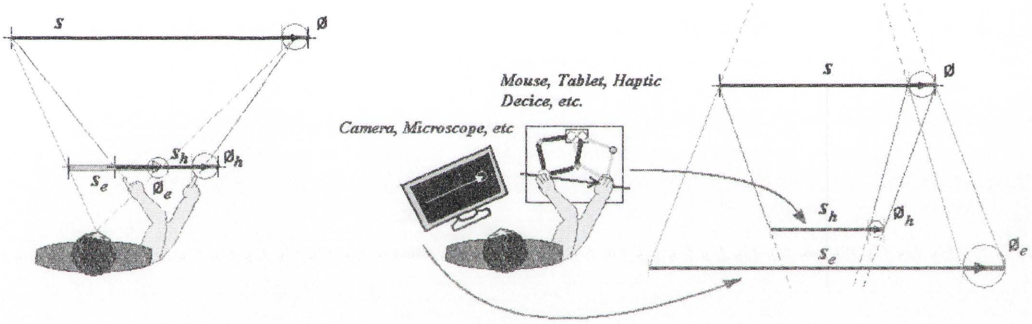

Figure 2.14 Control-Display scale and Control-Movement scale

Fitts's law and the Steering law have been modified by using CM and CD [12][30] and are shown in Equation 2.22 and Equation 2.23, respectively. For point-to-point movement, Fitts's law:

$$MT = a + b\log_2\left(\frac{s}{G_x\emptyset} + 1\right), \text{where} G_x = \frac{G_e}{G_h} \tag{2.22}$$

For contour movement, the Steering law

$$MT = a + b\int \frac{ds}{G_x\emptyset}, \text{where} G_x = \frac{G_e}{G_h} \tag{2.23}$$

where G_x is a control scale of the human hand movement.

2.5.4 Index of Performance

In Fitts's law, the Index of Performance (*IP*) [14] characterises how quickly a pointing task can be completed. There are two conventional definitions for *IP*: *IP=1/b* and *IP=ID/MT*. For *IP=1/b*, this *IP* is also called throughput *TP* [14][120]. For *IP=ID/MT*, *IP* is the index of overall performance that indicates the movement speed of the operator relative to the index of difficulty. Both definitions of *IP* depend upon a factor of time without considering the factor of pointing accuracy. Besides these two definitions, there are other definitions of operational performance such as *IP=speed×accuracy* in the manufacturing process[121], *IP=quality/cost* in the economic point-of-view, *IP=output/input* in general process control.

2.6 Summary

There is a significant body of literature on the topics related to HREI. In order to address the challenges in HERI, however, particularly when the robot is used in complex 3D environment, novel approaches are required. To the best of our knowledge, we have not seen a research that systematically addresses the issues inherent in developing a practically deployable HREI system. The major challenges in HEIR, which need to be addressed in a closely integrated approach, are summarised as follows.

Environmental awareness and online motion planning and collision avoidance: Motion planning in *C-space* is a time consuming process. For a multiple DOF robot manipulator operating in a complex and unstructured dynamic 3D environment, on-line motion planning in *C-space* is challenging. In *O-space*, Potential Field (PF) approaches have been used to generate a collision-free motion for a manipulator. However, their application in planning the collision-free motion of a robot manipulator in a complex 3D environment is limited. The elastic strip method which relies on the elastic tunnels can fail when a large obstacle suddenly appears between the current position and the goal position of the robot. This research will present a new Virtual Force Field (VF^2) approach for online collision-free motion planning for a multi DOF manipulator in a complex 3D environment, eliminating jerk motions at singularity conditions, and enabling real-time teleoperation.

Human-robot interaction by means of haptic robotics: Haptic-based HRI is an effective approach for an operator to interact with a robot manipulator operating remotely in complex and hazardous environments, such as those in steel bridge maintenance. Haptic devices can provide an operator with the kinesthetic feedback to enable safe and intuitive interaction. However, many challenges, including haptic force reflection, workspace mapping, system transparency, and computation time need to be addressed.

Human factors and their effect on human-robot interaction: In order to facilitate comfortable, safe and friendly human-robot interaction, and to improve operational performance, Human Factor (HF) models need to be investigated. Incorporation of HF models in human-robot interaction research will also significantly improve the speed and accuracy of operation, and improve operational performance.

This research aims to systematically address these research challenges in HREI, develop new methods and algorithms that enable safe, friendly and intuitive haptic-based human robot interact, and develop a practically deployable HREI system for a robotic steel bridge maintenance system that operates in compact, complex and hazardous steel bridge maintenance environments.

Chapter 3 Virtual Force Field Approach for Robot-Environment Interaction

This chapter presents a Virtual Force Field (VF^2) approach to efficient online motion planning and collision avoidance for a robot manipulator to interact with a complex 3D environment. The VF^2 approach generates an attractive force that 'pulls' the end-effector of the manipulator toward a target position, and repulsive forces that push the manipulator away from obstacles. Consequently, the robot manipulator is enabled to interact with the complex environment.

The VF^2 approach comprises of three components: the Attractive Force (AF) method, the Three-Dimensional Virtual Force Field (3D-VF^2) method, and the Force Control (FC) algorithm. A conceptual diagram of the VF^2 is shown in Figure 3.1(a). The AF method generates a driving force (also called an attractive force) to pull the end-effector of the robot manipulator towards a desired target position. The 3D-VF^2 method generates virtual repulsive forces, which act on the links of the manipulator when the manipulator moves into close proximity with surrounding obstacles. Both the AF and the 3D-VF^2 methods generate forces in *O-space*. All forces in *O-space* are converted to joint torques in joint space ($\mathfrak{R}_q^7$) by the FC algorithm. The joint torques then drive the robot manipulator in a complex 3D environment safely and efficiently, which is an essential issue in Robot-Environment Interaction (REI).

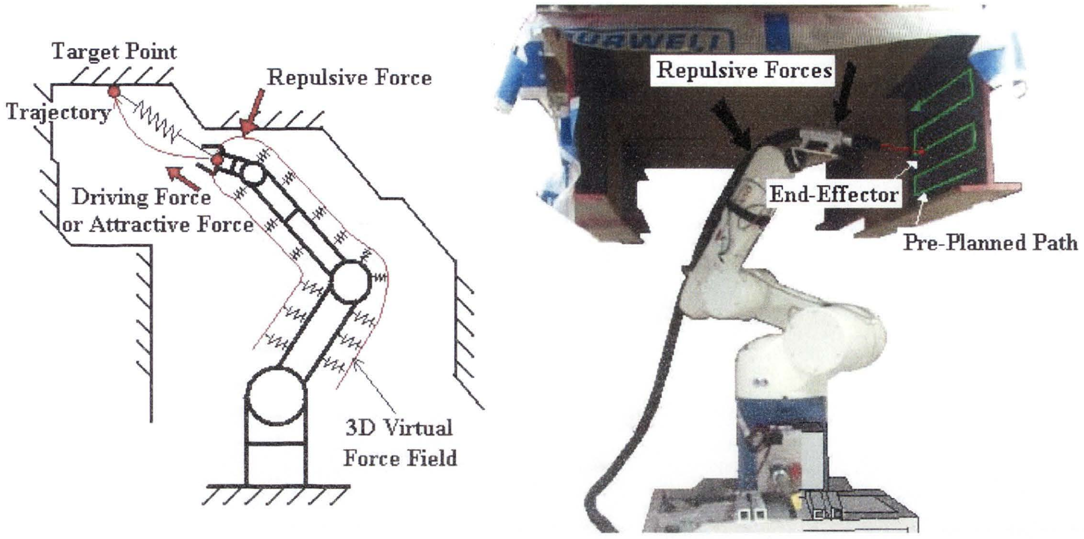

(a) (b)

Figure 3.1 (a) The Virtual Force Field (VF^2) approach that enables safe and efficient Robot-Environment Interaction (REI) (b) A sandblasting robotic system

3.1 Robot-Environment Interaction

In Robot Environment Interaction (REI), the environment consists of two spaces: a task space and an obstacle space. A robot manipulator behaves differently in these two spaces. In an obstacle space, the manipulator must avoid any potential collisions with obstacles. In a task space, the manipulator undertakes tasks which may require physical contact with the environment; example tasks include loading and unloading, welding, and assembly. Tasks such as painting and sandblasting do not require the robot to physically contact the environment, but the distance between the nozzle and the target surface needs to maintain a constant distance (or be in a certain range). It is therefore also considered to be a robot interaction with the environment. The complexity of an environment significantly affects the robot's performance, and efficient real-time motion planning and collision avoidance is a key issue in REI, particularly in complex 3D environments.

Figure 3.1(b) shows an example of REI in which a robot manipulator conducts a sandblasting operation in a complex steel bridge environment. While the manipulator end-effector is following a pre-planned path based on sandblasting requirements, the whole of the manipulator must avoid potential collisions. This is achieved by using the 3D virtual force field (VF^2) method proposed in this chapter. The 3D-VF^2 approach generates an enclosing virtual force field which is wrapped around the manipulator. Virtual repulsive forces are generated when obstacles come within the range of the virtual force field of the manipulator. The movement of the manipulator from its current position to a (instant) target position, which is a way point on the pre-planned path, is achieved by an attractive force.

3.2 Environmental Awareness

When a robot manipulator is placed in complex and unstructured environments, as in many field robot applications, acquiring knowledge about the environment is essential. The capability of a robot to gather information about the position of obstacles in the environment is fundamental to this research; consequently, a map of the geometry of the operating environment is built and used for collision-free motion planning.

In order to generate a map of the environment, a laser range scanner is mounted at the end-effector of the robot manipulator, and the manipulator orients its wrist to sweep the laser scanner. The range data is then used to construct a geometrical map of the environment.

As part of the Robotic System for Steel Bridge Maintenance Project, a technique was proposed to enable the exploration of an unknown environment: Autonomous eXploration to Build A Map (AXBAM) [34][133]. After sending the manipulator into an environment, the first scan is taken with moving joint 5 only to guarantee a safe scan. The environment is then identified to three categories: free-space, obstacles, or the remaining unknown area. The manipulator then moves the laser range scanner into the free-space area discovered in the first scan with the aim of discovering the state of the remaining unknown areas in the environment. The AXBAM technique continues to select an optimal viewpoint for the next scan based on the currently available information. The scanning process in AXBAM is repeated until the unknown environment has been reduced to a satisfactory level, as indicated by the information measurement [133].

The outcome of AXBAM, a 3D map, is then integrated with the surface material types classified by a Laser Range Classifier (LRC) [134]. Figure 3.2 shows the map of a complex 3D environment, which also includes rusty surfaces and painted surfaces that need to be sandblasted, and restricted surfaces that the sandblasting stream must avoid (e.g., plywood).

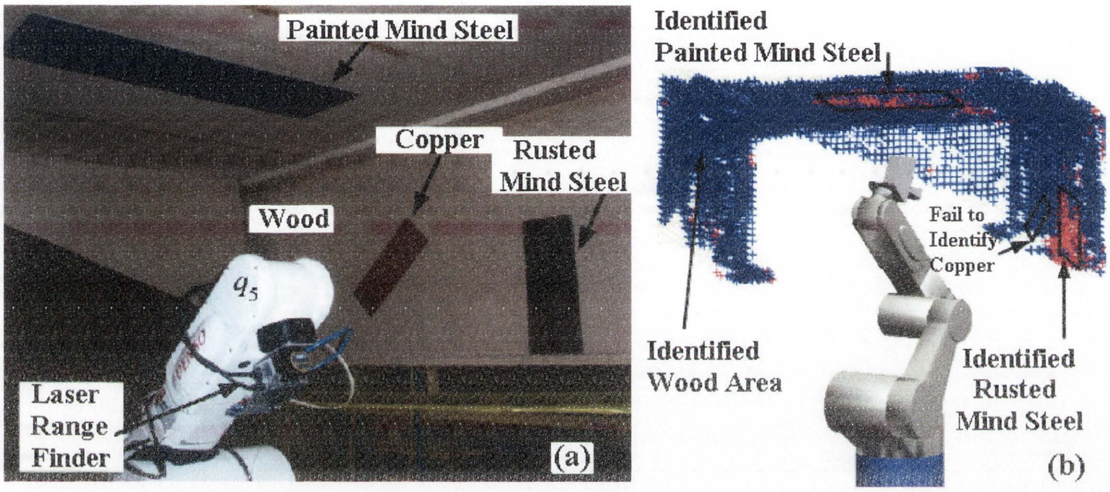

Figure 3.2 Environmental mapping and surface material-type classification using laser scanner [34] a)shows an environment, and a manipulator affixed with a laser range finder at the end-effector, b) shows a 3D map of the environment represented as a point cloud.

3.3 Extended Manipulator Model and Force Control Algorithm

To apply an industrial manipulator in an industrial application, restrictions from the application such as attachment tools, operating procedures, and control system need to be taken into consideration. Typically, the end-effector of an industrial manipulator is designed so that a tool can be mounted and the manipulator can use the tool to perform various operations. However, once the tool is changed, the control model of the manipulator is different. For example, in robotic sandblasting, a sandblasting operation requires that a sandblasting tool (e.g., a nozzle) be mounted on the end-effector, and that the blasting stream length (about 100 mm to 500 mm) should be considered as part of the blasting tool because of the blasting operation requirements. The blasting nozzle is therefore considered as an extra joint of the manipulator, and an extended manipulator model is required.

3.3.1 Extended Manipulator Model

In robotic sandblasting, a sandblasting stream is blown from the nozzle to a target surface and hits the surface at the blasting spot. The effective range of the sandblasting stream is from 100 mm to 500 mm. To model the sandblasting manipulator, the blasting stream is assumed to be an additional prismatic joint (Joint 7) of the manipulator. Thus, as shown in Figure 3.3, the extended robot manipulator is defined as a 6 + 1 DOF manipulator and the blasting spot becomes the end-effector of the extended manipulator. The link coordinate parameters of the extended manipulator are given in Table 3.1.

Table 3.1 Link coordinate system for the extended manipulator

Link Coordinate	Joint Coordinate	θ_i	α_i	a_i	b_i	Joint range
i	j	degree	degree	mm.	mm.	
1	1	q_1-90	0	0	290	-170° to +170°
2	...	0	0	0	185	
3	...	0	90	0	180	
4	2	0	q_2-90	-170	0	-100° to +100°
5	...	0	0	0	385	
6	3	0	q_3	170	0	-70° to +160°
7	...	0	-90	0	100	
8	4	q_4	90	0	116	-90° to +90°
9	5	0	q_5	0	329	-90° to +90°
10	6	q_6	0	0	90	-180° to +180°
11	...	0	-90	0	92	
12	...	0	110	0	267	
13	7	0	0	0	q_7	100-500 mm.

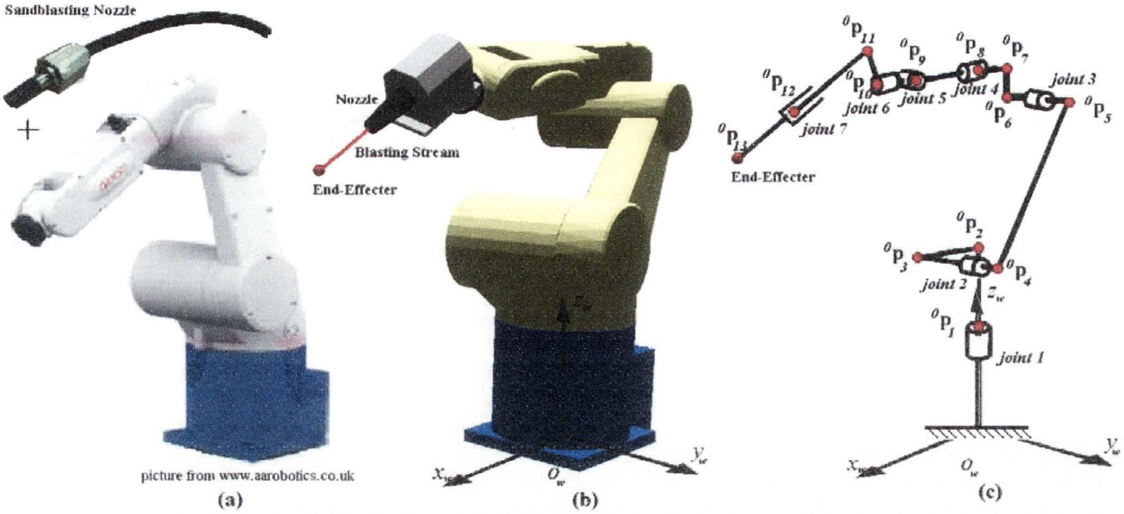

picture from www.aarobotics.co.uk

Figure 3.3 a) Denso manipulator VM6083 (from www.aarobotics.co.uk) and sandblasting nozzle, b) Graphic model of the manipulator, and c) Geometry outline structure of the manipulator

The benefit of the extra link assumption is to allow an operator to control the end of the blasting stream directly on the target surface during sand blasting.

3.3.1.1 Kinematics of a Manipulator

The kinematics of this 7DOF extended manipulator is described below. A transformation matrix, ${}^{i-1}\mathbf{T}_i(i = 1,2,...,13)$ is used to transfer the coordinate system from coordinate frame i-1to coordinate frame i where both coordinates are connected to each other by the link i. The dimensions of the link i are given by a_i and $b_i$as shown in Table 3.1. Each transformation matrix, ${}^{i-1}\mathbf{T}_i$, contains a rotation matrix, ${}^{i-1}\mathbf{R}_i$, and a position vector, ${}^{i-1}\mathbf{p}_i$, that is represented by the Denavit-Hartenberg matrix as

$${}^{i-1}\mathbf{T}_i = \begin{bmatrix} \multicolumn{3}{c}{{}^{i-1}\mathbf{R}_i} & {}^{i-1}\mathbf{p}_i \\ 0 & 0 & 0 & 1 \end{bmatrix} \tag{3.1}$$

$${}^{i-1}\mathbf{R}_i = \begin{bmatrix} \cos\theta_i & -\cos\alpha_i \sin\theta_i & \sin\alpha_i \sin\theta_i \\ \sin\theta_i & \cos\alpha_i \cos\theta_i & -\sin\alpha_i \cos\theta_i \\ 0 & \sin\alpha_i & \cos\alpha_i \end{bmatrix} \tag{3.2}$$

$$ {}^{i-1}\mathbf{p}_i = \begin{bmatrix} a_i \cos\theta_i \\ a_i \sin\theta_i \\ b_i \end{bmatrix} \tag{3.3} $$

where θ_i and α_i are rotation angles about the *z*-axis and the *x*-axis, respectively. a_i and b_i are the dimensions of a link in coordinate frame *i* along the *z*-axis and the *x*-axis. Thus, a transformation matrix of a link *k* on the world coordinate frame is given by ${}^0\mathbf{T}_k(\mathbf{q})$ as

$$ {}^0\mathbf{T}_k(\mathbf{q}) = \prod_{i=1}^{k} {}^{i-1}\mathbf{T}_i \quad ; k = 1,2,\ldots,13 \tag{3.4} $$

$$ \mathbf{q} = \begin{bmatrix} q_1 & q_2 & q_3 & q_4 & q_5 & q_6 & q_7 \end{bmatrix}^T \quad ; \mathbf{q} \in \Re_{\mathbf{q}}^7 \tag{3.5} $$

where q_1 to q_6 are joint angles of revolute joints 1 to 6 and q_7 is a joint length of joint 7.The position vector for the end-effector of the extended manipulator (i.e. the blasting spot) is given by

$$ {}^0\mathbf{p}_e = {}^0\mathbf{p}_{13} \tag{3.6} $$

The length of a blasting stream is thus equal to $\left\| {}^0\mathbf{p}_e - {}^0\mathbf{p}_{12} \right\|$.

3.3.1.2 Extended Manipulator Dynamic Model

The dynamic model of the extended manipulator is defined by

$$ \boldsymbol{\Gamma} = \mathbf{I}\ddot{\mathbf{q}} + \boldsymbol{\beta}\dot{\mathbf{q}} + \boldsymbol{\kappa}\mathbf{q} \tag{3.7} $$

$$ \boldsymbol{\Gamma} = \begin{bmatrix} \tau_1 & \tau_2 & \tau_3 & \tau_4 & \tau_5 & \tau_6 & \tau_7 \end{bmatrix}^T \tag{3.8} $$

where $\mathbf{I}$ is the mass-inertia matrix of the links of the manipulator, $\boldsymbol{\beta}$ is the damping coefficient matrix and $\boldsymbol{\kappa}$ is the stiffness coefficient matrix. $\boldsymbol{\Gamma}$ is the torque-force matrix in joint space ($\boldsymbol{\Gamma} \in \Re_{\mathbf{q}}^7$), which contains the joint torque components, τ_1 to τ_6 of the first six revolute joints and one linear force component τ_7 for the extra prismatic joint, Joint 7. $\mathbf{\Gamma}$ is calculated from the attractive force ($\mathbf{\Gamma}_{att}$) and the repulsive forces ($\mathbf{\Gamma}_{rep}$).

$$\mathbf{\Gamma} = \mathbf{\Gamma}_{att} + \sum_{i=1}^{13} \mathbf{\Gamma}_{rep_i} \tag{3.9}$$

Thus, the dynamic model of the extended manipulator can be rewritten as

$$\mathbf{\Gamma}_{att} + \sum_{i=1}^{13} \mathbf{\Gamma}_{rep_i} = \mathbf{I}\ddot{\mathbf{q}} + \boldsymbol{\beta}\dot{\mathbf{q}} + \boldsymbol{\kappa}\mathbf{q} \tag{3.10}$$

$\mathbf{\Gamma}_{att}$ in joint space is calculated using the attractive force ($\mathbf{F}_{att}$) in *O-space* based on the attractive force approach shown in Section 3.4. Each repulsive force ($\mathbf{\Gamma}_{rep}$) is transformed from a repulsive force ($\mathbf{F}_{rep}$) in the operational space which is generated by the Three-Dimensional Virtual Force Field (3D-VF^2) approach. The transformation from a force in *O-space* ($\mathbf{F}\in\Re^3$ or $\mathbf{F}\in\Re^6$) to a torque-force in joint space ($\mathbf{\Gamma}\in\Re_q{}^7$) is performed using the Force Control (FC) algorithm presented in Section 3.3.2.

3.3.2 Force Control Algorithm

This section presents the novel Force Control (FC) algorithm for a manipulator, which is developed in this research. The force control algorithm generates the instant motion for a manipulator based on the forces from surrounding objects and the task requirement. When an external force (**F**) in Cartesian space (i.e. the *O-space*)is applied to a link of a manipulator, the external force can be transformed into a torque-force ($\mathbf{\Gamma}$) in robot joint space for driving the joints of the manipulator. **F** is defined as

$$\mathbf{F} = \begin{bmatrix} \boldsymbol{\sigma} \\ \mathbf{f} \end{bmatrix} = \begin{bmatrix} \sigma_X & \sigma_Y & \sigma_Z & f_X & f_Y & f_Z \end{bmatrix}^T \tag{3.11}$$

F consists of a moment vector ($\boldsymbol{\sigma}$) and a force vector (**f**). A position vector ${}^0\mathbf{p}_f$ gives the location of **F** and a position vector ${}^0\mathbf{p}_i$ represents the origin position of the coordinate frame *i* on the world coordinate system.

$$
{}^{0}\mathbf{p}_{f} = \begin{bmatrix} {}^{0}p_{f\,x} \\ {}^{0}p_{f\,y} \\ {}^{0}p_{f\,z} \end{bmatrix} \tag{3.12}
$$

$$
{}^{0}\mathbf{p}_{i} = \begin{bmatrix} {}^{0}p_{i\,x} \\ {}^{0}p_{i\,y} \\ {}^{0}p_{i\,z} \end{bmatrix} \qquad ; i \in \{1,2,\ldots,13\} \tag{3.13}
$$

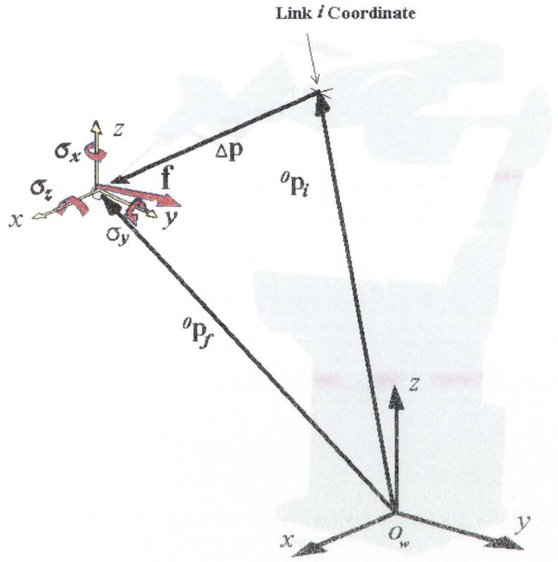

Figure 3.4 An external force acting on a link of a manipulator and the position of the force

The transformation of a force from *O-space* to joint space is defined as $\mathbf{H}_i(\mathbf{q}, {}^{0}\mathbf{p}_f)$ such that

$$
\boldsymbol{\Gamma} = \mathbf{H}_{i}(\mathbf{q}, {}^{0}\mathbf{p}_{f})\mathbf{F} \tag{3.14}
$$

where the current joint angles of the manipulator ($\mathbf{q}$) and the location of the force (${}^{0}\mathbf{p}_f$) are required for the transformation. Since the extended manipulator is a 7DOF manipulator, $\mathbf{H}$ is defined by a 7×6 matrix which is given by

$$
\mathbf{H}_{i}(\mathbf{q}, {}^{0}\mathbf{p}_{f}) = \begin{bmatrix} \mathbf{h}_1 & \mathbf{h}_2 & \mathbf{h}_3 & \mathbf{h}_4 & \mathbf{h}_5 & \mathbf{h}_6 & \mathbf{h}_7 \end{bmatrix}^{T} \tag{3.15}
$$

$$\mathbf{h}_j = \begin{cases} \mathbf{0}_{1\times 6} & \text{; if link } i \text{ is connected to joint } j \\ \mathbf{L}_j\,{}^{i}\mathbf{M}_0 & \text{; if link } i \text{ is not connected to joint } j \end{cases} \quad ; j = [1,2,\ldots,7] \tag{3.16}$$

where $\mathbf{L}_j$ is a matrix presenting the axis of motion of joint j expressed in the coordinate frame j.

$$\mathbf{L}_j = \begin{bmatrix} l_{r,x\,j} & l_{r,y\,j} & l_{r,z\,j} & l_{t,x\,j} & l_{t,y\,j} & l_{t,z\,j} \end{bmatrix} \tag{3.17}$$

$$l_{r,k\,j} = \begin{cases} 1 & \text{; if joint } j \text{ is a revolute joint about } k \text{ axis} \\ 0 & \text{; other else} \end{cases} \quad ; k \in \{x, y, z\} \tag{3.18}$$

$$l_{t,k\,j} = \begin{cases} 1 & \text{; if joint } j \text{ is a prismatic joint along } k \text{ axis} \\ 0 & \text{; other else} \end{cases} \quad ; k \in \{x, y, z\} \tag{3.19}$$

From Table 3.1, $\mathbf{L}_1$ to $\mathbf{L}_7$ can be given as

$$\begin{aligned} \mathbf{L}_1 &= \begin{bmatrix} 0 & 0 & 1 & 0 & 0 & 0 \end{bmatrix} \\ \mathbf{L}_2 &= \begin{bmatrix} 0 & 1 & 0 & 0 & 0 & 0 \end{bmatrix} \\ \mathbf{L}_3 &= \begin{bmatrix} 0 & 1 & 0 & 0 & 0 & 0 \end{bmatrix} \\ \mathbf{L}_4 &= \begin{bmatrix} 0 & 0 & 1 & 0 & 0 & 0 \end{bmatrix} \\ \mathbf{L}_5 &= \begin{bmatrix} 0 & 1 & 0 & 0 & 0 & 0 \end{bmatrix} \\ \mathbf{L}_6 &= \begin{bmatrix} 0 & 0 & 1 & 0 & 0 & 0 \end{bmatrix} \\ \mathbf{L}_7 &= \begin{bmatrix} 0 & 0 & 0 & 0 & 0 & 1 \end{bmatrix} \end{aligned}$$

${}^{i}\mathbf{M}_0$ is a matrix which is used to transfer a force in *O-space* on the world coordinate system to the coordinate frame i. ${}^{i}\mathbf{M}_0$ contains an inverse matrix of the homogenous rotation matrix (${}^{0}\mathbf{R}_i$) as presented in Section 3.3.1.1 and a skew-symmetric matrix ($S(\Delta\mathbf{p})$). The ${}^{0}\mathbf{R}_i^{-1}$ is equal to ${}^{i}\mathbf{R}_0^{T}$ and $\Delta\mathbf{p}$ in the skew-symmetric matrix is a displacement vector from the origin of the coordinate frame i to the position of the force, ${}^{0}\mathbf{p}_f$.

$${}^{i}\mathbf{M}_0 = \begin{bmatrix} {}^{i}\mathbf{R}_0^{T} & \mathbf{0}_{3\times 3} \\ \mathbf{0}_{3\times 3} & {}^{i}\mathbf{R}_0^{T} \end{bmatrix} \begin{bmatrix} \mathbf{1}_{3\times 3} & \mathbf{0}_{3\times 3} \\ -S(\Delta\mathbf{p}) & \mathbf{1}_{3\times 3} \end{bmatrix} \tag{3.20}$$

$$\mathbf{S}(\Delta\mathbf{p}) = \begin{bmatrix} 0 & -\Delta p_Z & \Delta p_Y \\ \Delta p_Z & 0 & -\Delta p_X \\ -\Delta p_Y & \Delta p_X & 0 \end{bmatrix} \tag{3.21}$$

$$\Delta\mathbf{p} = \begin{bmatrix} \Delta p_X \\ \Delta p_Y \\ \Delta p_Z \end{bmatrix} = {}^0\mathbf{p}_f - {}^0\mathbf{p}_i \tag{3.22}$$

From Section 3.3.1.2, the dynamic model of the extended manipulator (Equation 3.10) can be re-written as Equation 3.23:

$$\mathbf{H}_{13}(\mathbf{q}, {}^0\mathbf{p}_e)\mathbf{F}_{att} + \sum_{i=1}^{13} \mathbf{H}_i(\mathbf{q}, {}^0\mathbf{p}_{rep_i})\mathbf{F}_{rep_i} = \mathbf{I}\ddot{\mathbf{q}} + \boldsymbol{\beta}\dot{\mathbf{q}} + \boldsymbol{\kappa}\mathbf{q} \tag{3.23}$$

To drive a robot manipulator, the control commands (i.e. the joint angle vector **q**), which are generated from Equation 3.23, are sent to the controller of the manipulator. In this thesis, the attractive force $\mathbf{F}_{att}$ (i.e. the driving force) is generated by applying the Attractive Force (AF) method in the following section. The repulsive forces $\mathbf{F}_{rep}$ is generated by the Three-Dimensional Virtual Force Field (3D-VF^2) method which will be presented in Section 3.5.

3.4 Attractive Force Method

The Attractive Force (AF) method is an essential component of a Virtual Force Field (VF^2) approach. This AF method was first presented in [137].The AF method generates a virtual force which is an attractive force ($\mathbf{F}_{att}$) coupling between the end-effector of the manipulator and a target point. $\mathbf{F}_{att}$ drives the end-effector towards the desired target point. $\mathbf{F}_{att}$ is composed of two components: an attractive force, and an attractive moment.

3.4.1 Definition of Attractive Force

The attractive force ($\mathbf{F}_{att}$) is calculated based on the distance between the target configuration, (${}^0\mathbf{P}_t$) and the current configuration of the end-effector (${}^0\mathbf{P}_e$). Both ${}^0\mathbf{P}_e$ and ${}^0\mathbf{P}_t$ are defined by a directional vector ($\mathbf{n}$) and a position vector ($\mathbf{p}$) in Cartesian space as shown in Equation 3.24 and 3.25.

$$ {}^0\mathbf{P}_t = \begin{bmatrix} {}^0\mathbf{n}_t \\ {}^0\mathbf{p}_t \end{bmatrix} = \begin{bmatrix} {}^0n_{tx} & {}^0n_{ty} & {}^0n_{tz} & {}^0p_{tx} & {}^0p_{ty} & {}^0p_{tz} \end{bmatrix}^T \qquad (3.24) $$

${}^0\mathbf{p}_t$ is a position vector from a target point in a pre-planned path or a cursor position of a pointing device (e.g., a mouse, a joystick, a haptic device).${}^0\mathbf{n}_t$ is a directional vector, which relates to a surface normal of a target plane (i.e. a normal vector of a surface) or comes from a directional vector of the cursor of a 6DOF pointing device.

${}^0\mathbf{P}_e$is given by

$$ {}^0\mathbf{P}_e = \begin{bmatrix} {}^0\mathbf{n}_e \\ {}^0\mathbf{p}_e \end{bmatrix} = \begin{bmatrix} {}^0n_{ex} & {}^0n_{ey} & {}^0n_{ez} & {}^0p_{ex} & {}^0p_{ey} & {}^0p_{ez} \end{bmatrix}^T \qquad (3.25) $$

where ${}^0\mathbf{p}_e$ is the position vector of the end-effector as shown in Equation 3.6 and Figure 3.5. ${}^0\mathbf{n}_e$,which is the directional vector of the end-effector, is given by

$$ {}^0\mathbf{n}_e = {}^0\mathbf{R}_{13}(\mathbf{q})[0 \quad 0 \quad 1]^T \qquad (3.26) $$

where ${}^0\mathbf{R}_{13}(\mathbf{q})$ is calculated from Equation 3.2. A $\mathbf{F}_{att}$, which consisting of two components $\mathbf{f}_{att}$ and $\boldsymbol{\sigma}_{att}$, can be defined as the attractive force function δ_a shown in Equation 3.27.

$$ \mathbf{F}_{att} = \delta_a({}^0\mathbf{P}_e, {}^0\mathbf{P}_t) = \begin{bmatrix} \boldsymbol{\sigma}_{att} \\ \mathbf{f}_{att} \end{bmatrix} = \begin{bmatrix} \sigma_{att\,x} & \sigma_{att\,y} & \sigma_{att\,z} & f_{att\,x} & f_{att\,y} & f_{att\,z} \end{bmatrix}^T \qquad (3.27) $$

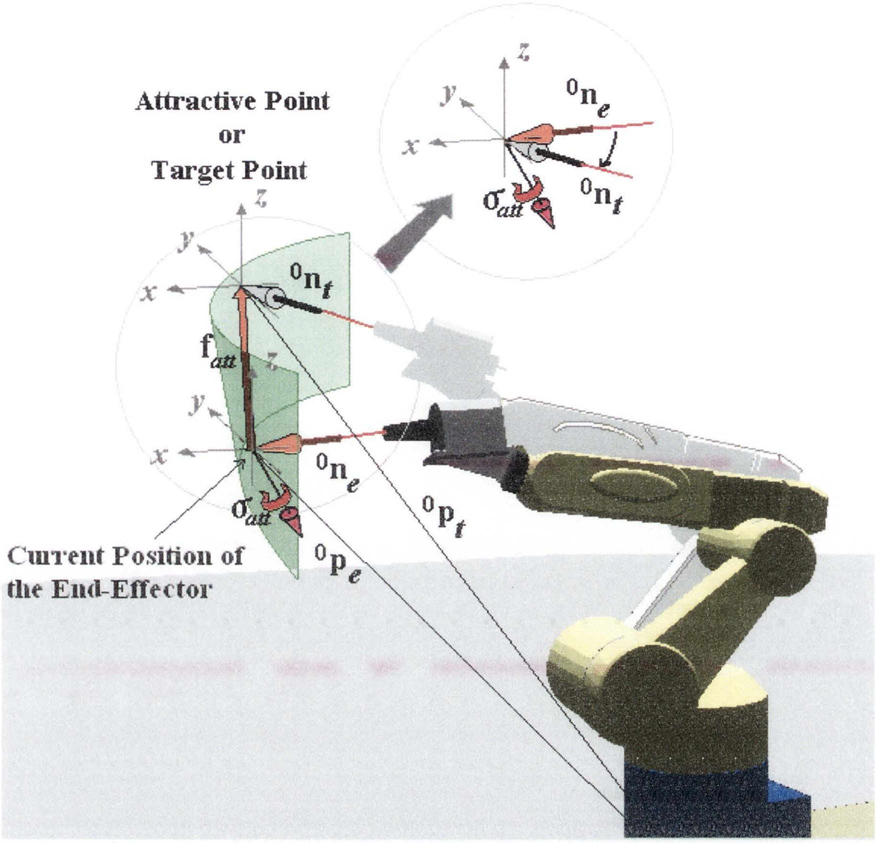

Figure 3.5 An example of attractive force at the end-effector of the extended manipulator

$\mathbf{f}_{att}$ is a force vector calculated based upon the distance between the current position of the end-effector ($^0\mathbf{p}_e$) and the position of the target point ($^0\mathbf{p}_t$). σ_{att} is a moment vector of the angular displacement between the directional vector of the end-effector ($^0\mathbf{n}_e$) and the normal vector of the desired target ($^0\mathbf{n}_t$). A sigmoid function is used to limit the amplitude of both $\mathbf{f}_{att}$ and σ_{att}.

$$\mathbf{f}_{att} = \begin{bmatrix} f_{att\,x} \\ f_{att\,y} \\ f_{att\,z} \end{bmatrix} = \frac{K_{att\,1}}{1+\left(\dfrac{e^{-K_s\ {}^0\mathbf{p}_e-{}^0\mathbf{p}_t}}{\varepsilon_0}\right)} \frac{{}^0\mathbf{p}_e-{}^0\mathbf{p}_t}{\left\|{}^0\mathbf{p}_e-{}^0\mathbf{p}_t\right\|} \tag{3.28}$$

$$\boldsymbol{\sigma}_{att} = \begin{bmatrix} \sigma_{att\,x} \\ \sigma_{att\,y} \\ \sigma_{att\,z} \end{bmatrix} = \frac{K_{att\,2}}{1+\left(\dfrac{e^{-K_s \sin^{-1}\left({}^0\mathbf{n}_e\times{}^0\mathbf{n}_t\ /\left({}^0\mathbf{n}_e\ \ {}^0\mathbf{n}_t\right)\right)}}{\varepsilon_0}\right)} \frac{{}^0\mathbf{n}_e\times{}^0\mathbf{n}_t}{\left\|{}^0\mathbf{n}_e\times{}^0\mathbf{n}_t\right\|} \tag{3.29}$$

K_{att1} and K_{att2} are parameters introduced for limiting the amplitude of $\mathbf{f}_{att}$ and σ_{att}, respectively. ε_0 is a small non-zero positive constant and K_s is a constant which is used to determine how the attractive force varies with respect to the distance between ${}^0\mathbf{P}_e$ and ${}^0\mathbf{P}_t$. Figure 3.6 shows a graph of the amplitude of $\mathbf{f}_{att}$ with $K_{att} = 1$, $\varepsilon_0 = 0.0001$, and various values of K_s.

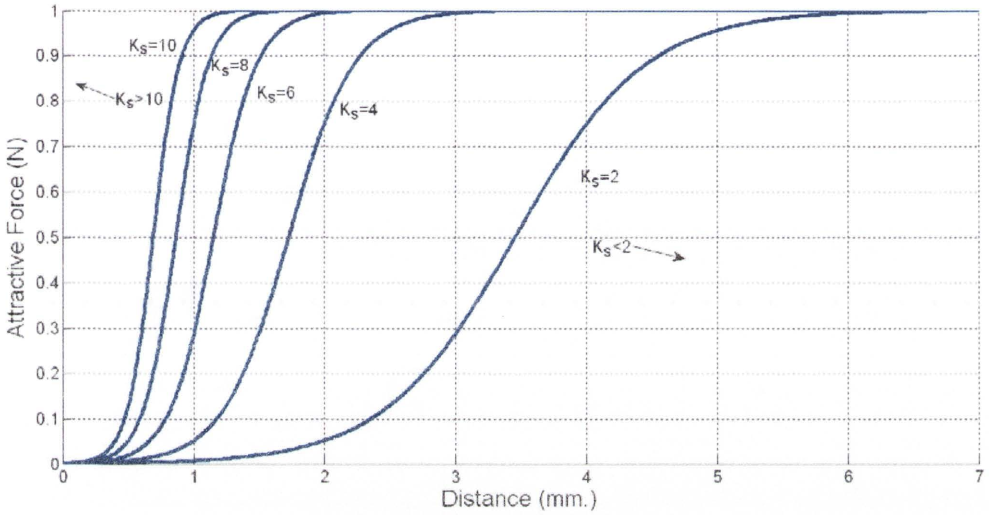

Figure 3.6 Graph of the amplitude of $\mathbf{f}_{att}$ with $K_{att} = 1$, $\varepsilon_0 = 0.0001$, and different values of K_s

This attractive force is presented in Cartesian space, thus a transformation has been defined in Equation 3.14 Section 3.3 to calculate the $\mathbf{\Gamma}_{att}$ from this $\mathbf{F}_{att}$.

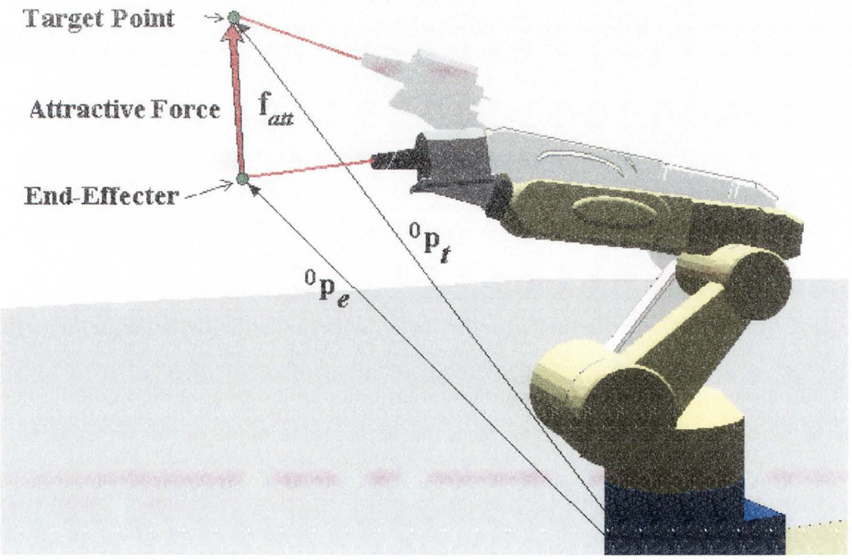

Figure 3.7 A single attractive force at the end-effector of the manipulator

When the orientation of the target point is not required, σ_{att} is zero (Figure 3.7). Then Equation 3.27 becomes:

$$\mathbf{F}_{att} = \delta_a({}^0\mathbf{p}_e, {}^0\mathbf{p}_t) = \begin{bmatrix} \mathbf{0}_{3\times1} \\ \mathbf{f}_{att} \end{bmatrix} = \begin{bmatrix} 0 & 0 & 0 & f_X & f_Y & f_Z \end{bmatrix}^T \tag{3.30}$$

3.4.2 Attractive Force

The definition of attractive force presented in 3.4.1 is then used to control the robot end-effector to achieve the target point with the expected orientation. But it can not be used to control the length of the prismatic joint (Joint 7). In some applications such as robotic sandblasting, the length of the blasting stream, i.e. the length of the prismatic joint (Joint 7), needs to be controlled. Therefore, a modified attractive force method is presented below to control the target point, the target orientation and the length.

To control Joint 7, another attractive force ($\mathbf{F}_{att2}$) is generated. As shown in Figure 3.8, $\mathbf{F}_{att\,2}$ is generated based on the distance between point ${}^0\mathbf{p}_{11}$ and a point on the line of the target orientation, ${}^0\mathbf{p}_{t2}$, using the same definition shown in Equation 3.30:

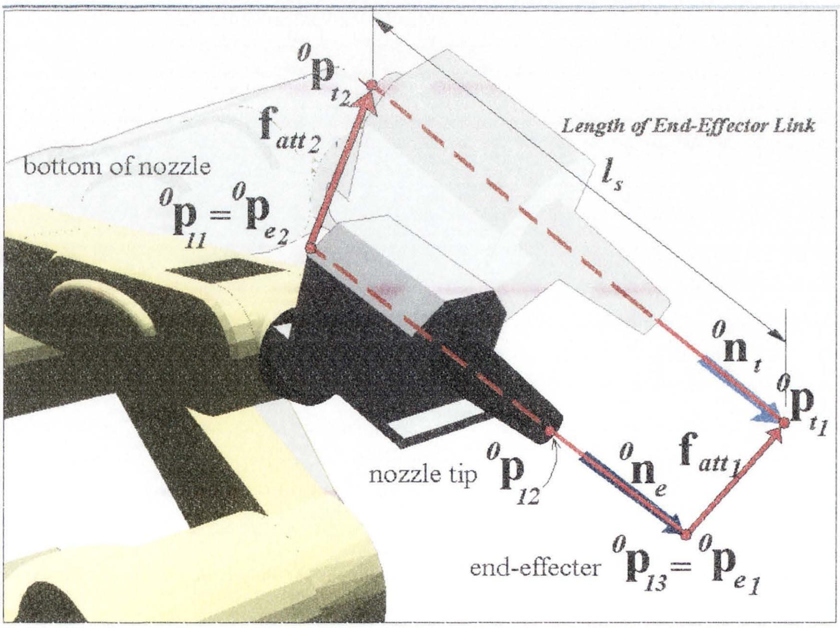

Figure 3.8 Two attractive forces on the end-effector link of the manipulator

$$\mathbf{F}_{att1} = \delta_a({}^0\mathbf{p}_{e1}, {}^0\mathbf{p}_{t1}) \tag{3.31}$$

$$\mathbf{F}_{att2} = \delta_a({}^0\mathbf{p}_{e2}, {}^0\mathbf{p}_{t2}) \tag{3.32}$$

where ${}^0\mathbf{p}_{t2}$ is generated by the normal vector of the desired target (${}^0\mathbf{n}_t$) and a desired length of the end-effector link (i.e. stream length + nozzle length) and ${}^0\mathbf{p}_{t2}$ is given by

$${}^0\mathbf{p}_{t2} = {}^0\mathbf{p}_{t1} - ({}^0\mathbf{n}_t l_s) \tag{3.33}$$

l_s is the required length of the end-effector link. $\mathbf{f}_{att\ 1}$ and $\mathbf{f}_{att\ 2}$ will stretch or compress the prismatic joint (Joint 7) when $\mathbf{f}_{att\ 1}$ and $\mathbf{f}_{att\ 2}$are not in parallel due to the difference between the current length of the end-effector link and the desired length of the prismatic joint. However, these two-attractive forces can control only 5DOF mobility of the end-effector link. The end-effector link is still able to rotate about $\overline{{}^0\mathbf{p}_{t1}\,{}^0\mathbf{p}_{t2}}$. In order to fully control the end-effector link (6DOF movement), another attractive force is needed to control the rotation of the end-effector link about $\overline{{}^0\mathbf{p}_{t1}\,{}^0\mathbf{p}_{t2}}$. Therefore, three attractive forces ($\mathbf{F}_{att\ 1}, \mathbf{F}_{att\ 2}, \mathbf{F}_{att\ 3}$) are defined to link three points on the end-effector link (${}^0\mathbf{p}_{e1}, {}^0\mathbf{p}_{e2}, {}^0\mathbf{p}_{e3}$) with three target points (${}^0\mathbf{p}_{t1}, {}^0\mathbf{p}_{t2}, {}^0\mathbf{p}_{t3}$). The three points on the end-effector link (${}^0\mathbf{p}_{e1}, {}^0\mathbf{p}_{e2}, {}^0\mathbf{p}_{e3}$) are defined as ${}^0\mathbf{p}_{13}, {}^0\mathbf{p}_{11}, {}^0\mathbf{p}_{10}$,respectively.

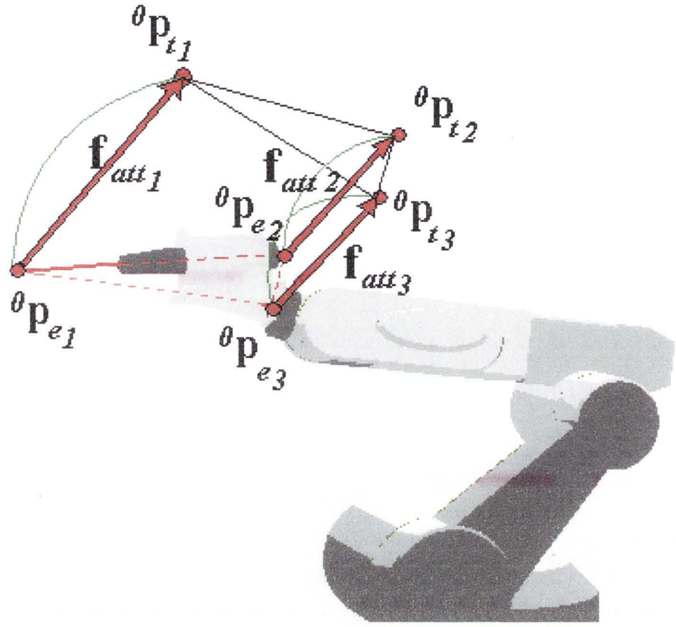

Figure 3.9 Three attractive forces at the end-effector link of the manipulator

$$\mathbf{F}_{att\ n} = \delta_a({}^0\mathbf{p}_{en}, {}^0\mathbf{p}_{tn}) \qquad n = 1,2,3 \tag{3.34}$$

For the sandblasting robotic system, the length of the end-effector link is given by Equation 3.33 and the additional distance between ${}^0\mathbf{p}_{t2}$ and ${}^0\mathbf{p}_{t3}$ must be equal to the length between ${}^0\mathbf{p}_{e2}$ and ${}^0\mathbf{p}_{e3}$ as shown in Figure 3.9.

$$\left\| {}^0\mathbf{p}_{t2} - {}^0\mathbf{p}_{t3} \right\| = \left\| {}^0\mathbf{p}_{e2} - {}^0\mathbf{p}_{e3} \right\| \tag{3.35}$$

This multiple attractive force control method can manipulate the manipulator to achieve its target-tracking task and can also be applied to the other link of a manipulator.

3.5 Three-Dimensional Virtual Force Field Method

To enable the robot manipulator to safely interact with a complex 3D environment that is either known or partially known, a Three-Dimensional Virtual Force Field (3D-VF^2) method is proposed for real-time motion planning and collision avoidance. This 3D-VF^2 method was originally presented in [137-140]. The map of the environment, which is generated by the exploration and map building algorithm presented in Section 3.2, is used by the 3D-VF^2 method for obstacle detection and repulsive force generation. The environment can be represented by points, lines, and polygons. The area vector and signed volume calculation [148][149]proposed by Guan and Zhang is basically to detect distance between a polygon and a line. They represent the robot's fingers as lines and a grasped object as closed surface polygons. This is suitable for a well constructed object/environment. The environment data in this research is obtained from a 3D laser scanner and represented as a point cloud set. Line segments and polygons can be generated from the point cloud as presented in [150] but it is time consuming and the result surface model may not make a big improvement in force rendering. Therefore, the environment map is represented by a point cloud or a set of points ($\mathbf{P}_{ob}$) [34]

$$\mathbf{P}_{ob} = \left\{ {}^{0}\mathbf{p}_{ob\,1}, {}^{0}\mathbf{p}_{ob\,2}, \ldots, {}^{0}\mathbf{p}_{ob\,m} \right\};\ m \text{ is number of points in the point cloud set} \tag{3.36}$$

The point cloud can be used to determine the distance between the obstacles and the robot manipulator, and thus to predict a potential collision. The distance calculation is performed in Cartesian space and thus the distance is measured by the Euclidean distance. Two techniques, Ellipsoid Bounding (EB) technique and Swept Sphere Bounding (SSB) technique are used to construct a force field, calculate the distance and generate a repulsive force in this thesis. The difference between these techniques is the shape of a force field which is selected to fit each link's shape.

3.5.1 Ellipsoid Bounding

The Ellipsoid Bounding (EB) technique [137][138] is used to simply represent the geometry of the manipulator links with ellipsoids. For a cylinder-like link of a robot manipulator, the two end points (${}^{0}\mathbf{p}_{cl1\,i}, {}^{0}\mathbf{p}_{cl2\,i}$) of the centre axis of the link on the coordinate frame i (Joint i) are used to generate two coaxial ellipsoids D_{min} and D_{max} as shown in Figure 3.10.

$${}^{0}\mathbf{p}_{cl1\,i} = {}^{0}\mathbf{T}_{i}\, {}^{i}\mathbf{p}_{cl1} \tag{3.37}$$

$${}^{0}\mathbf{p}_{cl2\,i} = {}^{0}\mathbf{T}_{i}\, {}^{i}\mathbf{p}_{cl2} \tag{3.38}$$

Both ends of the centre axis of the link are defined as the foci of the ellipsoids D_{min} and D_{max} and major diameters of the ellipsoids D_{min} and D_{max} are defined by d_{min} and d_{max}, respectively. The d_{min} and d_{max} are given by

$$d_{min} = K_p \left\| {}^0\mathbf{p}_{cl2\,i} - {}^0\mathbf{p}_{cl1\,i} \right\| \qquad ; K_p > 1 \tag{3.39}$$

$$d_{max} = \left(K_p + Er\right) \left\| {}^0\mathbf{p}_{cl2\,i} - {}^0\mathbf{p}_{cl1\,i} \right\| \qquad ; K_p > 1, Er > 0 \tag{3.40}$$

where K_p is a constant greater than 1 which is used for ensuring that these ellipsoids will cover the whole body of the link and Er is a positive constant that sets the space between D_{min} and D_{max}.

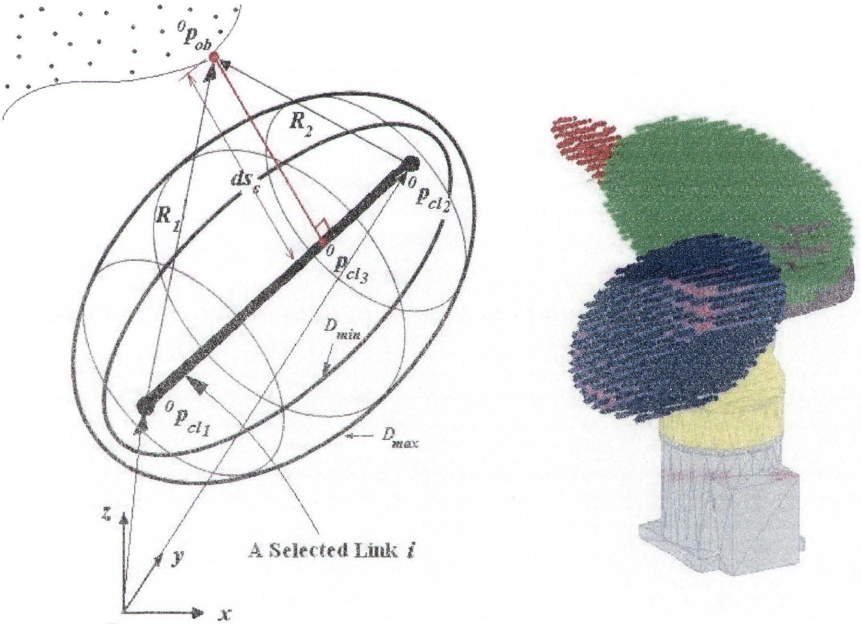

Figure 3.10 Parameters of the ellipsoids D_{min} and D_{max} and a robot manipulator covered by D_{min}

The distances from an obstacle point (${}^0\mathbf{p}_{ob\,s}$) to the foci of the ellipsoids are represented by vectors $\mathbf{R}_1$ and $\mathbf{R}_2$. The combination of these two vectors ($\|\mathbf{R}_1\|+\|\mathbf{R}_2\|$) is used to classify the location of the obstacle point into 3 regions: 1) outside D_{max}, 2) between D_{min} and D_{max}, or 3) inside D_{min}. Let Cx be the ratio between $\|\mathbf{R}_1\|+\|\mathbf{R}_2\|$ and the length of $\overline{{}^0\mathbf{p}_{cl1\,i}\;{}^0\mathbf{p}_{cl2\,i}}$.

$$Cx(s) = \frac{\left\|\mathbf{R}_1\right\| + \left\|\mathbf{R}_2\right\|}{\left\|{}^0\mathbf{p}_{cl2_i} - {}^0\mathbf{p}_{cl1_i}\right\|} = \frac{\left\|{}^0\mathbf{p}_{obs} - {}^0\mathbf{p}_{cl1_i}\right\| + \left\|{}^0\mathbf{p}_{obs} - {}^0\mathbf{p}_{cl2_i}\right\|}{\left\|{}^0\mathbf{p}_{cl2_i} - {}^0\mathbf{p}_{cl1_i}\right\|} \tag{3.41}$$

s is a member index of the point in the point cloud. If $\|\mathbf{R}_1\|+\|\mathbf{R}_2\|$ is less than d_{min}, then ${}^0\mathbf{p}_{obs}$ is inside the D_{min} ellipsoid field. If $\|\mathbf{R}_1\|+\|\mathbf{R}_2\|$ is greater than d_{max}, then ${}^0\mathbf{p}_{obs}$ is outside the D_{max}. If $\|\mathbf{R}_1\|+\|\mathbf{R}_2\|$ is between d_{min} and d_{max}, then ${}^0\mathbf{p}_{obs}$ is in the space between D_{min} and D_{max}. The nearest obstacle point can be identified as

$$\min_{s}\left\{ \ Cx(s) \ \right\} \tag{3.42}$$

If the nearest obstacle point, ${}^0\mathbf{p}_{obs}$ is inside the D_{max}, a virtual repulsive force, $\mathbf{F}_{rep}$ is generated at the obstacle point ${}^0\mathbf{p}_{obs}$ directed at ${}^0\mathbf{p}_{cl3\ i}$ where $\mathbf{F}_{rep}$ is orthogonal to the centre axis of the link. The point, ${}^0\mathbf{p}_{cl3\ i}$ can be calculated as

$${}^0\mathbf{p}_{cl3\ i} = {}^0\mathbf{p}_{cl1} + \left(\frac{{}^0\mathbf{p}_{cl2\ i} - {}^0\mathbf{p}_{cl1\ i}}{\left\|{}^0\mathbf{p}_{cl2\ i} - {}^0\mathbf{p}_{cl1\ i}\right\|} \left(\left({}^0\mathbf{p}_{obs} - {}^0\mathbf{p}_{cl1\ i}\right) \cdot \frac{{}^0\mathbf{p}_{cl2\ i} - {}^0\mathbf{p}_{cl1\ i}}{\left\|{}^0\mathbf{p}_{cl2\ i} - {}^0\mathbf{p}_{cl1\ i}\right\|} \right) \right) \tag{3.43}$$

then $\mathbf{F}_{rep}$ on the link with the coordinate frame i is given by

$$\mathbf{F}_{rep_i} = \delta_r({}^0\mathbf{p}_{obs}, {}^0\mathbf{p}_{cl3\ i}) = \begin{bmatrix} \mathbf{0}_{3\times1} \\ \mathbf{f}_{rep_i} \end{bmatrix} = \begin{bmatrix} 0 & 0 & 0 & f_{rep\,x_i} & f_{rep\,y_i} & f_{rep\,z_i} \end{bmatrix}^T \tag{3.44}$$

The force $\mathbf{F}_{repi}$ is defined as a repulsive force ($\mathbf{f}_{rep,i}$) when the repulsive moment is equal to zero (σ_{rep}=**0**). The amplitude of the repulsive force is given by Equation 3.45 and the repulsive force vector is shown in Equation 3.46.

$$\left\|\mathbf{f}_{rep\ i}\right\| = K_f - \left(\frac{K_f}{1 + e^{\left(-\frac{10(Cx(s) - K_p - 0.5Er)}{Er}\right)}} \right) \tag{3.45}$$

$\|\mathbf{f}_{rep}\|$ will be equal to zero when the obstacle point is outside D_{max} and $\|\mathbf{f}_{rep}\|$ will increase until it is equal to K_f where the obstacle point is close to D_{min}. K_f is determined as the maximum amplitude of the repulsive force. The function of $\mathbf{f}_{rep,i}$ uses a sigmoid function scheme to limit the maximum amplitude and define the transient state related to a distance *Er* (Figure 3.11),which is the space between D_{min} and D_{max}.

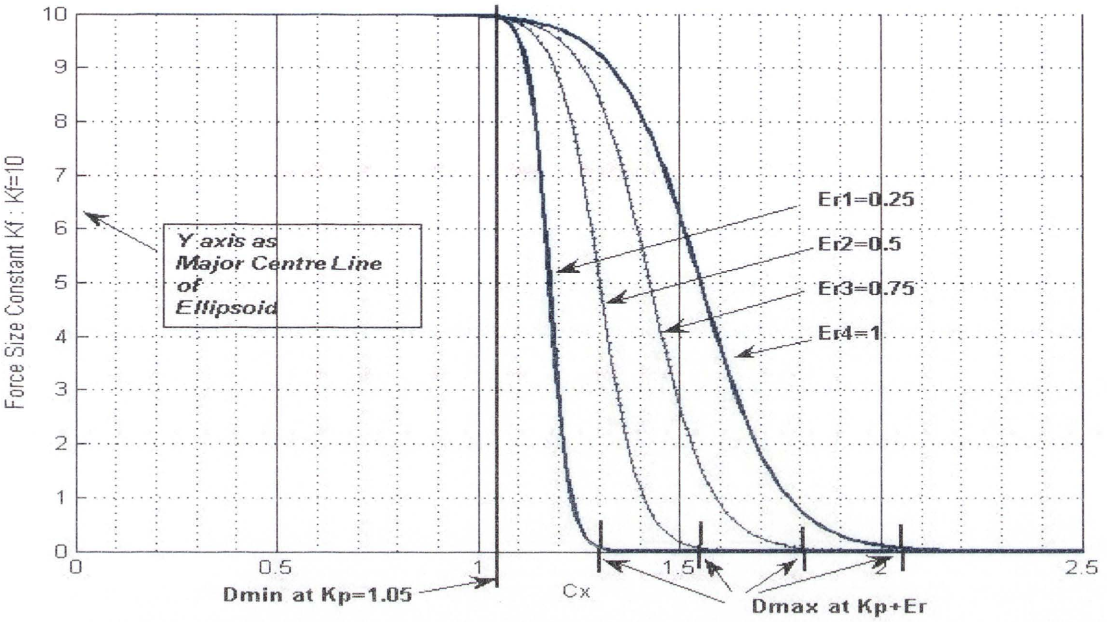

Figure 3.11 A graph of the amplitude of repulsive force with K_f=10, K_p=1.05 and *Er*.

The repulsive force vector is given by

$$\mathbf{f}_{rep_i} = \left\| \mathbf{f}_{rep_i} \right\| \frac{{}^{0}\mathbf{p}_{cl3\ i} - {}^{0}\mathbf{p}_{obs}}{\left\| {}^{0}\mathbf{p}_{cl3\ i} - {}^{0}\mathbf{p}_{obs} \right\|} \tag{3.46}$$

The repulsive force $\mathbf{F}_{rep\ i}$ is then used in the dynamic model of the manipulator (Equation 3.23 in Section 3.3) to generate a collision-free motion for the manipulator.

3.5.2 Swept Sphere Bounding

Similar to the ellipsoid bounding technique, the Swept-Sphere Bounding (SSB) technique can be used to generate a force field and to calculate a repulsive force. The SSB technique generates two coaxial virtual capsules (i.e. an inner capsule D_{min} and an outer capsule D_{max}) for covering a link of a manipulator and forming a three-dimensional virtual force field. Figure 3.12 shows how the centre axis of each link is defined as a sweeping line of a sphere which has a radius (r_c). Thus, the diameter of

D_{min} , at which the maximum repulsive force is generated, is equal to $2r_c$. The diameter of D_{max}, at which the repulsive force is zero, is defined by $2(r_c + Er)$.

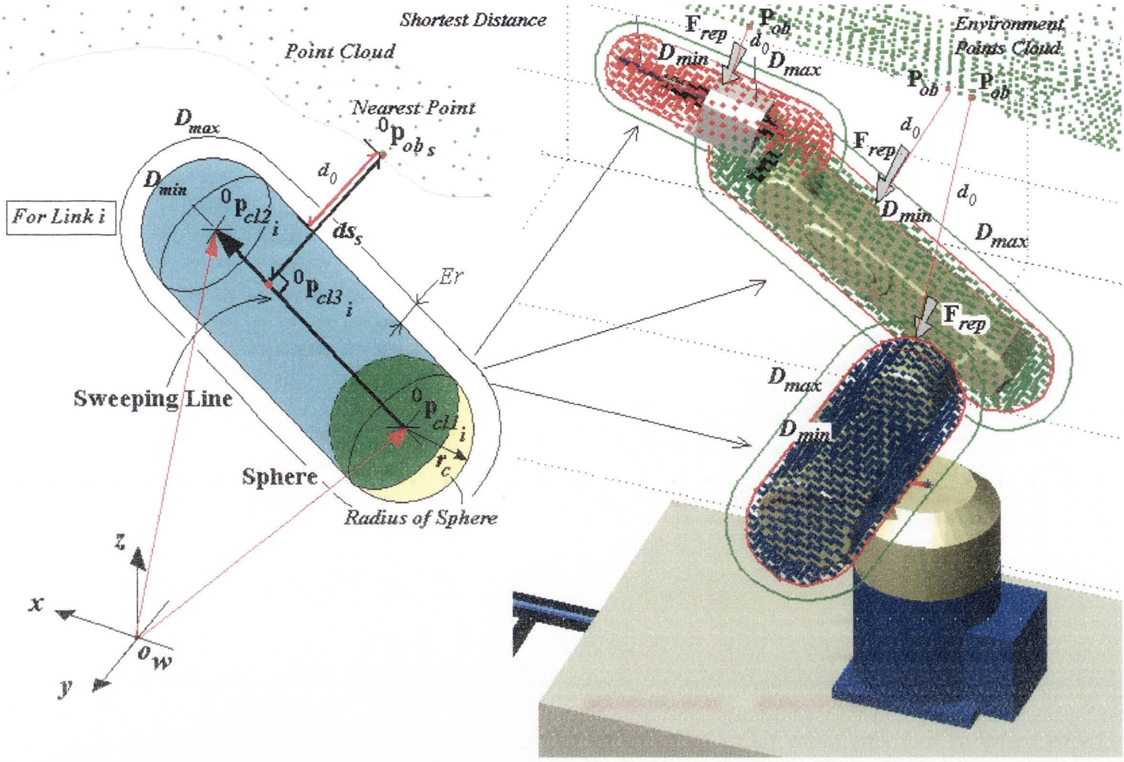

Figure 3.12 D_{min} and D_{max} generated by sphere-swept bounding

For link i, its centre axis (${}^0\mathbf{p}_{cl2_i}, {}^0\mathbf{p}_{cl1_i}$) gives a sweeping line as

$$ {}^0\mathbf{p}_{cl3_i}(u) = {}^0\mathbf{p}_{cl1_i} + u\left({}^0\mathbf{p}_{cl2_i} - {}^0\mathbf{p}_{cl1_i}\right) \quad ; u \in [0...1] \qquad (3.47) $$

where u is a variable between 0 to 1. The objective function is defined by

$$ \min_{s} \min_{u} \left\{ \left\| {}^0\mathbf{p}_{cl3_i}(u) - {}^0\mathbf{p}_{ob_s} \right\| \right\} \quad ; s \in [0,1,2...,m], u \in [0...1] \qquad (3.48) $$

Parameter u defines a point ${}^0\mathbf{p}_{cl3_i}(u)$ on the centre axis of D_{min} and D_{max} and index s defines the nearest obstacle point ${}^0\mathbf{p}_{ob_s}$.

$$ u = \left(\left({}^0\mathbf{p}_{ob_s} - {}^0\mathbf{p}_{cl1}\right) \cdot \left({}^0\mathbf{p}_{cl2} - {}^0\mathbf{p}_{cl1}\right)\right) / \left\| {}^0\mathbf{p}_{cl2} - {}^0\mathbf{p}_{cl1} \right\|^2 \quad ; u \in [0...1] \qquad (3.49) $$

The shortest distance (ds_s) between the link i and the obstacle point cloud is:

$$ds_s = \left\| {}^0\mathbf{p}_{cl3\,i} - {}^0\mathbf{p}_{obs} \right\| \tag{3.50}$$

and the shortest distance from the obstacle point ${}^0\mathbf{p}_{ob\,s}$ to the surface of D_{min} is d_0 and it is given by

$$d_0 = ds_s - r_c \tag{3.51}$$

Thus, when d_0 is equal to 0, the obstacle point ${}^0\mathbf{p}_{ob\,s}$ is on D_{min} surface, consequently, the repulsive force is at maximum. When d_0 is equal to Er, the obstacle point ${}^0\mathbf{p}_{ob\,s}$ is on D_{max} surface, thus the repulsive force is zero.

The 3D-VF^2 method generates virtual repulsive forces based on the virtual volume/field defined by the SSB technique and the distance between the obstacle point and the virtual volume of a manipulator. The repulsive force $\mathbf{F}_{rep,i}$ on a link on coordinate frame i is given by

$$\mathbf{F}_{rep_i} = \delta_r({}^0\mathbf{p}_{obs}, {}^0\mathbf{p}_{cl3\,i}) = \begin{bmatrix} \mathbf{0}_{3\times1} \\ \mathbf{f}_{rep_i} \end{bmatrix} = \begin{bmatrix} 0 & 0 & 0 & f_{rep\,x_i} & f_{rep\,y_i} & f_{rep\,z_i} \end{bmatrix}^T \tag{3.52}$$

Similar to the ellipsoid bounding technique, a repulsive force $\mathbf{f}_{rep,i}$ is calculated:

$$\mathbf{f}_{rep_i} = \left(K_f - \frac{K_f}{1 + e^{-10(d_0 - 0.5Er)/Er}} \right) \frac{{}^0\mathbf{p}_{cl3\,i} - {}^0\mathbf{p}_{obs}}{\left\| {}^0\mathbf{p}_{cl3\,i} - {}^0\mathbf{p}_{obs} \right\|} \tag{3.53}$$

where K_f is a coefficient that indicates the maximum amplitude of the repulsive force (equivalent to the K_f that is used in EB). The repulsive forces on all links of the manipulator are generated in Cartesian space, and will be used in the dynamic model of the manipulator (Equation 3.23).

Both the EB and SSB techniques are used for generating 3D force fields and calculating repulsive forces in this thesis. The main difference between them is the way in which a force field is constructed and a repulsive is calculated. The principle and performance of the two techniques are similar.

3.5.3 Constant *Er*

The speed of the robot manipulator has a significant effect on the capability of the robot in collision avoidance. High speed means that the robot manipulator needs to response to any potential collisions very quickly and early enough to allow time to take action to avoid potential collisions. The robot's speed should therefore be taken into account in the 3D-VF^2 method. This is achieved by the parameter *Er* which represents the volume of the force field. *Er* is defined as the ratio between the current speed ($\left\|{}^0\dot{\mathbf{p}}_e\right\|$) and the maximum speed of the end-effector $Ve_{\max}$:

$$Er = \frac{k_{Er}\left\|{}^0\dot{\mathbf{p}}_e\right\|}{Ve_{\max}} \tag{3.54}$$

This definition enlarges the force field when the manipulator moves faster. Even if the speed of the end-effector of an industrial robot manipulator is slow, some of the joints may move quickly. In this case, *Er* needs to be defined using joint angular velocity, and the joint angular velocity ($\dot{\mathbf{q}}$). The $\dot{\mathbf{q}}$ is a set of angular speed of joints and the ${}^0\dot{\mathbf{p}}_e$ is the linear speed of the end-effector of the robot arm on Cartesian space. In this section, the transpose Jacobian ($\mathbf{J}^T$) is used to estimate the inverse Jacobian when the change of the Jacobian parameter is very small, this approximation is to simplify the Jacobian matrix inverting. The maximum angular velocity ($\dot{\mathbf{q}}_{\max}$) are calculated by:

$$\dot{\mathbf{q}} = \mathbf{J}^T(\mathbf{q})\,{}^0\dot{\mathbf{p}}_e \tag{3.55}$$

$$\dot{\mathbf{q}}_{\max} = \mathbf{J}^T(\mathbf{q})\mathbf{Ve}_{\max} \tag{3.56}$$

where $\mathbf{J}^T$ is the Jacobian transpose matrix of the extended manipulator model. Equation 3.54 can be rewritten as

$$\mathbf{Er} = \frac{k_{Er}\dot{\mathbf{q}}}{\dot{\mathbf{q}}_{\max}} \tag{3.57}$$

where $\dot{\mathrm{q}}$ and $\dot{\mathbf{q}}_{\max}$ are a current angular velocity (i.e. current joint speed) and the angular velocity from $\mathbf{Ve}_{\max}$ in joint space ($\dot{\mathbf{q}} \in \Re_{\mathbf{q}}{}^{7} \text{and} \dot{\mathbf{q}}_{\max} \in \Re_{\mathbf{q}}{}^{7}$). The $\dot{\mathbf{q}}_{\max}$ can be approximately estimated by the maximum velocity of the end-effector (Equation 3.56).

$$\mathbf{Ve}_{\max} \approx \frac{\mathbf{Ve}}{\|\mathbf{Ve}\|} Ve_{\max} = \frac{\mathbf{J(q)\dot{q}}}{\|\mathbf{J(q)\dot{q}}\|} Ve_{\max} \tag{3.58}$$

Therefore, the $\dot{\mathbf{q}}_{\max}$ is given by

$$\dot{\mathbf{q}}_{\max} = \frac{\mathbf{J}^{T}\mathbf{(q)J(q)\dot{q}}}{\|\mathbf{J(q)\dot{q}}\|} Ve_{\max} \tag{3.59}$$

3.6 Self-Collision Avoidance Method

Self-collision between the force fields of two links of a manipulator and between the manipulator and the platform is another important problem that needs to be solved before implementing the VF^2 approach in an actual robotic system. For the targeted application of this thesis (i.e. the sandblasting robotic system), a manipulator mounted on a big mobile platform may collide with the mobile platform, and potential self-collision should therefore be avoided. In this section, the links of the manipulator are represented by virtual fields generated by the SSB technique, and a virtual field is used to cover the mobile platform. The distances of link-to-link and link-to-platform will be geometrically determined.

3.6.1 Collision Detection Between Links of the Manipulator

From the 3D-VF^2 presented in Section 3.5.2, the links of a manipulator are represented by virtual force fields. To measure the distance between two links of a manipulator, two links on coordinate frame *i* and coordinate frame *j* are parametrically represented by Equation 3.60 and Equation 3.61. The parameters u_i and u_j define ${}^{0}\mathbf{p}_{cl3\,i}(u_i)$ and ${}^{0}\mathbf{p}_{cl3\,j}(u_j)$ on the centre axes. Both u_i and u_j are between 0 and 1. Figure 3.13 shows the fields of two links and their parameters. The radiuses of the two capsules are set by r_{c_i} and r_{c_j} for the link on coordinate frames *i* and *j*, respectively.

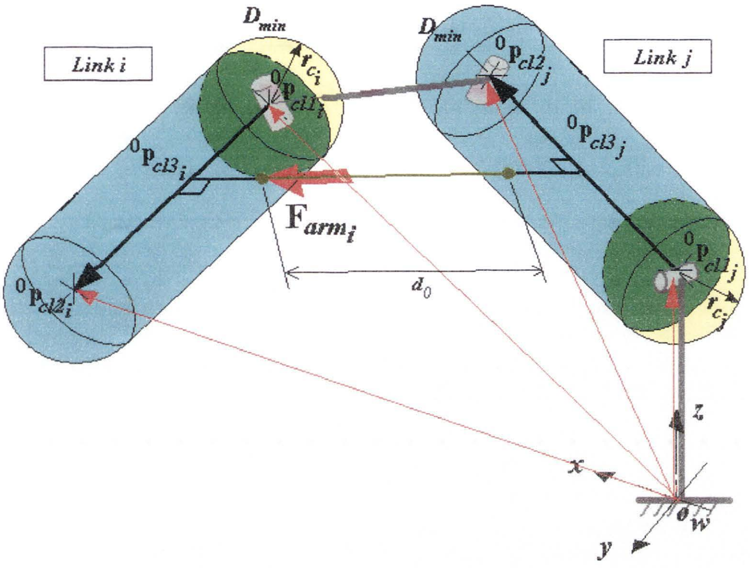

Figure 3.13 Distance between two D_{min}s defined by sphere-swept bounding

$$ {}^0\mathbf{p}_{cl3\,i}(u_i) = {}^0\mathbf{p}_{cl1\,i} + u_i\left({}^0\mathbf{p}_{cl2\,i} - {}^0\mathbf{p}_{cl1\,i}\right) \quad ; u_i \in [0...1] \tag{3.60} $$

$$ {}^0\mathbf{p}_{cl3\,j}(u_j) = {}^0\mathbf{p}_{cl1\,j} + u_j\left({}^0\mathbf{p}_{cl2\,j} - {}^0\mathbf{p}_{cl1\,j}\right) \quad ; u_j \in [0...1] \tag{3.61} $$

The shortest distance between link *i* and link *j* is defined by

$$ \min_{u_i} \min_{u_j} \left\{ \left\| {}^0\mathbf{p}_{cl3\,i}(u_i) - {}^0\mathbf{p}_{cl3\,j}(u_j) \right\| \right\} \quad ; u_i \in [0...1], u_j \in [0...1] \tag{3.62} $$

and is given by

$$ d_0 = \left\| {}^0\mathbf{p}_{cl3\,i}(u_i) - {}^0\mathbf{p}_{cl3\,j}(u_j) \right\| - r_{c_i} - r_{c_j} \tag{3.63} $$

When the D_{min}s of links *i* and *j* have interactions, d_0 will be equal to 0 and a maximum repulsive force ($\mathbf{F}_{arm}$) will be generated. For a typical robot manipulator, self-collision may occur between two links that are not directly connected. A repulsive force ($\mathbf{F}_{arm}$) on link *i* (in coordinate frame *i*) from link *j* in coordinate frame *j* is given by

$$\mathbf{F}_{arm\,i} = \sum_{j=i-2}^{0} \delta_r({}^{0}\mathbf{p}_{cl3\,j}, {}^{0}\mathbf{p}_{cl3\,i}) \tag{3.64}$$

$$\delta_r({}^{0}\mathbf{p}_{cl3\,j}, {}^{0}\mathbf{p}_{cl3\,i}) = \begin{bmatrix} \mathbf{0}_{3\times1} \\ \mathbf{f}_{arm\ ij} \end{bmatrix} = \begin{bmatrix} 0 & 0 & 0 & f_{arm\,x\,ij} & f_{arm\,y_{ij}} & f_{arm\,z\,ij} \end{bmatrix}^T \tag{3.65}$$

$$\mathbf{f}_{arm_{ij}} = \left(K_f - \frac{K_f}{1+e^{-10(d_0-0.5Er)/Er}} \right) \frac{{}^{0}\mathbf{p}_{cl3\,i} - {}^{0}\mathbf{p}_{cl3\,j}}{\left\| {}^{0}\mathbf{p}_{cl3\,i} - {}^{0}\mathbf{p}_{cl3\,j} \right\|} \tag{3.66}$$

3.6.2 Manipulator and Platform Collision Detection

The geometric shape of a mobile platform assumed in this thesis is a rectangular prism. A swept sphere bounding the rectangular prism is used to model the mobile platform (Figure 3.14).

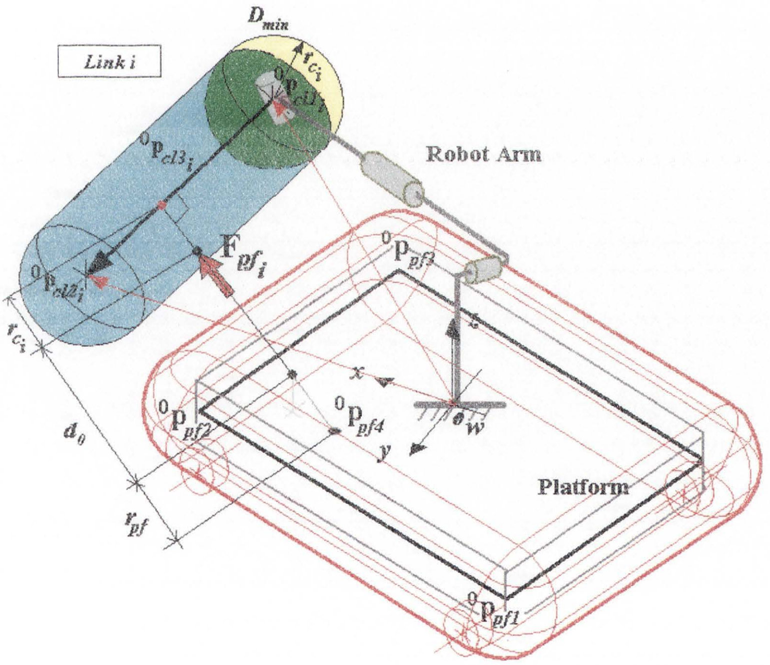

Figure 3.14 Distance d_0 between D_{min} of a link and D_{min} of the mobile platform

A link of the manipulator is represented by Equation 3.60 and the platform is represented by

$$ {}^{0}\mathbf{p}_{pf4}(u_j,u_k)=(1-u_j-u_k)^{0}\mathbf{p}_{pf1}+u_j\left({}^{0}\mathbf{p}_{pf2}\right)+u_k\left({}^{0}\mathbf{p}_{pf3}\right)\quad ;0\le u_j\le 1\ and 0\le u_k\le 1 \tag{3.67} $$

where ${}^{0}\mathbf{p}_{pf1}$, ${}^{0}\mathbf{p}_{pf2}$, and ${}^{0}\mathbf{p}_{pf3}$ represent the corner points of the mobile platform that can be seen in Figure 3.14. Parameter u_i defines a point, ${}^{0}\mathbf{p}_{cl3\,i}(u_i)$ on the centre axis of the field of a link and parameters u_j and u_k define a point, ${}^{0}\mathbf{p}_{pf4}(u_j,u_k)$ on the rectangular prism. The minimum distance between the link and the platform is defined by

$$ \min_{u_i}\min_{u_j}\min_{u_k}\left\{\left\|{}^{0}\mathbf{p}_{cl3\,i}(u_i)-{}^{0}\mathbf{p}_{pf4}(u_j,u_k)\right\|\right\} \tag{3.68} $$

and is given by

$$ d_0=\left\|{}^{0}\mathbf{p}_{cl3\,i}(u_i)-{}^{0}\mathbf{p}_{pf4}(u_j,u_k)\right\|-r_c-r_{pf} \tag{3.69} $$

The repulsive force on a link in coordinate frame i from the platform is defined as

$$ \mathbf{F}_{pf\,i}=\delta_r({}^{0}\mathbf{p}_{pf4},{}^{0}\mathbf{p}_{cl3\,i})=\begin{bmatrix}\mathbf{0}_{3\times1}\\ \mathbf{f}_{pf\,i}\end{bmatrix}=\begin{bmatrix}0 & 0 & 0 & f_{pf\,x\,i} & f_{pf\,y\,i} & f_{pf\,z\,i}\end{bmatrix}^T \tag{3.70} $$

$$ \mathbf{f}_{pf}=\left(K_f-\frac{K_f}{1+e^{-10(d_0-0.5Er)/Er}}\right)\frac{{}^{0}\mathbf{p}_{cl3\,i}-{}^{0}\mathbf{p}_{pf4}}{\left\|{}^{0}\mathbf{p}_{cl3\,i}-{}^{0}\mathbf{p}_{pf4}\right\|} \tag{3.71} $$

, when distance d_0 is less than Er, the $\mathbf{F}_{pf}$ will increase.

3.7 Case Studies

This section presents three case studies comprised of manipulator tasks in complex environments to validate the attractive force method, the 3D-VF^2 method, the force control algorithm and the self-collision avoidance method presented in this chapter. Simulation and implementation in a robotic system in complex 3D environments are presented. These methods are programmed in MATLAB and C++. Two robot manipulator models are used: the Denso® VS6556 manipulator is used in case studies

1 and 2, and the Denso® VM6083, a bigger manipulator, is used in case study 3. In the third case study, the manipulator is placed on a mobile platform inside a bridge maintenance environment which is constructed in a laboratory.

3.7.1 Case Study 1: The 3D-VF^2 Method for Collision Avoidance

This case study aims to validate the performance of the 3D-VF^2 method for on-line collision detection and avoidance of a robot manipulator in complex environments. The attractive force method and force control algorithm are not applied in this case study. To calculate the joint angles of the manipulator ($\mathbf{q}$) from a target point ($^0\mathbf{p}_t$) of the end-effector, inverse kinematics is used, but we do not aim to study the inverse kinematics because the focus of this experiment is only on the 3D-VF^2 method. In the case study, a robot manipulator (end-effector) undertakes the tasks of following expected paths in two different environments.

Environment 1: The robot manipulator undertakes sandblasting in a steel bridge maintenance environment (Figure 3.15 and Figure 3.17).

Figure 3.15 shows snapshots of the manipulator performing sandblasting on a ceiling surface. A pre-planned path shown in Figure 3.15 is determined from the target plane. Joint angle changes are recorded and presented in Figure 3.16. Results of simulation show that there is no collision, and joints of the manipulator usually ripple even when the manipulator moves along a straight line trajectory.

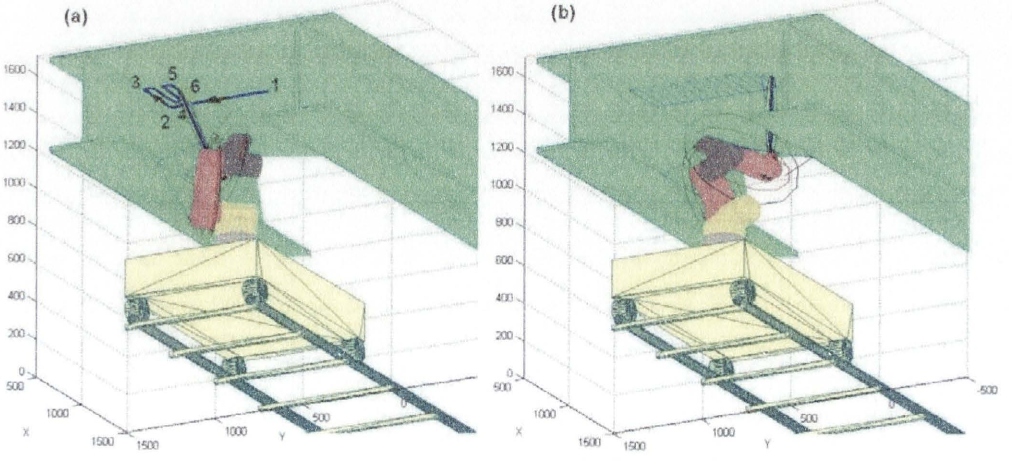

Figure 3.15 Sandblasting a surface (ceiling) of a steel bridge structure

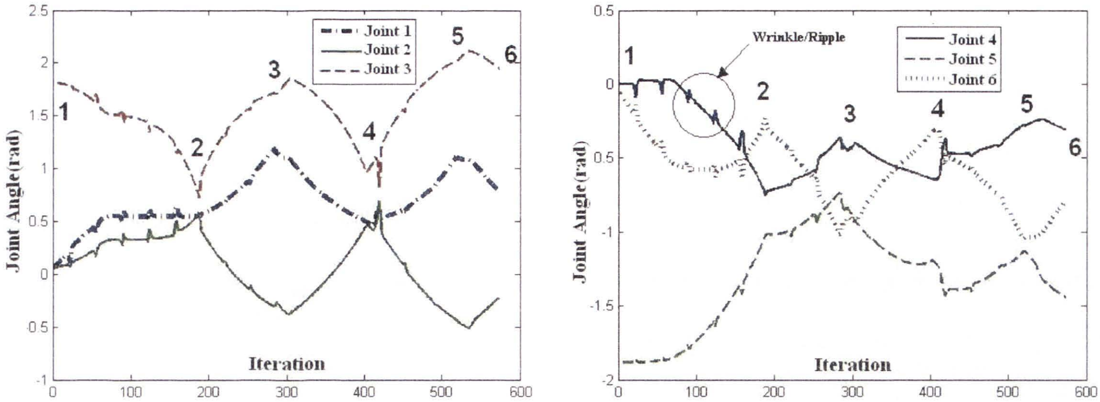

Figure 3.16 Joint angles of the manipulator tracking a path in Figure 3.15(a)

Figure 3.17 shows snapshots of the manipulator performing sandblasting on a surface of a steel bridge I-beam. A pre-planned path shown in Figure 3.17(d) is planned from the target surface which has a pipe blocking the manipulator trajectory. Joint angles are recorded and presented in Figure 3.18. Results of the simulation show that no collision occurred. The joint angle change of the manipulator is not smooth although the straight line trajectory is presented.

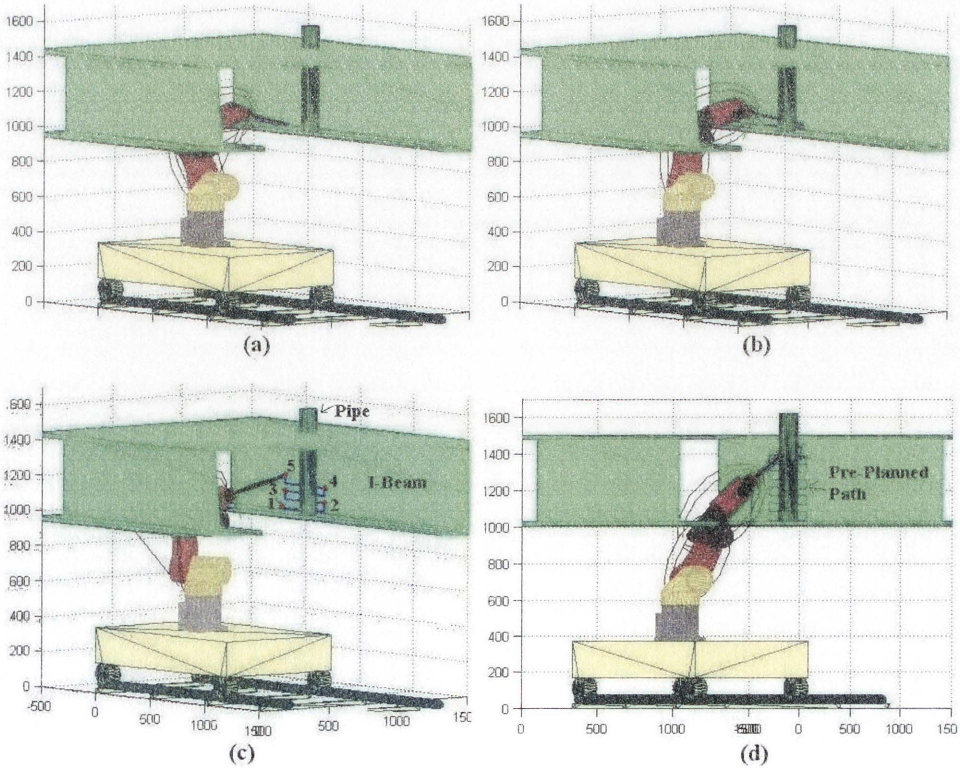

(a) (b)

(c) (d)

Figure 3.17 Snapshot of a manipulator performing a sandblasting task on an I-beam in a steel bridge maintenance environment

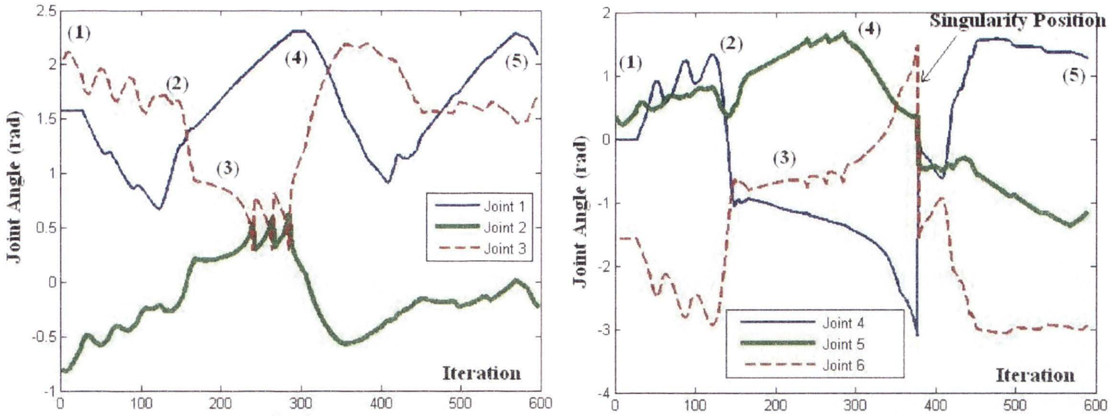

Figure 3.18 Joint angle changes of the manipulator following a pre-planned path shown in Figure 3.17(c)

A singularity problem is presented. The singularity condition of the manipulator causes the joints 4 and 6 of the manipulator to suddenly rotate 360 degrees (2π) or change from + to - while the end-effector of the manipulator is still the same position.

Environment 2: The manipulator undertakes tasks of spray-painting three surfaces in a complex and compact environment: a ceiling, a wall, and a cylinder ventilator.

This experiment aims to test the performance of the 3D-VF^2 method in a more compact environment than the first. Obstacles are located around the manipulator in close range. In the simulation, joint angle changes are recorded along the paths.

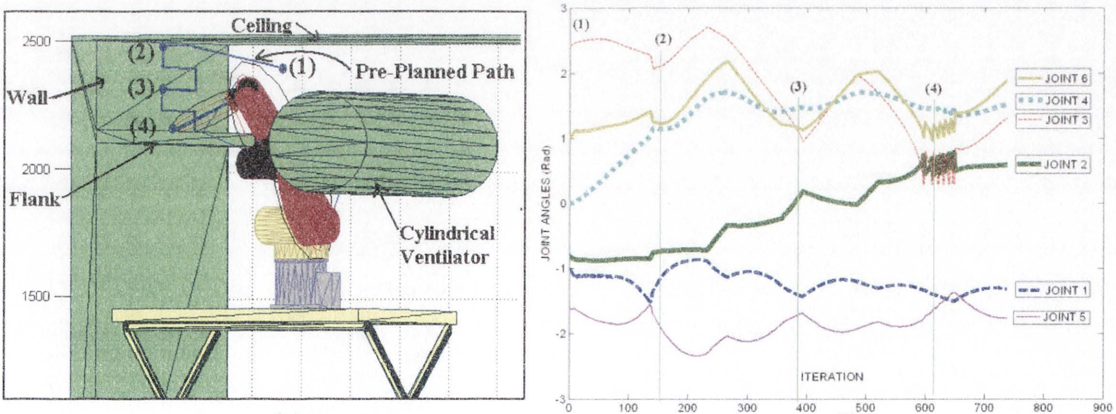

(a) (b)

Figure 3.19 (a) Manipulator spray-painting on a wall (b) Joint angle changes with a pre-planned path

Figure 3.19(a) shows a snapshot of the manipulator painting a wall in the compact environment. The pre-planned path starts at position 1 and ends at position 4. Figure 3.19(b) shows the joint angle changes of the manipulator and markers 1 to 4 show the angle changes in positions 1 to 4 on the pre-planned path. At position 4, two repulsive forces from the wall and the flank respectively are opposite each other, and consequently cause the end-effector link of the manipulator to oscillate. These two repulsive forces prevent the manipulator from colliding; at the same time, they cause joint angle oscillation of joints 2, 3 and 6 (Figure 3.19(b)).

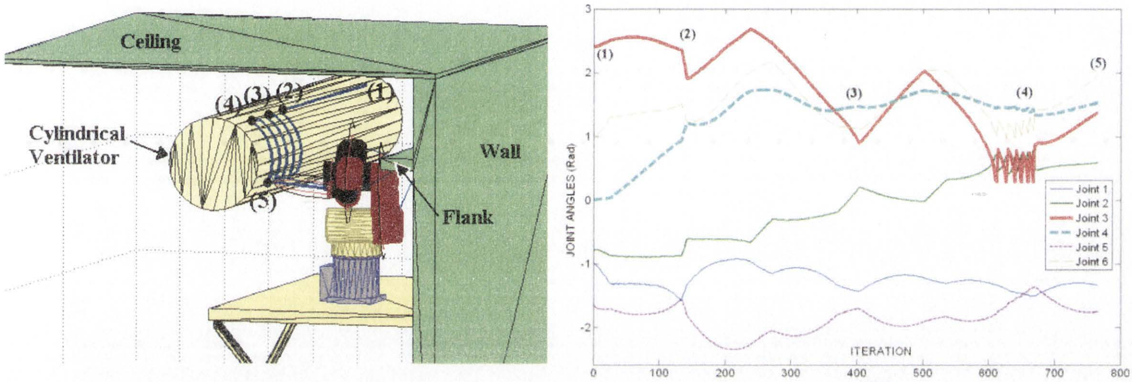

(a) (b)

Figure 3.20 (a) A manipulator spray-painting a cylinder ventilator, (b) Joint angle changes of the manipulator with a pre-planned path

Figure 3.20(a) shows a snapshot of the manipulator spray-painting a surface of the cylinder ventilator. The pre-planned path starts at position 1 and ends at position 5. The graph in Figure 3.20(b) shows the joint angle changes of the manipulator, and markers 1 to 5 in Figure 3.20(b) correspond to the positions 1 to 5 on the pre-planned path. At position 4, the manipulator suffers from repulsive forces which are generated from the cylindrical ventilator to the end-effector, and from the ceiling surface to link 5 of the manipulator. These forces caused oscillation of the joint angles of joints 3 and 6, although they successfully prevent the manipulator from colliding with the environment.

Figure 3.21 shows snapshots of the manipulator spray-painting a surface of the ceiling. The graph in Figure 3.22 shows the joint angles of the manipulator, and markers 1 to 4 in Figure 3.22 correspond to positions 1 to 4 on the pre-planned path in Figure 3.21(a). In this simulation, many repulsive forces are generated on the links of the manipulator. Additionally, a singularity condition of the manipulator occurs, as shown in Figure 3.22 (b): the 4th joint and the 6th joint of the manipulator suddenly rotate 360 degrees (2π) and the 5thjoint change from -1 to 1 while the end-effector of the manipulator is still in the same position.

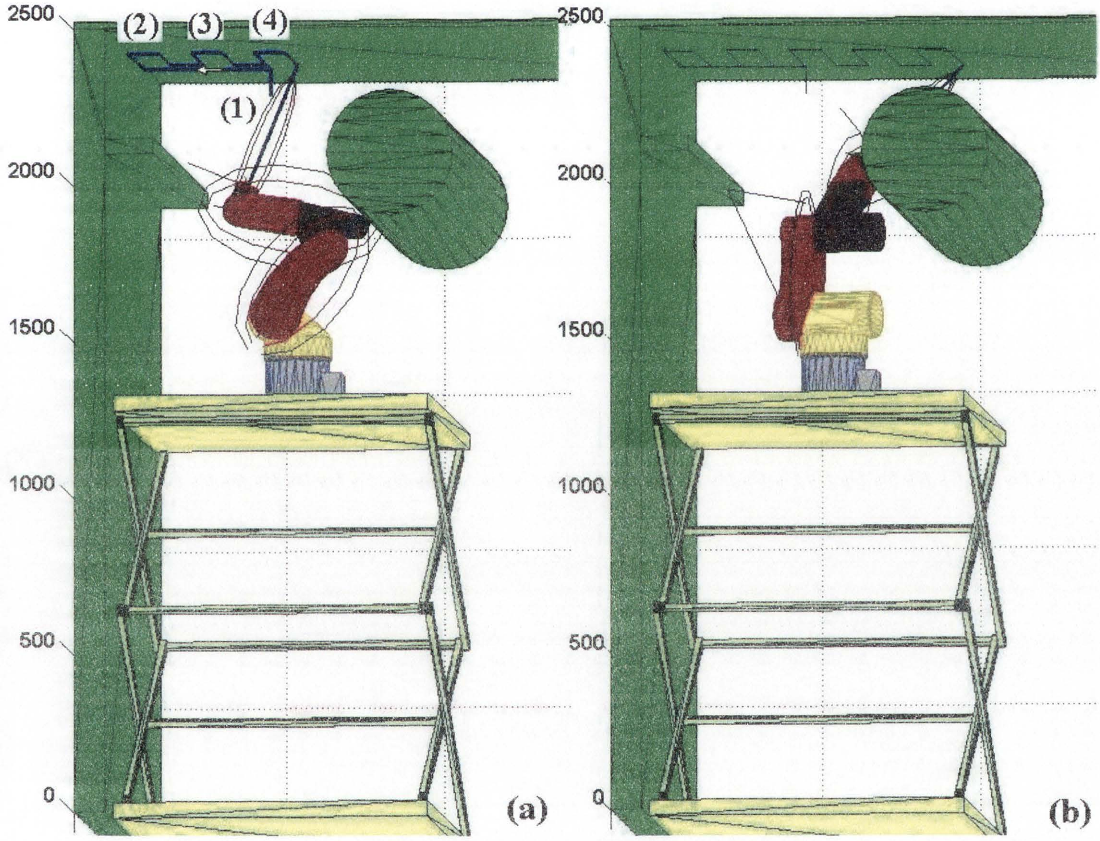

Figure 3.21 A manipulator spray-painting a ceiling surface

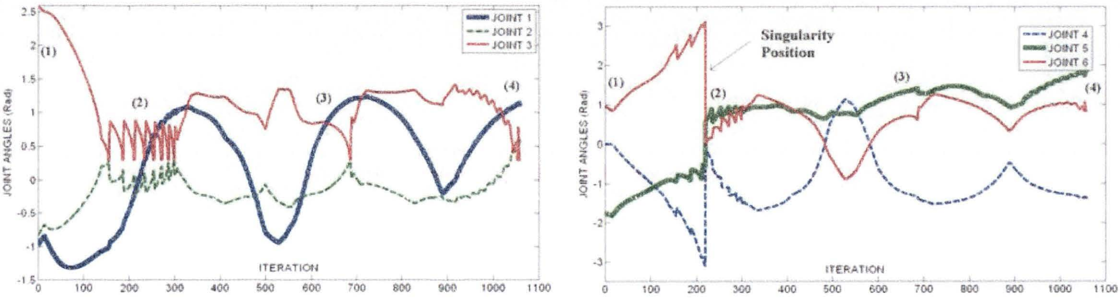

Figure 3.22 Joint angle changes of the manipulator with a pre-planned path in Figure 3.21a

In conclusion, the simulation results of the first case study show that the 3D-VF^2 method is able to prevent the manipulator from colliding with obstacles in complex environments. The joint angle changes are not always smooth even though the end-effector of the manipulator is still on a straight line path. Oscillations occur when the manipulator reaches narrow areas, in which several repulsive forces around the link are generated. A part from this result, singularity conditions of the manipulator cause jerky motions of the manipulator which is an issue related to inverse kinematics. Thus, this inverse kinematic method can not be implemented in a real robot manipulator. To overcome the singularity problem, the VF^2 approach, which includes the 3D-VF^2 method, the AF method, and FC algorithm, is applied and the case studies follow.

3.7.2 Case Study 2: The VF^2 Approach for Collision-free Motion

In this case study, the VF^2 approach, which includes the 3D-VF^2 method, the Attractive Force (AF) method and the Force Control (FC) algorithm, are tested in different environments. Figure 3.23 shows a control diagram of how this approach is applied in a robotic system. The AF method is used to calculate an attractive force based on a target point and the current position of the manipulator end-effector. The attractive force is transformed to torques in the joint space of the manipulator by the FC algorithm. The torques from the attractive force are combined with torques transformed from repulsive forces which are calculated by the 3D-VF^2 method. Resultant torques are applied to the dynamic model of the manipulator to generate a new pose for the manipulator.

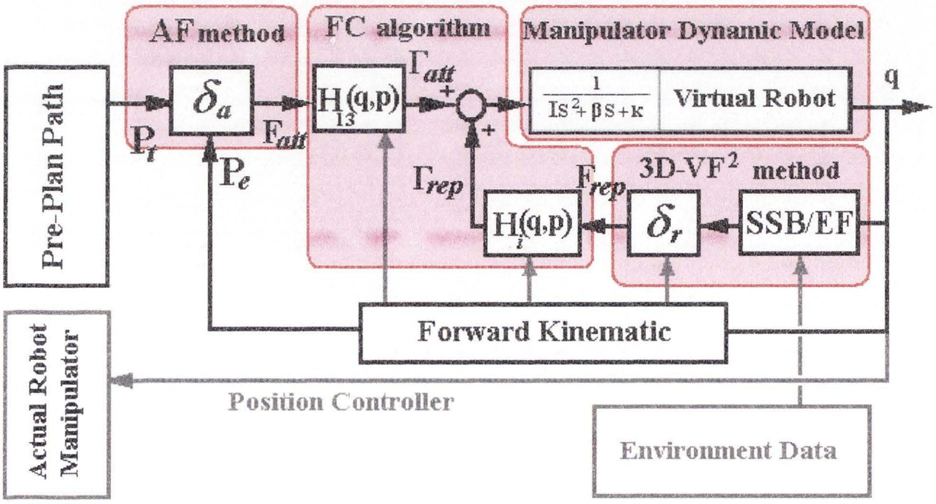

Figure 3.23 Block diagram of the VF^2 approach for motion planning for a manipulator

3.7.2.1 Simulation 1

This simulation test is conducted in a workspace where a manipulator moves its end-effector from the current position located in one side of a plate to target positions located in the other side of the plate by passing through a hole on the plate (Figure 3.24). The main purpose of this simulation is to show that the VF^2 approach can generate robot motion in confined space in real-time, which is different from other approaches that generate robot motion offline. In this simulation, the task is designed for the robot arm moving through small holes. The robot is acted by many repulsive forces generated by obstacles around its links. This situation is caused by the complex environment although there are not many obstacles around the robot. Only four target points (point 1, 2, 3, and 4) are defined and the whole trajectory (red line) is generated by the robot itself with the AF method, the 3D-VF^2 method, and the force control method.

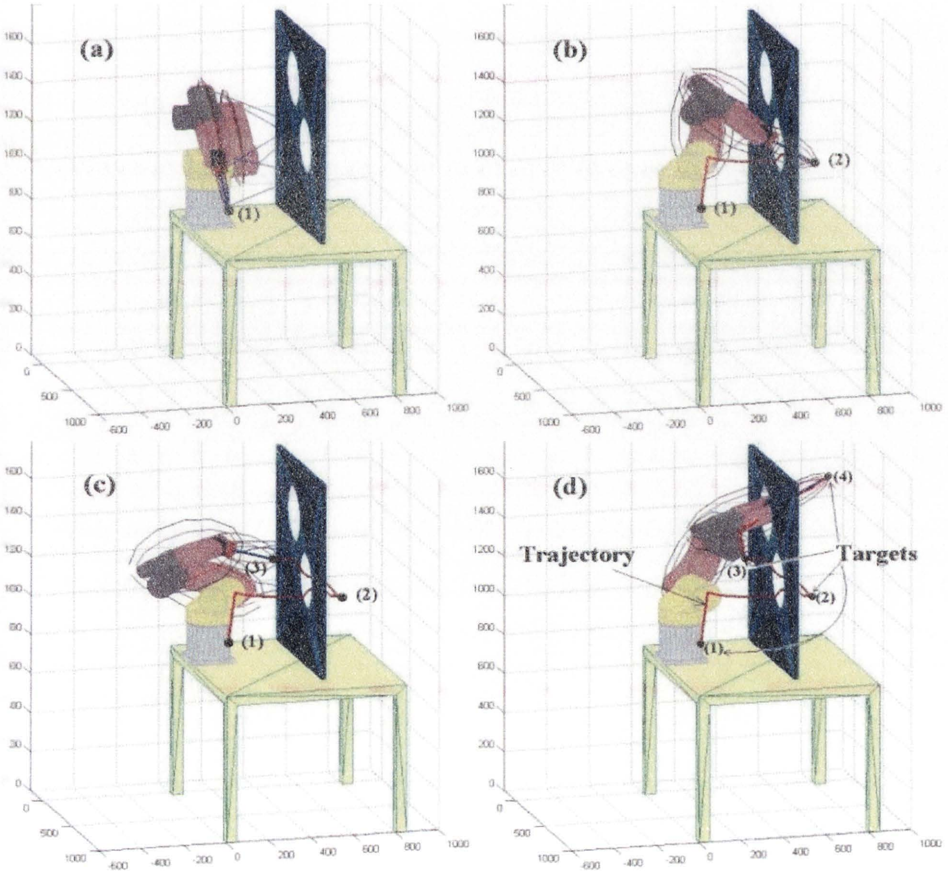

Figure 3.24 A manipulator approaching multiple target positions (2), (3) and (4)

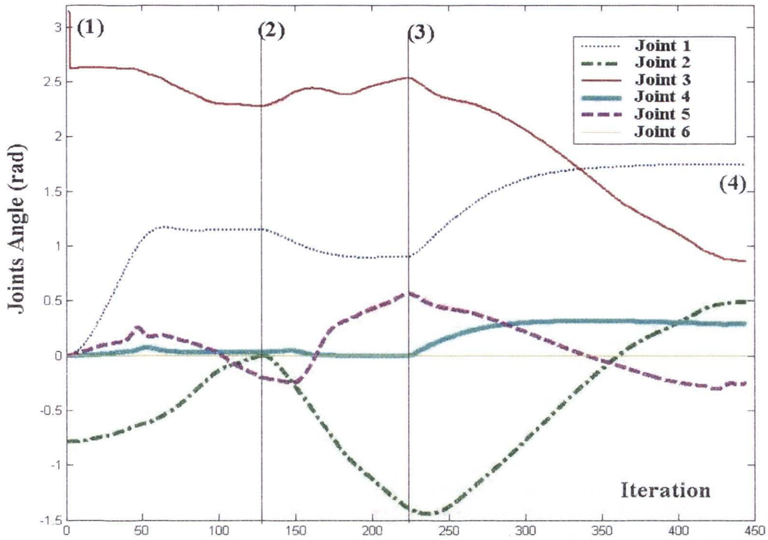

Figure 3.25 Joint angle changes of the manipulator approaching the target positions shown in Figure 3.24

Test results (Figure 3.24 and 3.26) show that the VF^2 approach is able to control the motion of a robot manipulator in complex and compact environments safely and smoothly. Although the manipulator suffers from several repulsive forces when it goes into a hole, the oscillation of the joint angle change is significantly reduced compared with the results of the first case study presented in Section 3.7.1. This is because the VF^2 approach does not calculate joint angles using inverse kinematics. The manipulator pose is calculated from the dynamic model of the manipulator, so safe and smooth motion of the manipulator is obtained.

3.7.2.2 Simulation 2

In many industrial applications, a constant speed of the end-effector is required. An attractive force, generated by the AF method, pulls the end-effector of the manipulator toward a target point. The amplitude of the attractive force is dependent on a distance between a target point and the current end-effector position. If a target point is moved along a pre-planned path with constant speed, the manipulator should follow along the pre-planned path at same speed. The purpose of conducting this test is to verify this.

In the test, the manipulator is simulated to work under a steel bridge channel. The task is to blast the surface of an I-beam by following a pre-planned path at a constant speed. The environment is represented by a point cloud map obtained from a 3D laser scanner.

A pre-planned path covers the target area of an I-beam which is 600 mm wide and 300mm high. This test is conducted at three different end-effector speeds: 15mm/sec, 35mm/sec, and 75mm/sec.

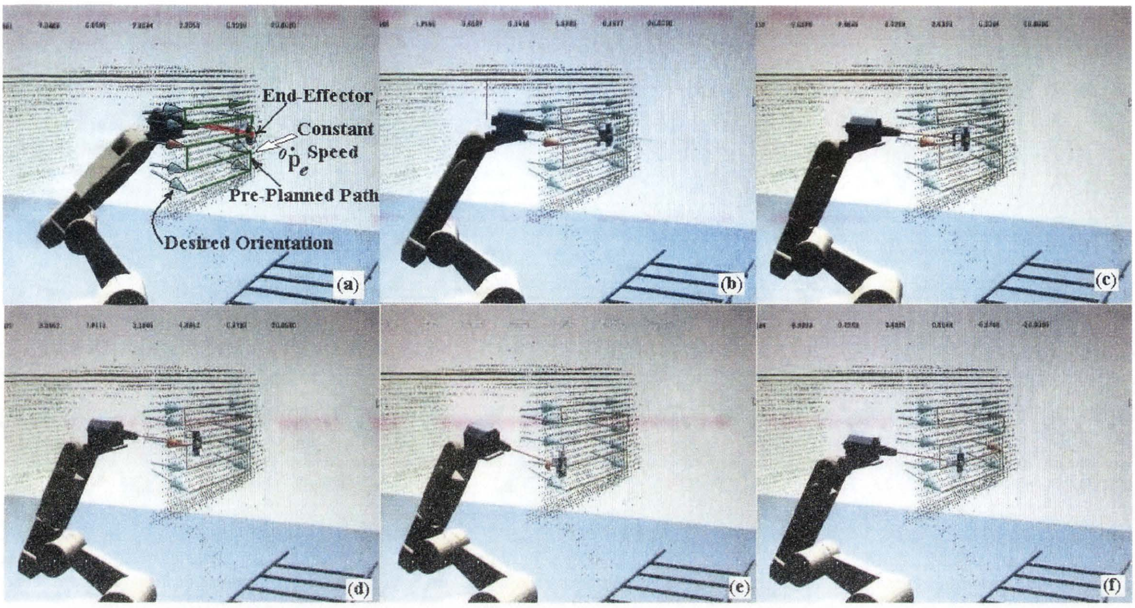

Figure 3.26 A manipulator following a pre-planned path

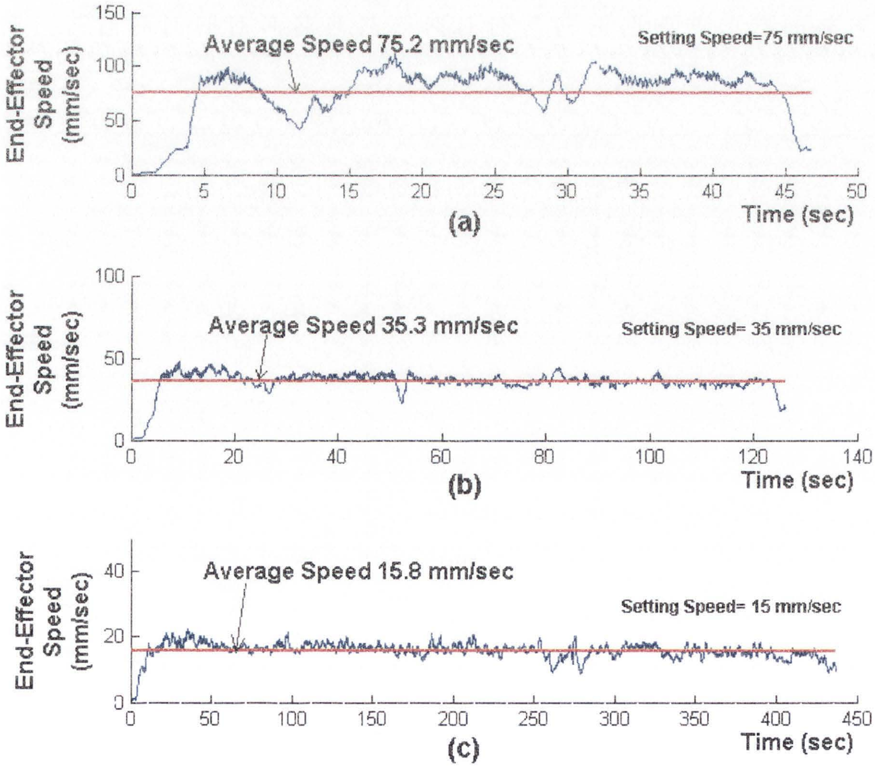

Figure 3.27 (a) Speed of the end-effector at 75 mm/sec, (b) Speed of the end-effector at 35 mm/sec, (c) Speed of the end-effector at 15 mm/sec

Figure 3.26 shows snapshots of the simulation. In Figure 3.26 (a), the pre-planned path is presented by lines, and arrows indicate the desired orientation for the end-effector (blasting spot on the surface). Figure 3.27 shows the recorded speeds of the end-effector. The results indicate that the VF^2 approach is able to control the speed of the end-effector. It is also noted that error between the expected speed and the actual speed is less when the speed is low, and that the VF^2 approach can not always maintain the desired orientation when the speed of the end-effector is high.

3.7.2.3 Simulation 3

Orientation of the manipulator end-effector needs to be controlled in many applications. In the sandblasting process, for example, the angle of the nozzle to a target surface must be controlled in order to achieve the required blasting quality. However, it was found in the last simulation that the VF^2 approach can not always maintain the desired orientation when the speed of the end-effector is high; therefore, a test is conducted to justify the effect of the end-effector speed on orientation.

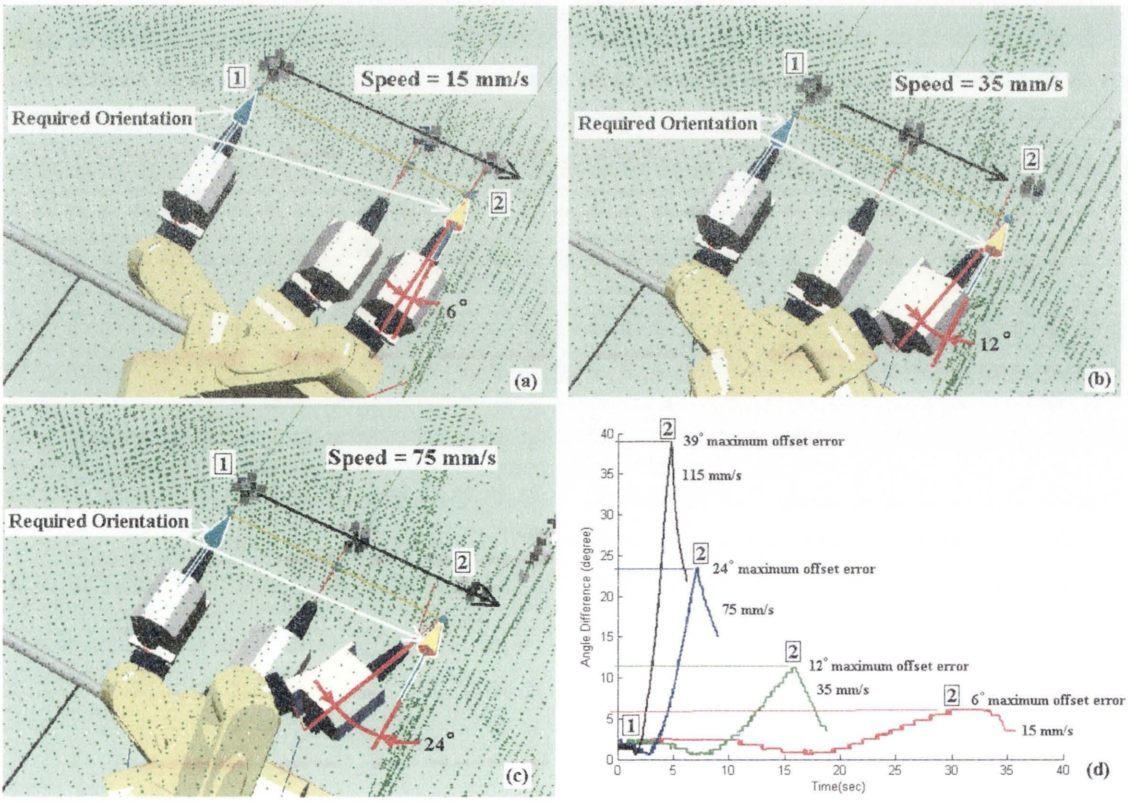

Figure 3.28 (a) Orientation change at speed 15 mm/sec, (b) Orientation change at speed 35 mm/sec, (c) Orientation change at speed 75 mm/sec, and (d) Orientation angle difference at different speeds

Figure 3.28 shows the testing setup and the orientation changes at different speeds. In the tests, the manipulator is controlled to perform sandblasting on a 500mm straight line path from point 1 to point 2 with speed of 15mm/sec, 35mm/sec, 75mm/sec, and 115mm/sec. The desired orientation is set to the target plane for all tests. The graphs in Figure 3.28 (d) show the orientation changes with different testing speeds, and a higher speed results in greater orientation change. The result shows that the VF^2 approach is not able to control the orientation of the end-effector precisely. This is an issue to be addressed in future work.

3.7.3 Case Study 3: Implementation

In this case study, the VF^2 approach has been implemented in the control system of a sandblasting robotic system. The control system is programmed in Matlab7® which is executed on a computer with 1.5GHz CPU. The control system sends movement commands to the position controller of the manipulator through serial communication (i.e. the RS232 serial port). Figure 3.29 shows the pre-planned path that the manipulator must follow in order to sandblast a surface of the I-beam. This implementation aims to test the VF^2 approach in a robotic system operating in a real environment.

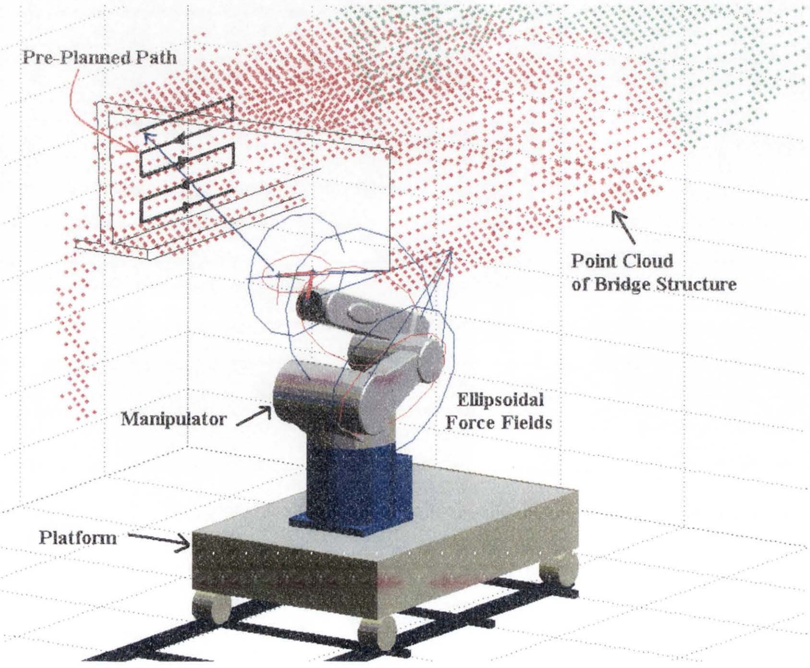

Figure 3.29 Pre-planned path for a sandblasting robotic system

Figure 3.30 shows snapshots of the sandblasting robot system performing sandblasting on an I-beam. An L-shaped piece of cardboard is used to represent the sandblasting nozzle and the blasting stream.

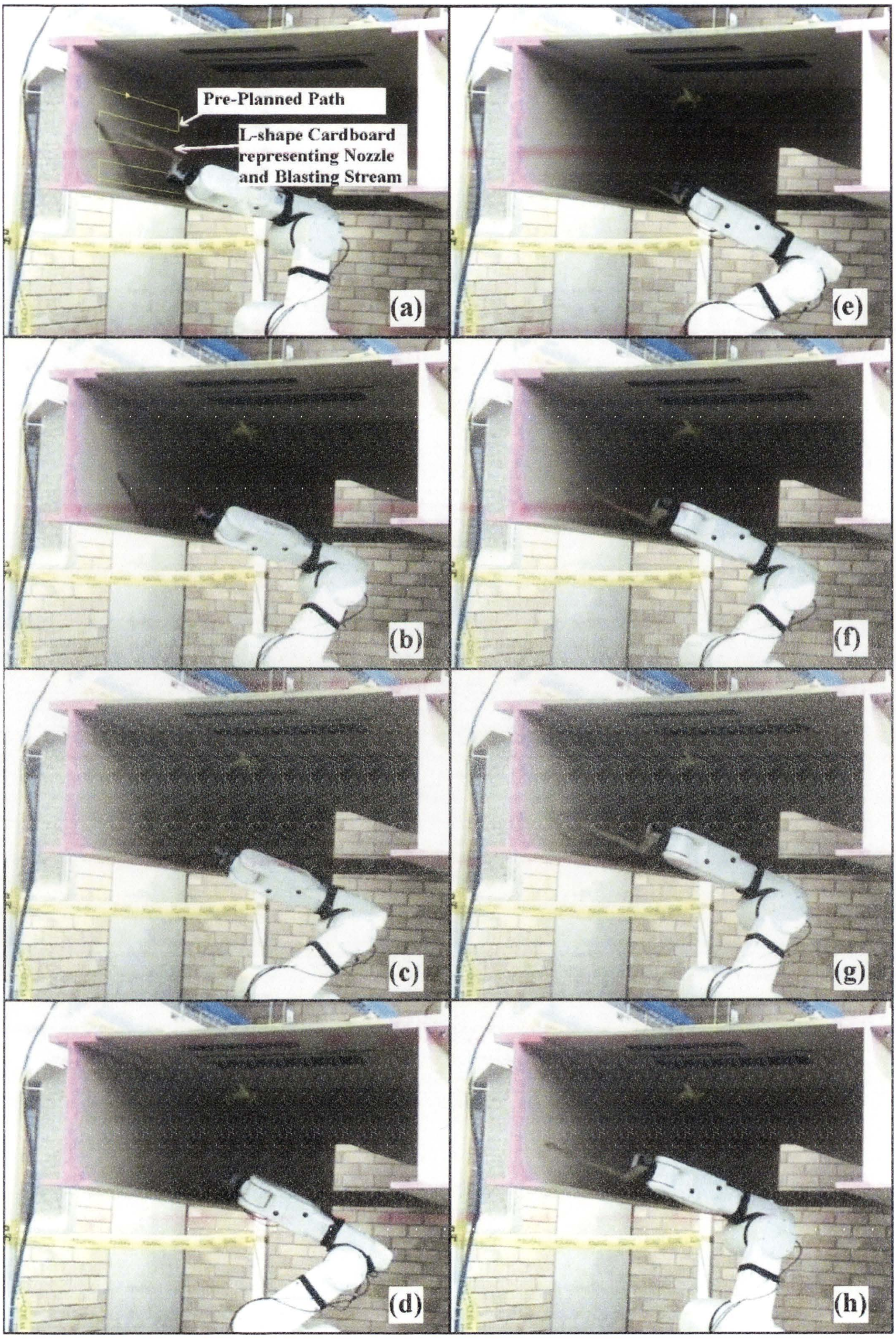

Figure 3.30 Snapshot of implementation in a sandblasting robot system

The implementation results verified the effectiveness and efficiency of the proposed VF^2 approach to on-line collision-free motion planning of a robot manipulator interacting with complex 3D environments. The total processing time per iteration (i.e. the cycle time of the control system) is 18 ms (55.55 Hz), including computation time of 12 ms and communication time of 6 ms per iteration.

3.8 Conclusion

This chapter has presented the Virtual Force Field (VF^2) approach for Robot-Environment Interaction (REI). The VF^2 includes the Force Control (FC) algorithm, the Attractive Force (AF) method, and the Three-Dimensional Virtual Force Field (3D-VF^2) method. The AF generates a driving force for the manipulator while the 3D-VF^2 generates repulsive forces to prevent the manipulator from colliding with obstacles in the surrounding environment. The forces are processed by the FC algorithm to determine the joint angles based on the dynamic model of the manipulator.

Simulation and implementation results have demonstrated that the VF^2 approach is an effective collision-free motion planning approach for a robot manipulator to interact with complex 3D environments.

Chapter 4 Effective Control Approach to Haptic Device-Robot Interface

The Virtual Force Field (VF^2) approach presented in Chapter 3 provides effective methods (i.e. 3D-VF^2 method, AF method, and FC algorithm) for Robot-Environment Interaction (REI). This approach generates collision-free motion for an industrial robot manipulator operating in complex 3D environments and undertaking tasks which are not amenable to a repetitive motion solution.

This chapter presents a Haptic Control (HC) approach to a haptic device-robot manipulator interface. HC is based on the virtual spring concept and the virtual force field (VF^2) approach. The HC approach enables safe and intuitive interaction in teleoperation. The key components of the HC approach include a haptic force generation method and a novel workspace mapping method.

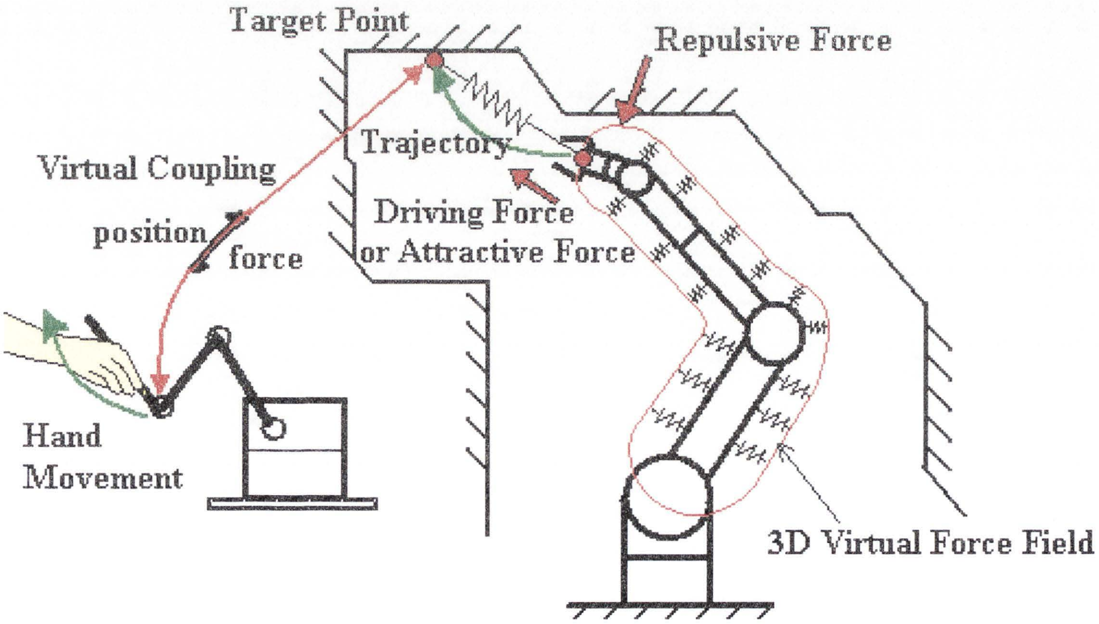

Figure 4.1 Haptic device-robot interface

For the targeted application of this thesis, a haptic device that provides force feedback is used to control the robot. Figure 4.1 shows a bi-directional interface between the haptic device and the robot manipulator. The haptic device is used to control the target point. Force feedback is then generated in the haptic device (i.e. feedback force to the operator) by a virtual spring based on the target point and the position of the robot manipulator. A virtual spring [96][13] is used for connecting the haptic cursor and the end-effector of the manipulator. The spring force, or haptic force, is generated to provide the operator with kinesthetic sense. The virtual spring also generates a virtual force by the attractive force field (AF) method presented in Chapter 3 to pull the robot manipulator to approach the target point, while the three-dimensional virtual force field (3D-VF^2) method provides the robot collision protection.

4.1 Haptic Device Coordination System

The coordinate system of a haptic device needs to be established in order to define a position and develop an interface between a haptic device and a manipulator. The position vector of a haptic cursor is defined by ${}^h\mathbf{P}_a$ on the haptic device coordinate frame (h), and it contains a position vector (${}^h\mathbf{p}_a$) and a direction vector (${}^h\mathbf{n}_a$). The position vector (${}^h\mathbf{P}_a$) is used to represent both the position of the handle of a haptic device in the physical workspace of the haptic device and the position of the haptic cursor in the virtual environment. For a 3DOF haptic device as shown in Figure 4.2, a direction vector (${}^h\mathbf{n}_a$) in ${}^h\mathbf{P}_a$ will be set equal to 0 as shown in Equation 4.1 because the 3DOF haptic device provides only the position vector of the haptic cursor without its orientation.

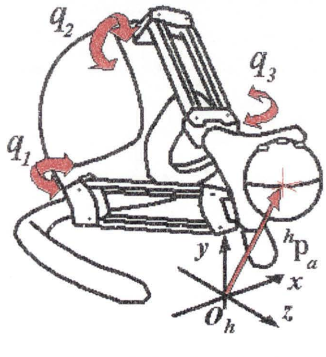

Figure 4.2 A 3DOF haptic device: Novint® Falcon

$$ {}^{h}\mathbf{P}_{a} = \begin{bmatrix} \mathbf{0} \\ {}^{h}\mathbf{p}_{a} \end{bmatrix} = \begin{bmatrix} 0 & 0 & 0 & {}^{h}p_{ax} & {}^{h}p_{ay} & {}^{h}p_{az} \end{bmatrix}^{T} \tag{4.1} $$

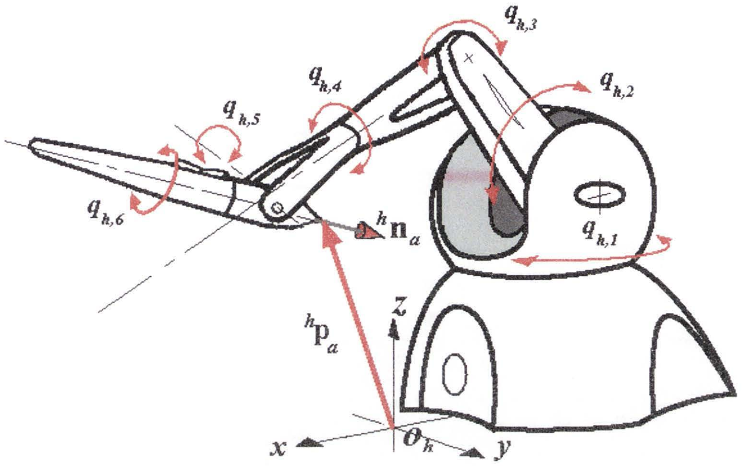

Figure 4.3 A 6DOF haptic device: Phantom® Omni

For a 6DOF haptic device such as Phantom® Omni shown in Figure 4.3, the position vector of the haptic device (${}^{h}\mathbf{P}_{a}$) is given by

$$ {}^{h}\mathbf{P}_{a} = \begin{bmatrix} {}^{h}\mathbf{n}_{a} \\ {}^{h}\mathbf{p}_{a} \end{bmatrix} = \begin{bmatrix} {}^{h}n_{ax} & {}^{h}n_{ay} & {}^{h}n_{az} & {}^{h}p_{ax} & {}^{h}p_{ay} & {}^{h}p_{az} \end{bmatrix}^{T} \tag{4.2} $$

where ${}^{h}\mathbf{p}_{a}$ is from the transformation matrix (${}^{h}\mathbf{T}_{a}$) of the 6DOF haptic device:

$$ {}^{h}\mathbf{T}_{a}(\mathbf{q}_{h}) = \begin{bmatrix} & {}^{h}\mathbf{R}_{a} & & {}^{h}\mathbf{p}_{a} \\ 0 & 0 & 0 & 1 \end{bmatrix} \tag{4.3} $$

where $\mathbf{q}_{h}$ is the current joint angle of the 6DOF haptic device. ${}^{h}\mathbf{n}_{a}$ is the normal unit vector of the z-axis of the end-effector of the haptic device, which is used to represent the axis of Joint 7 of the extended manipulator in the sandblasting robot system. ${}^{h}\mathbf{n}_{a}$ is the third column of the rotation matrix (${}^{h}\mathbf{R}_{a}$):

$$ {}^{h}\mathbf{n}_{a} = {}^{h}\mathbf{R}_{a}(\mathbf{q}_{h})[0 \quad 0 \quad 1]^{T} \tag{4.4} $$

In general, the position of a haptic cursor can be described by a position vector ${}^{h}\mathbf{P}_{a}$ for both 3DOF and 6DOF haptic devices. The position vector is on the haptic device coordinate frame h corresponding to the physical workspace of the haptic device.

Therefore, if the haptic device is required to control a manipulator which is on the world coordinate system, ${}^{h}\mathbf{P}_a$ on the coordinate frame h must be transferred to ${}^{0}\mathbf{P}_a$ on the world coordinate system.

4.2 Haptic Force Generation Method

The virtual force field (VF^2) approach, presented in Chapter 3 for collision-free motion planning and robot interaction with an environment, is once again used in this chapter to define a haptic force for haptic-based interaction. In this thesis a haptic device is assumed to be a pointing device with force feedback. An attractive force ($\mathbf{F}_{att}$) is generated based on the distance of the haptic cursor from the end-effector by the VF^2 approach, and is used to control the robot manipulator. A virtual spring approach [96][24] is used to generate a haptic force ($\mathbf{F}_h$), which is sent to the operator's hand through the force feedback function of the haptic device. Figure 4.4 shows a conceptual block diagram, which is modified from a block diagram in Figure 3.23 in Chapter 3 by using the virtual spring AF method for the haptic interface as highlighted in the figure.

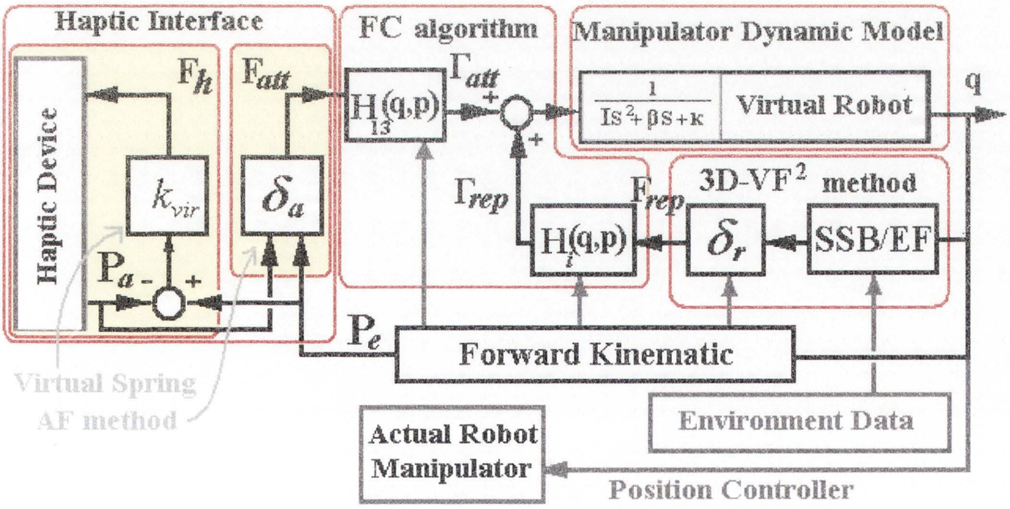

Figure 4.4 Block diagram of haptic-based interaction

Haptic force is generated by the virtual spring approach. The AF method is used to generate driving force to "move" the robot manipulator. The attractive force ($\mathbf{F}_{att}$) from the AF method and the repulsive force ($\mathbf{F}_{rep}$) from the 3D-VF^2 method are transformed from the operational space to the robot's joint space by the FC algorithm (i.e. from $\mathbf{F}_{att}$

to Γ_{att} and from $\mathbf{F}_{rep}$ to Γ_{rep}). Γ_{att} and Γ_{rep} are used to drive the virtual robot and the actual robot that is modelled in Section 3.3.

4.2.1 Haptic Force Generation for a 3DOF Haptic Device

Figure 4.5 shows an attractive force $\mathbf{F}_{att}$ and a haptic force $\mathbf{F}_h$. Both forces vary with the distance between the haptic cursor position (${}^0\mathbf{p}_a$) and the end-effector of a manipulator (${}^0\mathbf{p}_e$). $\mathbf{F}_h$ is calculated using a virtual spring approach based on the distance vector $\overline{{}^0\mathbf{p}_a\,{}^0\mathbf{p}_e}$ and an elastic constant k_{vir}:

$$\mathbf{F}_h = \begin{bmatrix} \mathbf{0}_{3\times 1} \\ k_{vir}({}^0\mathbf{p}_e - {}^0\mathbf{p}_a) \end{bmatrix} \tag{4.5}$$

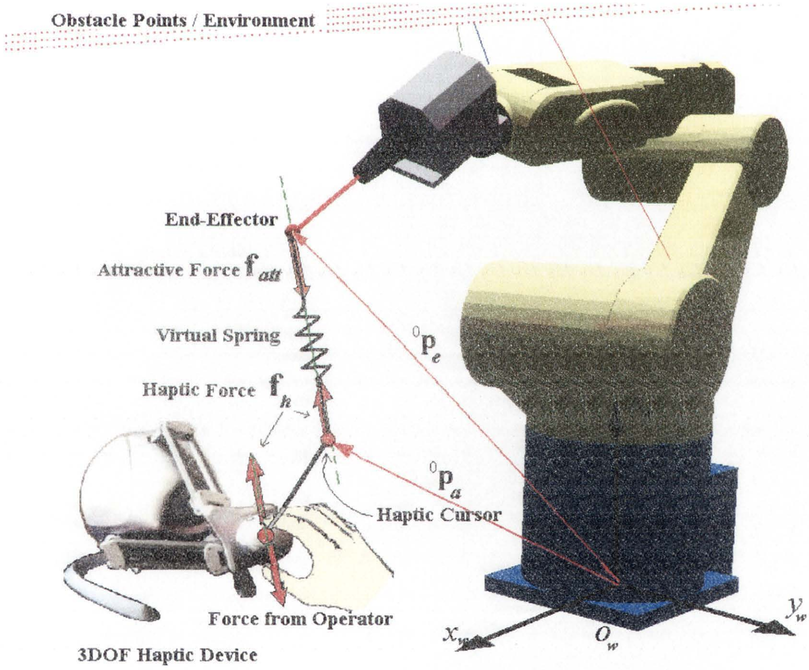

Figure 4.5 Attractive force and haptic force for a 3DOF haptic device

$\mathbf{F}_{att}$ is generated by the attractive force method presented in Chapter 3 based on the attractive force function δ_a (see Equation 3.30) and the distance $\overline{{}^0\mathbf{p}_a\,{}^0\mathbf{p}_e}$ .In the haptic control approach, the target point (${}^0\mathbf{p}_t$) is replaced by the haptic cursor position (${}^0\mathbf{p}_a$).

$$\mathbf{F}_{att} = \delta_a({}^0\mathbf{p}_e, {}^0\mathbf{p}_a) = \begin{bmatrix} \mathbf{0}_{3\times 1} \\ \mathbf{f}_{att} \end{bmatrix} = [0 \quad 0 \quad 0 \quad f_X \quad f_Y \quad f_Z]^T \tag{4.6}$$

$$\mathbf{f}_{att}=\begin{bmatrix} f_{att\,x} \\ f_{att\,y} \\ f_{att\,z} \end{bmatrix}=\frac{K_{att1}}{1+\left(\dfrac{e^{-K_s\;{}^0\mathbf{p}_e-{}^0\mathbf{p}_a}}{\varepsilon_0}\right)}\frac{{}^0\mathbf{p}_e-{}^0\mathbf{p}_a}{\left\|{}^0\mathbf{p}_e-{}^0\mathbf{p}_a\right\|} \tag{4.7}$$

$\mathbf{F}_{att}$ and $\mathbf{F}_h$ are defined as a spatial force $\mathbf{F} = [\sigma \;\; \mathbf{f}]^T$ but the moment component (σ) is set to be zero ($\mathbf{F} = [\mathbf{0} \;\; \mathbf{f}]^T$) for a 3DOF haptic device because it only provides a position vector.

Figure 4.6 shows an example where the haptic cursor is used to control the orientation of the blasting nozzle. Two attractive forces are generated at the end-effector and the wrist of the manipulator. The attractive force at the end-effector is used to keep the nozzle pointing to the target while the attractive force at the wrist of manipulator puts the nozzle rotate about the target. As a result, the blasting nozzle is oriented while the nozzle still aims at the target point.

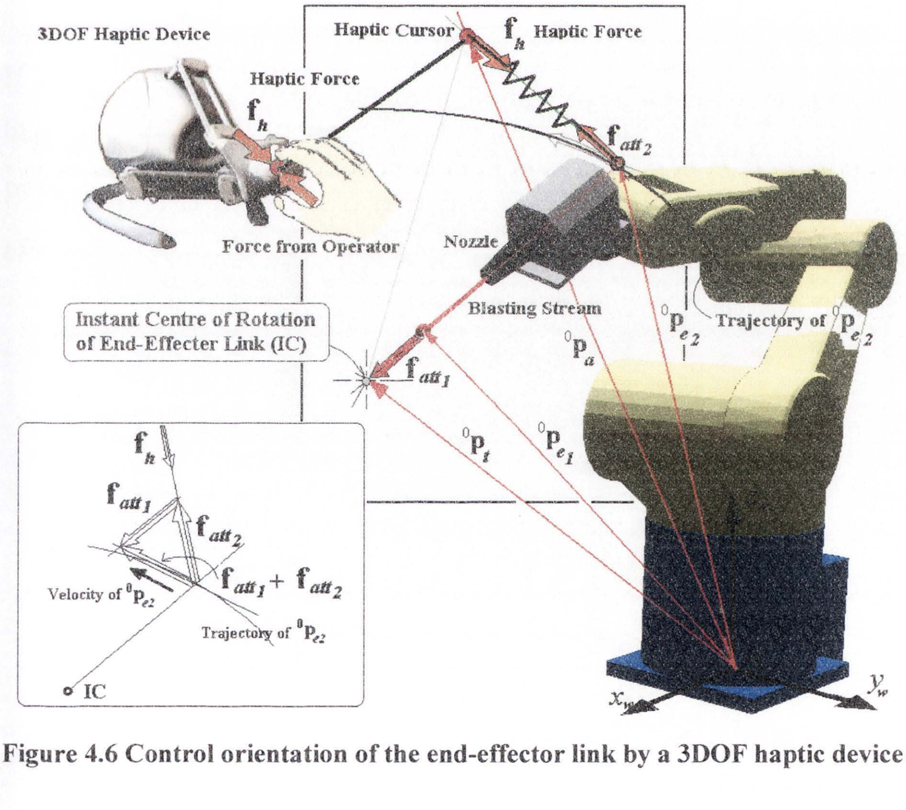

Figure 4.6 Control orientation of the end-effector link by a 3DOF haptic device

The end-effector of the manipulator (${}^0\mathbf{p}_{e1}$) is directed to a target point (${}^0\mathbf{p}_t$) by an attractive force ($\mathbf{F}_{att1}$) and the haptic cursor (${}^0\mathbf{p}_a$) is used to control another point on the end-effector link (${}^0\mathbf{p}_{e2}$) with the second attractive force ($\mathbf{F}_{att2}$).The ${}^0\mathbf{p}_t$ is necessary for locking the end of the blasting stream on the target point while the haptic cursor ($^0\mathbf{p}_a$) pushes/pulls the robot through the sandblasting nozzle.

$$\mathbf{F}_{att\,1} = \boldsymbol{\delta}_a({}^0\mathbf{p}_{e1}, {}^0\mathbf{p}_t) \tag{4.8}$$

$$\mathbf{F}_{att\,2} = \boldsymbol{\delta}_a({}^0\mathbf{p}_{e2}, {}^0\mathbf{p}_a) \tag{4.9}$$

From Equation 4.5, the haptic force ($\mathbf{F}_h$) is given by

$$\mathbf{F}_h = \begin{bmatrix} \mathbf{0}_{3\times 1} \\ k_{vir}({}^0\mathbf{p}_{e2} - {}^0\mathbf{p}_a) \end{bmatrix} \tag{4.10}$$

With the control of orientation of the end-effector, several attractive forces are applied to drive the manipulator but the manipulator is moved by the sum of the forces.

4.2.2 Haptic Force Generation for a 6DOF Haptic Device

If a 6DOF haptic device, such as the Phantom® Omni, is used, the generation of the haptic force is slightly different because a 6DOF haptic device can provide both position and orientation. It is also noted that a Phantom® Omni haptic device can only provide 3DOF force feedback.

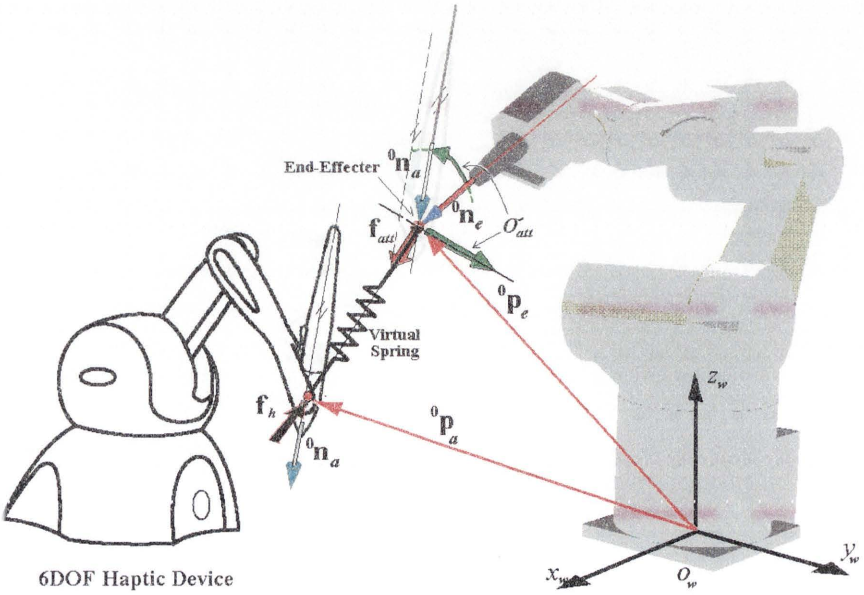

Figure 4.7 Attractive force and virtual spring when a 6DOF haptic device is used

With the position and orientation information of a haptic cursor provided by the 6DOF haptic device, the target configuration (${}^{0}\mathbf{P}_t$) in the attractive force function $\boldsymbol{\delta}_a$ is replaced by the haptic cursor (${}^{0}\mathbf{P}_a$) shown in Figure 4.7. Then an attractive force is generated by:

$$\mathbf{F}_{att} = \boldsymbol{\delta}_a({}^{0}\mathbf{P}_e, {}^{0}\mathbf{P}_a) \tag{4.11}$$

where ${}^{0}\mathbf{P}_a$ and ${}^{0}\mathbf{P}_e$ are defined by

$$ {}^{0}\mathbf{P}_a = \begin{bmatrix} {}^{0}\mathbf{n}_a \\ {}^{0}\mathbf{p}_a \end{bmatrix} = \begin{bmatrix} {}^{0}n_{a\,x} & {}^{0}n_{a\,y} & {}^{0}n_{a\,z} & {}^{0}p_{a\,x} & {}^{0}p_{a\,y} & {}^{0}p_{a\,z} \end{bmatrix}^T \tag{4.12}$$

$$ {}^{0}\mathbf{P}_e = \begin{bmatrix} {}^{0}\mathbf{n}_e \\ {}^{0}\mathbf{p}_e \end{bmatrix} = \begin{bmatrix} {}^{0}n_{e\,x} & {}^{0}n_{e\,y} & {}^{0}n_{e\,z} & {}^{0}p_{e\,x} & {}^{0}p_{e\,y} & {}^{0}p_{e\,z} \end{bmatrix}^T \tag{4.13}$$

The haptic force ($\mathbf{F}_h$) is defined by the virtual spring:

$$\mathbf{F}_h = \begin{bmatrix} \boldsymbol{\sigma}_h \\ \mathbf{f}_h \end{bmatrix} \tag{4.14}$$

where the $\mathbf{f}_h$ and $\boldsymbol{\sigma}_h$ are defined as

$$\mathbf{f}_h = k_{vir}({}^{0}\mathbf{p}_e - {}^{0}\mathbf{p}_a) \tag{4.15}$$

$$\boldsymbol{\sigma}_h = k_{vir}\left(\sin^{-1}\left(\left\|{}^{0}\mathbf{n}_e \times {}^{0}\mathbf{n}_t\right\| / \left(\left\|{}^{0}\mathbf{n}_e\right\|\left\|{}^{0}\mathbf{n}_t\right\|\right)\right)\right) \frac{{}^{0}\mathbf{n}_e \times {}^{0}\mathbf{n}_t}{\left\|{}^{0}\mathbf{n}_e \times {}^{0}\mathbf{n}_t\right\|} \tag{4.16}$$

$\boldsymbol{\sigma}_h$ is the moment component that is assumed to be generated from the virtual torsion spring. Since the 6FOF Phantom® Omni haptic device has only 3DOF force feedback, the haptic device can not reflect the $\boldsymbol{\sigma}_h$ on the haptic handle (i.e. the haptic stylus).

To control the target point, the target orientation and the length of the blasting stream, multiple attractive forces (as shown in Section 3.4.2) can be used. The position and orientation of the 6DOF haptic cursor is used to generate three controlling points for attracting the end-effector of the robot manipulator (see Figure 4.8).

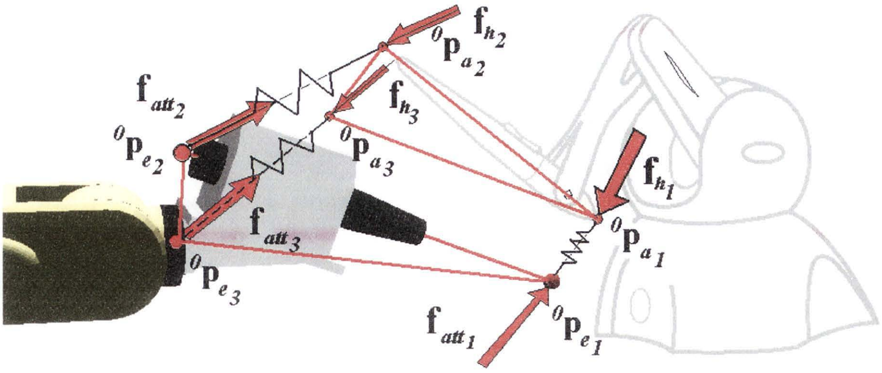

Figure 4.8 Multiple attractive forces to control the target point, the target orientation and the length of the blasting stream

Three virtual springs are generated between those three points (${}^0\mathbf{p}_{a\,1}, {}^0\mathbf{p}_{a\,2}, {}^0\mathbf{p}_{a\,3}$) and three points on the end-effector link of the manipulator at ${}^0\mathbf{p}_{e\,1}, {}^0\mathbf{p}_{e\,2}$, and ${}^0\mathbf{p}_{e\,3}$, which are shown in Section 3.4.2. For the three controlling points provided by the haptic device, the tip of the haptic stylus (${}^0\mathbf{p}_{a\,1}$) is linked to the end-effector (${}^0\mathbf{p}_{e\,1}$) and the other two points (${}^0\mathbf{p}_{a\,2}$ and ${}^0\mathbf{p}_{a\,3}$) are calculated:

$$ {}^0\mathbf{p}_{a2} = {}^0\mathbf{p}_{a1} - ({}^0\mathbf{n}_a l_s) \tag{4.17} $$

$$ {}^0\mathbf{p}_{a3} = {}^0\mathbf{R}_h \, {}^h\mathbf{R}_a \left({}^0\mathbf{p}_{e3} - {}^0\mathbf{p}_{e1}\right) \tag{4.18} $$

where l_s is the required stream length. ${}^h\mathbf{R}_a$ is the rotation matrix of the haptic cursor from Equation 4.4 and ${}^0\mathbf{R}_h$ is the rotation matrix of the haptic device according to the world coordinate frame. Three attractive forces ($\mathbf{F}_{att\,1}$, $\mathbf{F}_{att\,2}$, $\mathbf{F}_{att\,3}$) are then generated by:

$$ \mathbf{F}_{att\,n} = \delta_a({}^0\mathbf{p}_{e\,n}, {}^0\mathbf{p}_{a\,n}) \qquad n = 1,2,3 \tag{4.19} $$

and the three haptic forces ($\mathbf{f}_{h\,1}$, $\mathbf{f}_{h\,2}$, $\mathbf{f}_{h\,3}$) are generated by Equation 4.20.

$$ \mathbf{f}_{h\,n} = k_{vir}({}^0\mathbf{p}_{en} - {}^0\mathbf{p}_{an}) \qquad n = 1,2,3 \tag{4.20} $$

In order to feedback three haptic forces to the haptic device, haptic forces ($\mathbf{f}_{h1}$, $\mathbf{f}_{h2}$, and

$\mathbf{f}_{h3}$) are combined at the position of $\mathbf{f}_{h1}$ at the haptic stylus tip. When $\mathbf{f}_{h2}$ and $\mathbf{f}_{h3}$ are transferred to the position of the haptic stylus tip, they will generate moments ($\boldsymbol{\sigma}_{h2}$ and $\boldsymbol{\sigma}_{h3}$). Thus the resultant force on the haptic stylus is

$$\mathbf{F}_h = \begin{bmatrix} \boldsymbol{\sigma}_{h2} + \boldsymbol{\sigma}_{h3} \\ \mathbf{f}_{h1} + \mathbf{f}_{h2} + \mathbf{f}_{h3} \end{bmatrix} \tag{4.21}$$

However, the 6FOF Phantom® Omni haptic device has only 3DOF force feedback; it can not reflect $\boldsymbol{\sigma}_{h2} + \boldsymbol{\sigma}_{h3}$ on the haptic stylus.

4.3 Workspace Mapping Method

When a small haptic device is used to control a big industrial robot, a mapping is required because of the significant difference in the size of the two workspaces, in order to enable intuitive and effective human-robot interaction. This section presents an innovative method for mapping the small workspace of a haptic device to the large workspace of an industrial manipulator. The workspace mapping method is extended and modified from [13] which cannot be directly applied to control a robot arm. The proposed workspace mapping method consists of scaling control, drifting control and edge motion control. Scaling control allows the haptic workspace to be dynamically enlarged or reduced. Drifting control and edge motion control aims to avoid the low control resolution that occurs when the haptic workspace is enlarged. Drifting control allows the coordinate frame of the haptic workspace to be shifted as the end-effector of the manipulator is repositioned, in order to maintain the control resolution. Additionally, the coordinate frame of the haptic workspace needs to be oriented correctly from the operator's point of view, to ensure that the operator's hand and the haptic cursor on the screen move in the same direction.

Figure 4.9 shows a diagram of the coordinate frames of relevance to the workspace scaling method. There are two coordinate frames, i.e. the haptic workspace coordinate frame and the camera coordinate frame that need to be linked to the world coordinate (i.e. the workspace coordinate frame of the robot manipulator). The orientation of the haptic workspace coordinate frame must be set parallel to the camera coordinate frame in order to make the haptic cursor on the screen and the haptic handle or stylus move in the same direction.

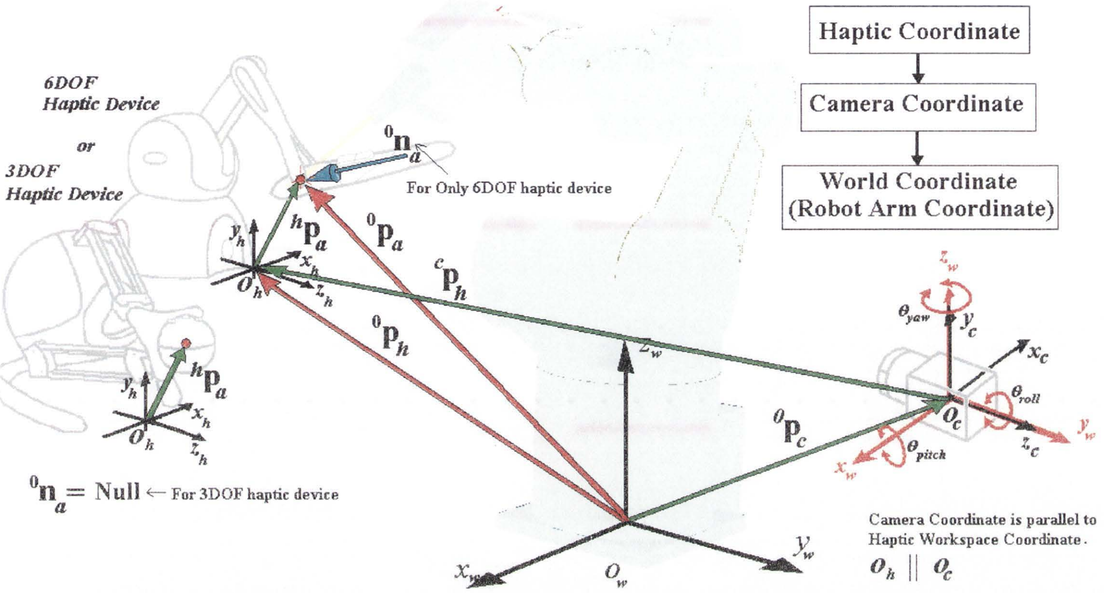

Figure 4.9 Haptic Coordinate System, Camera (operator view) Coordinate System, and Manipulator Coordinate System

4.3.1 Workspace Transformation

For easy operation and intuitive interaction, the coordinate frame of the haptic workspace needs be parallel to the coordinate frame of an observer camera (or the operator view). Therefore, the orientation matrix of the haptic workspace ($^0\mathbf{R}_h$) and an orientation matrix of observer camera ($^0\mathbf{R}_c$) should be identical ($^0\mathbf{R}_h = {}^0\mathbf{R}_c$).

$$^0\mathbf{R}_h = {}^0\mathbf{R}_c = \begin{bmatrix} \cos\theta_{yaw} & -\sin\theta_{yaw} & 0 \\ \sin\theta_{yaw} & \cos\theta_{yaw} & 0 \\ 0 & 0 & 1 \end{bmatrix} \begin{bmatrix} 1 & 0 & 0 \\ 0 & \cos\theta_{pitch} & -\sin\theta_{pitch} \\ 0 & \sin\theta_{pitch} & \cos\theta_{pitch} \end{bmatrix} \begin{bmatrix} \cos\theta_{roll} & 0 & \sin\theta_{roll} \\ 0 & 1 & 0 \\ -\sin\theta_{roll} & 0 & \cos\theta_{roll} \end{bmatrix} \tag{4.22}$$

θ_{yaw}, θ_{pitch}, θ_{roll} are the rotation angles of the observer camera about the z axis, x axis, y axis, respectively. In the world coordinate frame, $^0\mathbf{P}_a$ is defined by Equation 4.23, and includes a position vector ($^0\mathbf{p}_a \in \Re^3$) and a directional vector ($^0\mathbf{n}_a \in \Re^3$).

$$ {}^{0}\mathbf{P}_{a} = \left[{}^{0}\mathbf{n}_{a} \quad {}^{0}\mathbf{p}_{a} \right] \tag{4.23} $$

The direction vector of a haptic cursor on the world coordinate frame ${}^{0}\mathbf{n}_{a}$ depends on the type of haptic device, and is given by

$$ {}^{0}\mathbf{n}_{a} = \begin{cases} {}^{0}\mathbf{R}_{c}\,{}^{c}\mathbf{n}_{a} & ;\ \text{for 6DOF Haptic Device} \\ \mathbf{0} & ;\ \text{for 3DOF Haptic Device} \end{cases} \tag{4.24} $$

The position vector (${}^{0}\mathbf{p}_{a}$) of a haptic cursor in the world coordinate frame is given by

$$ {}^{0}\mathbf{p}_{a} = {}^{0}\mathbf{p}_{h} + k_{sc}\,{}^{h}\mathbf{p}'_{a} \tag{4.25} $$

$$ {}^{h}\mathbf{p}'_{a} = {}^{0}\mathbf{R}_{c}\,{}^{h}\mathbf{p}_{a} \tag{4.26} $$

where ${}^{h}\mathbf{p}'_{a}$ is the position of the haptic cursor on the haptic coordinate frame after ${}^{h}\mathbf{p}_{a}$ is oriented to be parallel to the screen using ${}^{0}\mathbf{R}_{c}$. k_{sc} is the workspace scaling coefficient used to enlarge or reduce the size of the haptic workspace. ${}^{0}\mathbf{p}_{h}$ is the position vector that represents the origin of the haptic workspace in the world coordinate frame. The three controls in the workspace mapping method, namely scaling control, drifting control and edge motion control, use the workspace transformation factors (${}^{0}\mathbf{p}_{a}$, k_{sc}, ${}^{h}\mathbf{p}_{a}$, ${}^{0}\mathbf{p}_{h}$) and are presented in Figure 4.10 and in the following sections.

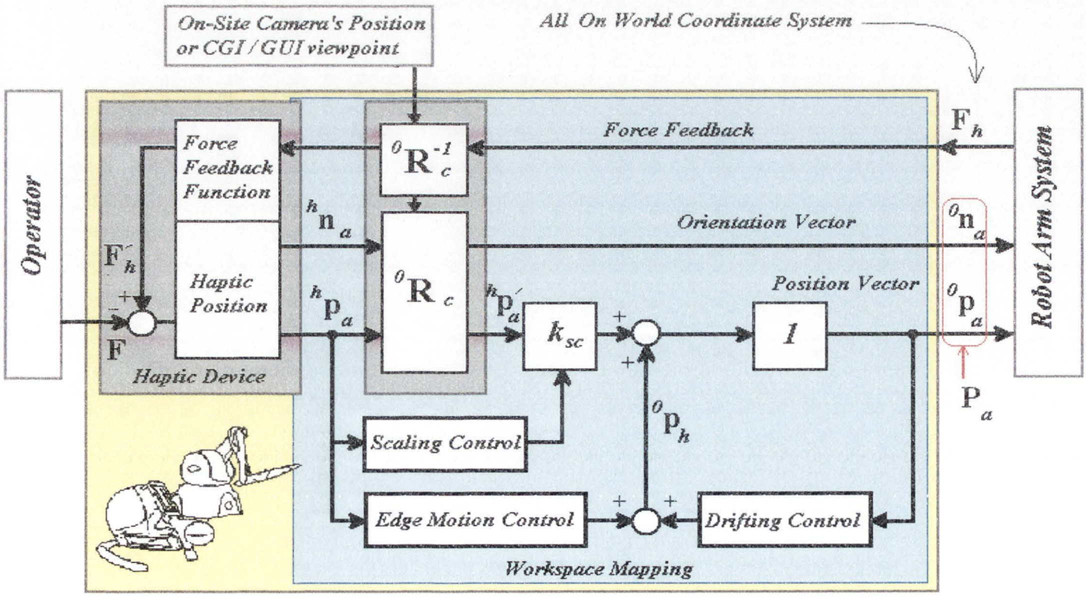

Figure 4.10 Control diagram of workspace mapping

Figure 4.10 shows the extension of the block diagram of the haptic interface shown in Figure 4.4. Inside of the haptic interface is the workspace mapping method. The haptic device receives the signal from the control system of the manipulator and sends the position of the haptic cursor back to the control system. The workspace mapping method consists of three controls; scaling control, drifting control, and edge motion control.

4.3.2 Scaling Control

From Equation 4.25, a workspace scaling coefficient (k_{sc}) is used to dynamically adjust the size of the haptic workspace in the robot workspace from the physical haptic workspace. The scaling factor changes based upon the speed of the haptic cursor which is related to the speed of an operator's hand movement. When the haptic cursor is moving at a speed ($\|{}^{h}\dot{\mathbf{p}}_a\|$) that is greater than a haptic cursor's speed threshold (v_{ht}), the haptic workspace will be expanded by k_{sc} times. The expansion rate ($\dot{k}_{sc}$) in equation 4.27 is used to amplify the haptic device's physical workspace to the haptic virtual workspace in the operational space. It is defined to be proportional to the expansion coefficient (k_{sp}), and the speed of the haptic cursor. In contrast, when the speed of the haptic cursor is smaller than the haptic cursor's speed threshold (v_{ht}), the haptic workspace is reduced at a constant rate (k_{sn}).

$$\dot{k}_{sc} = \begin{cases} k_{sp}\left\|{}^{h}\dot{\mathbf{p}}_{a}\right\| & ; \text{if } \left\|{}^{h}\dot{\mathbf{p}}_{a}\right\| > v_{ht} \\ k_{sn} & ; \text{if } \left\|{}^{h}\dot{\mathbf{p}}_{a}\right\| \leq v_{ht} \end{cases} \tag{4.27}$$

Thus, k_{sp} is a positive constant and k_{sn} is a negative constant.

From Equation 4.25 and Equation 4.27, when the operator moves the haptic device handle and the haptic cursor moves faster than a setup of the speed threshold, the virtual haptic workspace will start to enlarge by $\dot{k}_{sc}$. Otherwise, the virtual haptic workspace will be scaled down to the original size by given $\dot{k}_{sc}$ equal to the k_{sn}, which is a negative value.

4.3.3 Drifting Control

Drifting control is an efficient way to move the coordinate frame of the haptic workspace. It is modified from a ballistic approach by F. Conti and O. Khatib [13]. The purpose is for scaling the speed of the haptic cursor in the operational space based on the speed of the haptic device handle in the haptic device physical workspace. This method aims to maintain the control resolution of the haptic device, while the haptic workspace is mapped to the large workspace. This section shows the integration of the drifting control in the control method for the manipulator. Drifting control is defined as a ballistic function so that the velocity of the haptic workspace coordinate frame (${}^{0}\dot{\mathbf{p}}_h$) is proportional to the haptic cursor velocity in the world coordinate (${}^{0}\dot{\mathbf{p}}_a$).

$$ {}^{0}\dot{\mathbf{p}}_h = \begin{cases} k_{dp}\,{}^{0}\dot{\mathbf{p}}_a & ;\text{if } \left\|{}^{0}\dot{\mathbf{p}}_a\right\| > v_{ht} \\ -k_{sn}\,{}^{0}\dot{\mathbf{p}}_a & ;\text{if } \left\|{}^{0}\dot{\mathbf{p}}_a\right\| \leq v_{ht} \end{cases} \tag{4.28} $$

where k_{dp} is a positive drifting rate. The drifting control scale (k_{dp}) will emphasis the haptic cursor movement speed when the operator intents to move the handle fast and it will increase the accuracy of the haptic cursor movement when the operator moves the handle at a slow speed. Otherwise the $-k_{sn}$ is used when the haptic device handle is moved slower than the speed threshold (v_{ht}). Therefore, the $-k_{sn}$ will compensate the k_{sp} from Equation 4.27 and this will make the haptic cursor stay at the same position while the haptic workspace is scaled down

4.3.4 Edge Motion Control

At the edge of the physical workspace of the haptic device, the speeds of the haptic handle and the cursor are decreased to zero, reflecting the physical workspace limit. In practical operation, the haptic cursor should remain at the same speed in the world coordinate frame in order to achieve a smooth and continuous movement of the end-effector. Therefore, the drifting speed (${}^{0}\dot{\mathbf{p}}_h$) of the haptic workspace is defined as Equation 4.29 where k_{em} is the edge motion rate.

$$
{}^{0}\dot{\mathbf{p}}_{h} = k_{em}\frac{{}^{0}\mathbf{p}_{a}}{\left\|{}^{0}\mathbf{p}_{a}\right\|} \qquad ;\text{if } \left\|{}^{h}\mathbf{p}_{a}\right\| > 0.9\left\|{}^{h}\mathbf{p}_{a,\max}\right\| \tag{4.29}
$$

The number 0.9 in the Equation 4.29 is used to define a range of the haptic workspace (i.e. 90% of the haptic workspace). It is heuristically selected. Figure 4.11 shows the movements of the haptic workspace using the proposed control methods.

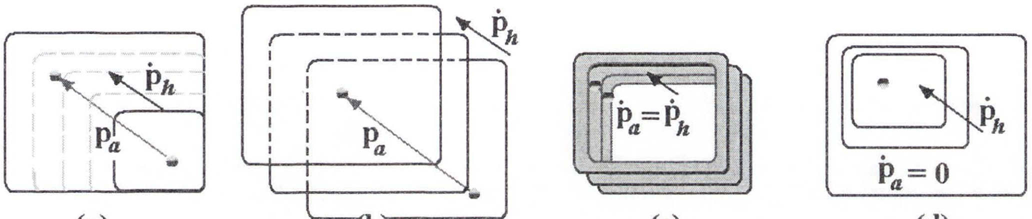

(a) (b) (c) (d)

Figure 4.11 Haptic workspace mapping: a) Up scaling and drifting, b) Drifting when haptic workspace is in maximum, c) Drifting when the cursor is on the edge of the haptic workspace, d) Down scaling and drifting when the cursor is stopped

4.3.5 Experimental Testing

An experiment is devised to test the workspace mapping method. The haptic device used is a ‘Novint® Falcon’ haptic device with 3DOF force feedback. The workspace of this haptic device is approximately 100×100×100 mm^3 (0.001 m^3) and its position resolution is at least 400 dots per inch [141]. The manipulator (presented in detail in Section 3.3) used in this experiment has a workspace of approximately 4 m^3, and a maximum reachable length of 1.6m. For the given haptic/manipulator combination, the workspace of the haptic device must be scaled up 32 times to match the workspace of the manipulator when scaling control is used. Consequently, the resolution is significantly reduced.

The environment in which the experiment is conducted is a mock-up bridge in a laboratory. Initially, a geometric model of the environment is developed using a laser scanner and an exploration and mapping algorithm, described in [34].The geometric model is represented by a point cloud. The haptic workspace is represented by a cubic workspace (in green in Figure 4.12). The path of the end-effector of the manipulator is shown by the solid black line. The manipulator is controlled by an operator through the haptic device. The manipulator starts to move from a safe pose in Figure 4.12 (a) and continues to move until the end-effector is pointing at the left-hand side I-beam of the bridge structure.

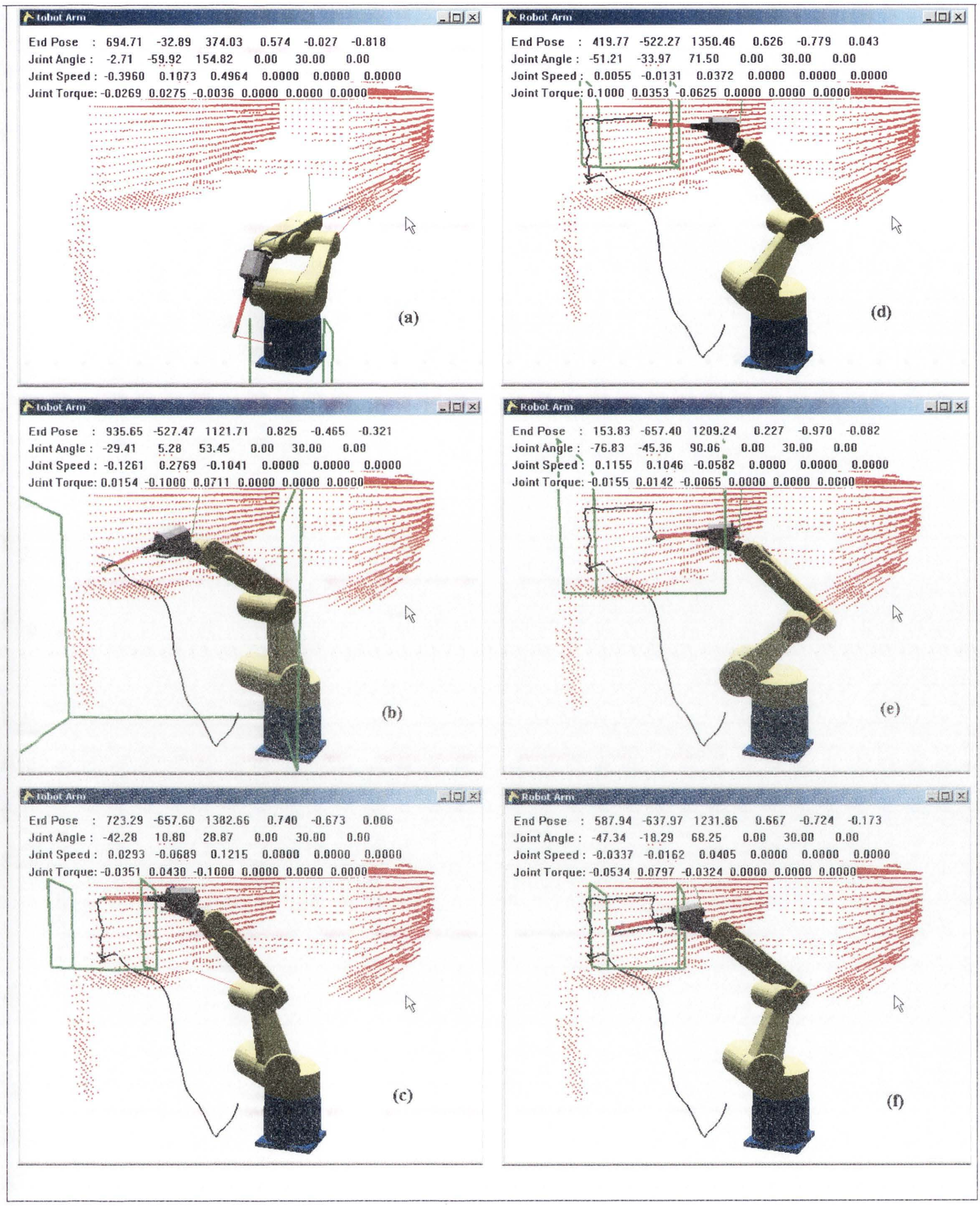

(a)

```
End Pose   :  694.71   -32.89   374.03    0.574  -0.027   -0.818
Joint Angle :  -2.71   -59.92   154.82    0.00    30.00    0.00
Joint Speed : -0.3960   0.1073   0.4964   0.0000   0.0000   0.0000
Joint Torque: -0.0269  0.0275  -0.0036  0.0000  0.0000  0.0000
```

(b)

```
End Pose   :  935.65  -527.47  1121.71    0.825   -0.465   -0.321
Joint Angle : -29.41     5.28    53.45    0.00    30.00    0.00
Joint Speed : -0.1261   0.2769  -0.1041   0.0000   0.0000   0.0000
Joint Torque: 0.0154  -0.1000  0.0711  0.0000  0.0000  0.0000
```

(c)

```
End Pose   :  723.29  -657.60  1382.66    0.740   -0.673    0.006
Joint Angle : -42.28    10.80    28.87    0.00    30.00    0.00
Joint Speed :  0.0293  -0.0689   0.1215   0.0000   0.0000   0.0000
Joint Torque: -0.0351  0.0430  -0.1000  0.0000  0.0000  0.0000
```

(d)

```
End Pose   :  419.77  -522.27  1350.46    0.626   -0.779    0.043
Joint Angle : -51.21   -33.97    71.50    0.00    30.00    0.00
Joint Speed :  0.0055  -0.0131   0.0372   0.0000   0.0000   0.0000
Joint Torque: 0.1000  0.0353  -0.0625  0.0000  0.0000  0.0000
```

(e)

```
End Pose   :  153.83  -657.40  1209.24    0.227   -0.970   -0.082
Joint Angle : -76.83   -45.36    90.06    0.00    30.00    0.00
Joint Speed :  0.1155   0.1046  -0.0582   0.0000   0.0000   0.0000
Joint Torque: -0.0155  0.0142  -0.0065  0.0000  0.0000  0.0000
```

(f)

```
End Pose   :  587.94  -637.97  1231.86    0.667   -0.724   -0.173
Joint Angle : -47.34   -18.29    68.25    0.00    30.00    0.00
Joint Speed : -0.0337  -0.0162   0.0405   0.0000   0.0000   0.0000
Joint Torque: -0.0534  0.0797  -0.0324  0.0000  0.0000  0.0000
```

Figure 4.12 Snapshots of a simulation test to validate the workspace mapping method.

The operator controls the end-effector of the manipulator so that it follows a rectangular path on the I-beam side. In Figure 4.12, when the haptic cursor starts moving (Figure 4.12 (a)), the haptic workspace begins to enlarge and to drift. In Figure 4.12 (b), when the haptic cursor movement is slower than the haptic cursor's speed threshold (v_{ht}), the haptic workspace returns to the original size and drifts to the new coordinate frame. In Figure 4.12 (c) to Figure 4.12 (f), the haptic cursor movement is controlled at about the haptic cursor's speed threshold (v_{ht}), thus the haptic workspace tries to remain at the original size.

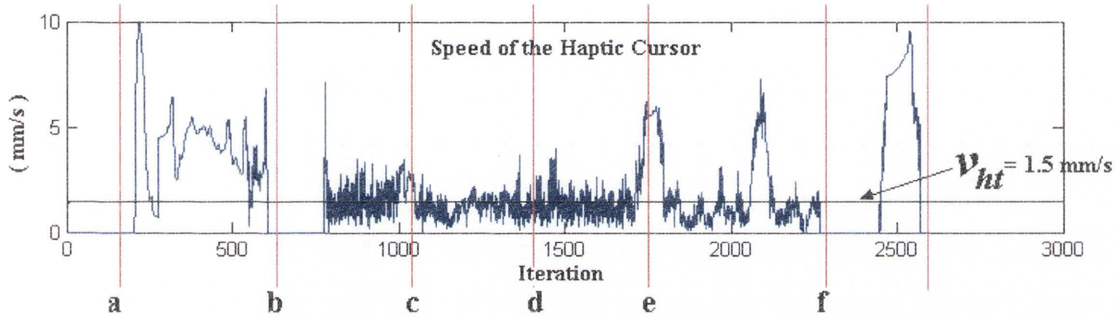

Figure 4.13 Speed of the haptic cursor in the simulation test shown in Figure 4.12.

Figure 4.13 shows the speed of the haptic cursor in the simulation shown in Figure 4.12. In Figure 4.13, the speed of the haptic cursor from a to b is higher than v_{ht}, and the haptic workspace, which is shown as a green box in Figure 4.12 (a), is enlarged to be the large haptic workspace shown in Figure 4.12 (b). When the speed of the haptic cursor is then slowed down to be under v_{ht}, the haptic workspace is shrunk and remains small in order to maintain control resolution.

4.4 Determination of Parameters and Computation Time

In Chapter 3, the parameters of the attractive force and the repulsive force were heuristically determined to suit the robotic system used with the AF method and the 3D-VF^2 method. The attractive force is generated based on the distance between the end-effector of the manipulator and a haptic cursor (or the target point). To enable safe operation of the robot manipulator, the attractive force and the repulsive force should match. If the attractive force is much greater than the repulsive force, the robot will penetrate a wall (or surface). On the other hand, if the attractive force is much less than the repulsive force, the robot will move very slowly and consequently may cause a large haptic force (see Equations4.5 and 4.15) because of the large distance between the haptic cursor and the end-effector. Therefore, the magnitudes of the repulsive force and the attractive force must be determined empirically.

The fidelity of haptic rendering depends on the resolution of the environmental map and the refresh rate of the haptic force feedback. The refresh rate of haptic force feedback, in turn, depends on the computational time of the algorithms, including collision detection and avoidance using 3D-VF^2 and attractive force generation, based on the VF^2 approach.

This section presents the research on determination of the magnitudes of the repulsive force and the attractive force, and an approach to reducing the computational time.

4.4.1 Magnitudes of Repulsive Force and Attractive Force

An experiment is devised to determine the relationship between the repulsive force and the attractive force. The amplitude of an attractive force should be defined in relation to the amplitude of a repulsive force which is given by the coefficient K_f in order to limit the maximum attractive force to less than the resultant repulsive force. This definition prevents links of the manipulator from colliding into an obstacle.

In the AF method, the attractive force ($\mathbf{F}_{att}$) is generated based on the distance between the end-effector and the target point (or haptic cursor). Sigmoid function is used to define the amplitude of the attractive force as shown in Equation 3.28.This sigmoid function (a kind of s-curve function) is perform well in the attractive force method but it is not suitable to use in consideration of the dynamic response of the robot, thus the attractive force must be estimated by a linear function in order to determine the relationship between the repulsive force and the attractive force.

From Figure 4.14, the estimated attractive force from Equation 3.28 can be given as a modulus function, of which the elastic modulus is E_{af}, where ε_0 in the attractive force function is set at 0.0001. Therefore, the elastic modulus is given as

$$E_{af} = \frac{K_{att}K_s}{13.8} \tag{4.30}$$

This elastic modulus (E_{af}) is used to estimate the linear relation between the attractive force and the displacement between the end-effector and the target point.

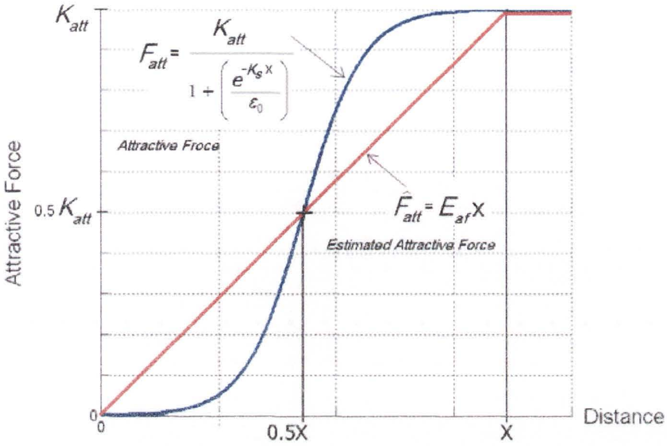

Figure 4.14 Attractive force estimated by a linear function of a virtual spring

The potential energy that is generated by the attractive force ($\mathbf{F}_{att}$) can be estimated by Hooke's law:

$$\mu_{af} = \frac{1}{2} E_{af} \left\| {}^{0}\mathbf{p}_e - {}^{0}\mathbf{p}_t \right\|^2 \tag{4.31}$$

$$\mu_{af} = \frac{K_s K_{att} \left\| {}^{0}\mathbf{p}_e - {}^{0}\mathbf{p}_t \right\|^2}{27.6} \tag{4.32}$$

According to the definition of the D_{min} and D_{max} in the 3D-VF^2 (Section 3.5.2), a repulsive force changes from 0 at D_{max} to K_f (i.e. the maximum repulsive force) at D_{min}. Therefore the linear function of the repulsive force can be estimated by

$$E_{rep} \cong \frac{K_f}{Er} \tag{4.33}$$

Where Er is the distance between the D_{max} and D_{min} (i.e. $Er = D_{max} - D_{min}$). By Hooke's law, the potential energy generated by the 3D-VF^2 is given by

$$\mu_{rep} = \frac{1}{2} E_{rep} (Er - d_0)^2 \tag{4.34}$$

where d_0 is the distance between the obstacle and the D_{min} as defined in Chapter 3. When an attractive force pulls the moving manipulator to approach an obstacle and the obstacle is within D_{max} (or the force field is moving to an obstacle), the potential energy generated by the force field will be increased. Therefore, when the obstacle is at D_{min} (i.e. $d_0=0$) where it has maximum repulsive force, the potential energy generated by the 3D-VF^2 is given as

$$\mu_{rep} = \frac{1}{2} K_f Er \tag{4.35}$$

To avoid a potential collision between an obstacle and the robot, the repulsive force amplitude factor K_f is determined by letting $\mu_{rep} \geq \mu_{af}$, then

$$K_f \geq \frac{K_s K_{att} \left\| {}^0\mathbf{p}_e - {}^0\mathbf{p}_t \right\|^2}{13.8 Er} \tag{4.36}$$

Figure 4.15 (a) shows the experiments with K_f which is obtained from Equation 4.36. It is demonstrated that, with the proposed approach, although the haptic cursor and the end-effector can be at any distance, the attractive force will be limited by the attractive force coefficient K_{att} via the function δ_a. Consequently, the manipulator cannot penetrate obstacles such as walls. The haptic forces presented in Figure 4.15 (a) and Figure 4.15 (b) are approximately the same amplitude. Figure 4.15 (b) shows a case in which the manipulator breaks through the virtual wall when the K_f does not satisfy the constraint of Equation 4.36.

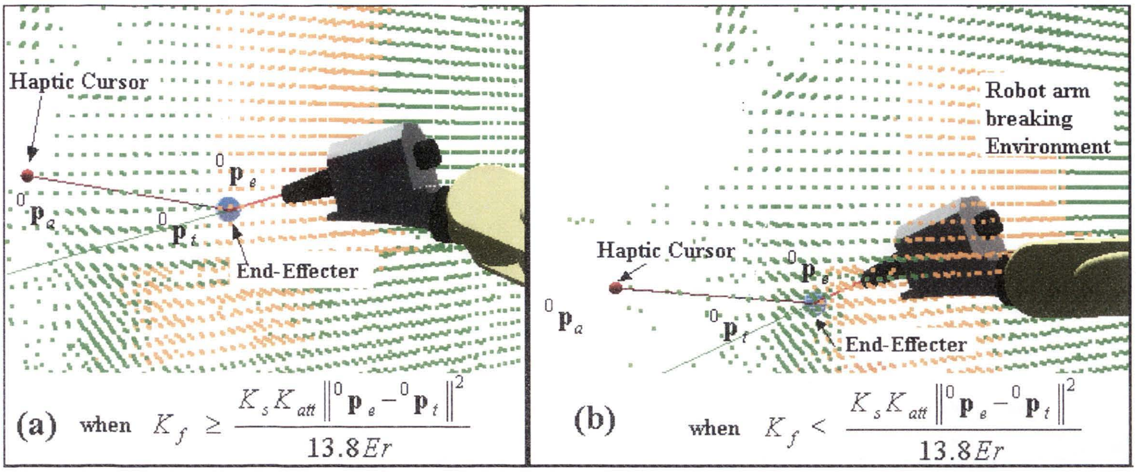

Figure 4.15 Two case studies: (a) the manipulator cannot move to penetrate obstacles such as walls, (b) the manipulator breaks through the wall when the K_f does not satisfy the constraint of Equation 4.36

4.4.2 Computational Time

The fidelity of haptic rendering depends on the resolution of the environmental map and the refresh rate of the haptic force feedback. The refresh rate depends on the computational time of the algorithms, including collision detection and avoidance using 3D-VF^2 and attractive force generation, based on the VF^2 approach. As a result, computational cost is one of the major issues in a haptic-based interaction system. The major factor that affects the computation time in the presented human-robot-environment interaction system and its application is the number of points in the environment point cloud set (representing obstacles), because every point in the point cloud set needs to be checked in collision detection and collision avoidance by the 3D-VF^2 method. The software component of the haptic-based interaction is programmed by two parallel threads: the haptic control thread and the graphic-rendering thread. The haptic control thread is implemented by the haptic force generation method, the haptic workspace mapping method, the AF method, the 3D-VF^2 method, and the FC algorithm. The graphic-rendering thread is used to render the robot model and environment map on the monitor of the controlling computer.

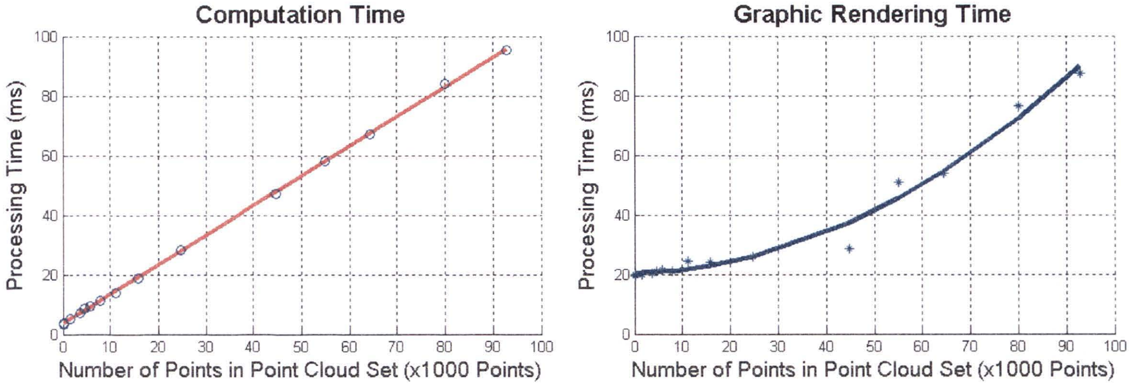

Figure 4.16 Computation time with respect to the number of points in the point cloud set of an environment

A timing test is conducted to find the computation times of the haptic control thread, by varying the number of points in the point cloud set of an environment. As shown in Figure 4.16, the computation time of the haptic control thread is proportional to the number of points in the point cloud set. The computational time can therefore be reduced if the number of points in a point cloud set can be reduced. The occupancy voxel indexing approach presented below aims to reduce the point cloud, and consequently reduce the computational time.

4.4.3 Occupancy Voxel Indexing Approach

To minimise the computational time, point cloud density has been reduced by applying an occupancy voxel indexing approach. In this approach, only the points in the point cloud set that are close to the manipulator are used for collision detection and collision avoidance in the 3D-VF^2 method.

By applying a voxel index, the point cloud of the environment from the laser scanner has been grouped into grid voxel cubes. Each cube contains a sub-set of points. In collision detection and avoidance, only the points within the voxel cubes which are near the manipulator are taken into account. The environment is represented as a point cloud set ($\mathbf{P}_{ob}$) as:

$$\mathbf{P}_{ob} = \left\{ {}^{0}\mathbf{p}_{ob\,1}, {}^{0}\mathbf{p}_{ob\,2}, \ldots, {}^{0}\mathbf{p}_{ob\,m} \right\};\ m \text{ is number of points in the point cloud set} \qquad (3.36)$$

${}^{0}\mathbf{p}_{ob\,i}$ is the position (mm) of a point in the point cloud set. A cubic voxel ($\mathbf{P}_{vox}(\mathbf{g})$) is a subset of the point cloud set in the world coordinate frame:

$$\mathbf{P}_{vox}(\mathbf{g}) \subseteq \mathbf{P}_{ob} \in \Re^{3} \tag{4.37}$$

g is an index of a cubic voxel which relates to the world coordinate frame:

$$\mathbf{g} = [u_x, u_y, u_z]^T \; ; u_x, u_y, u_z \in \mathbf{Z} \text{ and } \mathbf{g} \in \mathbf{Z}^3 \tag{4.38}$$

Then a voxel is represented by:

$$\mathbf{P}_{vox}(\mathbf{g}) = \left\{ \mathbf{P}_{ob} \mid \mathbf{g} = floor\left(\frac{{}^{0}\mathbf{p}_{ob\,i}}{d_{vx}} \right) \right\} \quad ; i=[1 \ldots m] \tag{4.39}$$

where d_{vx} is the size (mm)of a cubic voxel, ${}^{0}\mathbf{p}_{ob_i}$ is a point in the point cloud set and m is the number of points in point cloud set. The function "*floor*" is to calculate the integer number. The result of the point location divided by the size of the voxel (d_{vx}) is index of the voxel coordinate that is used to group the points into voxels, which can limit the number of points in calculation of the obstacle detection (i.e. the Ellipsoid Bounding in Section 3.5.1 and the Swept Sphere Bounding in Section 3.5.2). The value of d_{vx} is from the widest dimension of the robot arm to confirm that calculated voxels will cover whole body of the root arm. After a point cloud set is represented with grid cubic voxels, two groups of voxels will be taken into account by the 3D-VF^2 approach. The first group of voxels are those through which the centre line of a manipulator link intersects (the main voxels, $\mathbf{g}_1$). The second group are those adjacent to the voxels in the first group (the neighbourhood voxels, $\mathbf{g}_2$). In Figure 4.17, the main voxels are in red and their neighbourhood voxels are in green. All points in these voxels $\mathbf{g}_1$ and $\mathbf{g}_2$ will be used for collision detection and avoidance.

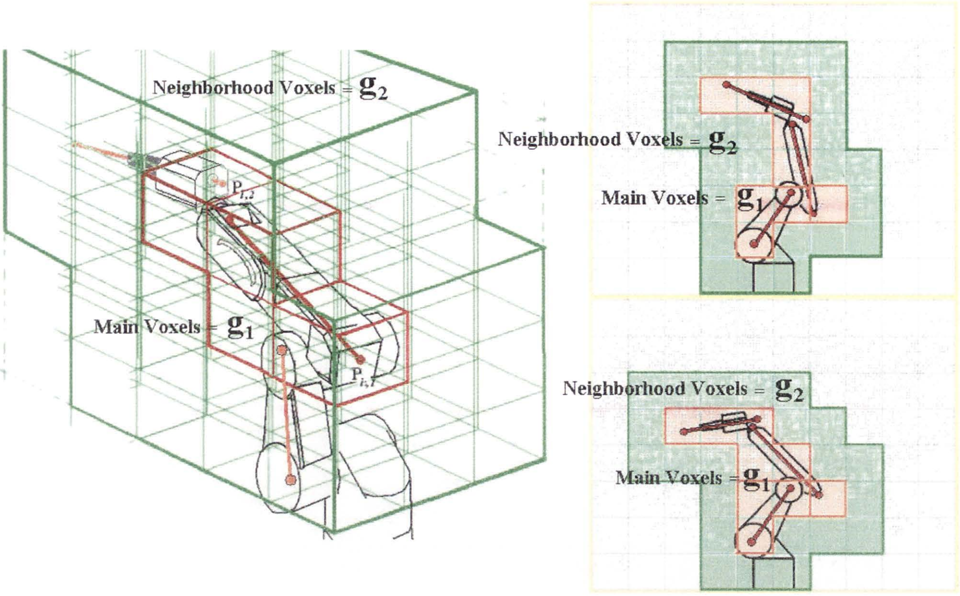

Figure 4.17 Occupancy voxel map of a link of manipulator

In this research, a Denso robot manipulator, in which the thickness of the links is between 100 mm and 200 mm, is used in the experiments, and the dimensions of the voxels is set to be 100×100×100 mm^3. The point cloud set of the tested environment has 92,841 points. With the occupancy voxel indexing approach, the computational time (t_{ct}) of the algorithms as implemented in the robotic system is only 8.7ms on average. That is about eleven times less than the computational time in the robotic system without the voxel indexing approach.

4.5 Implementation and Experimental Testing

4.5.1 System Setup for Implementation

In addition to the simulation studies presented above, the haptic force generation method, the workspace mapping method and the parameter determination presented in this chapter are implemented and tested in a real robotic system which has been developed for sandblasting in a steel bridge maintenance application. The sandblasting robotic system consists of a Denso® VM6083 robot manipulator with a control unit, a mobile platform, a Novint® Falcon haptic device with 3DOF force feedback, and a laser ranger scanner. The test is conducted in a mock-up steel bridge structure in a laboratory. A 3D map of the environment is built using the laser range scanner and is used as a virtual environment in teleoperation (Figure 4.18). The methods have also been tested in an onsite bridge maintenance situation.

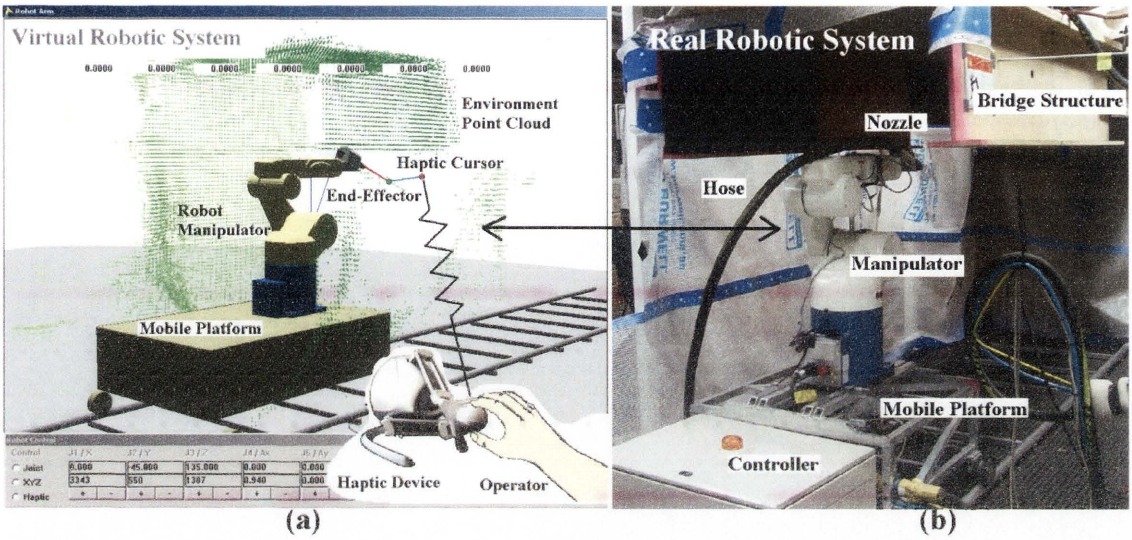

Figure 4.18 (a) A virtual environment,(b) The sandblasting robotic system under a mock-up steel-bridge structure

Figure 4.19 shows snapshots of the first implementation using a real robot manipulator and a sandblasting robotic system under a mock-up bridge structure in a laboratory. The manipulator is controlled by an operator via the Novint® Falcon haptic device to move around its environment to test the collision avoidance of the VF^2 approach.

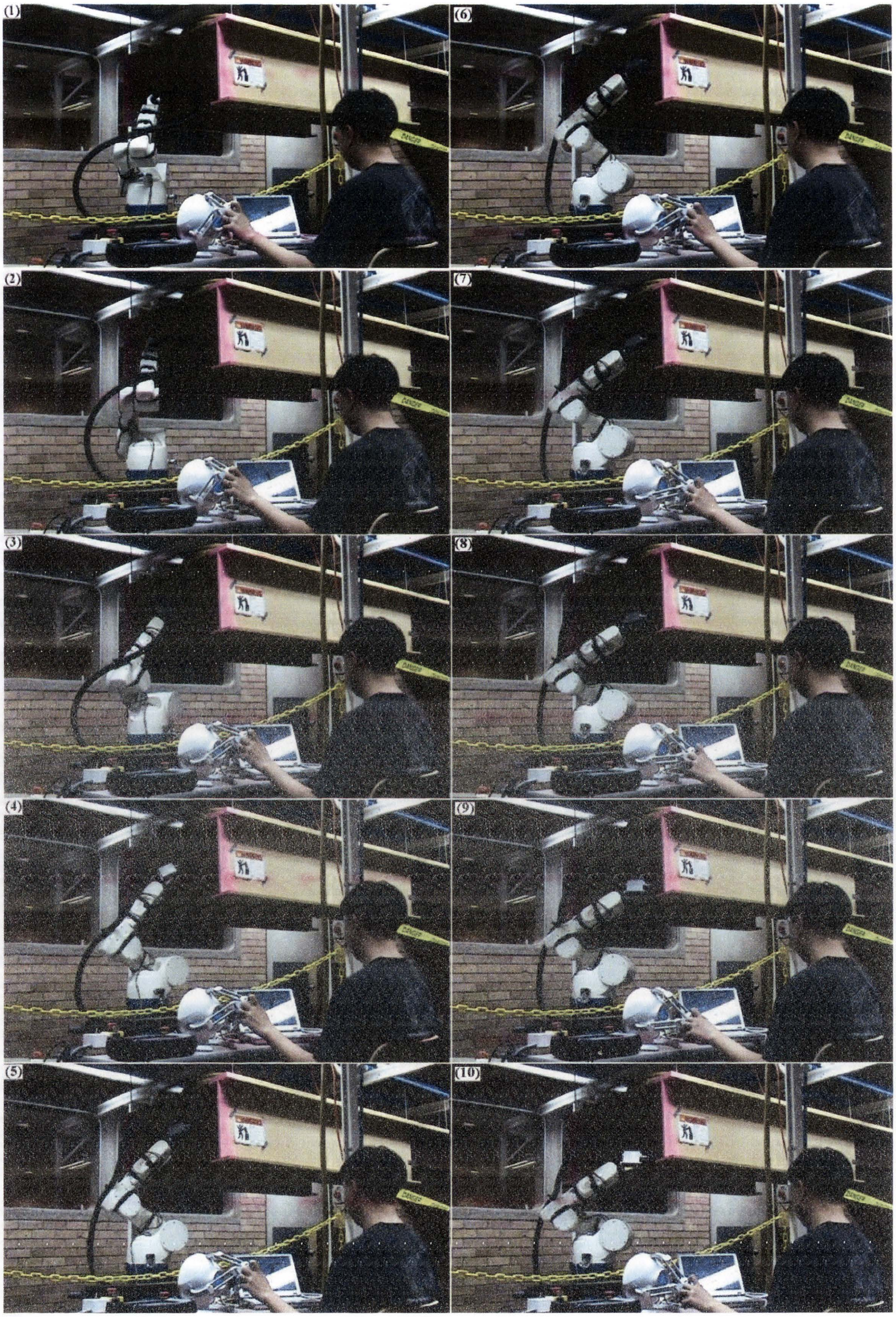

Figure 4.19 Snapshots of the first implementation with haptic device interface

4.5.2 Processing Time

An experiment is devised to measure the processing time which is composed of computational time and communication time. The robot manipulator in the haptic-based interaction system is controlled by an operator via the Novint® Falcon haptic device with both an open-loop control method and a closed-loop control method. In the open-loop control, the haptic device (i.e., master) streams joint position commands at a constant rate to the control unit of the actual manipulator (i.e. slave).

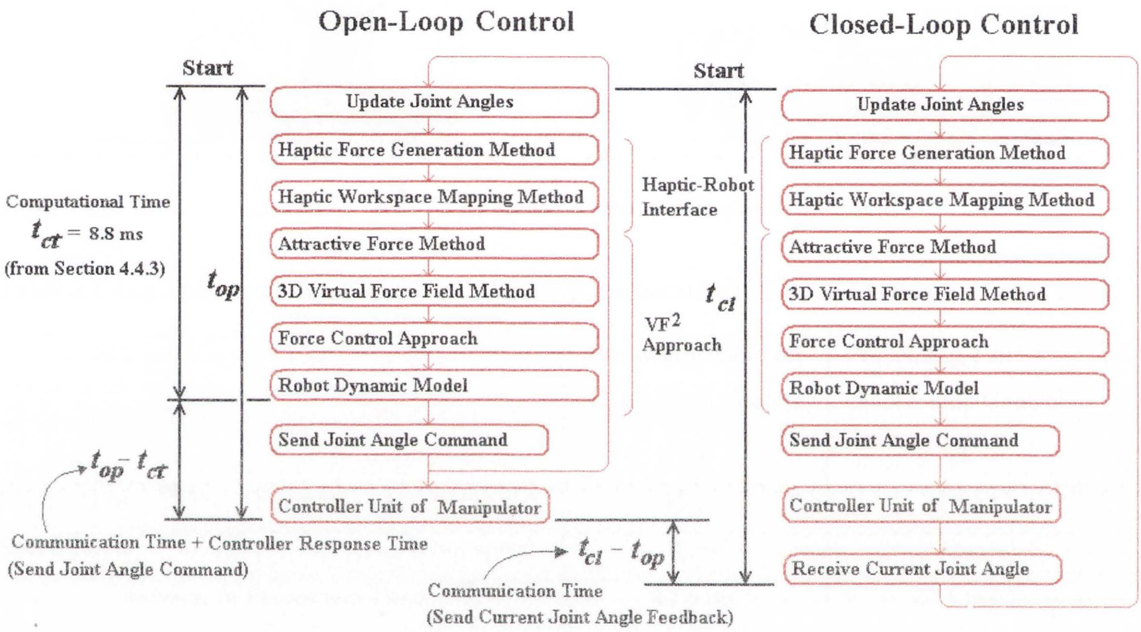

Figure 4.20 Timing diagram of the open-loop control and closed-loop control

As shown in Figure 4.20, the processing time for open-loop control (t_{op}) consists of computational time (required for calculating the attractive force, repulsive force and force control), the time required for sending the pose of the robot at the instant target position to the robot control unit, and the response time that the robot control unit requires to process the receiving command. In closed-loop control, the processing time (t_{cl}), consists of the processing time of open-loop control plus the waiting time to receive the current pose of the manipulator from the robot control unit, after sending the target pose of the robot to the robot control unit.

In this experiment, the operator controls the manipulator by using the haptic device to move the end-effector to follow the path defined from points 1 to 6 (Figure 4.21).The speed of the manipulator is at 25% and 50% of its maximum speed for safety reasons.

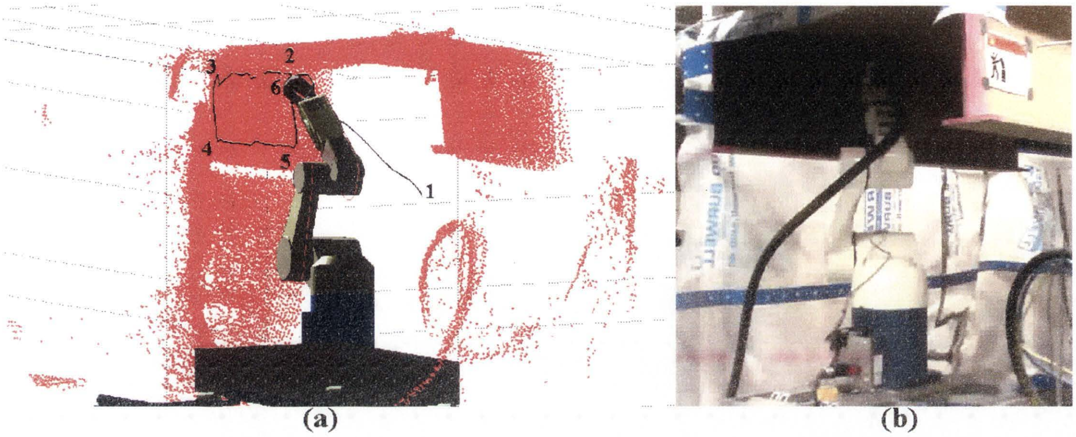

(a) (b)

Figure 4.21 a) A testing plan, b) The manipulator movement in this experiment

Table 4.1 Average Processing Times per Iteration (Computational time and Communication time)

		Processing Time for Open-Loop Control t_{op}	Processing Time for Closed-loop Control t_{cl}
Manipulator Speed Limit	25% of the maximum robot speed	17 ms	24 ms
	50% of the maximum robot speed	18 ms	23 ms
Average of Processing Time		17.5 ms	23.5 ms

As shown in Table 4.1, the average processing times in open-loop control for the 25% and 50% speed limits of the manipulator are 17 ms and 18 ms respectively, and the average processing time of the open-loop control (t_{op}) is 17.5 ms. In closed-loop control, the average processing times for the 25% and 50% speed limits of the manipulator are 24 ms and 23 ms respectively, and the average processing time of the closed-loop control (t_{cl}) is 23.5 ms. These processing times show that the effect of the manipulator speed on the processing time is not obvious.

It can be seen from Figure 4.20 and Table 4.1 that, in open-loop control, the communication times (sending joint angle command from the master system to the robot control unit) and the response time of the control unit, which is calculated from t_{op}-t_{ct}=17.5-8.8, is about 8.7 ms. The joint angle command, which is 67 bytes long and transferred at 112 kbps (kilo-bits per second), required approximately 6 ms for the communication. Therefore, the response time of the robot control unit is 2.7 ms.

For closed-loop control, the master system sends another 11 byte command to request the current joint angle of the manipulator from the robot control unit. This request command is next sent from the joint angle command; thus the communication time of this request command is included in the 2.7 ms response time. After the control unit of the manipulator receives the request command, it will send 67 bytes of the current joint angle back to the master system to update the current pose of the manipulator. This 67 bytes data transferred at 112 kbps takes 6 ms, which is equal to t_{cl}-t_{op} from the experiment.

The results of this section demonstrate justification of the processing time, including the computational time and the communication time. Since the processing time is not dependent on the movement speed of the real robot, the processing time is considerably consistent for an implementation as long as the processer of the master system has not been changed.

4.5.3 Time Delay

Time delay in this research is defined as the time difference between the time when the virtual robot end-effector reaches a target position and the time when the real robot end-effector reaches the same target position. This delay is mainly caused by the time required for communication between the master system and the slave robot (i.e. real robot manipulator), and the movement speed difference between the virtual robot and the real robot. In this research, the position of the haptic cursor is linked to the position of the robot end-effector. The speed of the haptic cursor and the speed of the robot end-effector can be theoretically linked. However, our robotic system does not have this speed control feature. The robot takes only a joint position command and the speed of the manipulator (maximum speed) is set manually on the teach pendant of the robot.

This experiment is conducted by using the speed of the manipulator at 25% and 50% of its maximum speed, and in both open-loop control and closed-loop control, similar to the test in Section 4.5.2. Points 1 to 6 shown in Figure 4.21 are marked on the mock-up bridge structure, which show a target path. The operator controls the manipulator follow the path. Although there is difference or error when the end-effector of the manipulator follows the path in every test, but the joint motion is expected to be similar. This test aims to justify the time delay of the open-loop control and the closed-loop control based on the speed limit of the real robot.

4.5.3.1 Time Delay in Open-Loop Control

Test results are shown Figure 4.22 at 25% of the maximum robot speed, i.e. the manipulator joint angle changes with time. The joint angle graph of joint 1 shows the time delays on a time scale which is used to create the time delay graph in Figure 4.23.

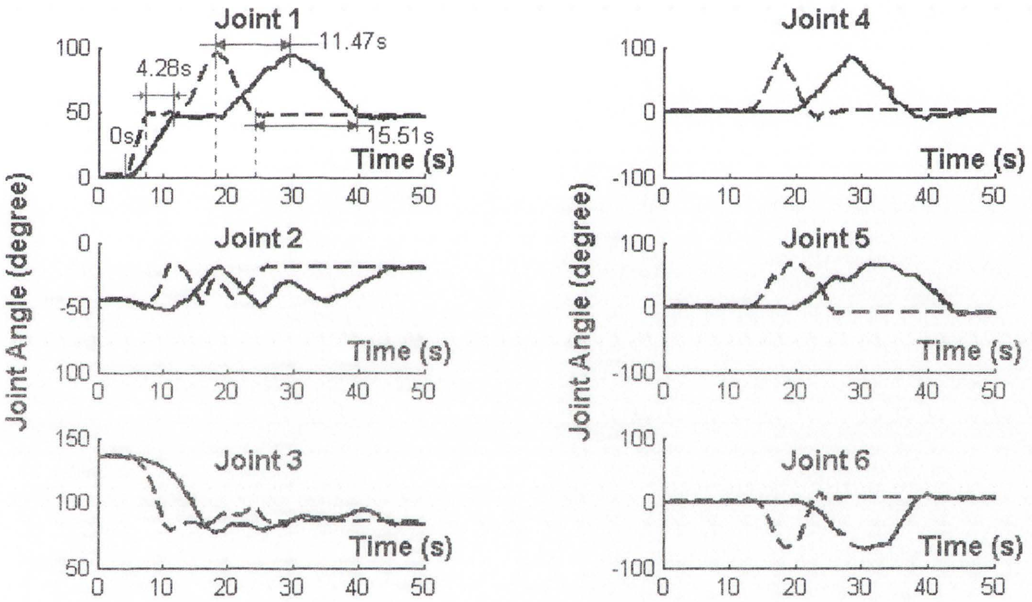

Figure 4.22 The manipulator's joint angles in open-loop control at 25% of maximum speed of the manipulator, indicated by dash lines for the virtual manipulator and solid lines for the actual manipulator

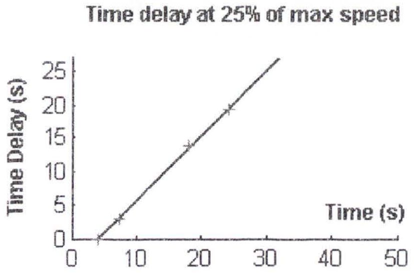

Figure 4.23 Time delay at 25% of the maximum speed in open-loop control from Figure 4.22

In Figure 4.23, the delay times between the movement of the virtual manipulator and the movement of the actual manipulator measured from the graphs increase when the robot manipulator is moved, and the control unit of the robot manipulator has to buffer the joint angle commands which have yet to be processed. For this experiment, the current buffer size of the control unit is large enough to store the joint angle commands for a 1 minute operating period at 25% of the maximum robot speed. However, this thesis has not addressed the issue of determining the buffer size, because this problem will disappear when the speed limit of the manipulator is much higher than 25%.

Figure 4.24 shows a graph of the haptic force, which is generated during the experiment with the speed of 25% of the maximum speed of the manipulator and open-loop control. The average of the haptic force is approximately 0.29 kgf (kilogram-force). The haptic force change is dependent on many factors, namely, the properties of the virtual spring, speed limit of the robot manipulator, type of control system and the control style of an operator. Thus, the amplitude of the haptic force is not considered for comparison between the closed-loop and open-loop controls.

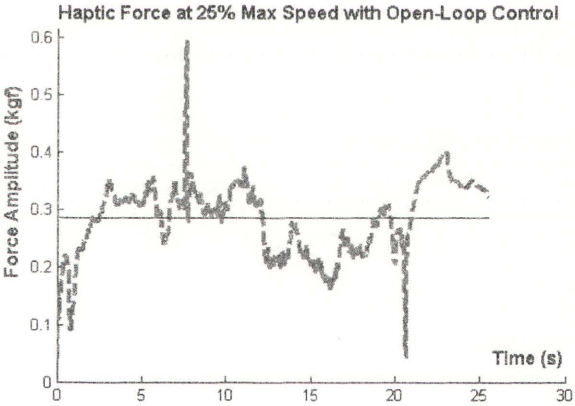

Figure 4.24 Haptic force in the test at 25% of the maximum speed with open-loop control

At 50% of the maximum speed of the manipulator, Figure 4.25 shows changes of joint angles of the manipulator over time (testing period). The delay time shown in Figure 4.26 is stable at about 0.95 sec. This means that the speed of the manipulator in this particular experimental test is similar to the speed of the virtual robot manipulator.

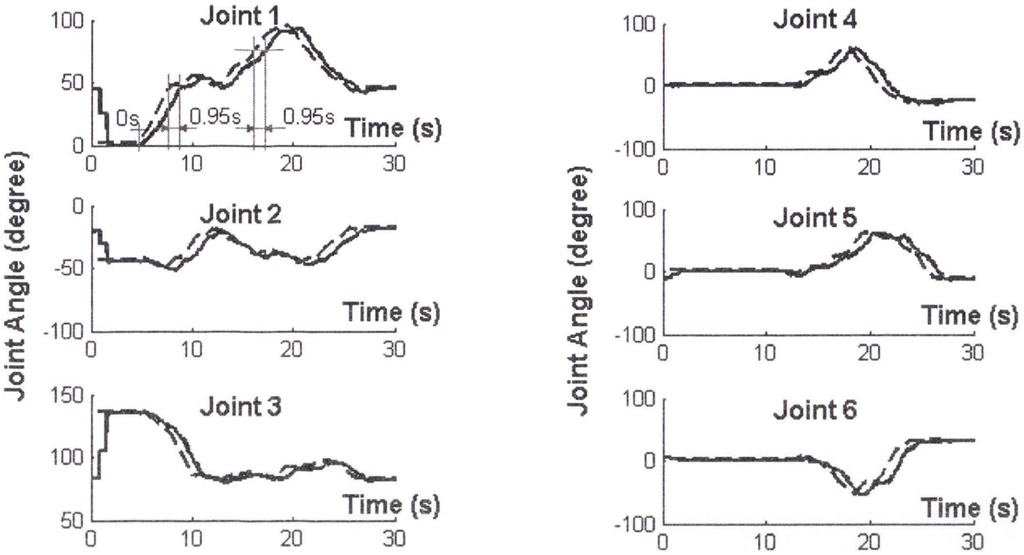

Figure 4.25 The manipulator's joint angles obtained from open-loop control at 50% of the maximum speed of the manipulator: dash lines for virtual manipulator and solid lines for actual manipulator

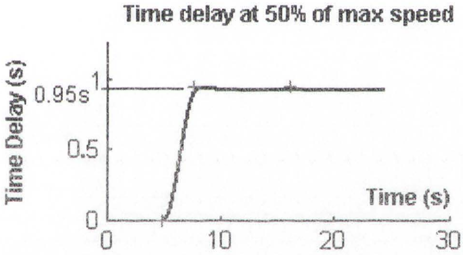

Figure 4.26 Time delay at 50% of the maximum speed in open-loop control from Figure 4.25

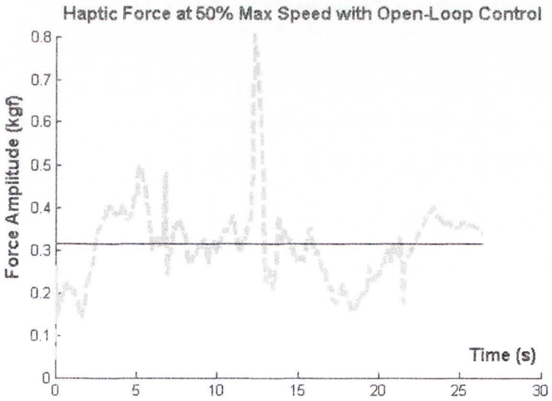

Figure 4.27 Haptic force in the test at 50% of the maximum speed with open-loop control

Figure 4.27 shows a graph of the haptic force generated during the experiment at 50% of the maximum speed of the manipulator with the open-loop control. The average of the haptic force is 0.31 kgf and it does not relate to the haptic force from Figure 4.24.

4.5.3.2 Time Delay in Closed-Loop Control

As the virtual robot has its pose updated by the current pose (i.e. joint angles) of the manipulator in iteration, the time delay is constant. The time delay in closed-loop control includes communication times (i.e. the command from the master to the slave, the current pose from the slave to the master), the response time of the robot control unit, and the movement time of the manipulator. The movement time is the time that the manipulator takes to move each joint angle command received from the master control system (the virtual robot). Figure 4.28 shows that the manipulator joint angle changes with time. The delay time between movements of the virtual manipulator and the actual manipulator measured from the graphs are 167 ms and 16ms for 25% and 50% of the maximum speed of the manipulator respectively.

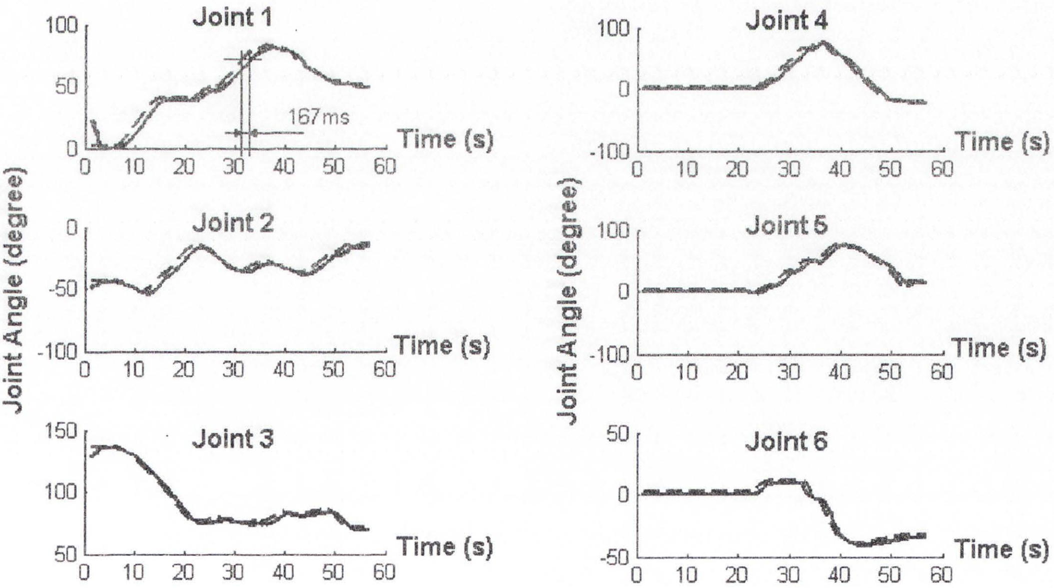

Figure 4.28 The manipulator's joint angles obtained from closed-loop control at 25% of the maximum speed of the manipulator, indicated by dash lines for the virtual manipulator and solid lines for the actual manipulator

As noted in Section 4.5.2, the communication time for sending a command from the master to the slave is 6 ms, the communication time for sending the current pose from the slave to the master is 7 ms, and the response time of the robot control unit is 2.7 ms. The summation of the communication times and the response time is 15.7 ms. As show in Figure 4.31, the time delay in the closed-loop control at 25% of the maximum speed of the manipulator is 167 ms; thus, the movement time for a joint angle command is about 151 ms.

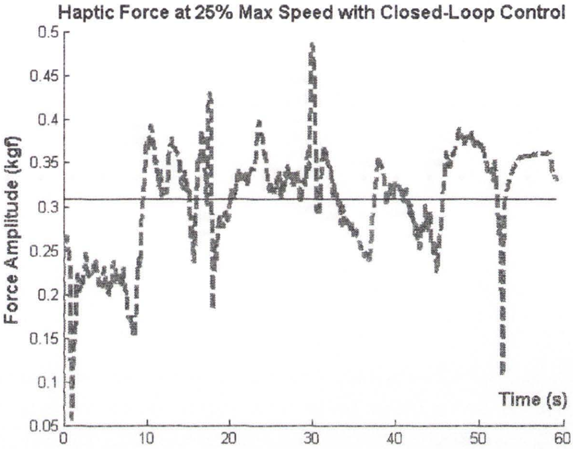

Figure 4.29 Haptic force in the test at 25% of the maximum speed with closed-loop control

Figure 4.29 shows a graph of the haptic force generated during this experiment at a speed of 25% of the maximum speed of the manipulator and the closed-loop control. However, the average of the haptic force in this test is 0.31 kgf, which is similar to the result from the tests in the open-loop control but the haptic force is the individual character of an operator.

In Figure 4.30, the time delay for the closed-loop control at 50% of the maximum speed of the manipulator is 16 ms; thus, the movement time for a joint angle command is less than 1 ms.

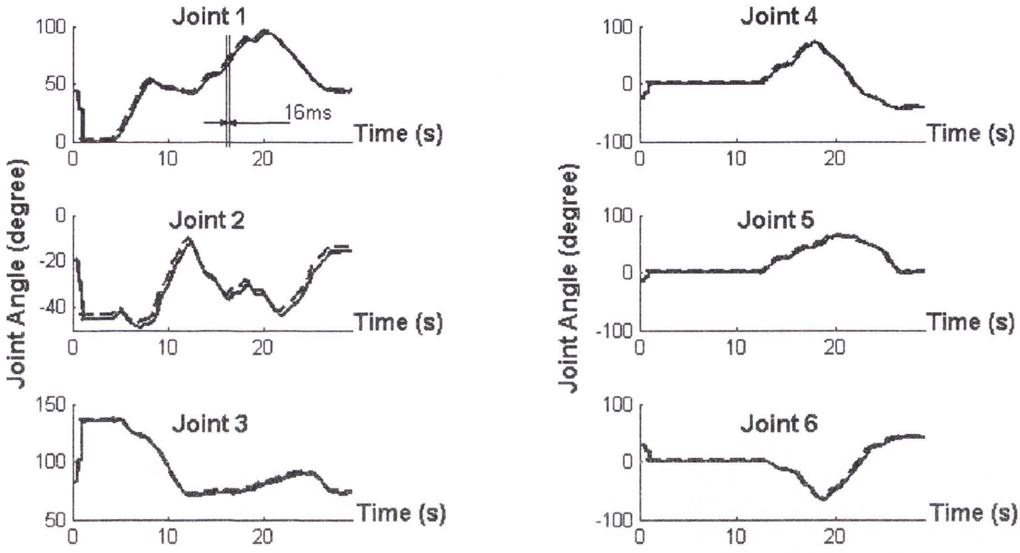

Figure 4.30 The manipulator's joint angles obtained from closed-loop control at 50% of the maximum speed of the manipulator, indicated by dash lines for the virtual manipulator and solid lines for the actual manipulator

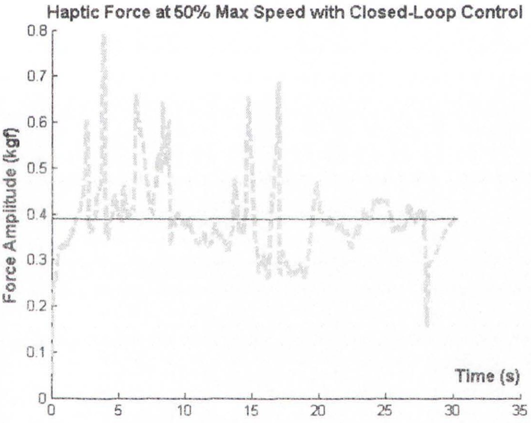

Figure 4.31 Haptic force in the test at 50% of the maximum speed with closed-loop control

Figure 4.31 shows a graph of the haptic force generated during this experiment with a speed of 50% of the maximum speed of the manipulator and closed-loop control. The average of the haptic force is about 0.4 kgf, which is slightly higher than the haptic force of the last test because the operator in this test can control the robot moving at a higher speed.

4.5.4 Field Testing

Field testing was conducted inside a channel section of the Sydney Harbour Bridge, Sydney, Australia. In this field test, the robot was placed in a hanging scaffold and an operator remotely controlled the manipulator by means of a haptic device from an adjacent room. The bridge section has been scanned across the whole chamber of the hanging scaffold and is represented as a point cloud set as shown in Figure 4.32.

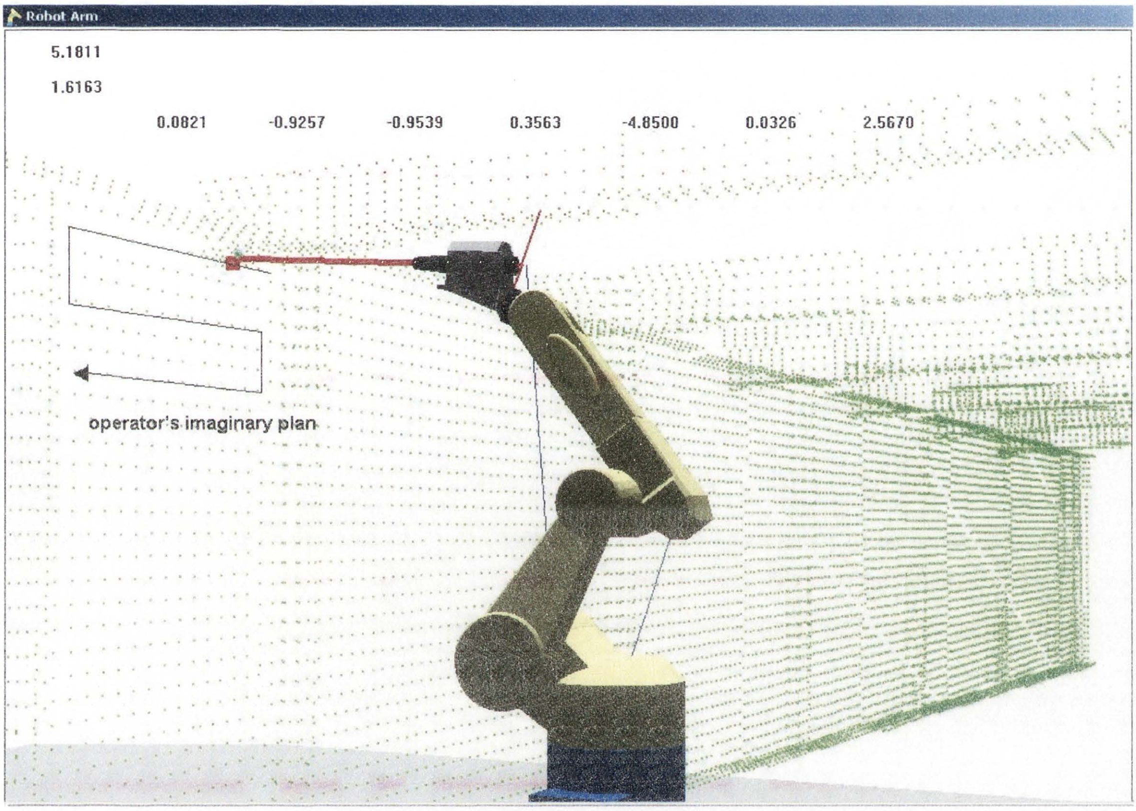

Figure 4.32 Virtual environment of a steel bridge channel section in the field test

This field test aims to examine the haptic-based interaction system, which is implemented in an industrial application performed in a real-world environment. Figure 4.33shows the operator and the manipulator performing a blasting task, with a laser pointer representing the sandblasting stream (dry run). The actual path taken by the laser pointer, which is projected onto the wall, is superimposed on the images in Figure 4.33.

Figure 4.33 Snapshots of the field test: the manipulator performs a dry run sandblasting

Figure 4.34 shows the trajectory of the manipulator controlled by an operator and the haptic forces recorded from the experiment. The haptic force and the movements of the manipulator create kinesthetic feedback on the operator's hand through the haptic device. The amplitude of the haptic forces on the haptic device is shown in Figure 4.35 (a). The haptic force ranges from 0.2 kgf to 0.8 kgf in this experimental test. The speed of the end-effector of the manipulator during the testing period is shown in Figure 4.35 (b). The average speed of the end-effector is about 0.27 m/sec along the testing duration.

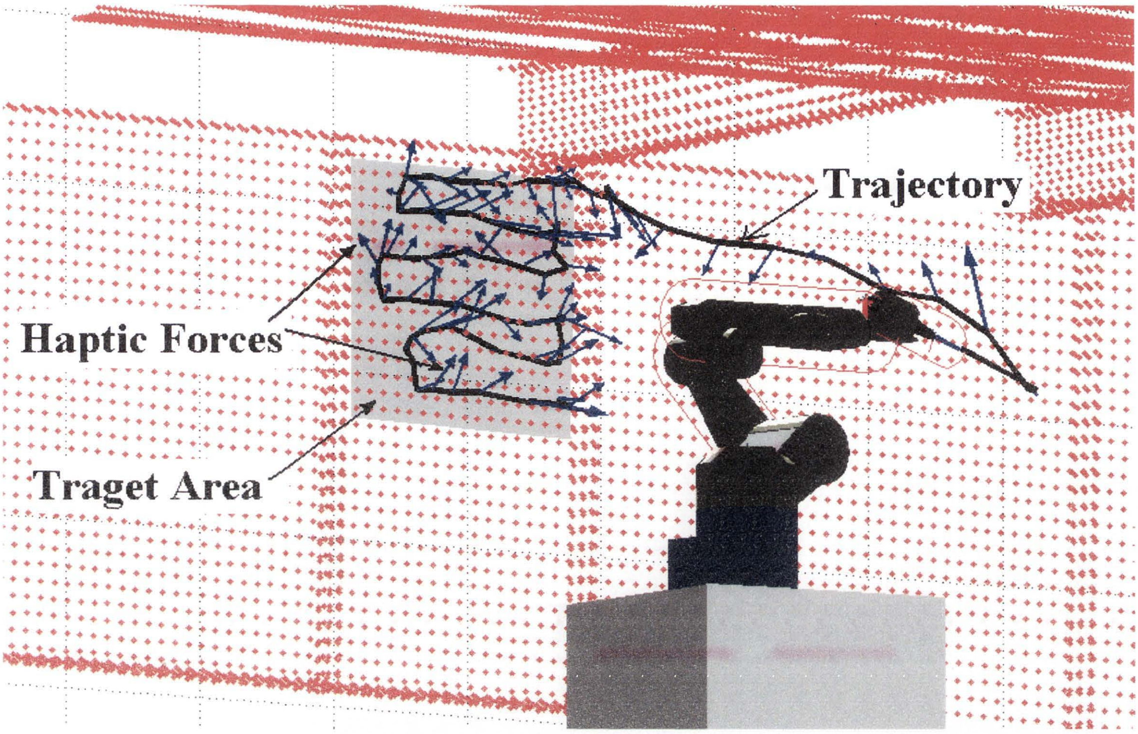

Figure 4.34 Haptic force along the trajectory of the manipulator

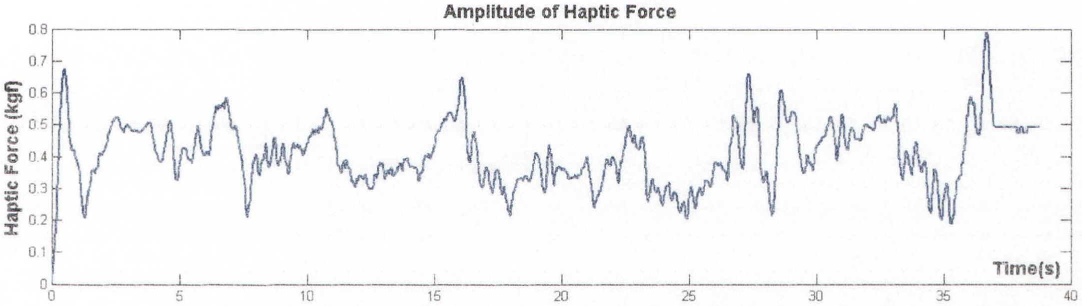

(a)

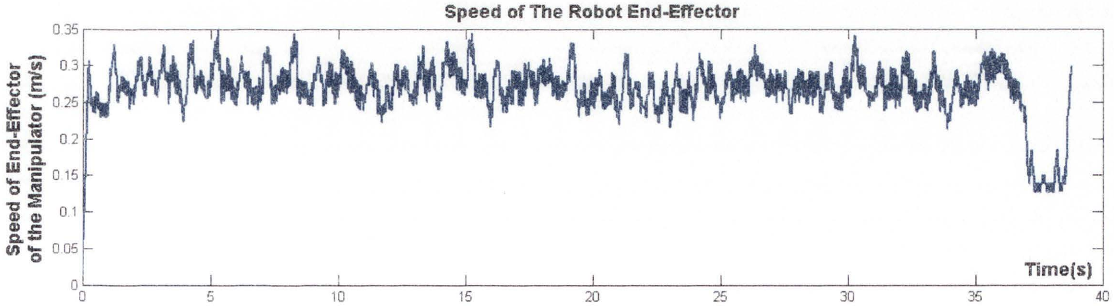

(b)

Figure 4.35 (a) Amplitude of the haptic force shown in Figure 4.34 (b) Speed of the end-effector of the manipulator along the path shown in Figure 4.34

4.6 Conclusion

This chapter has demonstrated that the haptic control approach is able to facilitate safe and effective haptic-based interaction. It has also demonstrated that the VF^2 approach is an effective collision-free motion planning approach for a multi-DOF manipulator operating in a complex 3D environment; the haptic force generation method can provide an effective interface between the haptic device, manipulator and the environment; and the workspace mapping method enables smooth and easy operation of a large manipulator by means of a small haptic device.

The proposed approaches have been implemented and tested in an industrial application for validation. The application addressed in this thesis, the sandblasting robotic system for steel bridge maintenance, which requires the manipulator to operate in complex3D environments in which there is limited space for a big robot manipulator to operate, is used as a sample application. The results of testing show that safe and intuitive haptic-based interaction can be achieved.

The haptic force generation for 6DOF haptic device is presented. However, no simulations and experiments with a 6DOF haptic device to control the robot arm are provided. Because of the limit of equipment, only experiments with a 3DOF haptic device (Novint® Falcon) are presented. The position and the orientation of the end-effector of the robot arm are controlled once a time, separately.

Chapter 5 Human Factor Model for Haptic-based Human-Robot-Environment Interaction

In haptic-based human-robot interaction (HRI), a human operator provides high-level decision-making and planning and a manipulator provides the power and accuracy to perform a task. The operator makes decisions based upon observations and defines a target path by using a haptic device, and then the robot controls the position of its end-effector to follow the defined path. The operational performance can be measured by the *Index of Performance* (*IP*), which is defined based on the speed and the pointing/control accuracy of the manipulator end-effector. Human factors such as human viewpoint (i.e. operator's eyesight) and hand movement (e.g. position, speed, strength) have significant effect on the performance [30][14][142] (Figure 5.1). The operator's viewpoint and hand movement are closely related to the operator's cognition, perception and decision-making abilities.

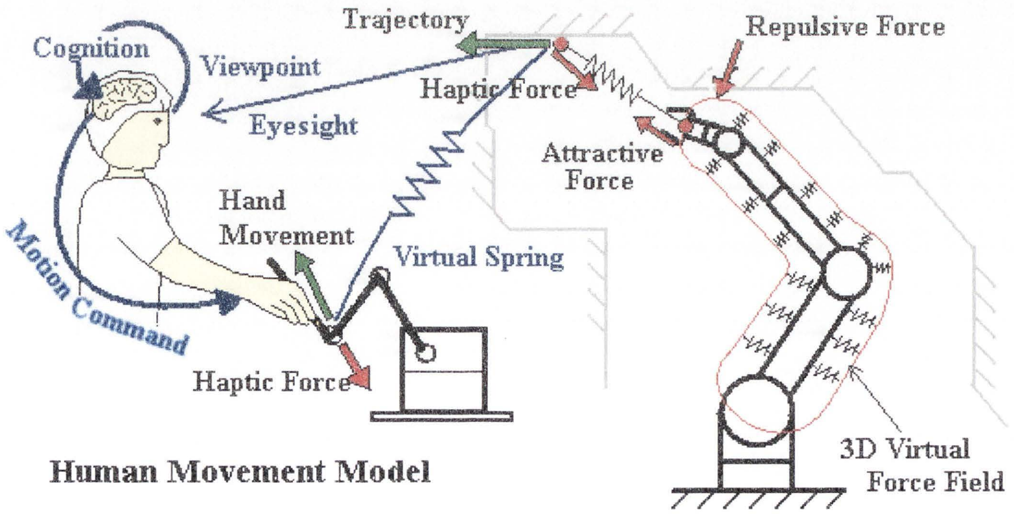

Figure 5.1 Example of human factors affecting Human-Robot-Environment Interaction (HREI)

An operator's viewpoint can be defined by the distance between the operator and the task space, and the angle between the direction of the operator's eyesight and the plane of the task space. In teleoperation, the location of an observing camera which is used to monitor the operation, is considered instead of the location of an operator.

An operator's hand movement can be modelled by position, speed and strength. In haptic-based HRI, a kinesthetic feedback presents a haptic force by a haptic device to the operator's hand. The haptic force resists the movement of the operator's hand and thus affects pointing/control accuracy, i.e. the operational performance.

In this chapter, the *Index of Performance (IP)* is formulated by the speed and the pointing accuracy of the manipulator end-effector on a target path with a defined path width (Section 5.1). The effect of operator viewpoint on the performance (*IP*) and an experimental approach to determining the view distance are investigated in Section 5.2. Hand movement model based on Fitts's law [14] and Steering law [30][31] is then reviewed, and an extended hand movement model is subsequently developed in Section 5.3. Based on the extended hand movement model, a control method is designed and integrated into the haptic device-robot interaction system to improve the performance of human-robot-environment interaction (HREI) (Section 5.4). Experiments are conducted to verify the model and the control method.

5.1 Index of Performance

In order to investigate the effect of human factors on the performance of HRI, a performance measurement needs to be defined. When an operator interacts with a robot manipulator using a haptic device, such as in the application of a sandblasting robotic system, the operator indirectly controls the movement of the end-effector of the manipulator by moving the haptic cursor through a haptic device to follow a desired path with a defined path width. The pointing accuracy of the end-effector is defined as the error of position offset (i.e. distance x) between the end-effector trajectory and the desired trajectory (i.e. the centerline of the desired path) as shown in Figure 5.2. The distribution of x is defined as Gaussian distribution (i.e. normal distribution

$x \sim \mathcal{N}(0, \sigma^2)$). Assume the width of the desired path is ϕ and the robot end-effector needs to stay within the desired path boundary, the pointing accuracy is related to the times that the end-effector stays inside the path track boundary. This can be defined by a probability density function (φ):

$$\varphi = P\left(-\frac{\phi}{2} < x < \frac{\phi}{2}\right) \tag{5.1}$$

In order to use the lookup table of standard normal distribution in Appendix C:

$$\varphi = P\left(-\frac{\phi}{2\sigma} < Z < \frac{\phi}{2\sigma}\right) \tag{5.2}$$

Z is a parameter used in the lookup table. σ^2 is the variance of distribution, σ is a standard deviation of x. The upper limit and lower limit of a desired path boundary are defined as $\frac{\phi}{2}$ and $-\frac{\phi}{2}$. For a path tracking task, the pointing accuracy (O_{acc}) can be defined by

$$O_{acc} = \frac{\varphi}{\sigma} \tag{5.3}$$

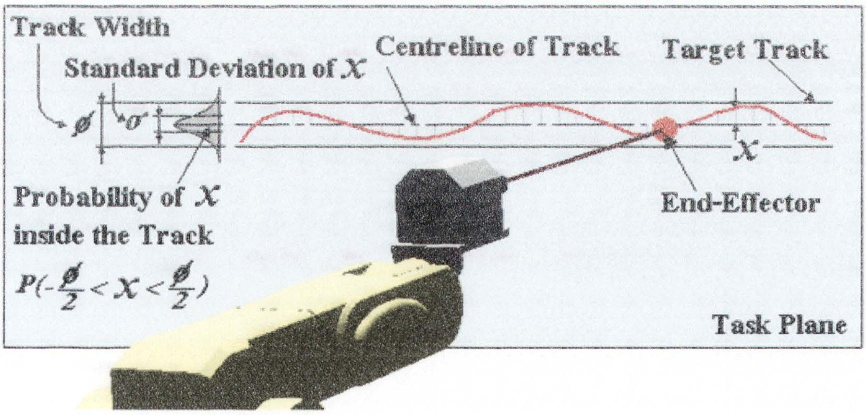

Figure 5.2 Error distribution

This research focuses on pointing and path tracking tasks in a manufacturing process such as sandblasting or spray painting. The quality of these operations is depended on the pointing accuracy; thus, the index of performance used in this thesis is defined by the product ofthe speed and the pointing accuracy of the manipulator end-effector (e.g.

the blasting spot in sandblasting operation) when it moves along a target path with a defined boundary:

$$IP = \dot{p}_e O_{acc} = \frac{\dot{p}_e\, P\left(-\frac{\phi}{2} < x < \frac{\phi}{2}\right)}{\sigma} \tag{5.4}$$

5.2 Determination of View Distance

5.2.1 Definition

View distance, which is related to the location of an operator or a camera, has a significant effect on the performance of HRI. As reviewed in Chapter 2, the scale of the task space and the distance between the viewpoint and the target plane are not included in Fitts's law and Steering law. The research presented in [12][30] discussed the control-movement scale which amplifies human hand movement, and the control-display scale which enlarges or reduces the task space. However, the view distance is not explicitly addressed. In this thesis, therefore, the view distance (d_v) between a camera screen plane and a task plane or an object plane is studied as a human factor that affects the operator's performance.

With a fixed viewpoint, i.e. camera position, the relationship between an object plane and a display screen plane (Figure 5.3) is defined as:

$$\emptyset_{obj} = 2d_v \tan\left(\frac{\alpha_v}{2}\right) + \emptyset_{scn} \tag{5.5}$$

where $\emptyset_{obj}$ is the dimension of an object plane and $\emptyset_{scn}$ is the dimension of a display screen plane. Thus d_v is the distance between an object plane and a display screen plane and α_v is the angle of view (i.e. the field of view) of a surveillance camera (Figure 5.3).

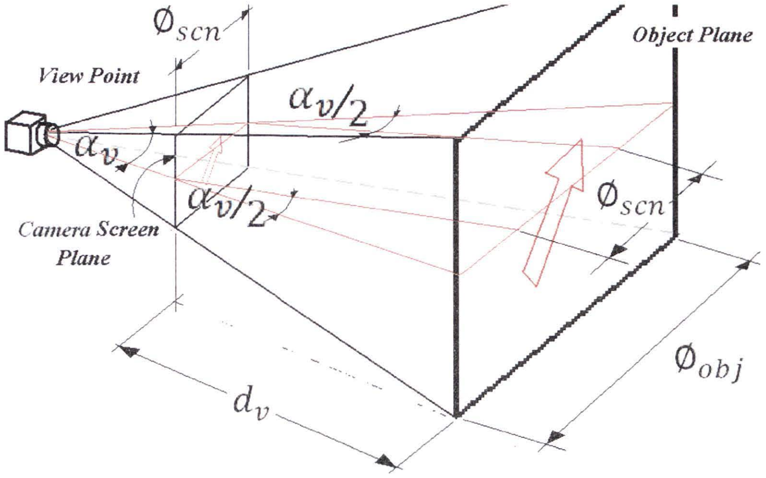

Figure 5.3 Object-to-screen projection

According to the control display scale [12] reviewed in Section 2.5.3, G_e is now defined as

$$G_e = \frac{\emptyset_{scn}}{\emptyset_{obj}} \tag{5.6}$$

$$G_e = \frac{\emptyset_{scn}}{2d_v \tan\left(\frac{\alpha_v}{2}\right) + \emptyset_{scn}} \tag{5.7}$$

By varying d_v and α_v, the projection can be zoomed in or out. For most industry applications, G_e is less than 1 because the object plane is always bigger than the display screen place, therefore

$$\frac{\emptyset_{scn}}{2d_v \tan\left(\frac{\alpha_v}{2}\right) + \emptyset_{scn}} < 1 \tag{5.8}$$

Moreover, G_e should be determined to provide a view that is able to show the whole body of an interested object or a specific section on one screen. Thus, if the dimension of an object is D_{obj}, the control-display scale should be

$$\emptyset_{scn} > G_e D_{obj} \tag{5.9}$$

Note that this definition of projection is for a normal camera but the definition of microscope projection must be different.

The control-movement scale (G_h) [30] is used to amplify or reduce human hand movement. As discussed in Section 4.3.2, the size of the haptic workspace in the virtual environment is enlarged or reduced by k_{sc} times of the physical workspace of the haptic device. That is to say, the hand movement (i.e. the movement of the haptic device handle) is enlarged or reduced by k_{sc} times. Then G_h, the relationship between the haptic cursor moving distance (in virtual environment) and the hand moving distance, is the inverse of k_{sc}:

$$G_h = \frac{1}{k_{sc}} \tag{5.10}$$

Therefore, the control scale (G_x) defined in Equation 2.26 (Chapter 2) can be re-written as

$$G_x = \frac{G_e}{G_h} = \frac{k_{sc}\emptyset_{scn}}{2d_v \tan\left(\frac{\alpha_v}{2}\right)+\emptyset_{scn}} \tag{5.11}$$

As shown in Equations 2.22 and 2.23, increasing G_x can reduce the index of difficulty (*ID*) of a task based upon Fitts's law and Steering law, and G_x is determined by d_v. The selection of a view distance (d_v) is normally empirical. In this research, an experimental approach is used to select d_v with statistical judgment. In this experiment, the effect of different distances (d_v) on the performance of an operation is investigated.

5.2.2 Experimental Test Design

This experiment is conducted by using an industrial robot (the same manipulator as the sandblasting robot presented in Section 3.3 and implemented in Section 4.5.4) with a Novint® haptic device. In this experiment, the view distance is determined for the control of the end-effector position, as the orientation of the end-effector is not required. Only three joints (Joints 1, 2 and 3) of the robot manipulator are controlled and the other three joints are set to be rigid joints. Using three joints only can avoid the redundancy of the manipulator in position calculation.

According to the dynamic robot model presented in Section 3.2 (Equation 3.10) and the definition of the index of performance in Section 5.1, the resistant force (or damping force) affects the speed of the manipulator end-effector and the operational performance in the haptic-based interaction. For the purpose of investigating the effect of the resistant force (damping force) on haptic-based HRI, three different levels of resistant force are simulated in this experiment: level 1 - low resistant force (with damping coefficients of the three joints as β_1 = [0.2, 0.35, 0.35] N.m.sec/rad); level 2 - medium resistant force (damping coefficients are assumed as β_2 = [0.4, 0.7, 0.7] N.m.sec/rad), and level 3 - high resistant force (damping coefficients are assumed as β_3 = [0.8, 1.4, 1.4] N.m.sec/rad).

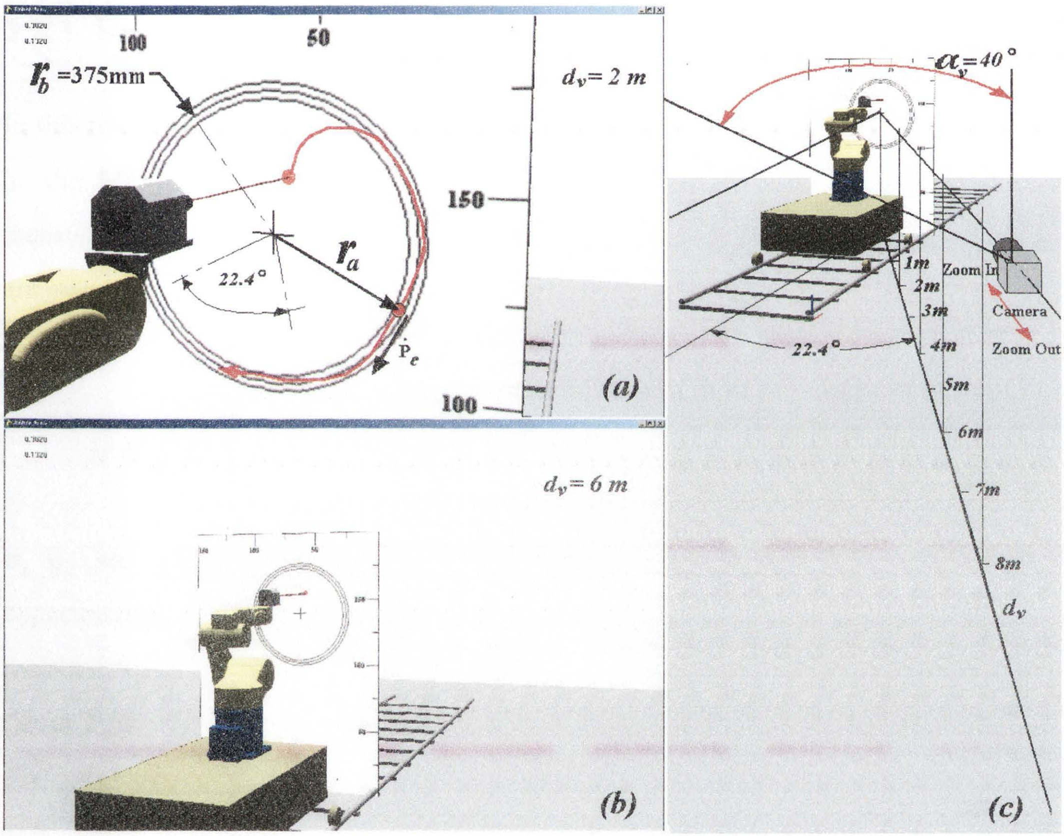

Figure 5.4 Setup of the robot steering test with different view distances (d_v); (a) Image of view distance at d_v=2m, (b) Image of view distance at d_v=6m, and (c) Diagram of the camera's position

In this experiment, an operator controls the end-effector of the manipulator using the Novint® haptic device to move within a circular path track for three minutes, as shown in Figure 5.4. The width of the circular path track (ϕ) is 40 mm, and the radius of the track (r_b) is 375 mm. The view distance (d_v) is set at 2 m, 4 m, 6 m, and 8 m respectively, and the control-display scales (G_e) calculated by Equation 5.7 from these view distances are 0.185, 0.102, 0.070, and 0.054 respectively. The angle of view between the camera axis and a normal vector of the target plane is set to 22.4 degrees (as shown in detail in Figure 5.4). The field of view (α_v) of the surveillance camera is 40 degrees. In this experiment, a 13 inch screen (diagonal) with 1280×800 resolutions is used for monitoring the operation. For the control-movement scale (G_h), the k_{sc} is tested at 5 different scales: 43.5, 36.85, 22.2, 14.9, and 11.1 (i.e. G_h={0.023, 0.027, 0.045, 0.067, 0.09}). All participants are trained for several minutes for them to get familiar with the system. They were told the objectives of the experiments and explained the developed method.

5.2.3 Results

In this test, the cursor (which is equivalent to the end-effector of the robot manipulator, or the blasting spot in the sandblasting application) speed ($\dot{\mathbf{P}}_e$) and distance ($\boldsymbol{r}_a$) measured from the centre of the circular path track to the current position of the cursor are recorded over the test period. The standard deviation (σ) of distribution of $\boldsymbol{r}_a$ is represented by

$$\sigma = \sqrt{\frac{1}{N}\sum_{i=1}^{N}\left(r_{a_i} - r_b\right)^2} \quad ; N \text{ is sampling number} \tag{5.12}$$

σ, $\dot{\mathrm{p}}_\mathrm{e}$ are used to calculate the index of performance (*IP*) (Equation 5.4). The experimental results are shown in Table 5.1, Table 5.2 and Table 5.3 for the low resistant force (level 1: β_1 = [0.2, 0.35, 0.35] N.m.sec/rad), the medium resistant force (level 2:β_2 = [0.4, 0.7, 0.7] N.m.sec/rad), and the high resistant force (level 3:β_3 = [0.8, 1.4, 1.4] N.m.sec/rad) respectively.

Base upon Table 5.1, Table 5.2 and Table 5.3 the graphs in Figure 5.5 show the standard deviation (σ) of $\boldsymbol{r}_a$, the end-effector speed ($\dot{p}_e$) of the manipulator, and the index of performance (*IP*). Left-hand graphs in Figure 5.5 are based on d_v while right-hand graphs in Figure 5.5 are based on k_{sc}. Graphs (a) and (b) are from the experiments with low resistant force (β_1), Graphs (c) and (d) are from the experiments with medium resistant force (β_2), and the graphs (e) and (f) are from the experiments with high resistant force (β_3).

Table 5.1 Index of performance (*IP*) of 6 participants with low resistant force (level 1: β_l)

		k_{sc} ($\underline{G_h}$)					
		11.1(0.09)	14.9(0.067)	22.2(0.045)	32.85(0.027)	43.5(0.023)	Average
d_v=2m	Participant1	10.791	13.148	12.46	3.2481	8.3083	9.5912
	Participant2	15.202	18.33	10.016	10.589	0.52725	10.933
	Participant 3	14.113	2.7621	3.1066	11.048	4.1379	7.0335
	Participant 4	0.6355	11.04	7.858	0.3816	5.5714	5.0972
	Participant5	5.8747	9.1235	8.7697	2.3238	0.91812	5.402
	Participant6	3.6893	1.1667	13.444	5.1305	7.9193	6.2699
Average		8.3842	9.2618	9.2756	5.4535	4.5637	
d_v=4m	Participant1	0.61362	8.8917	11.269	0.71071	11.655	6.628
	Participant2	21.603	13.22	0.87447	8.1808	0.38933	8.8534
	Participant3	1.1911	0.83044	0.74771	5.3465	5.661	2.7553
	Participant4	14.567	18.797	12.201	9.8226	5.2543	12.128
	Participant5	14.688	7.0144	9.1629	3.0066	5.4432	7.8631
	Participant6	5.3393	4.8781	1.576	4.0071	2.88	3.7361
Average		9.667	8.9384	5.9719	5.1791	5.2138	
d_v=6m	Participant1	0.86347	4.3567	5.0759	0.47807	9.0982	3.9745
	Participant2	13.877	16.19	0.40223	0.91361	13.658	9.0082
	Participant3	12.066	5.3297	3.6582	6.4773	7.9445	7.0952
	Participant4	19.18	21.407	0.98651	5.2855	9.1369	11.199
	Participant5	3.6893	1.1667	13.444	5.1305	7.9193	6.2699
	Participant6	19.443	3.5381	7.261	0.95703	1.4736	6.5346
Average		11.52	8.6646	5.1379	3.207	8.2051	
d_v=8m	Participant1	8.5257	3.8524	11.537	9.0052	3.9312	7.3702
	Participant2	15.807	14.693	0.96439	3.8894	7.7779	8.6264
	Participant3	13.294	9.8363	5.7517	5.8077	4.9195	7.9218
	Participant4	6.4573	1.3327	4.6034	0.50143	3.8401	3.347
	Participant5	5.3393	4.8781	1.576	4.0071	2.88	3.7361
	Participant6	20.92	0.48109	8.9033	4.2846	2.1447	7.3467
Average		11.724	5.8456	5.5559	4.5826	4.2489	

Table 5.2 Index of performance (*IP*) of 6 participants with medium resistant force (level 2: β_2)

		k_{sc} (G_h)					
		11.1(0.09)	14.9(0.067)	22.2(0.045)	32.85(0.027)	43.5(0.023)	Average
d_v=2m	Participant1	22.61	5.2712	4.3163	12.738	8.1647	10.62
	Participant2	0.6343	3.3815	24.541	1.004	7.2426	7.3607
	Participant3	0.31496	4.2517	15.812	11.954	12.509	8.9683
	Participant4	4.6391	9.9075	5.7018	17.585	11.887	9.944
	Participant5	9.1181	0.5544	12.789	4.2292	0.006240	5.3394
	Participant6	1.1085	1.6747	1.6446	2.2386	3.6671	2.0667
Average		6.4042	4.1735	10.801	8.2914	7.2462	
d_v=4m	Participant1	5.0979	16.115	24.455	13.725	16.142	15.107
	Participant2	5.756	6.2144	23.748	9.8839	7.3271	10.586
	Participant3	14.781	0.81742	23.398	21.982	10.516	14.299
	Participant4	22.071	0.95855	17.575	0.47636	0.38987	8.2941
	Participant5	4.5885	13.461	7.8951	5.7895	0.026275	6.3521
	Participant6	1.5473	7.9665	2.9739	4.9382	3.7055	4.2263
Average		8.9736	7.5888	16.674	9.4658	6.3512	
d_v=6m	Participant1	10.042	12.327	14.286	16.126	10.64	12.684
	Participant2	0.87219	11.352	15.937	12.072	4.5009	8.9468
	Participant3	18.577	19.153	14.647	12.7	14.455	15.906
	Participant4	6.073	23.09	0.4862	13.146	0.6767	8.6944
	Participant5	1.1085	1.6747	1.6446	2.2386	3.6671	2.0667
	Participant6	12.466	0.41486	8.1515	6.1453	4.9467	6.4248
Average		8.1896	11.335	9.192	10.405	6.4809	
d_v=8m	Participant1	14.547	10.555	15.817	13.447	9.7949	12.832
	Participant2	8.7846	15.652	0.94191	8.1077	9.85	8.6672
	Participant3	0.63541	4.9804	14.052	4.913	0.87118	5.0904
	Participant4	5.6197	5.8586	0.85085	8.3488	0.99559	4.3347
	Participant5	1.5473	7.9665	2.9739	4.9382	3.7055	4.2263
	Participant6	0.38801	1.96	0.59097	4.7876	5.0044	2.5462
Average		5.2537	7.8288	5.8711	7.4238	5.0369	

Table 5.3 Index of performance (*IP*) of 6 participants with high resistant force (level 3: β_3)

		k_{sc} (G_h)					
		11.1(0.09)	14.9(0.067)	22.2(0.045)	32.85(0.027)	43.5(0.023)	Average
d_v=2m	Participant1	20.881	22.443	13.898	0.53253	7.6389	13.079
	Participant2	0.24917	15.435	3.8989	11.556	3.6553	6.959
	Participant3	0.27757	16.848	0.58103	12.884	14.42	9.0023
	Participant4	2.2722	3.8115	14.903	3.8008	13.974	7.7523
	Participant5	0.69854	3.9962	1.1329	0.008520	0.004322	1.1681
	Participant6	2.393	2.385	3.494	4.3002	0.003833	2.5152
Average		4.462	10.82	6.3179	5.5138	6.6161	
d_v=4m	Participant1	14.306	2.8258	10.954	17.736	0.49776	9.2638
	Participant2	11.454	3.4618	18.315	15.332	9.3792	11.588
	Participant3	12.282	17.144	14.82	4.8707	0.71222	9.9659
	Participant4	0.68607	12.368	9.9027	10.985	11.25	9.0384
	Participant5	0.83054	3.0411	9.8336	4.7411	0.072305	3.7037
	Participant6	3.5229	1.1293	1.4516	0.36427	2.9372	1.881
Average		7.1804	6.6617	10.879	9.0049	4.1415	
d_v=6m	Participant1	13.485	0.67275	4.927	11.031	11.131	8.2494
	Participant2	0.16292	4.5936	10.077	13.399	11.091	7.8648
	Participant3	4.3908	16.379	11.11	0.7322	14.677	9.4577
	Participant4	0.69384	16.11	5.2745	0.71842	11.582	6.8757
	Participant5	2.393	2.385	3.494	4.3002	0.003833	2.5152
	Participant6	11.051	12.391	3.6858	0.60051	2.2123	5.9882
Average		5.3628	8.7551	6.4281	5.1303	8.4495	
d_v=8m	Participant1	1.8446	14.314	6.9169	0.70188	7.4424	6.2439
	Participant2	0.32359	8.9751	17.251	11.408	3.4006	8.2716
	Participant3	0.22063	13.117	10.283	6.8502	0.72986	6.2401
	Participant4	11.733	0.74404	6.2963	12.698	8.8285	8.06
	Participant5	3.5229	1.1293	1.4516	0.36427	2.9372	1.881
	Participant6	9.6361	11.477	17.697	9.2315	0.6785	9.744
Average		4.5468	8.2927	9.9826	6.8756	4.0028	

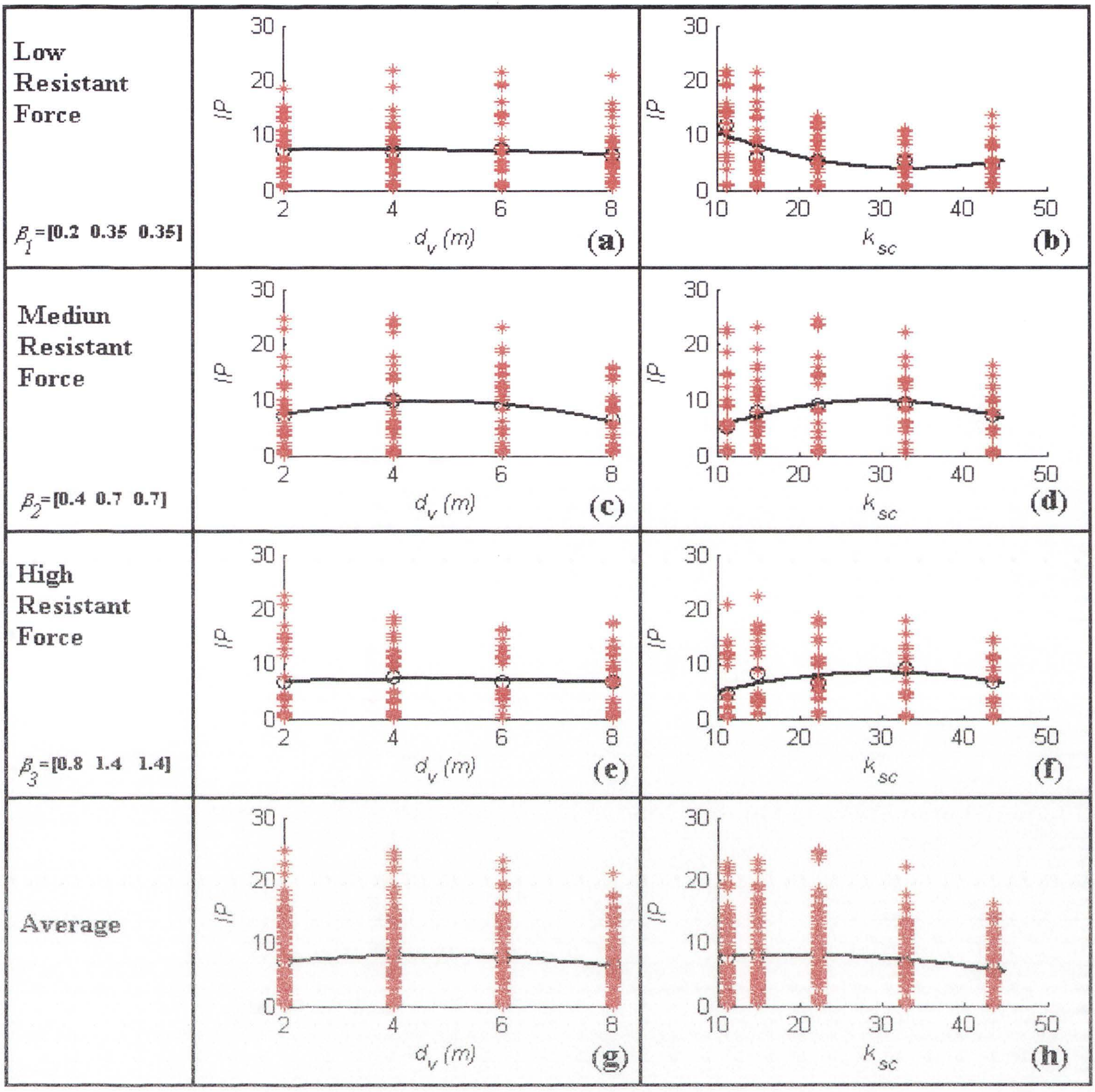

Figure 5.5 ***IP*** **of the 6 participants are shown as red points and the Average** ***IP*** **of the 6 participants are shown in black lines.**

5.2.4 Discussion

It can be seen from Figure 5.5 (a) and (e) that the performance in the haptic-based interaction does not significantly change between 2 m to 5 m of view distance when the resistant force is low or high. The *IP* is reduced when the view distance exceeds 5 m. With medium resistant force, Figure 5.5 (c) shows that operators can perform better when the view distance is around 3 m to 6 m. Figure 5.5 (b) shows that the performance is the highest at $k_{sc} \approx 10$ for the robot with the low resistant force and that it reduces when the k_{sc} is increased. For medium and high resistant force, a good performance in the haptic-based interaction is achieved when the k_{sc} is from 20 to 35. This suggestion is made based on the sandblasting robotic system which is operated at the specific angle of view (22.4 degree). For other systems and different view angles, it may need to be conducted similar experiments. Although these three levels of resistant force are selected empirically, the results show that the medium level resistant force helps to improve the performance. It proofs that a reasonable amount of haptic force feedback helps the operator to achieve a better performance in human-robot interaction. The difference in performance of the six participants (as shown in Figure 5.5, red points) is mainly caused by individual ability of hand movement, operator's eyesight, and experience with computer operation, haptic device and robot operation.

5.3 Extended Hand Movement Model

Hand movement is another factor studied in this research that affects the performance of HRI. In haptic-based HRI, the haptic force generated by a haptic device resists the movement of an operator's hand, and also the haptic cursor. The haptic force therefore affects the accuracy of an operator's hand movement, and consequently affects the pointing accuracy of the haptic cursor in the virtual environment and the position accuracy of the manipulator end-effector in the real task plane. It is assumed that the positioning accuracy of the end-effector is very similar to the pointing accuracy of the haptic cursor because of the high accurate motion control of the robot. Therefore, the relationship between the pointing accuracy and the haptic force is investigated in this section, and an eXtended Hand Movement (XHM) model is then developed.

5.3.1 Pointing Accuracy

When the cursor of a pointing device is manually controlled to point to a target area or trace a predefined path, the distribution of the cursor positions inside the target area is a normal distribution about a mean (μ) which is approximated as the centre of the target area or the centreline of the target path. The standard deviation (σ) can be used to measure the pointing accuracy.

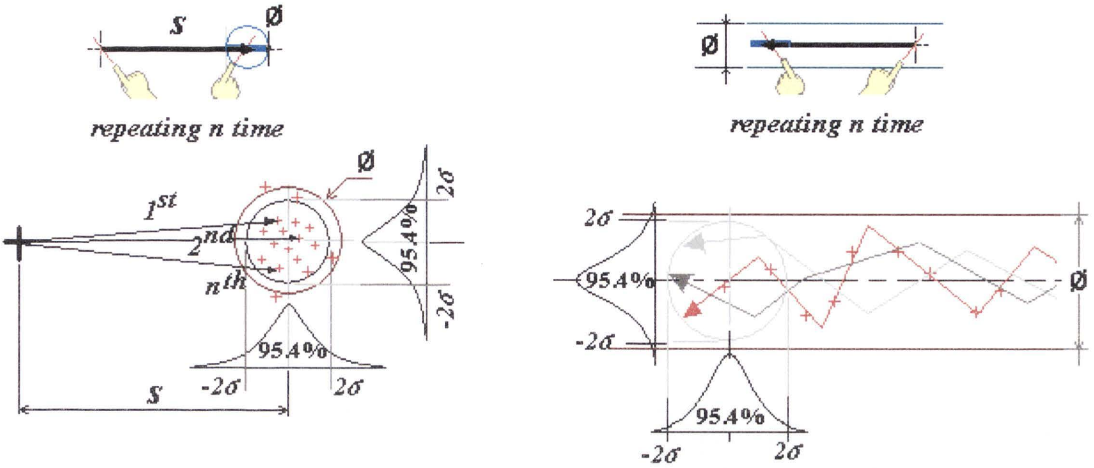

Figure 5.6 Pointing accuracy at 4σ of point-to-point task and path tracking task

For example, if the size (diameter) of the target area $\emptyset$ is equal to 4σ, the pointing accuracy is about 95.4% (Figure 5.6) and if $\emptyset$ is larger than 5σ,the pointing accuracy is about 100%. Therefore, $Z_{ac}\sigma$ defines the pointing accuracy, where$Z_{ac}$is the coefficient of standard deviation.

In Fitts's law and Steering law, the movement time is defined by the travelling distance (s), target size or path width ($\emptyset$), and the control scale (G_x), as shown in Section 2.5. When the cursor of a pointing device has been repeatedly moved from a starting point to the target area, the position of the haptic cursor distributes around the centre of the target area or the middle line of the path-track. The distribution can be presented as$Z_{ac}\sigma$. The models of human hand movement in Fitts's law and Steering law can be modified as:

$$MT = a + b\log_2\left(\frac{s}{G_x(\emptyset - Z_{ac}\sigma)} + 1\right) \tag{5.13}$$

$$MT = a + b\int \frac{ds}{G_x(\emptyset - Z_{ac}\sigma)} \tag{5.14}$$

Therefore, the path width or target size needs to be greater than the pointing accuracy ($Z_{ac}\sigma$). When a haptic device with force feedback is used as a pointing device, the distribution of the cursor position, which is represented by σ, is affected by the haptic force (F_h) and the speed of the operator's hand (i.e. the haptic cursor speed; v_a). In this thesis, σ is therefore assumed to be a function of haptic force and hand movement speed, F_h and v_a:

$$\sigma = Q(F_h, v_a) \tag{5.15}$$

The research presented in [144][145] only provides a relationship between feedback force and pointing errors. To the best of my knowledge, there is no analytical approach to defining this function Q. In this research, an experimental approach is taken to define the function Q.

5.3.2 Experimental Test

To define the function $Q(F_h, v_a)$as shown in Equation 5.15, an experiment is conducted to measure the standard deviation (σ) of the haptic cursor position when the haptic force is presented.

5.3.2.1 Design of Experiment

In point-to-point movement [12], the hand movement time is defined in two steps of movement: 1) primary movement; and 2) corrective movement. A primary movement is a movement over a large distance where the operator moves the hand (or the cursor) quickly without being concerned about accuracy. Primary movements often miss the target (i.e. overshooting or falling short), therefore a further corrective movement is required to move the cursor towards the target. In a corrective movement, the operator pays more attention to the precision of the movement and moves with slower speed than the primary movement. If there is no time limit for a movement, then an operator can control the cursor with high accuracy [144].This experiment is conducted to find the relationship between the standard deviation and the haptic force and hand movement speed.

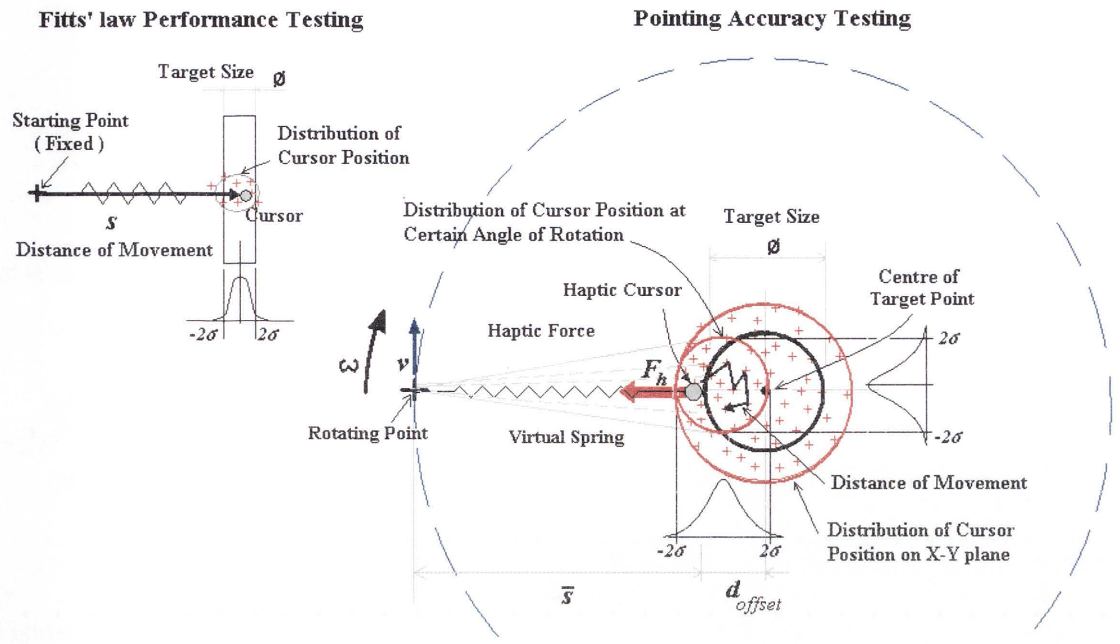

Figure 5.7 Pointing accuracy testing diagram

As shown in Figure 5.7, this experimental test is modified from Fitts's law performance testing (i.e. an operator moves the cursor from a fixed starting point to a fixed target point) by rotating the starting point, which is called the rotating point, around a specified target point. The angular speed (ω) of rotation of the starting point is set to be constant for the purpose of controlling the rotation consistently. A haptic force is generated based on the distance between the rotating point and the haptic cursor position, and the stiffness of the virtual spring. This haptic force is applied to the operator's hand through the haptic device and attempts to pull the haptic cursor out of the target area. The operator attempts to hold the haptic cursor on to the target point. Before the tests are conducted, every participant is trained about how to use the testing system and to get familiar with the force generated by the testing system.

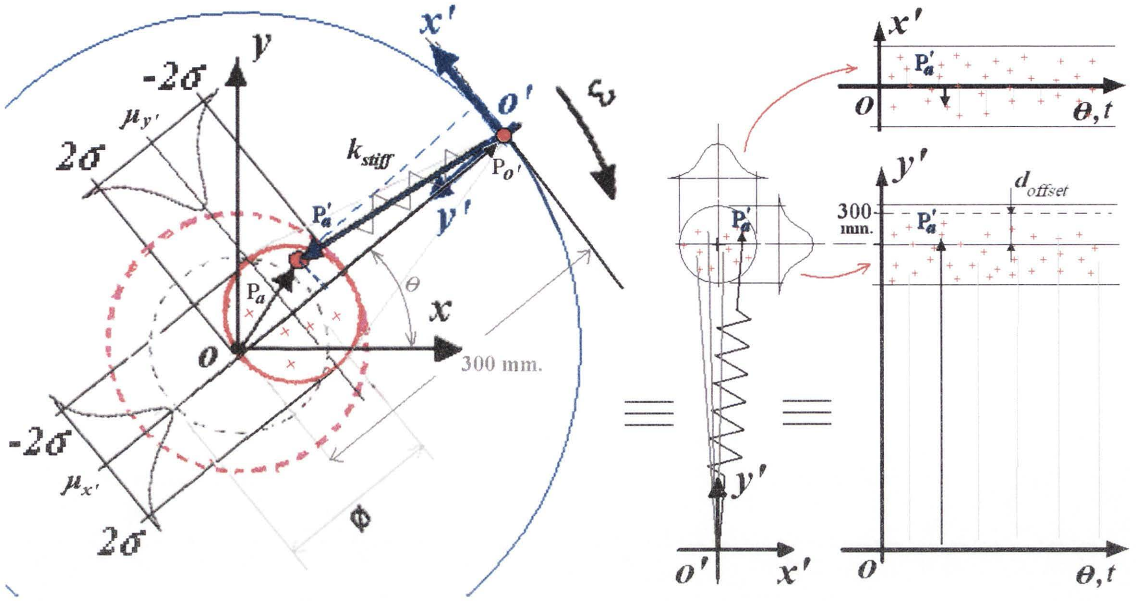

Figure 5.8 Coordinate transformation

The positions ($\mathbf{P}_a$) of the haptic cursor are on the X-Y plane (2D) in the screen coordinate frame (Figure 5.8). In order to match up to the test in the Fitts's law performance test, these positions ($\mathbf{P}_a$) in the screen coordinate frame need to be transformed to be positions ($\mathbf{P}'_a$) in the coordinate frame of the rotating point X'-Y'. This transformation as shown in Figure 5.8 is defined by the orthogonal matrix for 2D space as

$$P'_a = \begin{bmatrix} \cos(\theta + 90°) & -\sin(\theta + 90°) & 0.3 \\ \sin(\theta + 90°) & \cos(\theta + 90°) & 0 \\ 0 & 0 & 1 \end{bmatrix}^{-1} P_a \tag{5.16}$$

where θ is a rotation angle for the rotating point. The number 0.3 m. (300 mm.) is a distance between coordinate frames o and o' as show in Figure 5.8. This distance time by stiffness of the virtual spring (k_{stiff}) is the maximum haptic force. The standard deviation (σ) iscalculated from the distribution of $\mathbf{P}'_a$ on the coordinate frame of the rotating point X'-Y'. This experiment design and transformation gives the corrective movement. Primary movement is not included in this experiment test. There the position of $\mathbf{P}'_a$ is the result of corrective movement. An offset (d_{offset}) is presented in the experiment because the virtual spring pulls the haptic handle and the operator's hand throughout the testing period. This is not taken into account, however, because this experiment only aims to measure the standard deviation (σ) of the distribution of $\mathbf{P}'_a$.

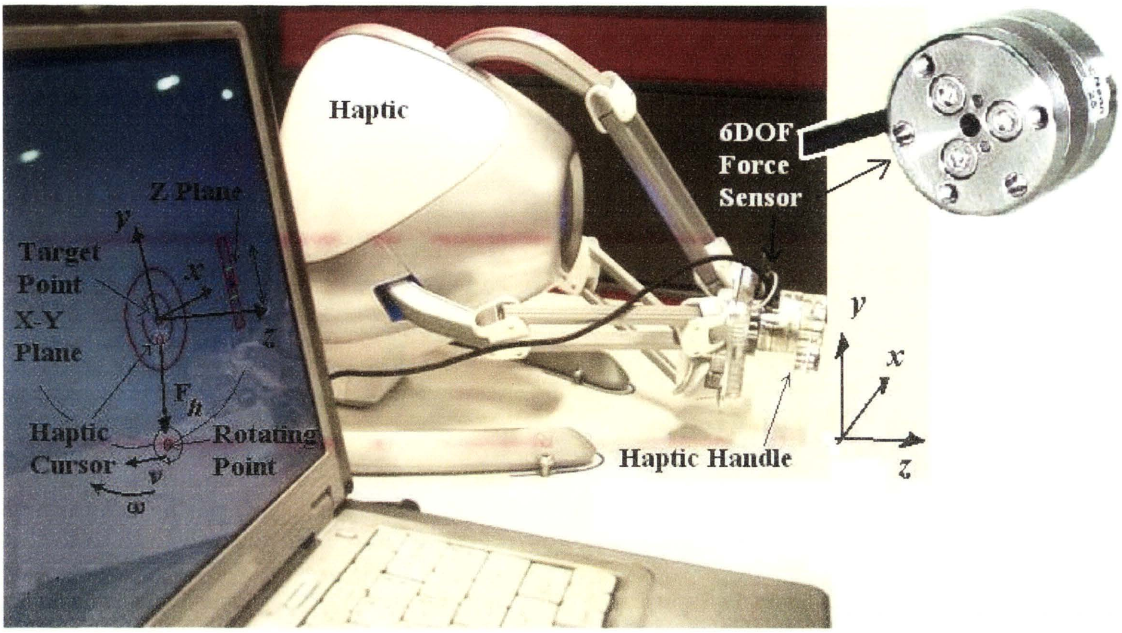

Figure 5.9 Pointing accuracy experiment setup

In order to measure the haptic force, a 6DOF force sensor is installed at the handle of the haptic device. The haptic force and the position of the haptic cursor are recorded during the test.

5.3.2.2 Parameters

Testing parameters such as haptic force and angular speed need to be determined for the experimental test. For haptic force calibration, the force sensor affixed on the haptic handle is rigidly connected to a post. The haptic device generates low amplitude haptic force at first and then increases the haptic force until the motors in the haptic device are at their torque limits.

Force calibration of the haptic device is carried out to find the range of linear relationship between the actual haptic force and the setting force in the program of the haptic-based interaction system. Figure 5.10 shows the actual haptic forces that are generated from the Novint® Falcon haptic device in X, Y, and Z axes. The result of calibration shows that the maximum force of the Novint® Falcon haptic device is 0.7 kgf (kilogram-force) on both X and Y axes and 1.8 kgf on the Z axis.

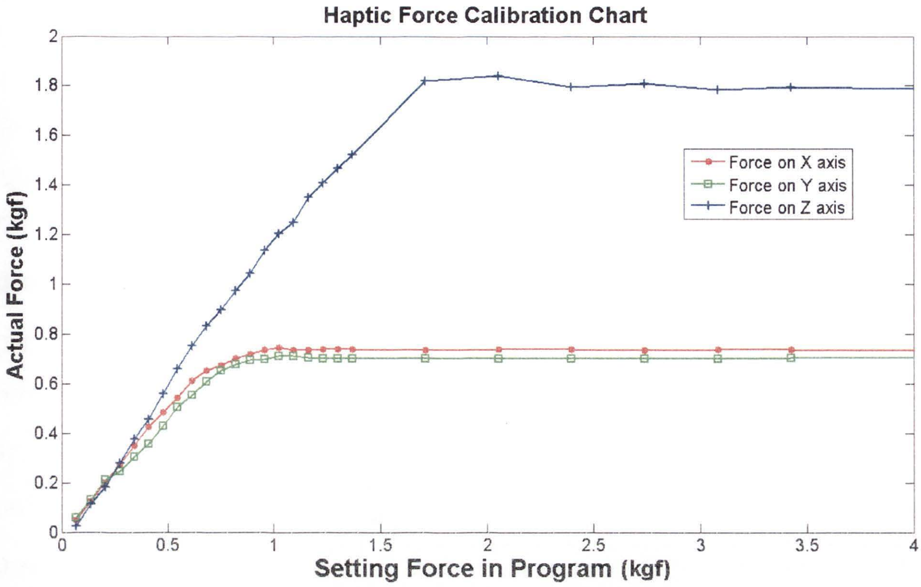

Figure 5.10 Force calibration of a haptic device (Novint® Falcon)

Three different haptic forces are selected in this experiment: 0.7 kgf, 0.467 kgf, and 0.23 kgf. The selection is made from the maximum haptic force of X-Y plane and distributed evenly into three ranges. The rotating point is programmed to rotate around the target point with a radius (r_c) of 0.3 m, and it is assumed that the length of the virtual spring at rest is zero. The stiffness properties of the virtual spring are 2.33, 1.56, and 0.78 kgf/m, corresponding to the three forces.

To confirm that the haptic device will not overload during the tests, the maximum power usage of the haptic device must less than 30W based upon the specification of the Novint® Falcon haptic device [141]. For the maximum haptic force 0.7 kgf and the maximum angular speed of the rotating point 87 RPM (1.45Hz),the maximum power usage of the haptic device at 19W (from power = F_h*r_c*ω), which is about 63% of maximum capacity. From the maximum angular speed limitation (87 RPM), the angular speeds used in the experiment are set by dividing the maximum angular speed to three levels at same difference and the three levels of angular speed are 15.6 RPM, 51.4 RPM, and 87 RPM (0.26Hz, 0.856Hz, and 1.45Hz).

As there are three force levels (from three stiffness properties of the virtual spring) and three angular speeds, each participant will do nine different tests.

5.3.2.3 Testing Setup

Eight participants are selected for these experimental tests. All of them are healthy and aged between 20 and 35. Each participant undergoes nine tests with different haptic force and angular velocity combinations (3 haptic forces and 3 angular velocities). Each test takes five minutes to complete. There is no predetermined testing order. All participants must take a break of at least five minutes between tests in order to minimise interference by residual exhaustion. The haptic cursor can be moved in a 3D space with 3DOF, but in this experiment, it is programmed to move on the X-Y plane only. The movement on Z axis of the haptic cursor is limited by virtual walls, which are positioned at ±2.5 mm above and below the X-Y plane.

5.3.2.4 Result 1: Measured Haptic Force

The actual force generated by the haptic device is recorded during the test period. After all eight participants complete the tests, the averages of the actual haptic force ($\bar{F}_h$) (Figure 5.11) for all the angular speeds among the eight participants are 0.2015, 0.3829, and 0.5254 kgf, corresponding to the three spring stiffness properties: 0.78, 1.56, and 2.33 kgf/m, respectively. The centre of all haptic force circles on the Y axis has dropped by -0.2 kgf because of the weight of the haptic handle (with the force sensor installed). However, this does not affect the distribution of the position of the haptic cursor.

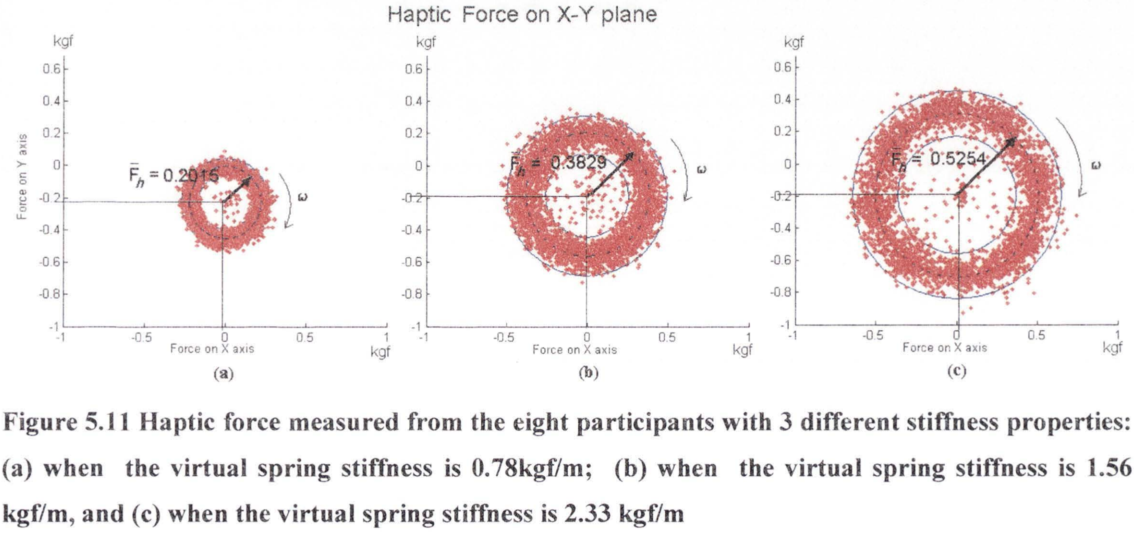

Figure 5.11 Haptic force measured from the eight participants with 3 different stiffness properties: (a) when the virtual spring stiffness is 0.78kgf/m; (b) when the virtual spring stiffness is 1.56 kgf/m, and (c) when the virtual spring stiffness is 2.33 kgf/m

5.3.2.5 Result2: Standard Deviation of Haptic Cursor Positions

Figures 5.12 to 5.19 show the haptic cursor position ($\mathbf{P'}_a$) data obtained from the eight participants. Each figure shows the position distribution of the nine tests of one participant. The standard deviation (σ_i) of each participant in a particular test setting is presented at the top-right corner of each graph. The averages of the standard deviation (σ) of the haptic cursor distributionfor all eight participants in the nine tests are shown in Table 5.4.

Table 5.4 Average of standard deviation σ_i (mm) for all 8 participants in nine tests

Average Force measured (kgf)	Angular Speed(RPM)		
	15.6	51.4	87
0.2015	0.5772	0.8753	1.0297
0.3829	0.8012	1.4337	1.8062
0.5254	1.0975	1.6247	2.1941

In Figures 5.12 to 5.19, each figure presents the results of nine tests of one participant, and the results of each test include: a haptic cursor position graph and two histograms of the haptic cursor distribution on X and Y axes. Each $\sigma_i(F_h, \omega)$ in the haptic cursor position graph is the standard deviation of the haptic cursor on X-Y plane (the average of the standard deviations in X axis and Y axis). Although every participant has performed differently, as shown in the haptic cursor position graph in Figures 5.12 to 5.19 and Table 5.4, the standard deviation σchanges in the same way among the tests, i.e. $\sigma$is increased when the haptic force (F_h) or the angular speed (ω) increases.

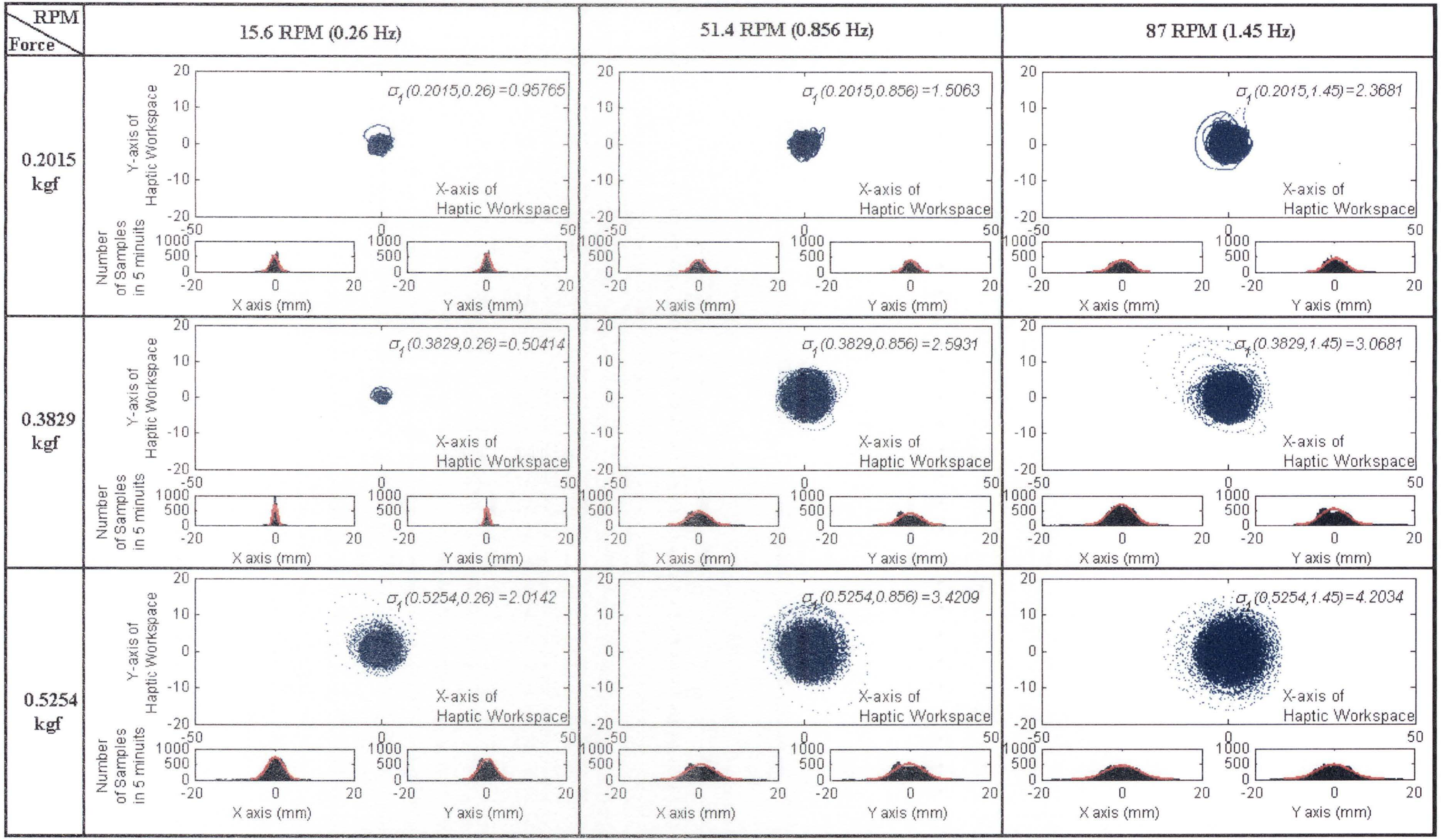

Figure 5.12 Distribution of the haptic cursor position: Results from the 1st participant

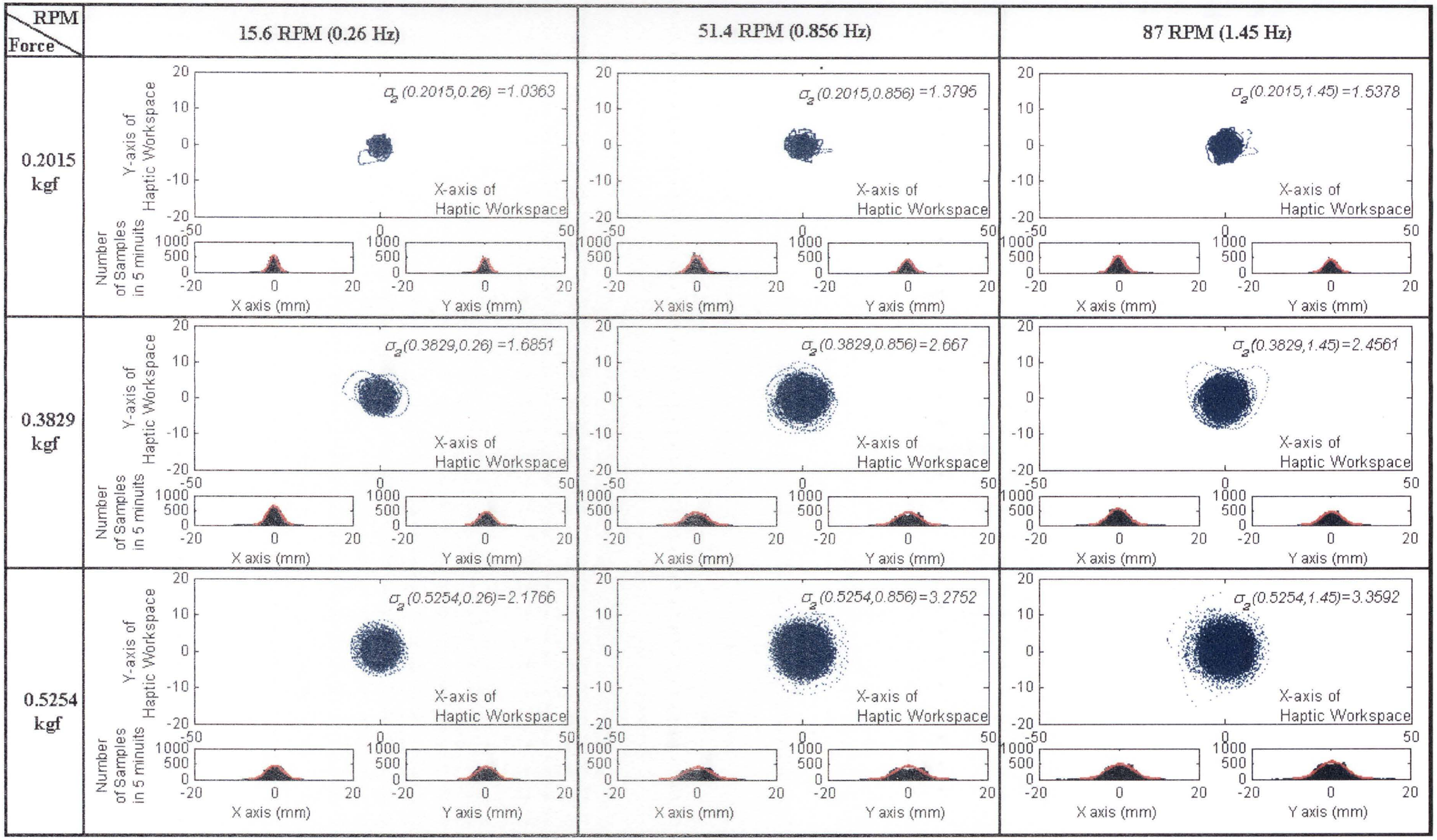

Figure 5.13 Distribution of the haptic cursor position: Results from the2nd participant

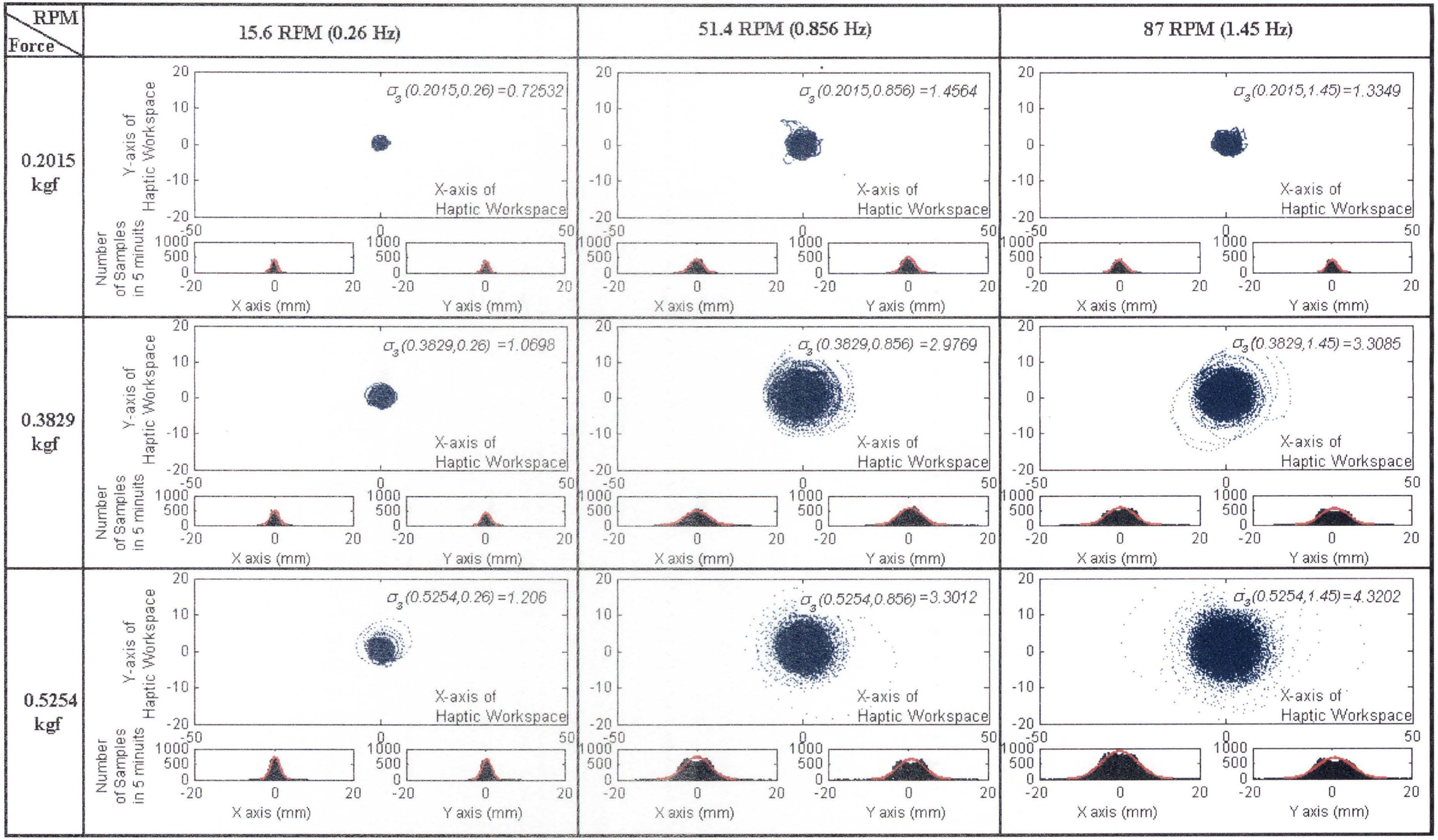

Figure 5.14 Distribution of the haptic cursor position: Results from the3rd participant

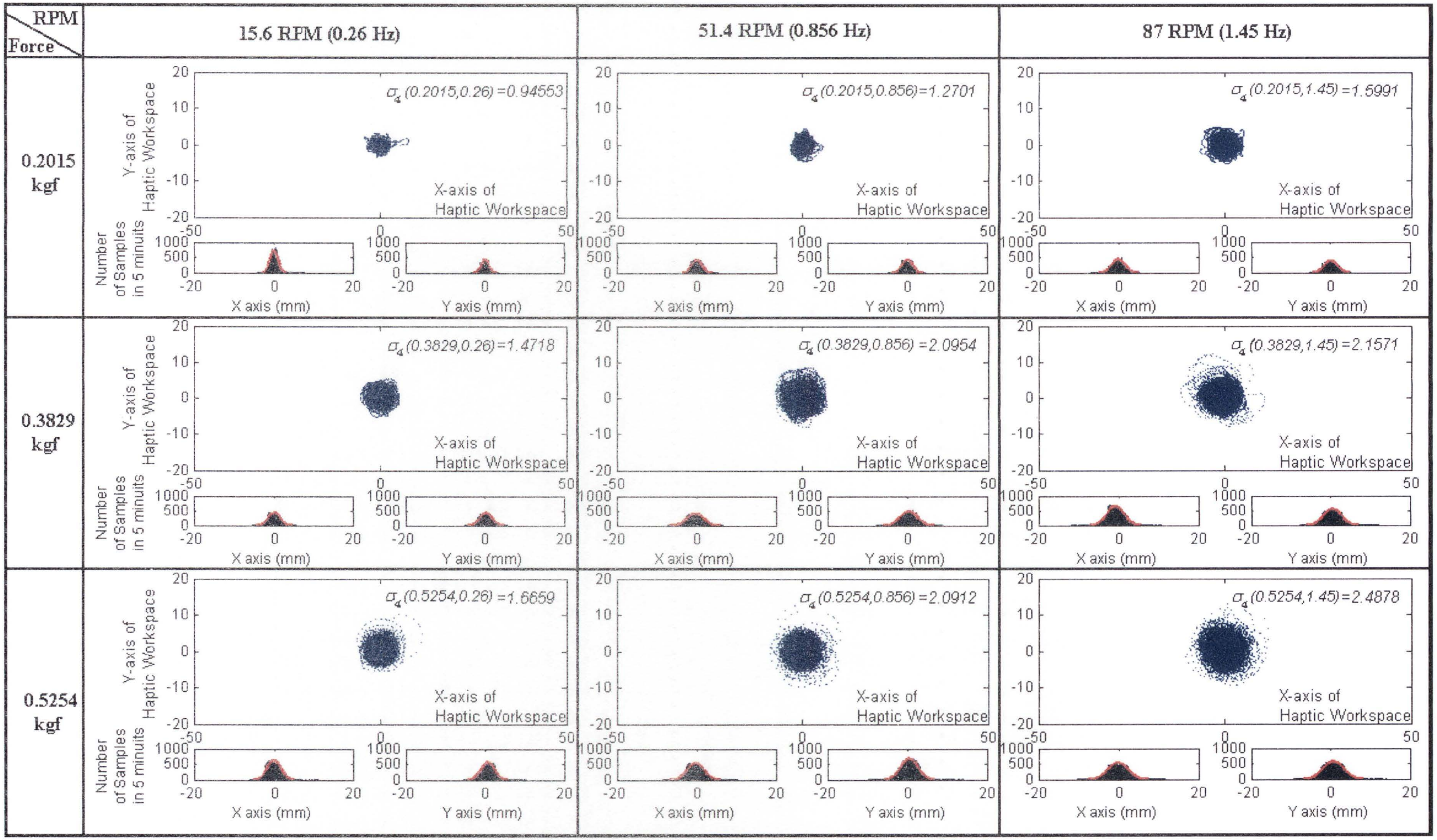

Figure 5.15 Distribution of the haptic cursor position: Results from the4th participant

RPM Force	15.6 RFM (0.26 Hz)	51.4 RPM (0.856 Hz)	87 RPM (1.45 Hz)
0.2015 kgf	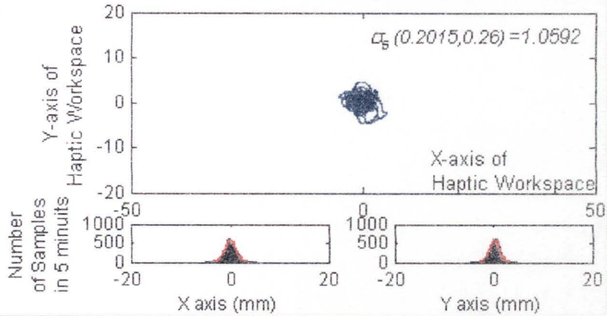	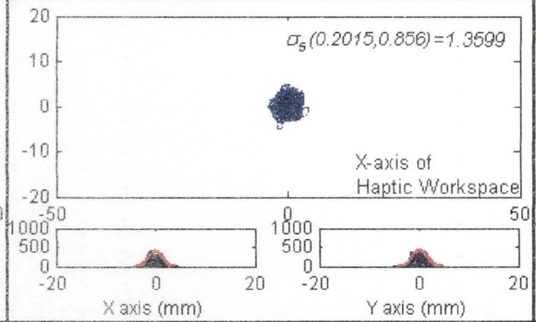	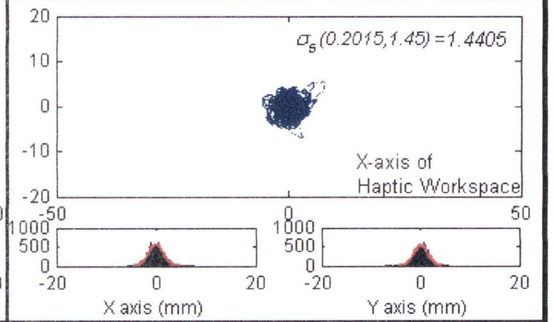
0.3829 kgf	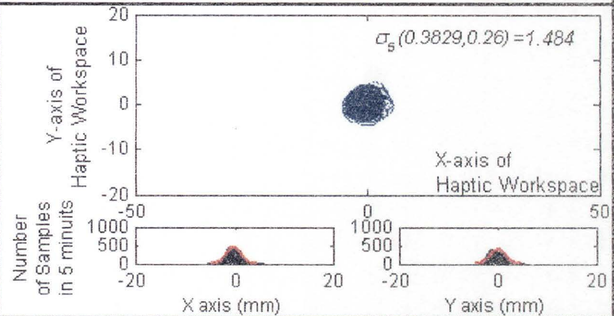	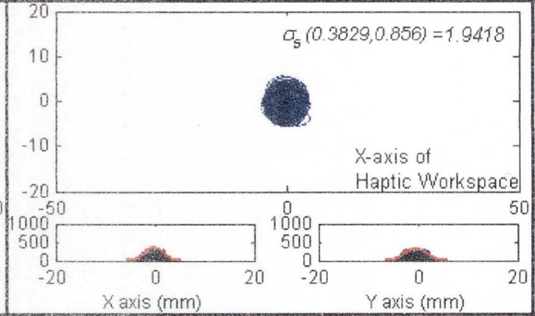	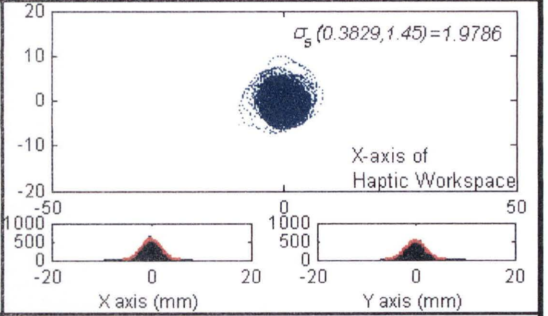
0.5254 kgf	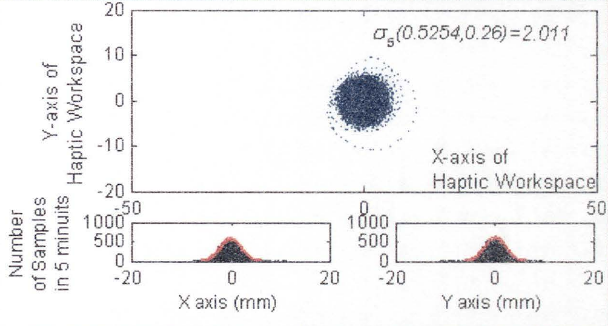	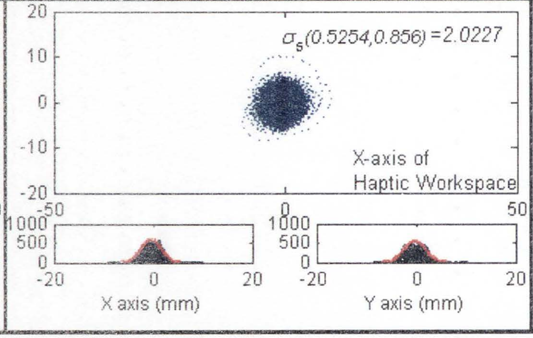	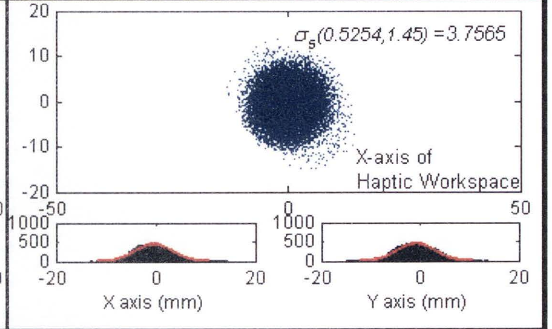

Figure 5.16 Distribution of the haptic cursor position: Results from the5th participant

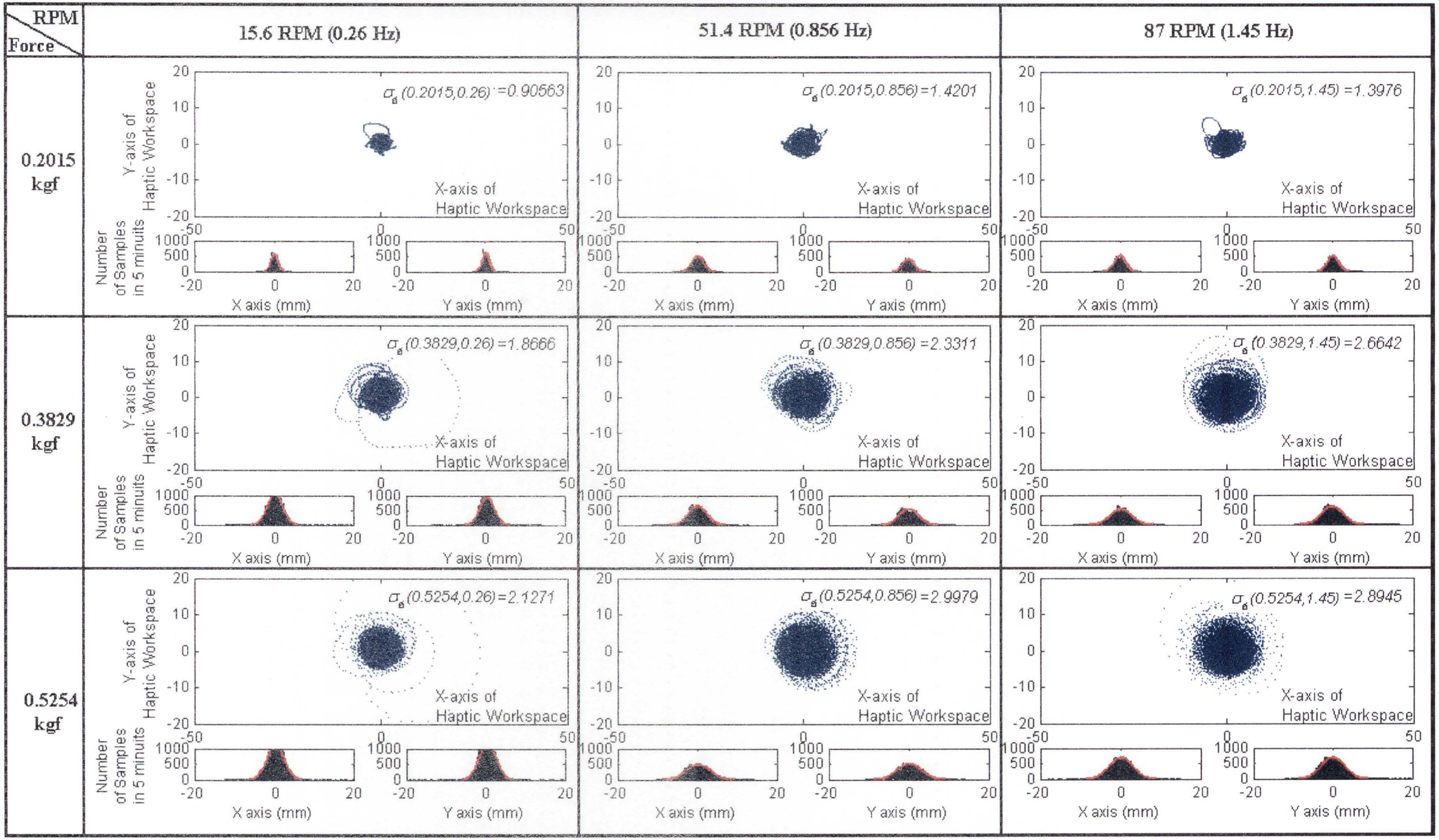

Figure 5.17 Distribution of the haptic cursor position: Results from the6th participant

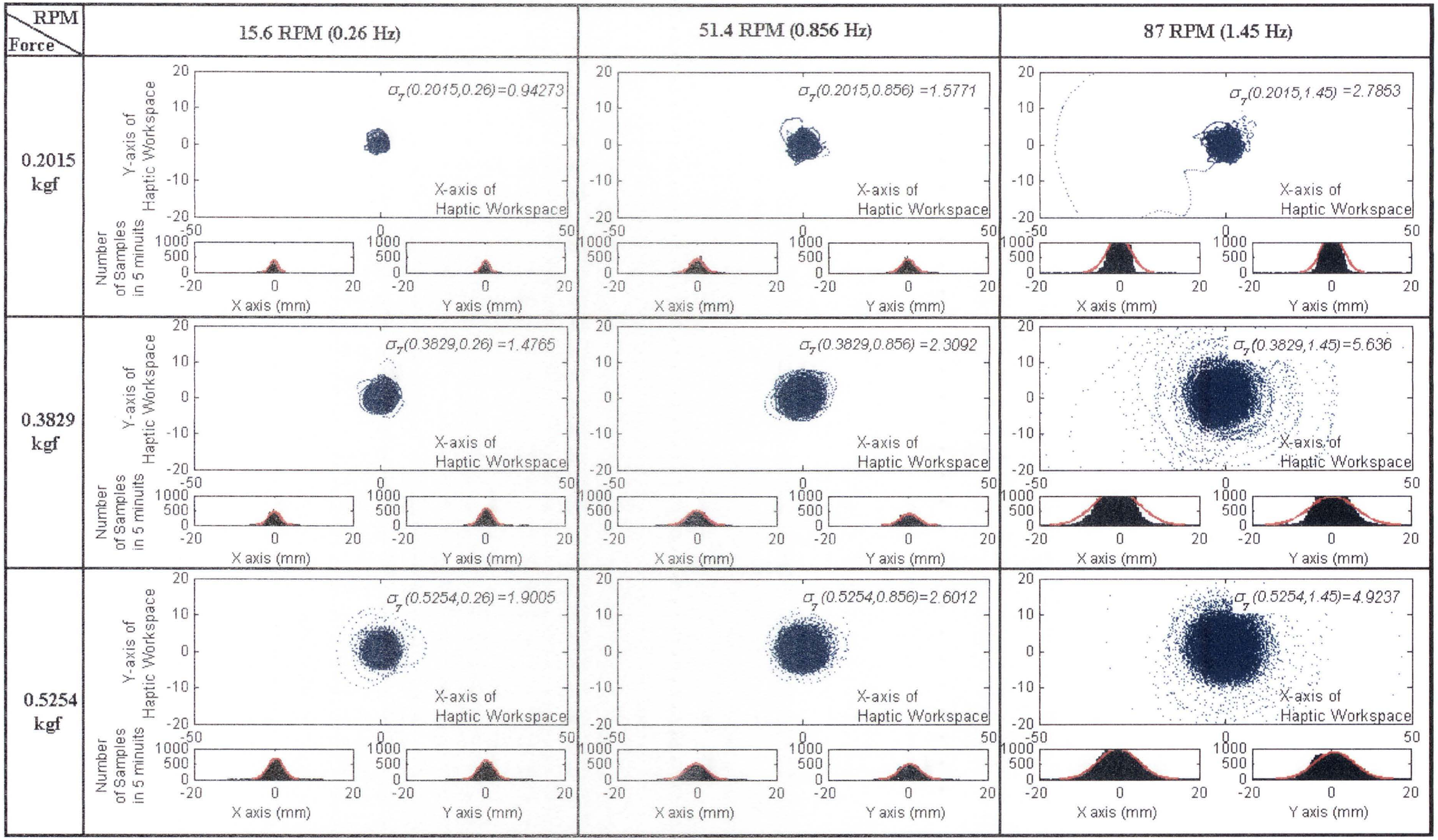

Figure 5.18 Distribution of the haptic cursor position: Results from the7th participant

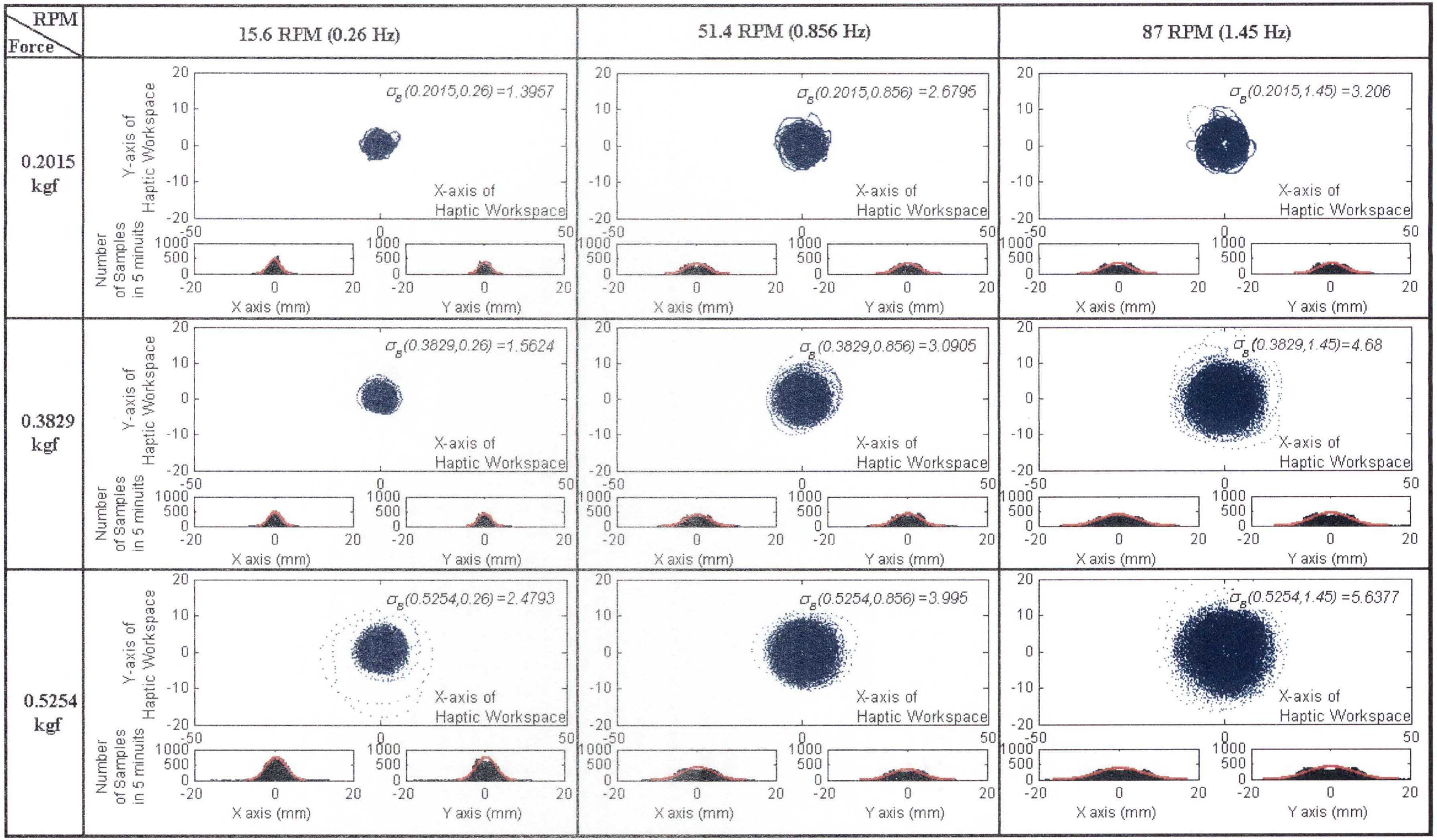

Figure 5.19 Distribution of the haptic cursor position: Results from the8th participant

The data in Table 5.4 has been tested by the two-way ANalysis Of VAriance (ANOVA). ANOVA is a common statistic tool that is used to test the hypothesis of what factors (i.e. the Haptic Force; F_h and the Angular Speed;ω) affect the outcome (i.e. the standard deviation of the haptic cursor distribution;σ). The ANOVA table identifies the effect of the haptic force and the rotating speed of the rotating point on the standard deviation σ (i.e. pointing accuracy). The ANOVA results in Table 5.5 show that there is no significant indication to reject the hypothesis that the standard deviation of the haptic cursor distribution (σ) depends on the haptic force and the angular speed of the rotating virtual spring.

Table 5.5 ANOVA table of standard deviation (σ)of the haptic cursor position distribution

Source	SS	df	MS	F	Prob>F
Haptic Force (F_h)	8.7557	2	4.37787	35.95	0
Angular Speed (ω)	8.1075	2	4.05376	33.28	0
Interaction (F_h ω)	1.0332	4	0.25831	2.12	0.0886
Error	7.6728	63	0.12179		
Total	25.5693	71			

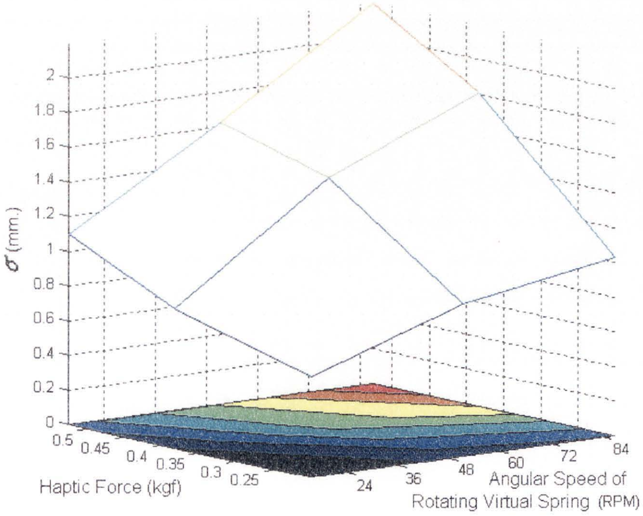

Figure 5.20 Average of standard deviation of all participants

Figure 5.20 shows the relationship between the standard deviation (σ) of the haptic cursor position distribution, haptic force (F_h), and angular speed (ω) of the rotating point. Based on the test results, a function $\sigma = Q(F_h, \omega)$ is obtained by the linear regression method (i.e. the least square method):

$$\sigma = 2.3F_h\omega + 0.5675 \qquad \text{unit of mm.} \tag{5.17}$$

where F_h is the amplitude of haptic force in units of kgf, ω is the angular speed of the rotating point with units of radian/sec. More generally, the function of σ can be presented as

$$\sigma = \hat{k}_{pw}F_h\omega + \sigma_0 \qquad \text{unit of mm.} \tag{5.18}$$

and for linear movement, the function of σ is equivalent to

$$\sigma = k_{pw}F_h v_a + \sigma_0 \qquad \text{unit of mm.} \tag{5.19}$$

where k_{pw} is the coefficient of power expense in the haptic interaction. The power expense is the power that the haptic device consumes while it is operated. This power is related to the power that the operator experiences. For this experiment setup (the radius is 0.3 m) the Equation 5.17can be reformed as

$$\sigma = 0.00767F_h v_a + 0.0005675 \qquad \text{unit of m.} \tag{5.20}$$

This equation shows the relationship between the standard deviation of the haptic cursor position and the haptic force and hand movement speed. It is obtained from the experiments with eight participants each undertaking nine tests. This function will be applied in the next section in the development of a hand movement model.

5.3.3 Extended Hand Movement Model

From the hand movement model of the Steering law in Equation 5.14 where $\emptyset$ is a function of s, if the path-track width ($\emptyset$) is now constant, the hand movement model can be written as:

$$MT = a + b\frac{s}{G_x(\emptyset - Z_{ac}\sigma)} \tag{5.21}$$

where *MT* consists of the start/stop time (a) and the movement time which is calculated from $b\frac{s}{G_x(\emptyset-Z_{ac}\sigma)}$. Thus the average speed of the haptic cursor (v_a) can be calculated from $\frac{s}{MT-a}$ and defined as from Equation 5.21

$$v_a = \frac{G_x(\emptyset-Z_{ac}\sigma)}{b} \tag{5.22}$$

When the standard deviationσin Equation 5.22 is replaced by the function of σ in Equation 5.19, the extended hand movement model (XHM) is defined by

$$v_a = \frac{\emptyset-Z_{ac}\sigma_0}{b/G_x+Z_{ac}k_{pw}F_h} \tag{5.23}$$

For example, if the accuracy requirement is 4σ(95.4% pointing accuracy), then $Z_{ac} = 4$,i.e. between $-2\sigma$and 2σ, the two-side probability of normal distribution is 0.954 and σ is equal to $2.3F_h\omega + 0.5675$. From an experiment shown in Appendix B, the operator hand speed b is obtained as 0.1958 and G_x is 1. Thus, the extended hand movement model is:

$$v_a = \frac{\emptyset-0.0023}{0.1958+0.0306F_h} \text{ unit of m/s ; for 95.4\% pointing accuracy} \tag{5.24}$$

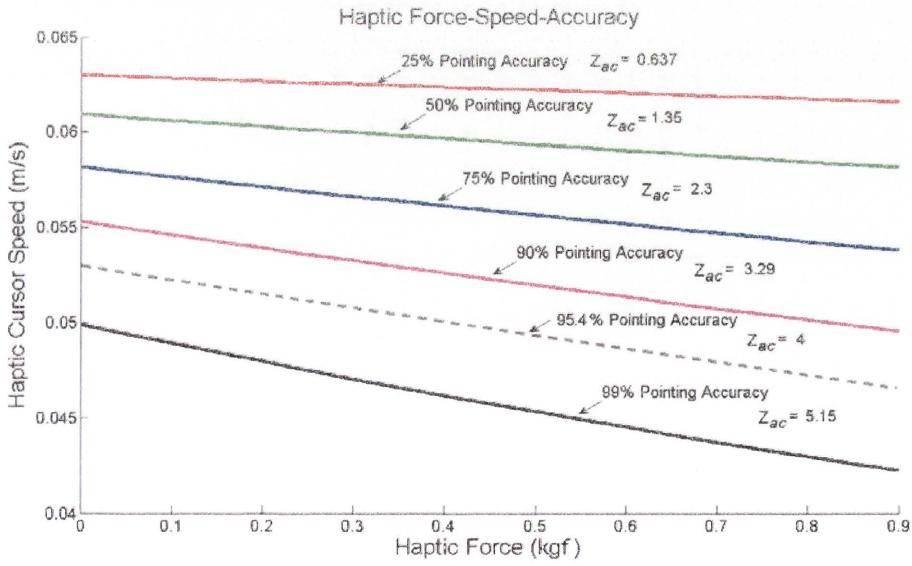

Figure 5.21 Haptic force-cursor speed (m/s) graph with different pointing accuracy,∅ = 12.7mm.

Figure 5.21 shows the extended hand movement model with different accuracy requirements. If the required accuracy of movement is low (e.g., 25%), the movement speed can be high. At the same level of accuracy, if a big force is needed, the movement speed is reduced. On the other hand, if the required accuracy of movement is high (e.g., 99%), the hand movement needs to be slow in order to achieve the accuracy. When an operator has to apply a force (including a haptic force) to move an object (which is similar to applying a haptic force to move a cursor of a haptic device), the operator normally moves slowly in order to ensure the movement is accurate. If the required force to move an object is small, the operator normally tries to move faster until the movement is found to be inaccurate, and the operator then reduces the speed of the movement.

5.4 Haptic Force-Speed Control Method

In order to improve the haptic-based HRI, the extended hand movement (XHM) model has been integrated into a Haptic Force-Speed Control (HFSC) method. Figure 5.22 shows two control diagrams: the control diagram of the haptic-based interaction system without the HFSC method (Figure 5.22a, from Section 4.2 and Figure 4.4) and the control diagram with the HFSC method (Figure 5.22b).

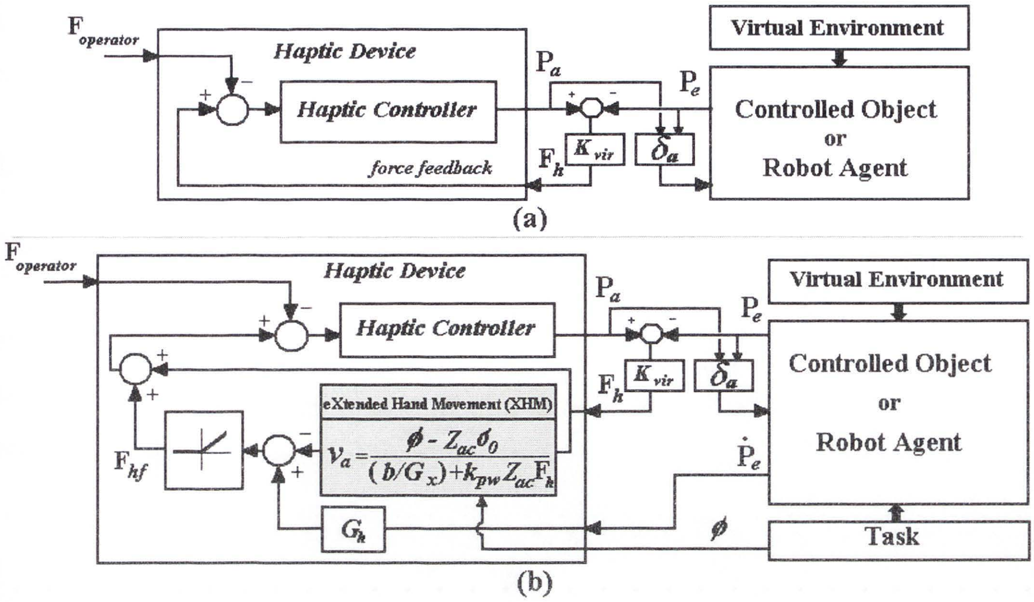

Figure 5.22 (a) Control diagram of haptic based interaction without HFSC, (b) Control diagram of haptic based interaction with HFSC

As shown in Figure 5.22b, in this HFSC method, the extended hand movement model is used to calculate a haptic speed (v_a) from an instant haptic force. The v_a is compared with the actual haptic cursor speed calculated by $G_h\ {}^0\dot{P}_e$. If $G_h\ {}^0\dot{P}_e$ is greater than v_a, the speed difference (i.e. $G_h\ {}^0\dot{P}_e - v_a$) is amplified and converted to force (F_{hf}) that is added into the haptic force. Because of this force addition, the movement of the operator's hand is subject to more resistance than usual. As a result, the speed of the operator's hand is reduced and therefore the point accuracy is increased. When the haptic force and the speed of the haptic cursor are controlled by the HFSC method, the control accuracy is increased to the desired accuracy as set by Z_{ac} in the XHM model.

To verify this HFSC control method, two experimental tests are conducted. In the first test, the haptic cursor (without a robot manipulator) is controlled to move on a 2D plane. The second test is conducted with the sandblasting robot that is required to follow a defined path on the surface of a wall. In order to reduce the redundancy in robot pose and joint force calculation, only the first three joints (Joints 1, 2, and 3) of the manipulator are controlled and the other three joints are set to rigid. The haptic force is generated by the virtual spring-based haptic force generation method (Section

4.2, Chapter 4). In both tests, the index of performance (*IP*) is measured and used to compare the improvement in performance.

5.4.1 Test 1: Steering Test in a Simple 2D Environment

5.4.1.1 Test Setup

In this test, the haptic cursor is represented by a circle with 3 mm diameter on the plane of the computer screen. The haptic cursor is pulled by a virtual spring force and controlled by an operator to follow a defined path track.

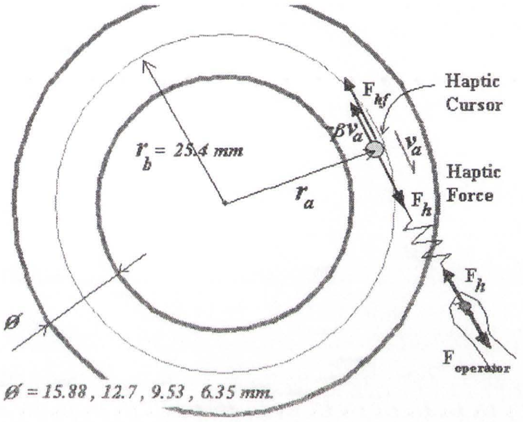

Figure 5.23 Steering test in a simple 2D environment

A circular testing track is drawn on the plane of the computer screen, as shown in Figure 5.23. The radius at the middle line of the track is 25.4 mm and the travelling distance (s) along the middle line is 159.6 mm. The track widths (ϕ) are varied in four different sizes in this test: 15.88 mm, 12.7 mm, 9.53 mm, and 6.35 mm.

The haptic cursor is assumed to move on a plane with resistance force. The resistance force is simulated as viscous damping force in this test, with two levels of force selected empirically: level 1 a low resistant force generated using damping coefficient of $\beta = 2$ kgf.sec/m, and level 2 a high resistant force with $\beta = 7$ kgf.sec/m .The haptic force, which is generated by the virtual spring, must be equal to or greater than the resistance force in order to move the haptic cursor. The virtual spring stiffness is set to be 300 kgf/m; therefore, in order to generate a force that is less than the maximum force the haptic device can provide (0.7 kgf) (Section 5.3.2.2, Figure 5.10), the elongation of the virtual spring will be no greater than 0.0023m.For the control scale, G_x is set to be 1 to normalise the control scale parameter. Four people participated in this experimental test. Each participant conducted sixteen tests: i.e. 4 (four track widths) * 2 (two resistance forces (related to the two levels of resistant force) * 2 (two control methods: with or without the HFSC method) = 16 tests. Each participant is asked to move the haptic cursor along the circular track repeatedly for one minute. The position and speed of the haptic cursor and the haptic force are recorded in each test.

5.4.1.2 Testing Result

Four males between 25 and 35 years old are selected to participate in this experiment. Figures 5.24 to 5.31 show the results of one participant in the sixteen experiments. Each figure has three graphs: the top graph shows the recorded data of the haptic cursor speed and the haptic force from the experiments with (in green) and without (in red) the HFSC method; the middle and bottom graphs show the records of $\boldsymbol{r}_a$ (cursor position from the centre of the path track) and σ obtained from the experiments with and without the HFSC method. From the speed-force graph, the distribution of speed and force data is changed from red dots to green dots when the HFSC is used. Lines of 25% and 99% pointing accuracy, which are from the XHM (Equation 5.23 Section 5.3.3),are given to present the improvement by the HFSC.

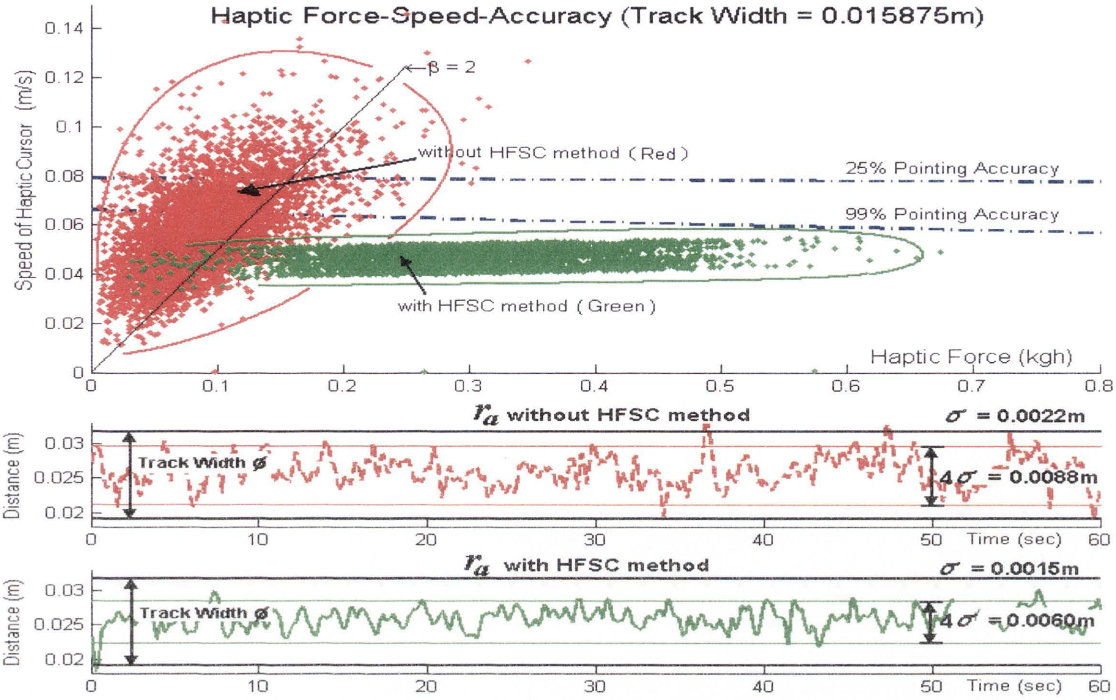

Figure 5.24 Results of steering test with 15.9mm track width and low resistant force (level 1); standard deviations (σ) are 2.2mm and 1.5mm for tests with (green) and without (red) the HFSC method.

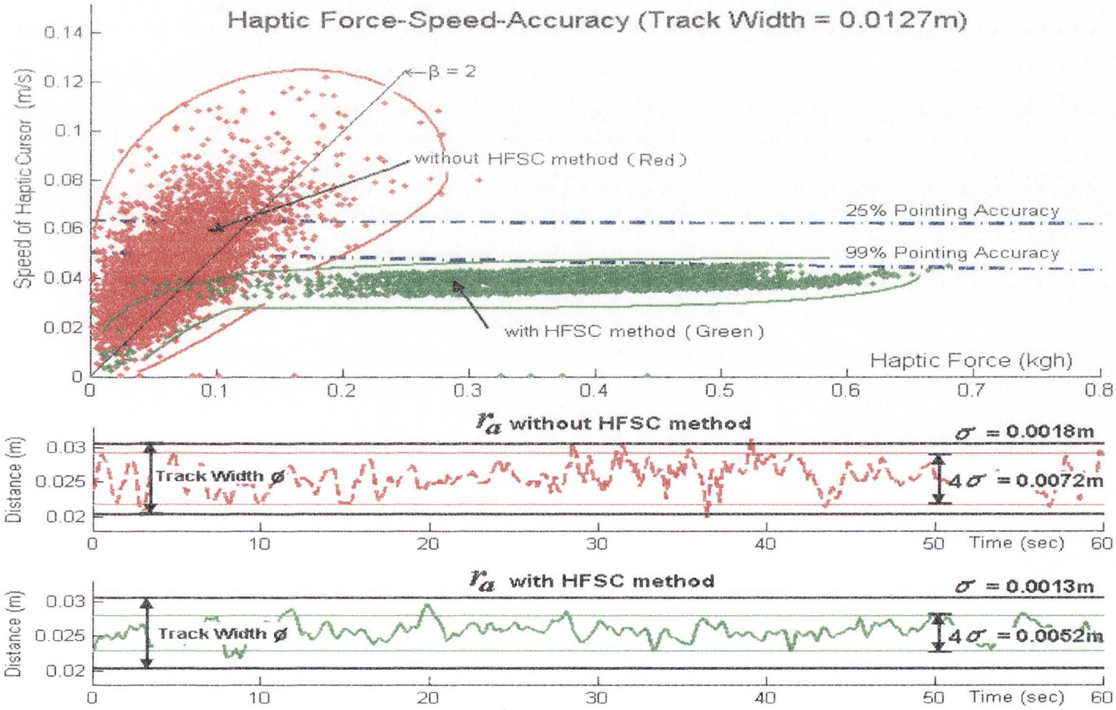

Figure 5.25 Results of steering test with 12.7mm track width and low resistant force (level 1); standard deviation (σ) are 1.8mm and 1.3mm for tests with (green) and without (red) the HFSC method.

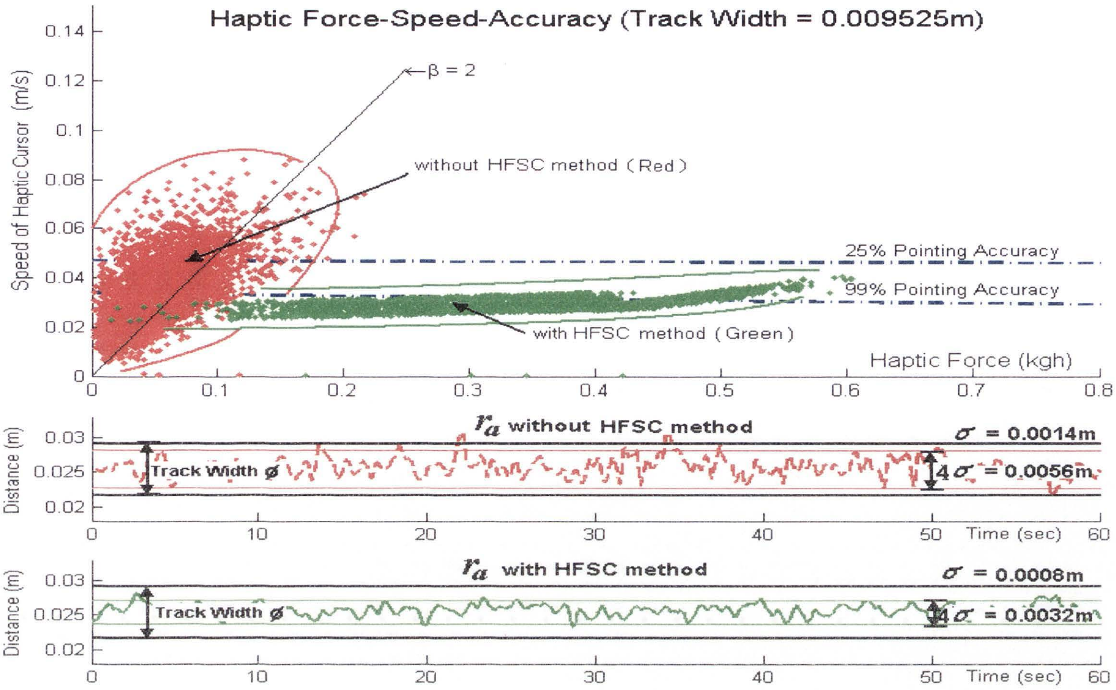

Figure 5.26 Results of steering test with 9.53mm track width and low resistant force (level 1); standard deviation (σ) are 1.4mm and 0.8mm for tests with (green) and without (red) the HFSC method.

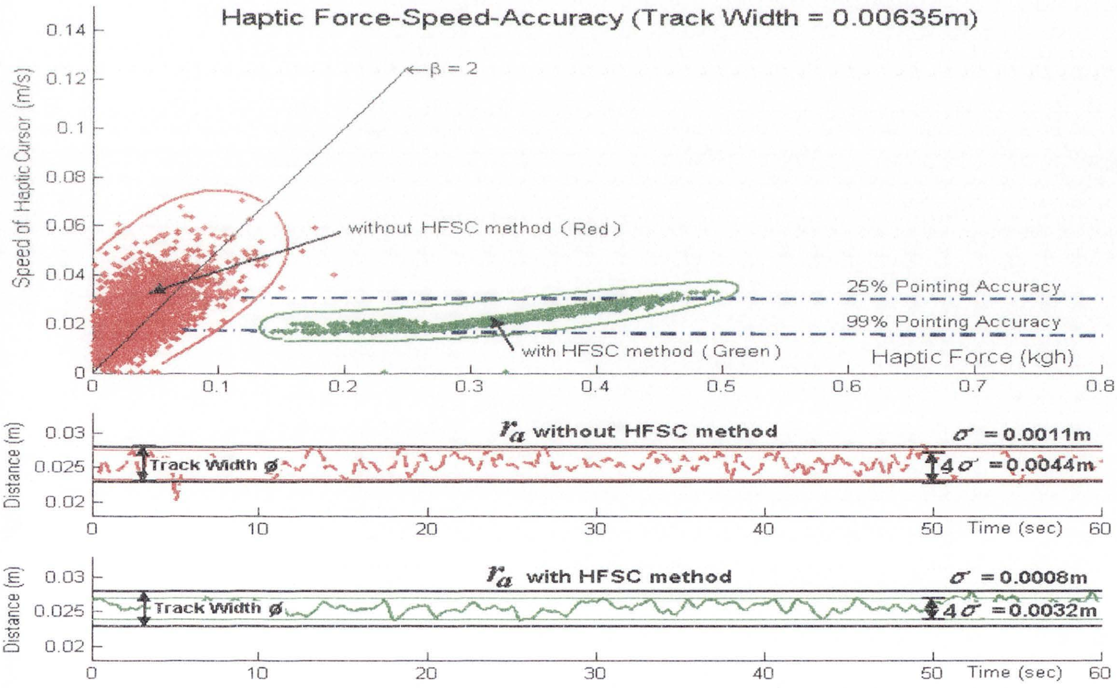

Figure 5.27 Results of steering test with 6.35mm track width and low resistant force (level 1); standard deviation (σ) are 1.1mm and 0.8mm for tests with (green) and without (red) the HFSC method.

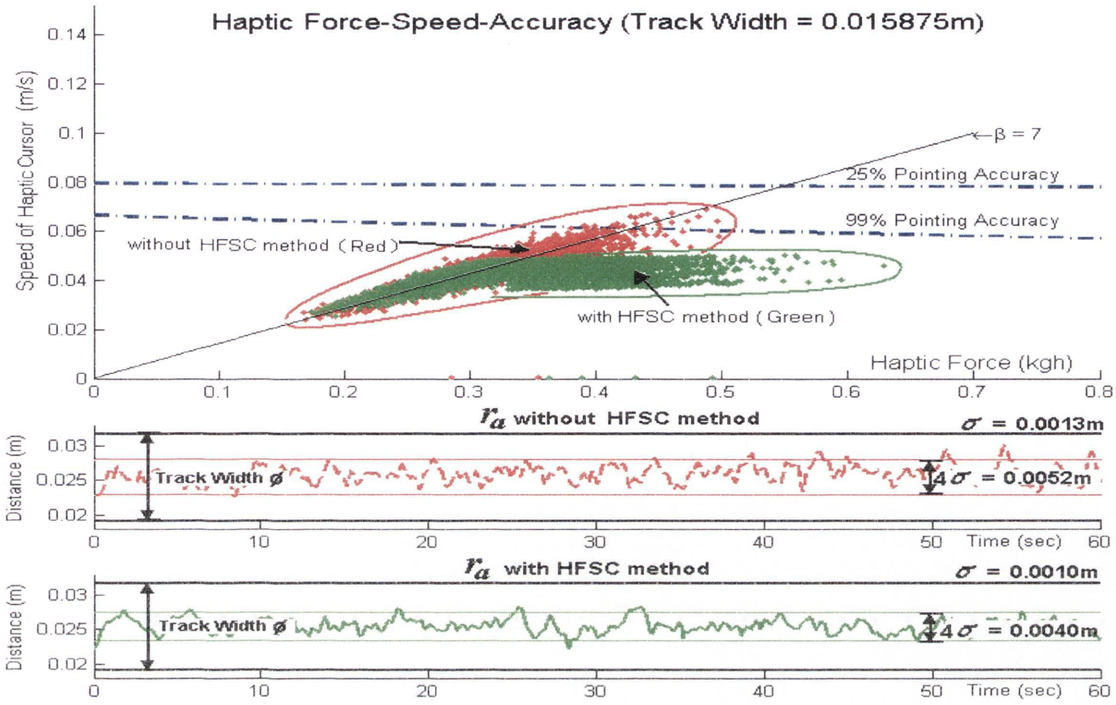

Figure 5.28 Results of steering test with 15.9mm track width and high resistant force (level 2); standard deviation (σ) are 1.3mm and 1.0mm for tests with (green) and without (red) the HFSC method.

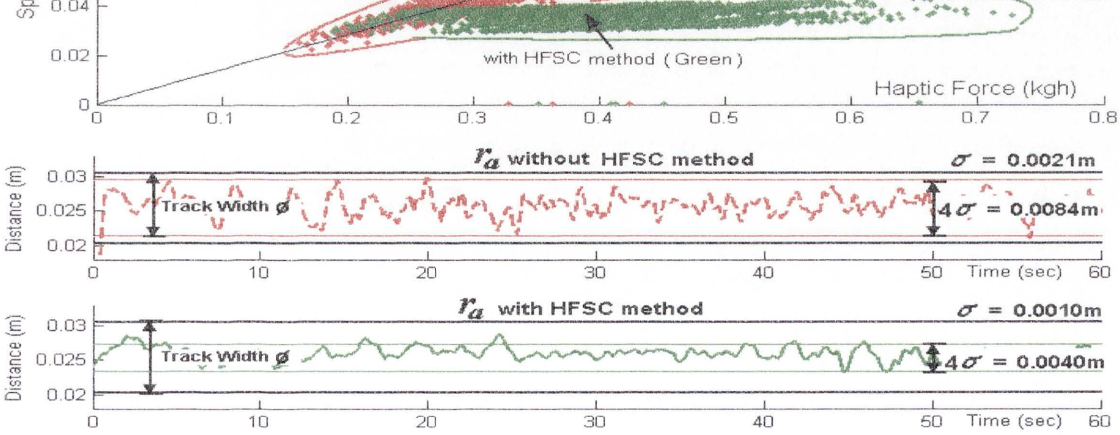

Figure 5.29 Results of steering test with 12.7mm track width and high resistant force (level 2); standard deviation (σ) are 2.1mm and 1.0mm for tests with (green) and without (red) the HFSC method.

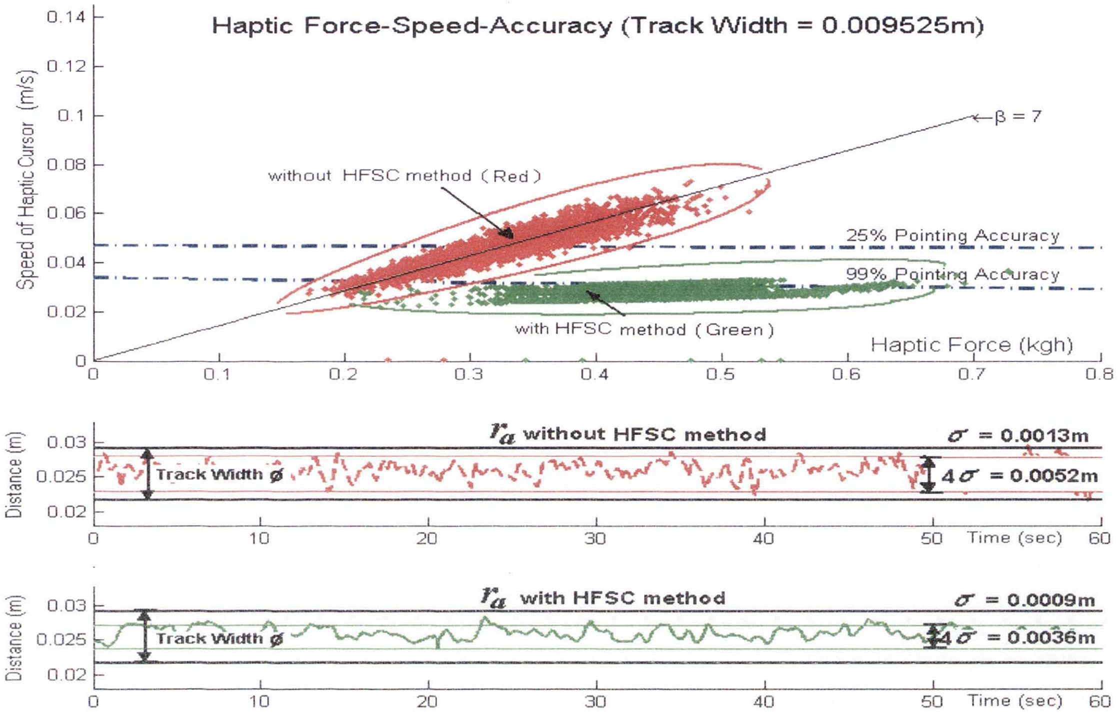

Figure 5.30 Results of steering test with 9.53mm track width and high resistant force (level 2); standard deviation (σ) are 1.3mm and 0.9mm for tests with (green) and without (red) the HFSC method.

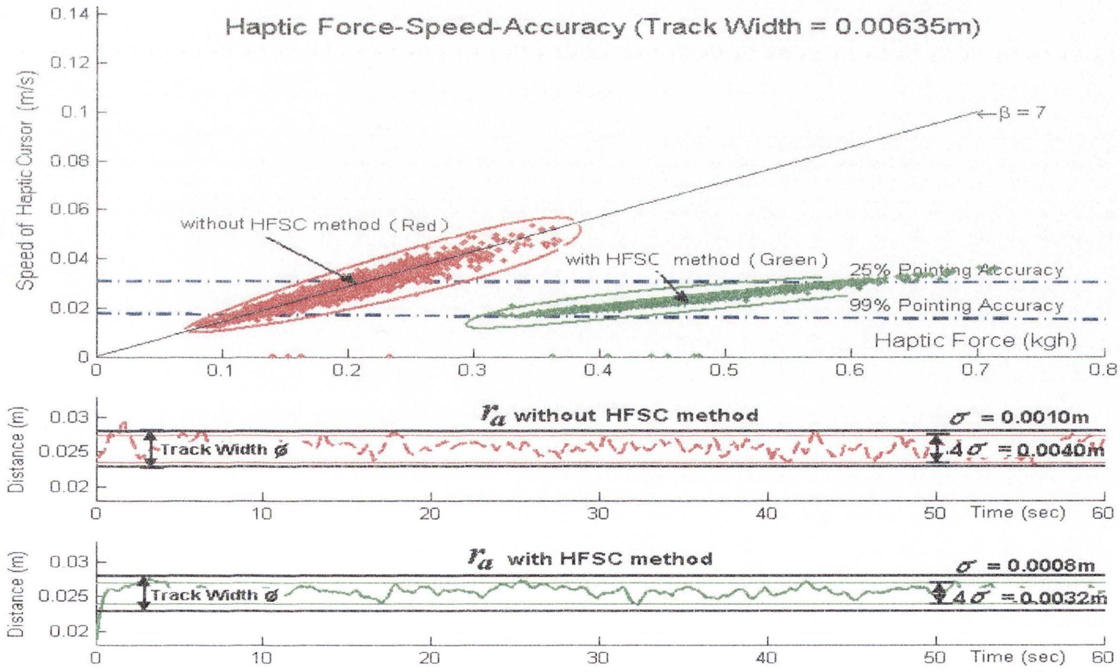

Figure 5.31 Results of steering test with 6.35mm track width and high resistant force (level 2); standard deviation (σ) are 1.0mm and 0.8mm for tests with (green) and without (red) the HFSC method.

From the graphs of the haptic cursor position, which is represented by $\boldsymbol{r}_a$, the standard deviations (σ) are significantly decreased by using the HFSC method. The decrease in the standard deviation (σ) means an increase in the pointing accuracy. The index of performance *IP,* which is calculated from Equation 5.4 in Section 5.1, is related to the speed, the pointing accuracy, and the standard deviation of $\boldsymbol{r}_a$. Table 5.6 and Figure 5.32 show the *IP* of each participant in each experiment, and the average *IP* of the four participants.

Table 5.6 Index of performance (*IP*) of the 4 participants in the test

		Index of Performance *IP*			
		without HFSC method		with HFSC method	
		Low Resistant Force (level 1)	High Resistant Force (level 2)	Low Resistant Force (level 1)	High Resistant Force (level 2)
ϕ=6.35mm	Participant 1	20.8	25	27. 1	28.2
	Participant 2	26	22.7	21	29.8
	Participant 3	21.5	25	25	34.8
	Participant 4	19.2	25.3	24.2	22.6
Average		21.875	24.5	23.4	28.85
ϕ=9.53mm	Participant 1	23.9	34.9	32.6	30.1
	Participant 2	32.5	24.2	28	35.1
	Participant 3	18.6	29.5	29.6	34.6
	Participant 4	29.2	28.2	26.8	28.4
Average		26.05	29.2	29.25	32.05
ϕ= 12.7mm	Participant 1	22.4	23.2	28.8	34.1
	Participant 2	31.2	30.4	28.3	25.9
	Participant 3	20.5	31.4	28.7	32
	Participant 4	28.4	27.8	25.5	21.4
Average		25.625	28.2	27.825	28.35
ϕ= 15.9mm	Participant 1	25.7	32.3	29.4	39.8
	Participant 2	36.2	43.4	27.1	41.9
	Participant 3	23.2	29	33.4	35.4
	Participant 4	17.9	34	28.7	21.3
Average		25.75	34.675	29.65	34.6

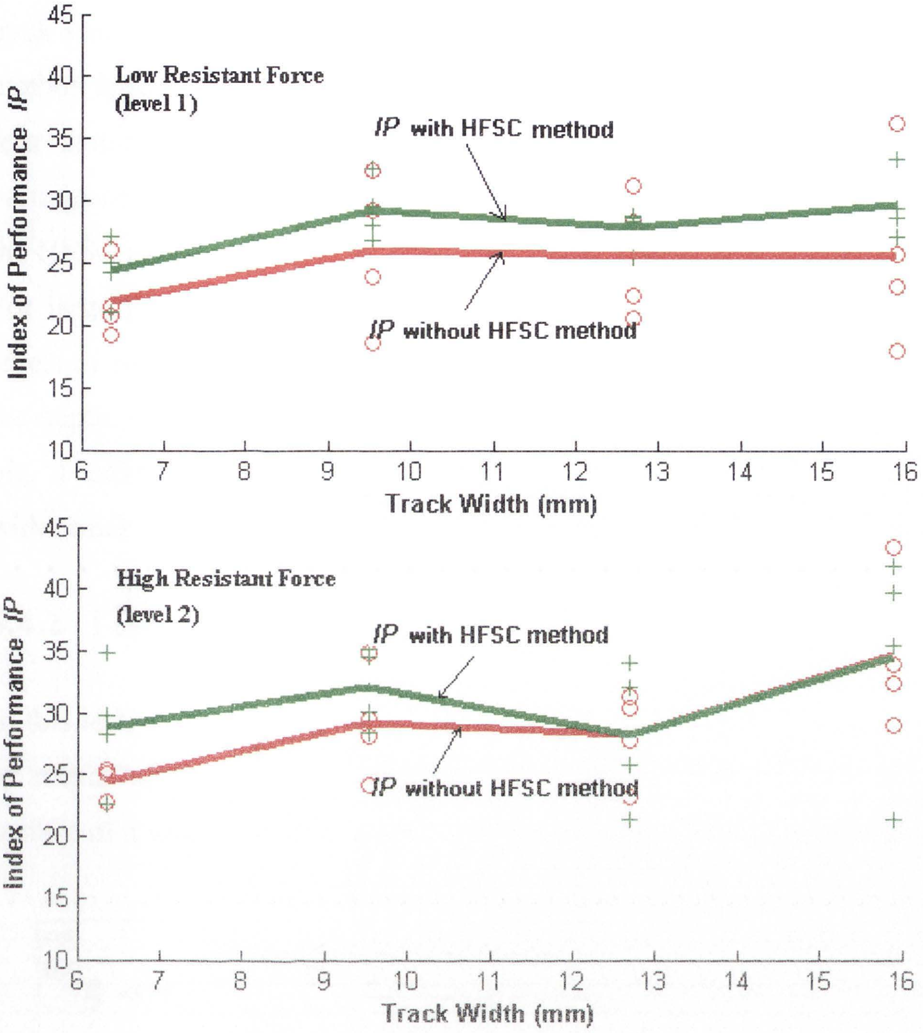

Figure 5.32 Index of performance with different resistance force, (a) at low resistant force (level 1), (b) high resistant force (level 2)

Figure 5.32 shows the overall index of performance and the averages of four participants from Table 5.6. When the resistance force is small (for example, with low resistant force), the average *IP* in different path track widths is higher (i.e. better performance) with the HFSC method than the average *IP* without the HFSC method. For example, with the track width of 15.9 mm, the average *IP* of the four participants with the HFSC method is 29.65, but the average *IP* of the four participants without the HFSC method is only 25.75. At big resistant force (for example level 2), when the path track is narrow, the average *IP* obtained with the HFSC method is better than the average *IP* without the HFSC method. For example, with the track width of 6.35 mm, the average *IP* of the four participants with the HFSC method is 28.85, but the average

IP of the four participants without the HFSC method is only 24.5. However, if the path track width is increased, the difference in the average *IPs* with and without the HFSC method is small. For example, with the track width of 15.9 mm, the average *IP* of the four participants with the HFSC method is 34.6, and the average *IP* of the four participants without the HFSC method is 34.675. Therefore, it can be concluded that the HFSC method can significantly improve performance in small the path-track width. For large path-track width, the improvement by the HFSC method is limited on all levels of resistance force. Increasing the resistance force can help operators to control the haptic cursor to be inside the path track. However, when the resistant force is too big, it makes it difficult to move the haptic handle and the haptic cursor even in the wider track.

5.4.2 Test 2: Steering Test with a Robot Manipulator

In this test, an operator controls the end-effector of the sandblasting robot manipulator by means of the Novint® haptic device to move along a circular path track on the surface of a wall. Figure 5.33 shows the setup of this experimental test

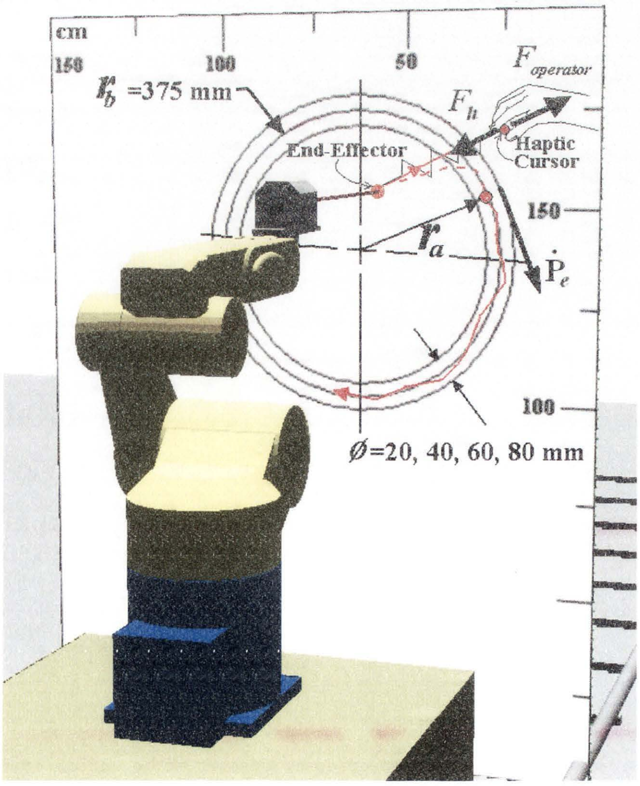

Figure 5.33 Test setup

5.4.2.1 Test Setup

Similar to the tests before, to reduce the redundancy in robot pose and joint force calculation, only the first three joints (Joints 1, 2 and 3) of the manipulator are controlled and the other three joints are set to rigid. Like Test 1, the resistant force in each of the thee joints is assumed to be viscous damping force. When operating in a real 3D environment, repulsive forces generated from the 3D-VF^2 method based on the obstacles are a kind of resistant force. All the damping forces in the three joints will affect the speed and displacement of the end-effector according to the dynamic model of the robot (Equation 3.10), and will consequently affect the haptic force according to the haptic force generation method presented in Section 4.2, Chapter 4.

Three levels of resistant force for the three joints are tested: level 1 - low level resistant force (for example, β_1= [0.2, 0.35, 0.35] N.m.sec/rad), level 2 - medium level resistant force (with β_2= [0.4, 0.7, 0.7] N.m.sec/rad), and level 3 - high level resistant force (with β_3= [0.8, 1.4, 1.4] N.m.sec/rad).The circular path track is set up on a vertical wall in front of the manipulator. The medium radius ($\boldsymbol{r_b}$) of the track is 375 mm and four track widths are used: 20 mm, 40 mm, 60 mm and 80 mm.

According to the recommended view distance (d_v =3 m) and scaling factor (k_{sc}=25) from Section 5.2, G_x is equal to 1.75 calculated from Equation 5.11 where screen size ($\emptyset_{scn}$) is equal to 0.3302 m and the field of view of the surveillance camera (α_v) is set to 40 degrees. The camera is located 22.4 degrees on the right-hand side of the testing task plane normal. Figure 5.33 shows the view that participants have from their viewpoint.

In this test, the participant controls the end-effector of the manipulator (the blasting spot) using the haptic device to move clockwise inside the circular path. The participant is required to move the blasting spot (similar to the cursor in Test 1) as close as possible to the middle line of the track and to keep it inside the track boundaries. The test period is one minute.

5.4.2.2 Testing Results

The position of the end-effector of the manipulator is represented by $\boldsymbol{r}_a$ and the speed of the end-effector of the manipulator is represented by $\dot{P}_e$ as shown in Figure 5.33. One participant is involved in this test and conducts 24 experiments: 4 (four path-track widths) * 3 (three levels of resistant force) * 2 (two control methods: with and without the HFSC method) = 24 experiments. The position and the speed of the end-effector and the haptic force are recorded in this test. The recorded data are shown in Figures 5.34 to 5.45. In each figure, the graph on the left-hand side shows the haptic force-end-effector speed distribution. The top-right graph presents the end-effector position, $\boldsymbol{r}_a$, obtained in the test without the HFSC method. The bottom-right graph presents $\boldsymbol{r}_a$ in the test with the HFSC method. The standard deviation (σ) of the end-effector position $\boldsymbol{r}_a$ is calculated and shown in the two right-hand graphs. Every σ of the 24 experiments are shown in Table 5.8.

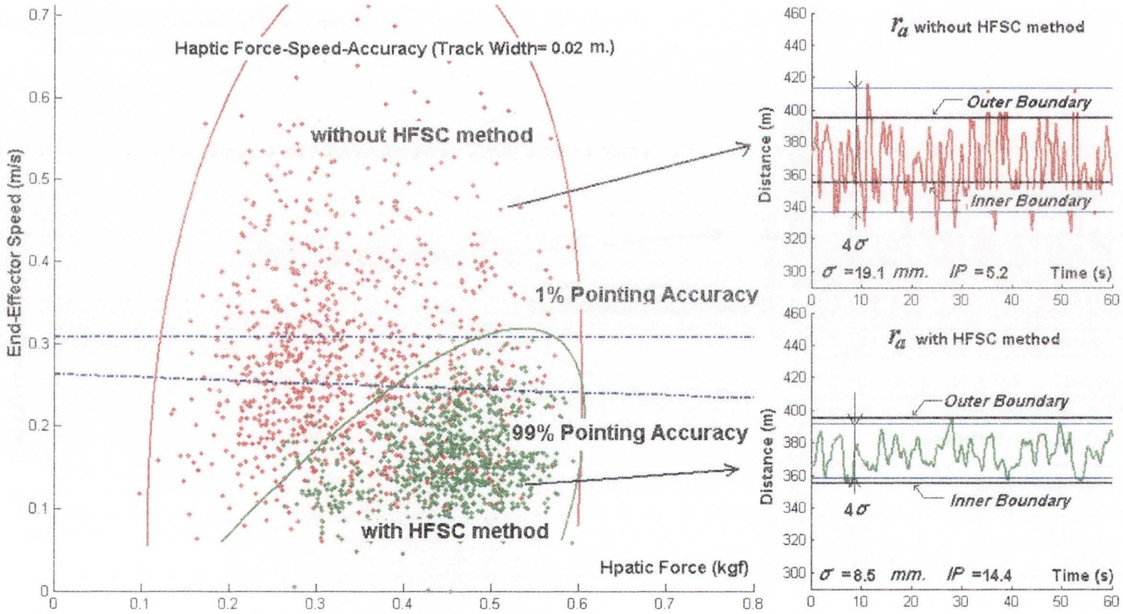

Figure 5.34 Results of steering test with a robot manipulator: low level resistant force (level 1) and 20mm track width. Left: haptic force - end-effector speed data; top right: end-effector position during the experiment without the HFSC method; bottom right: end-effector position during the experiment with the HFSC method

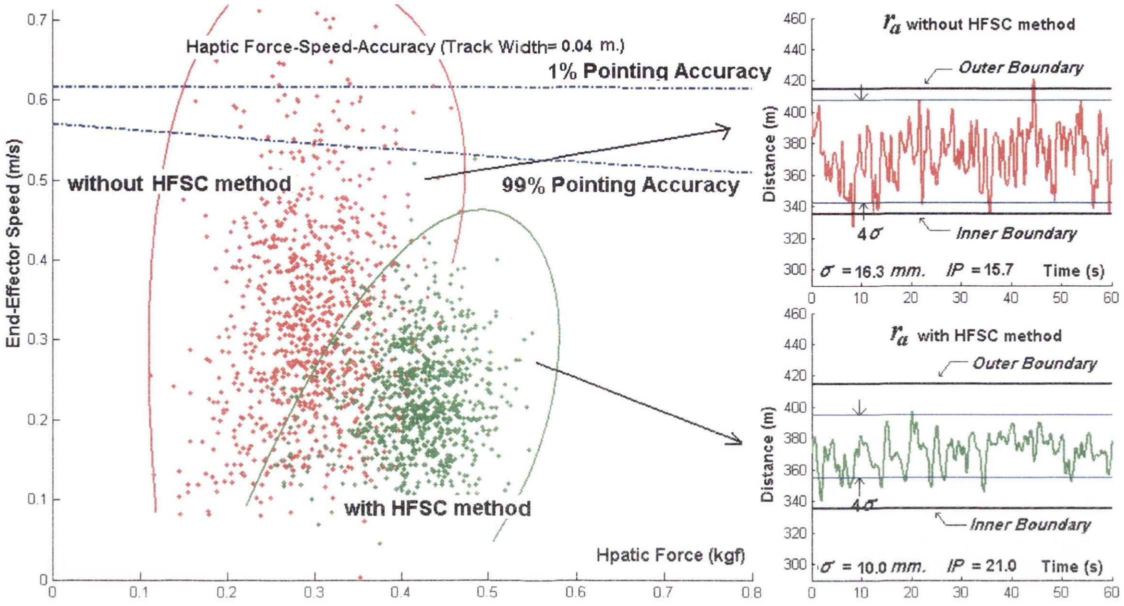

Figure 5.35 Results of steering test with a robot manipulator: low level resistant force (level 1) and 40mm track width. Left: haptic force - end-effector speed data; top right: end-effector position during the experiment without the HFSC method; bottom right: end-effector position during the experiment with the HFSC method

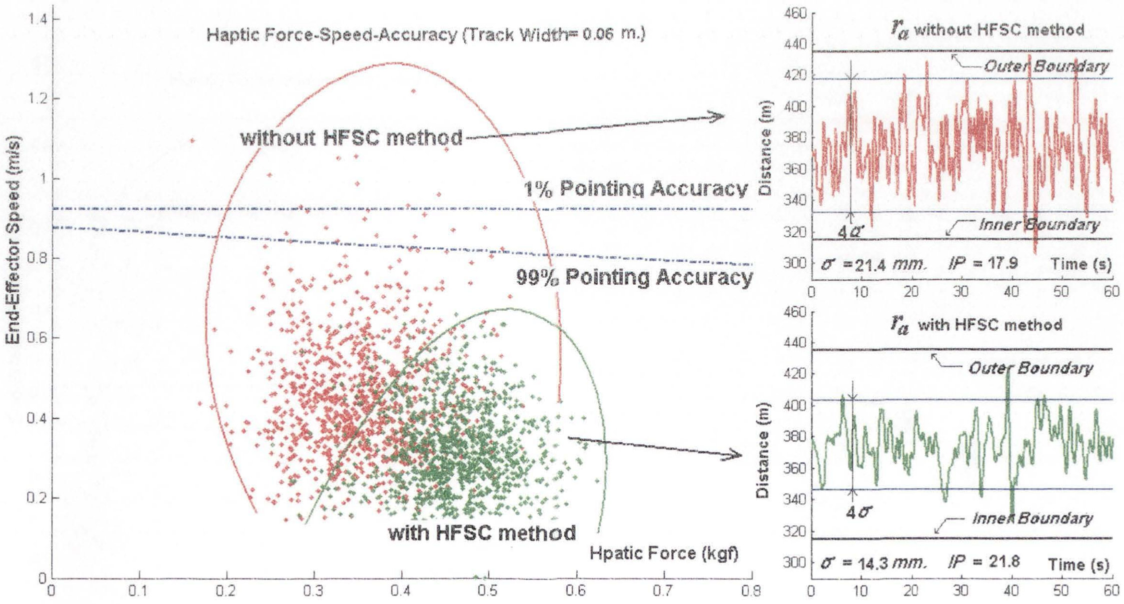

Figure 5.36 Results of steering test with a robot manipulator: low level resistant force (level 1) and 60mm track width. Left: haptic force - end-effector speed data; top right: end-effector position during the experiment without the HFSC method; bottom right: end-effector position during the experiment with the HFSC method

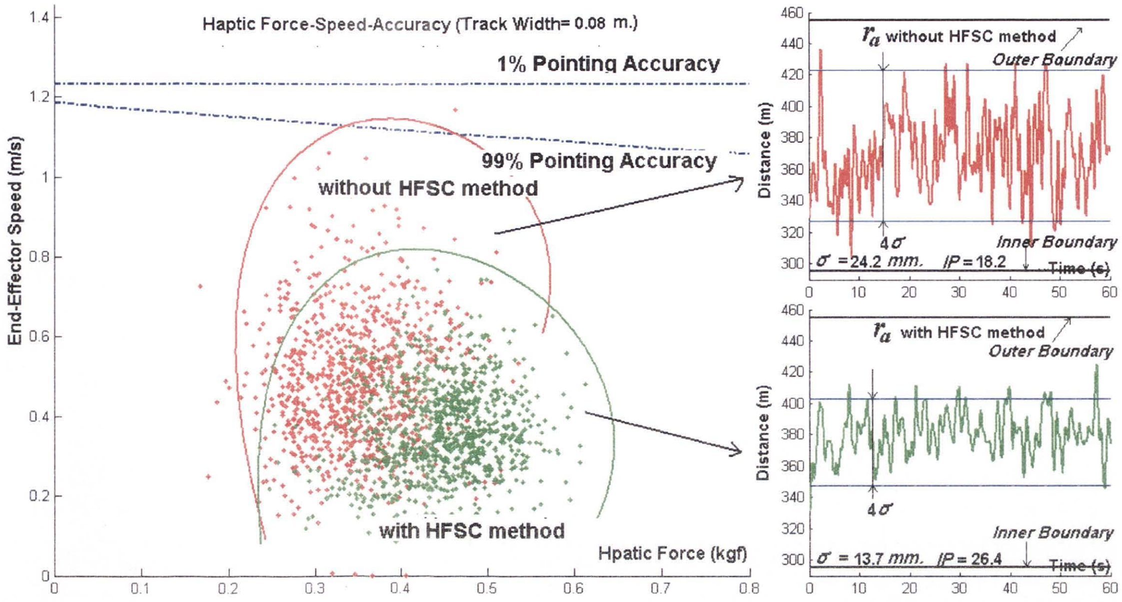

Figure 5.37 Results of steering test with a robot manipulator: low level resistant force (level 1) and 80mm track width. Left: haptic force - end-effector speed data; top right: end-effector position during the experiment without the HFSC method; bottom right: end-effector position during the experiment with the HFSC method

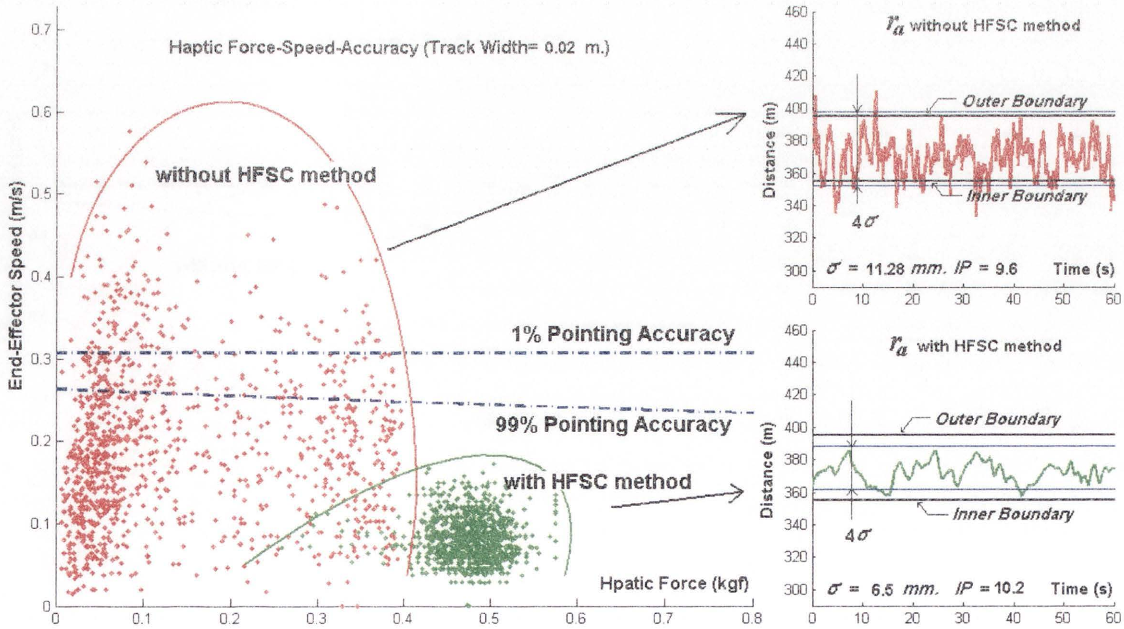

Figure 5.38 Results of steering test with a robot manipulator: medium level resistant force (level 2) and 20mm track width. Left: haptic force - end-effector speed data; top right: end-effector position during the experiment without the HFSC method; bottom right: end-effector position during the experiment with the HFSC method

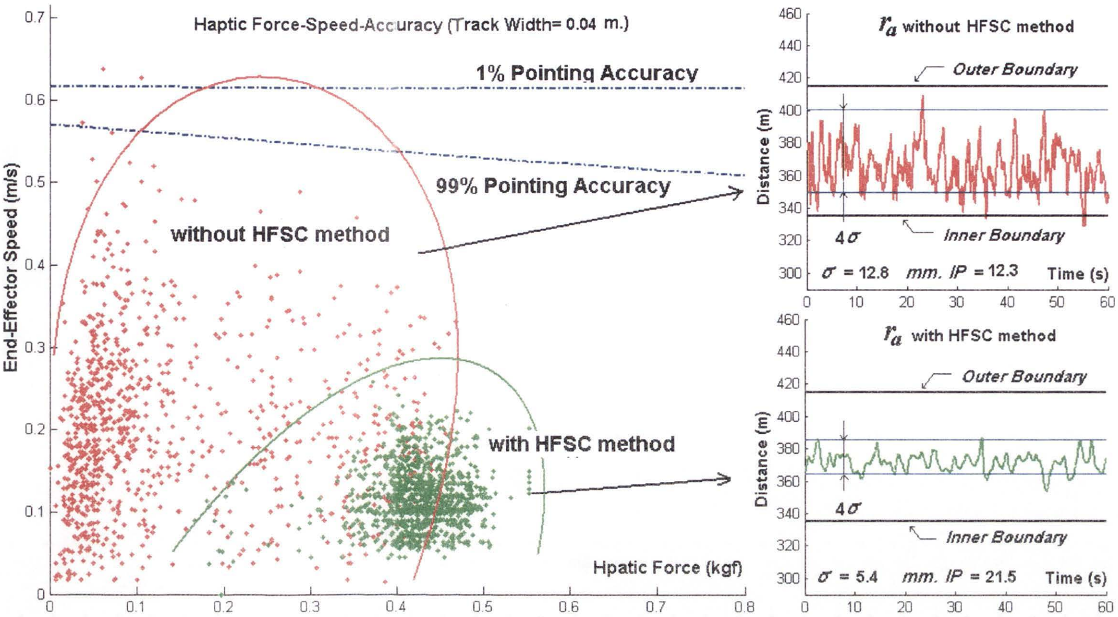

Figure 5.39 Results of steering test with a robot manipulator: medium level resistant force (level 2) and 40mm track width. Left: haptic force - end-effector speed data; top right: end-effector position during the experiment without the HFSC method; bottom right: end-effector position during the experiment with the HFSC method

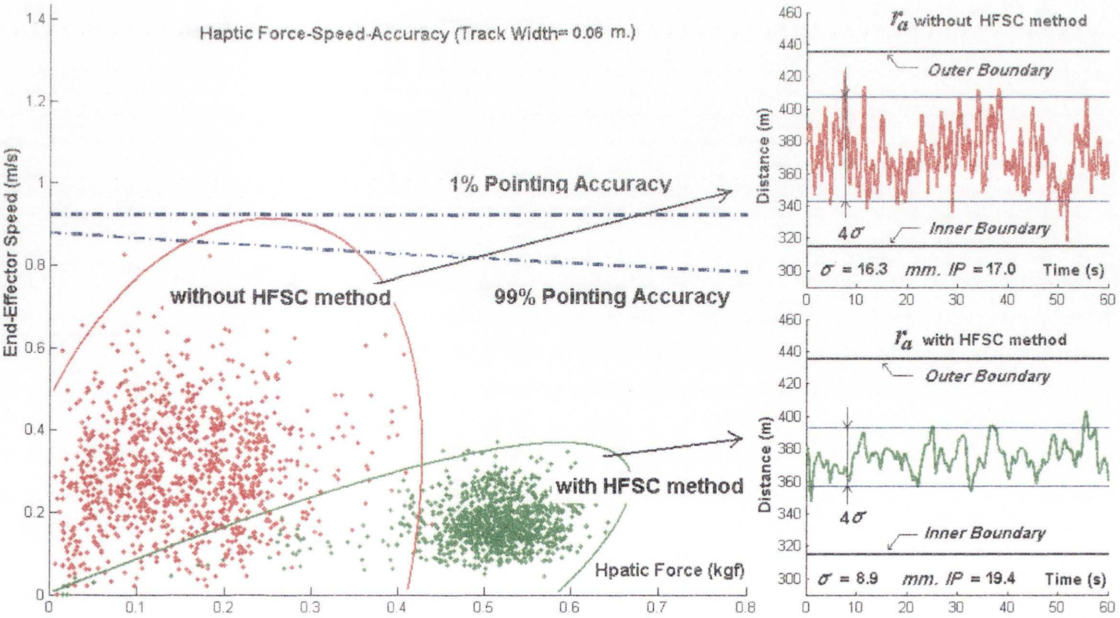

Figure 5.40 Results of steering test with a robot manipulator: medium level resistant force (level 2) and 60mm track width. Left: haptic force - end-effector speed data; top right: end-effector position during the experiment without the HFSC method; bottom right: end-effector position during the experiment with the HFSC method

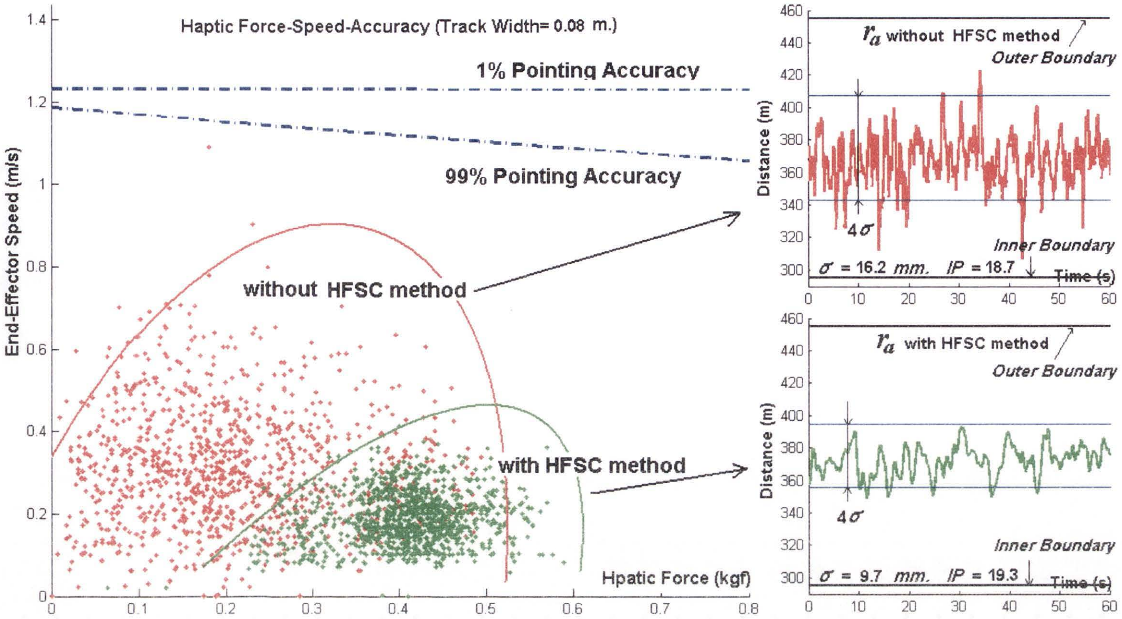

Figure 5.41 Results of steering test with a robot manipulator: medium level resistant force (level 2) and 80mm track width. Left: haptic force - end-effector speed data; top right: end-effector position during the experiment without the HFSC method; bottom right: end-effector position during the experiment with the HFSC method

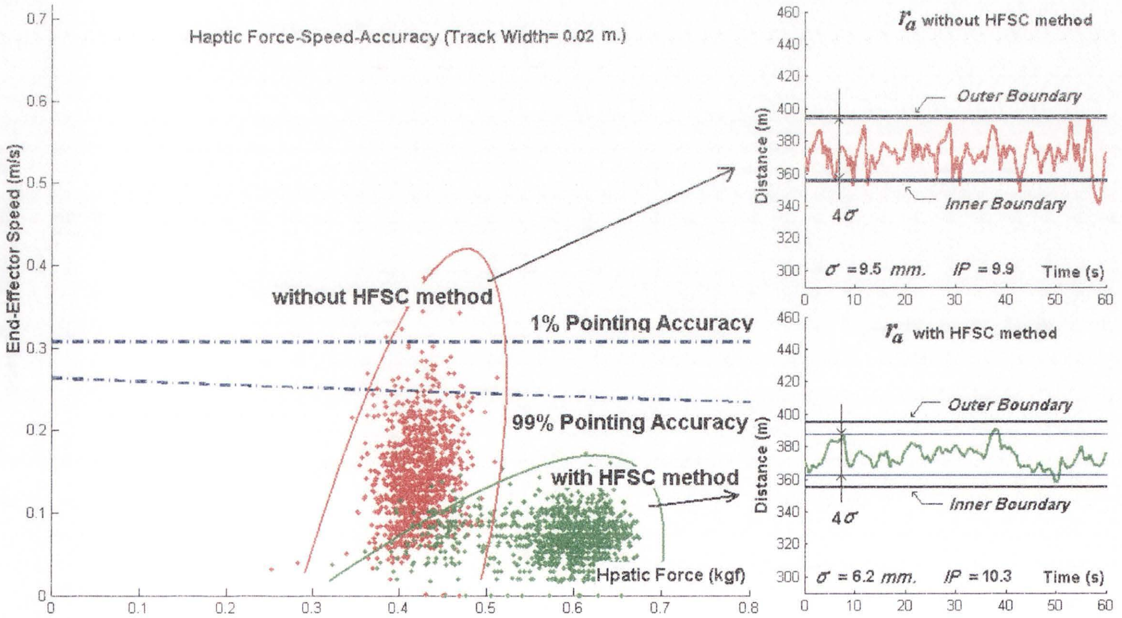

Figure 5.42 Results of steering test with a robot manipulator: high level resistant force (level 3) and 20mm track width. Left: haptic force - end-effector speed data; top right: end-effector position during the experiment without the HFSC method; bottom right: end-effector position during the experiment with the HFSC method

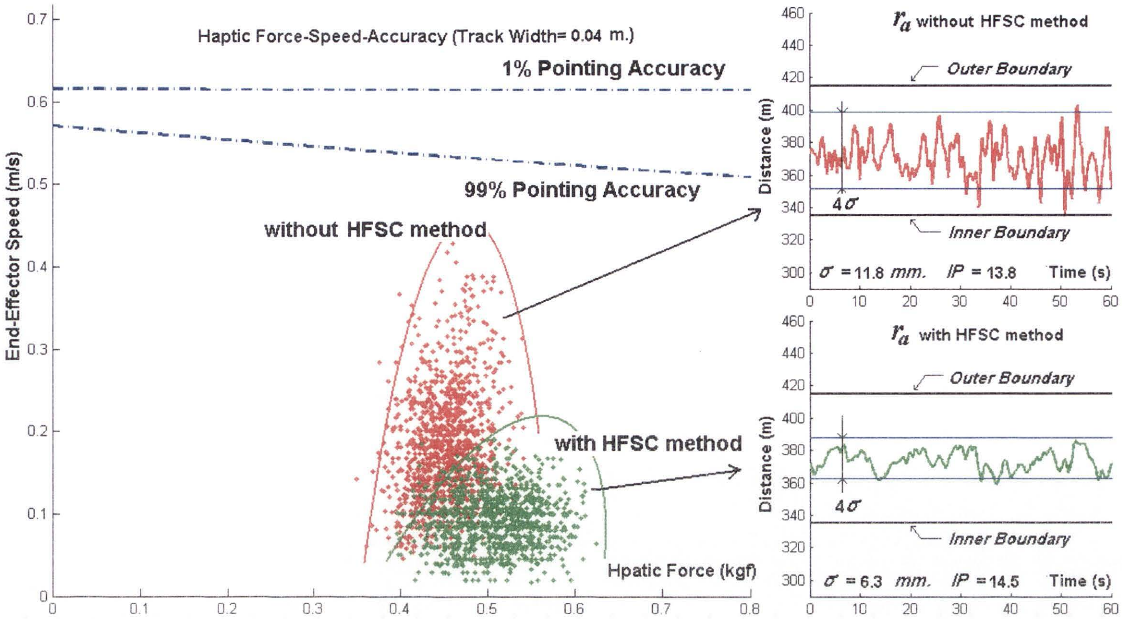

Figure 5.43 Results of steering test with a robot manipulator: high level resistant force (level 3) and 40mm track width. Left: haptic force - end-effector speed data; top right: end-effector position during the experiment without the HFSC method; bottom right: end-effector position during the experiment with the HFSC method

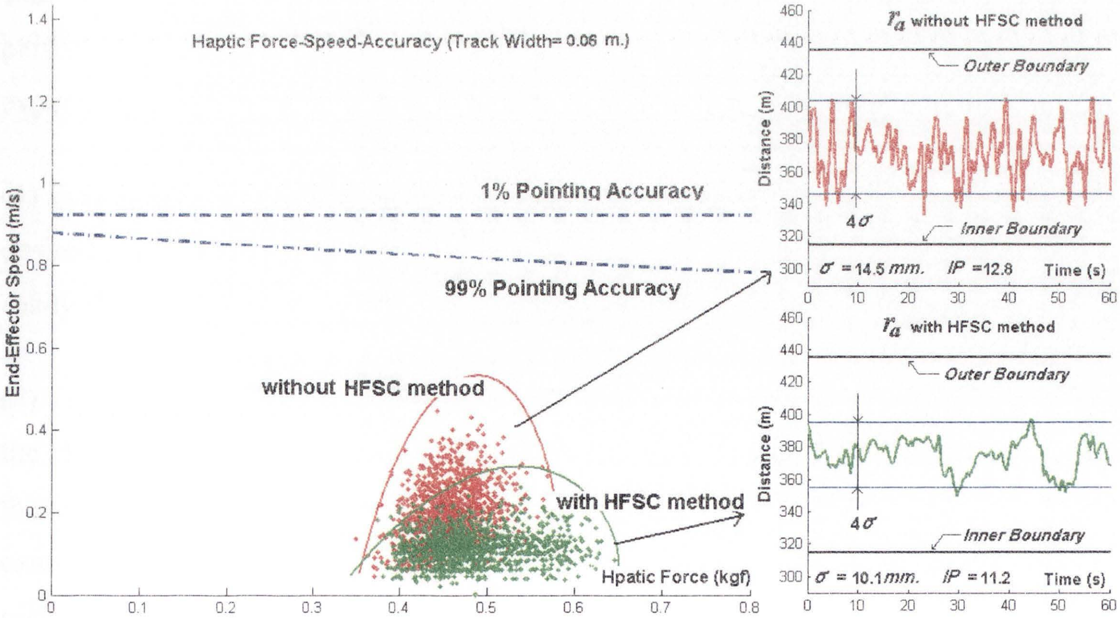

Figure 5.44 Results of steering test with a robot manipulator: high level resistant force (level 3) and 60mm track width. Left: haptic force - end-effector speed data; top right: end-effector position during the experiment without the HFSC method; bottom right: end-effector position during the experiment with the HFSC method

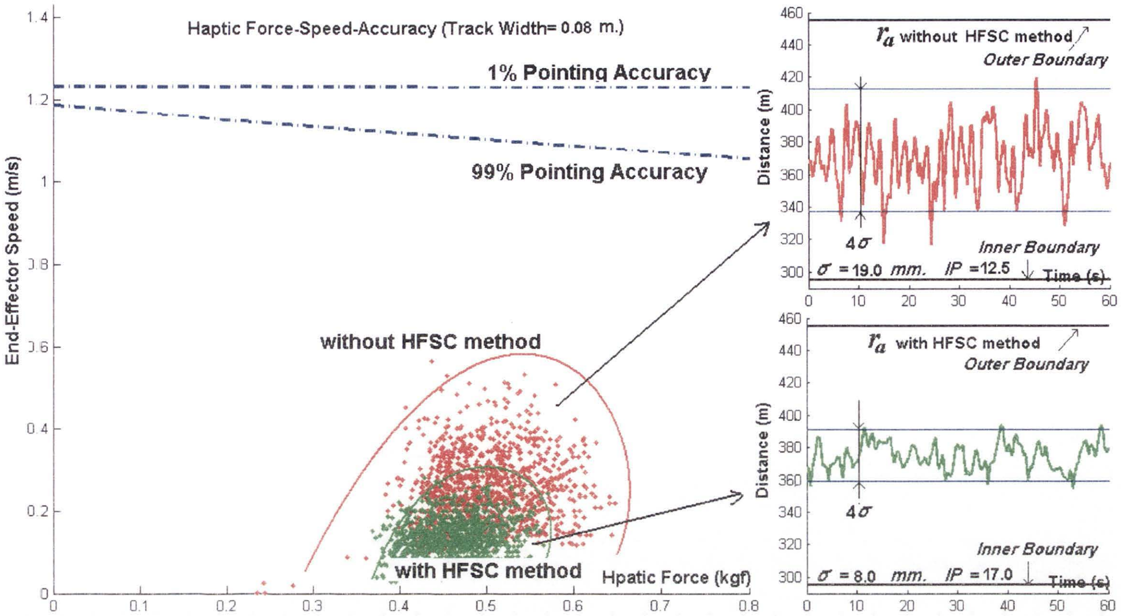

Figure 5.45 Results of steering test with a robot manipulator: high level resistant force (level 3) and 80mm track width. Left: haptic force - end-effector speed data; top right: end-effector position during the experiment without the HFSC method; bottom right: end-effector position during the experiment with the HFSC method

This test is repeated five times. Table 5.7 and Figure 5.46 show the index of performance (*IP*) calculated using Equation 5.4 in Section 5.1 in all 24*5(repeats)=120 experiments. It can be seen from these results that:

(1) Performance in the haptic-based HRI is increased when the path-track width of the desired task is getting wider, which enables the operator to control the robot more easily than in the narrow path-track width.

(2) The HFSC method helps operators to perform better than a system that does not use the HFSC method when the resistant force is not too high. The highest performance in the test occurs when the resistant force in the haptic-based HRI is low (level 1). For example, at d_v of 2 m, *IP* at low resistant force is about 15 while *IP* at medium and high resistant forces are around 10.

(3) At high resistant force, the HFSC method cannot help operators to improve their performance because at high resistant force, the haptic cursor speed (i.e. hand movement speed) is very low until the operator cannot keep the pointing accuracy.

Table 5.7 Performance (IP) of the Test with 5 repeats

		Index of Performance *IP*					
		Without the HFSC method			With the HFSC method		
		Low Resistant Force (Level 1)	Medium Resistant Force (Level 2)	High Resistant Force (Level 3)	Low Resistant Force (Level 1)	Medium Resistant Force (Level 2)	High Resistant Force (Level 3)
ϕ = 20 mm	1st repeat	5.2	8.8	10.1	14.4	10.5	10.3
	2nd repeat	7.8	9.3	11.7	20.3	6.6	6.8
	3rd repeat	6.1	12.4	9.7	15.2	11.4	15.2
	4th repeat	9.5	8.9	12.4	14.0	13.6	16.2
	5th repeat	4.0	7.6	11.2	10.5	17.7	7.1
Average		6.5	9.4	11.0	14.9	12. 0	11.1
ϕ = 40 mm	1st repeat	15.7	12.4	14.2	21.0	21.5	14.5
	2nd repeat	17.6	13.0	13.4	24.9	12.7	12.0
	3rd repeat	15.9	16.0	17.2	18.7	16.1	16.6
	4th repeat	13.8	25.5	22.8	26.7	17.9	12.7
	5th repeat	10.1	18.9	21.4	18.9	23.1	14.1
Average		14.6	17.2	17.8	22.1	18.3	14.0
ϕ = 60 mm	1st repeat	17.9	17.1	12.5	21.8	19.5	11.5
	2nd repeat	24.3	11.5	20.9	21.0	16.4	11.4
	3rd repeat	20.6	20.8	22.4	29. 9	24.7	17.3
	4th repeat	17.6	23.3	20.2	21.0	18.9	14.4
	5th repeat	23.3	22.6	19.1	29.2	20.1	17.6
Average		20.8	19.1	19.0	24.6	19.9	14.4
ϕ = 80 mm	1st repeat	18.2	18.6	12.7	26.4	19.7	17.0
	2nd repeat	28.4	20.4	20.9	24.6	17.4	18.1
	3rd repeat	20.9	16.6	20.4	23.7	23.3	9.8
	4th repeat	20.0	24.4	23.9	22.7	21.6	16.8
	5th repeat	23.7	25.2	15.3	29.1	19.8	21.9
Average		22.2	21.0	18.6	25.3	20.4	16.7

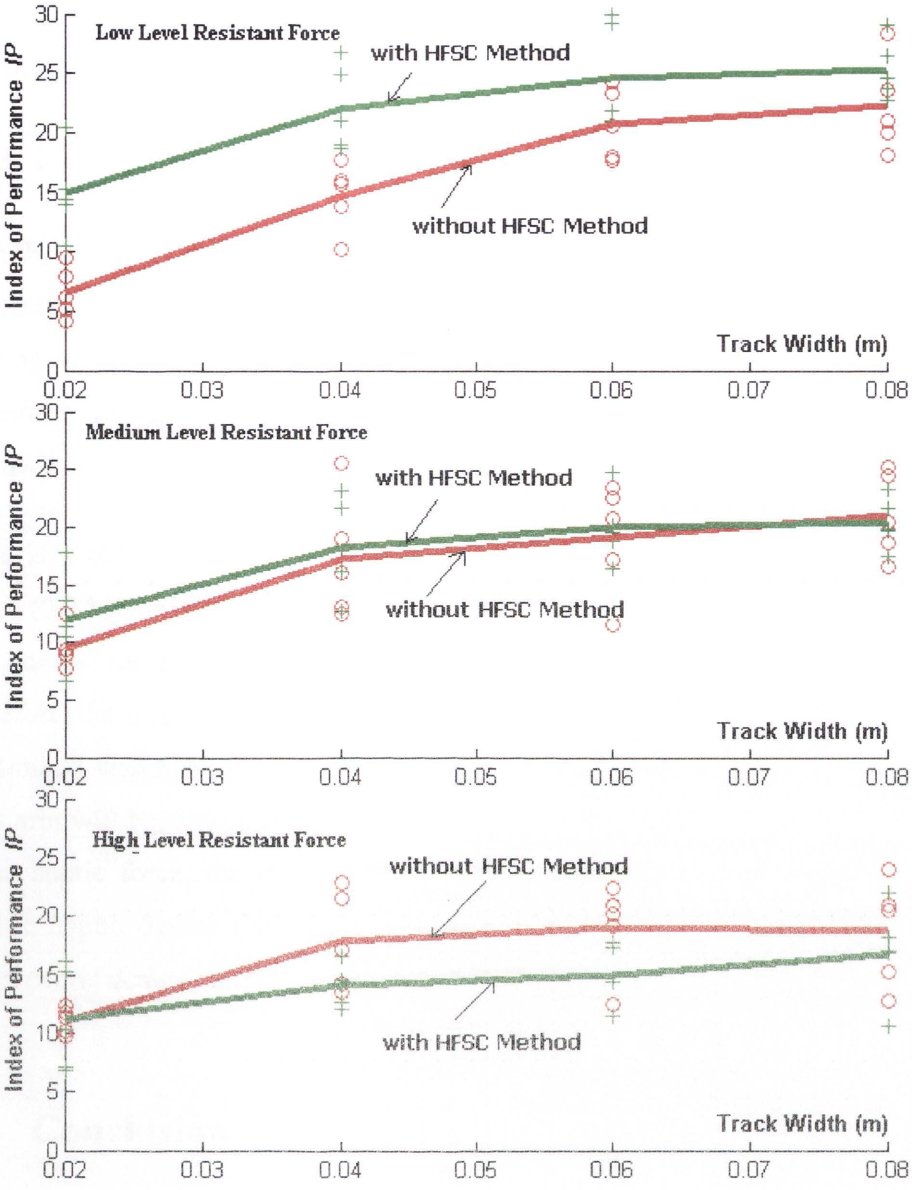

Figure 5.46 Index of performance with path-track width

Table 5.8 Average standard deviations (σ; mm) of 5 repeats with different path-track widths

Level of Resistant Force	Low (Level 1)				Medium (Level 2)				High (Level 3)			
ϕ(mm)	20	40	60	80	20	40	60	80	20	40	60	80
without HFSC	19.1	16.3	21.4	24.2	11.3	12.8	16.3	16.2	9.5	11.8	14.5	19.0
with HSFC	8.5	10.0	14.3	13.7	6.5	5.4	8.9	9.7	6.2	6.3	10.1	8.0

Table 5.8 shows the average standard deviations (σ) of end-effector position, $\boldsymbol{r}_a$, in the 120 experiments. It can be seen from the table that the standard deviation with the

HFSC method (4th row) is lower than the standard deviation without the HFSC method (3rd row); therefore, the pointing accuracy is improved with the HFSC method.

5.4.3 Discussion

From the two tests presented above, the standard deviations of the end-effector position (or haptic cursor position) with the HFSC method are reduced. Consequently, the pointing accuracy and index of performance (*IP*) are improved. However, when the movement of the robot manipulator is resisted by large resistant forces, the improvement in index of performance (*IP*) is limited.

There is a chance that the resistance force exceeds the force capacity of the haptic device (0.7 kgf on X-Y axis and 1.4 kgf on Z axis) as shown in Figure 5.10. When this case occurs, the movement of the end-effector of the robot arm will be inaccurate. Therefore, the resistance force (i.e. the haptic force) from the virtual spring approach is soft-limited under the force capacity of the haptic device. Then the movement of the robot arm will be slowed down and the control accuracy will increase. Due to the limit of the haptic force, the results of experiments in this thesis have suggested for the specific haptic device (Novint Falcon). However, the presented methodology of the experimental design can be used for different size and different type of haptic devices.

5.5 Conclusion

This chapter has investigated the effect of human factors on haptic-based human-robot interaction (HRI) and an HFSC method to improve interaction performance. Two human factors, the human's viewpoint and hand movement, have been studied.

The results of the experiments show how the optimal distance between the viewpoint (or camera) and the task plane can be selected for high-performance interaction. The correct distance has been identified by experiments.

The effect of haptic force on operator hand movement, i.e. speed and accuracy, has also been studied by experiments with the haptic-based interaction system. An eXtended

Hand Movement (XHM) model, based on Steering law, has been developed. This XHM model presents human hand movement as a quantitative equation between the haptic force, human hand movement speed, and pointing accuracy.

To evaluate this XHM model, a control method, i.e. the Haptic Force-Speed Control (HFSC) method, has been developed and integrated into the sandblasting robotic control system. Two experimental tests have been conducted to verify this HFSC method. Testing results from experiments show the HFSC method can significantly improve the performance of the haptic-based interaction.

Chapter 6 Conclusion

In order to use mobile industrial robots to assist human workers to undertake hazardous tasks in complex, unstructured and unknown (or partially known) environments, this thesis aimed to address the challenges haptic based in Human-Robot-Environment Interaction (HREI). Effective methods have been developed for the three key research issues in HREI: 1) Robot-Environment Interaction (REI); 2) haptic device-robot interface; and 3) haptic-based intuitive human-robot interaction (HRI).

To enable safe and effective robot-environment interaction, the Virtual Force Field (VF^2) approach has been developed and demonstrated to be an effective motion planner for a robot manipulator interacting with complex 3D environments. The VF^2 approach includes the 3DVirtual Force Field (3D-VF^2) method for collision avoidance, the Attractive Force (AF) method to control a multi-DOF manipulator, and the Force Control (FC) algorithm.

The haptic device-robot interface developed in this research has been shown to be capable of enabling an operator to remotely control a robot manipulator while perceiving intuitive kinesthetic feedback through a haptic device. A haptic force is generated by a haptic device based on the virtual spring concept to reflect the kinesthetic forces and the repulsive forces from the environment. Furthermore, the proposed workspace mapping method has been proved by simulation and experiments to provide intuitive HRI.

Human factors have been studied for improving the performance of human-robot-environment interaction (HREI) in this research. An extended hand movement (XHM) model has been developed and integrated in a haptic force-speed control method to enable comfortable and intuitive HRI. Extensive simulations and experiments have verified that the performance of HRI can be significantly improved by the extended hand movement model and the haptic force-speed control method.

6.1 Summary of Contributions

6.1.1 Three Dimensional Virtual Force Field Method

The 3D-Virtual Force Field (3D-VF^2) method aims to solve the real-time collision detection and avoidance problem when a multi-DOF mobile manipulator operates in a complex and compact 3D environment. The 3D-VF^2 method generates volumetric virtual fields covering every link of a manipulator. The 3D-VF^2 method plans a movement of the robot based on the nearby environment. It is different from the potential field [5][6] that needs the whole environment information before planning a trajectory of a robot. The virtual field Ellipsoidal Bounding (EB) and Swept-Sphere Bounding (SSB) are used to calculate repulsive forces based on the distances between the body of a mobile robot manipulator and the environment (i.e. the point cloud). In this thesis, simulations and experiments have been conducted to verify the method. Results from extensive experiments on the 3D-VF^2 method confirm that the 3D-VF^2 method is an effective real-time collision detection and avoidance algorithm for a multi-DOF robot manipulator operating in a complex 3D environment.

6.1.2 Attractive Force Method

The Attractive Force (AF) method generates an attractive force based on the current position of the manipulator end-effector and a target point to pull the end-effector along the pre-planned path. The amplitude of the attractive force depends on the distance between the end-effector and the target point. Additionally, the force control (FC) algorithm is used to transfer attractive forces and repulsive forces in *O-space* to joint torques and joint forces in joint space. The combination of the AF method, the 3D-VF^2 method, and the FC algorithm has established a novel contribution called the VF^2 approach. Experiments have been conducted in both simulated and actual complex 3D environments. The sandblasting robotic system is used as a testing system to test the

VF^2 approach. Results show that effective real-time collision-free motions have been generated by the VF^2 approach for Robot-Environment Interaction.

6.1.3 Workspace Mapping Method

A new workspace mapping method has been developed based on the concept from [13] to enable the use of a small haptic device to effectively control a large industrial robot manipulator exploring large environments. The workspace mapping method has been proved capable of maintaining high control resolution and high accuracy, and of responding rapidly when the operator attempts to move the end-effector for a large distance. The integration of the workspace mapping method and the haptic force generation method enables a small haptic device to render a large environment through a robot manipulator with minimal distortion.

6.1.4 Extended Hand Movement Model

When a human operator is physically in the control loop of a robotic system, human factors, such as viewpoint and hand movement, have significant effect on the operational performance of haptic-based HRI. The eXtended Hand Movement (XHM) model developed in this research provides a relationship among haptic force, hand movement (or haptic cursor) position and speed, and pointing accuracy. The XHM gives the relationship between the feedback force and pointing accuracy whereas the Fitts' law [14][15] and the Steering law [30][31] of hand movement cannot provide this relationship. This model has been integrated in the Haptic Force-Speed Control (HFSC) method which has been implemented and tested in a sandblasting robotic system. The experimental results show that the performance and accuracy of HRI are improved with the extended hand movement model.

6.1.5 Haptic-based Human-Robot-Environment Interaction for Sandblasting Robotic System

The thesis has also made a significant practical contribution through the integration of the devised methods and approaches, and the application of these methods and approaches in a real sandblasting robotic system for maintenance of complex steel bridges. Each method has been implemented as a software component in the sandblasting robotic system. The sandblasting robotic system has been tested in both the laboratory environment and a real industrial environment under the Sydney Harbour Bridge, Sydney, Australia.

6.2 Discussion and Future Work

This thesis has developed effective methods for haptic based human-robot-environment interaction (HREI). A haptic device is used to remotely control an industrial manipulator. The interaction between the human operator, the robot manipulator, and a complex environment is facilitated by the haptic device-robot interface and the VF^2 approach. The VF^2 approach includes the AF method, the $3D\text{-}VF^2$ method, and the FC algorithm. To improve the operational performance, the eXtended Hand Movement (XHM) model has been developed. The sandblasting robotic system implemented with the proposed approaches has been verified. However, there are limitations to the developed methods and approaches. Based on the research outcomes in this thesis, a number of future research tasks have been identified for the development of enabling methodologies and a practical HREI system.

The VF^2 approach requires a prior map of the application environment (i.e. the point cloud set). The prior environment map needs to be built before the operation is conducted. Therefore, the environment is considered as a static environment. In order to apply the approach in dynamic environments, efficient real-time sensing techniques need to be used to provide real-time environmental awareness. Capacitive sensors, stereo vision cameras [146], etc., to provide a wide field of view and complete update of environment changes could be used. The use of a skin-type sensor could be considered in dynamic and unknown or partially known environments. The skin-type sensor can be arranged as a proximity sensor network or a tactile sensor network. A tactile sensor network would provide contact force and location of contact point, while a proximity sensor network provides the range to obstacles. Both of these sensor readings can be used by the $3D\text{-}VF^2$ method for collision detection. If a manipulator were covered with this skin-type sensor, the sensor would provide an ideal additional data source for the VF^2 approach in order to cover all known and unknown areas.

Due to the normal of a surface in the environment is not provided in the environment map (point cloud), the direction of a repulsive force generated by the 3D-VF^2 method is assumed to point to the centre axis of a link of the manipulator. Therefore, a repulsive force generated from a surface may not be in parallel with the surface normal vector. Thus, the kinesthetic feedback may not be able to provide the correct geometric shape of the environment surface.

Since the VF^2 approach is a force control-based motion planning approach, it has the local minima problem. Future work on an additional re-planning method to correct this problem is required.

Efficiency and performance of the VF^2 approach are implicitly shown in the experiments but there is no comparison between the VF^2 approach and other existing approaches. This comparison will be definitely considered in future work.

The workspace mapping method has been demonstrated to be capable of providing an intuitive interface for HRI, but most of the parameters in this method are heuristically determined. Only the scaling control has been investigated by a human factor experiment; therefore, further research in parameter selection is needed.

The HFSC method is formulated based upon the extended hand movement model and the results of the experiments on eight healthy male volunteers with a small haptic device (i.e. the Novint® Falcon). The parameters in the HFSC method and the hand movement model are obtained from experiments. When applying this control method and the hand movement model in other applications with different group of operators (e.g., different gender and age) and different haptic devices, the parameter values in the model need to be re-determined from experiments. Nevertheless, the experiment design and process presented in this thesis are generic and provide a guideline for other applications.

Appendix A. Sandblasting Robotic System

This appendix describes the details of the sandblasting robotic system for steel bridge maintenance that is shown in Figure 1.2. Figure A.1shows a wiring diagram of the sandblasting robotic system. The robotic system consists of a 6DOF manipulator, a moving platform, a laser range finder, an onboard computer, sandblasting system, and other controlling accessories.

Manipulator - Denso® manipulator model VM6083 is used to manipulate a sandblasting nozzle. The Denso's manipulator is an articulate robot which consists of six links and six rotary joints. So it has six degree of freedoms (6DOF). With 6DOF, the position and orientation of the end-effecter can be controlled.

Platform - The structure of platform and its rail-track are made from aluminium bars. The platform is driven on an extendable track by two pneumatic motors (air motors).Track-clamp breaks are used to hold the platform to the track. Proximity switches under the platform are used to locate the platform along the track.

Control Unit - The robot control unit includes power drivers, robot controller's processer, and a teach pendant. A PC is used to run the programs of exploration, mapping, path planning and collision avoidance, and communication with the robot control unit.

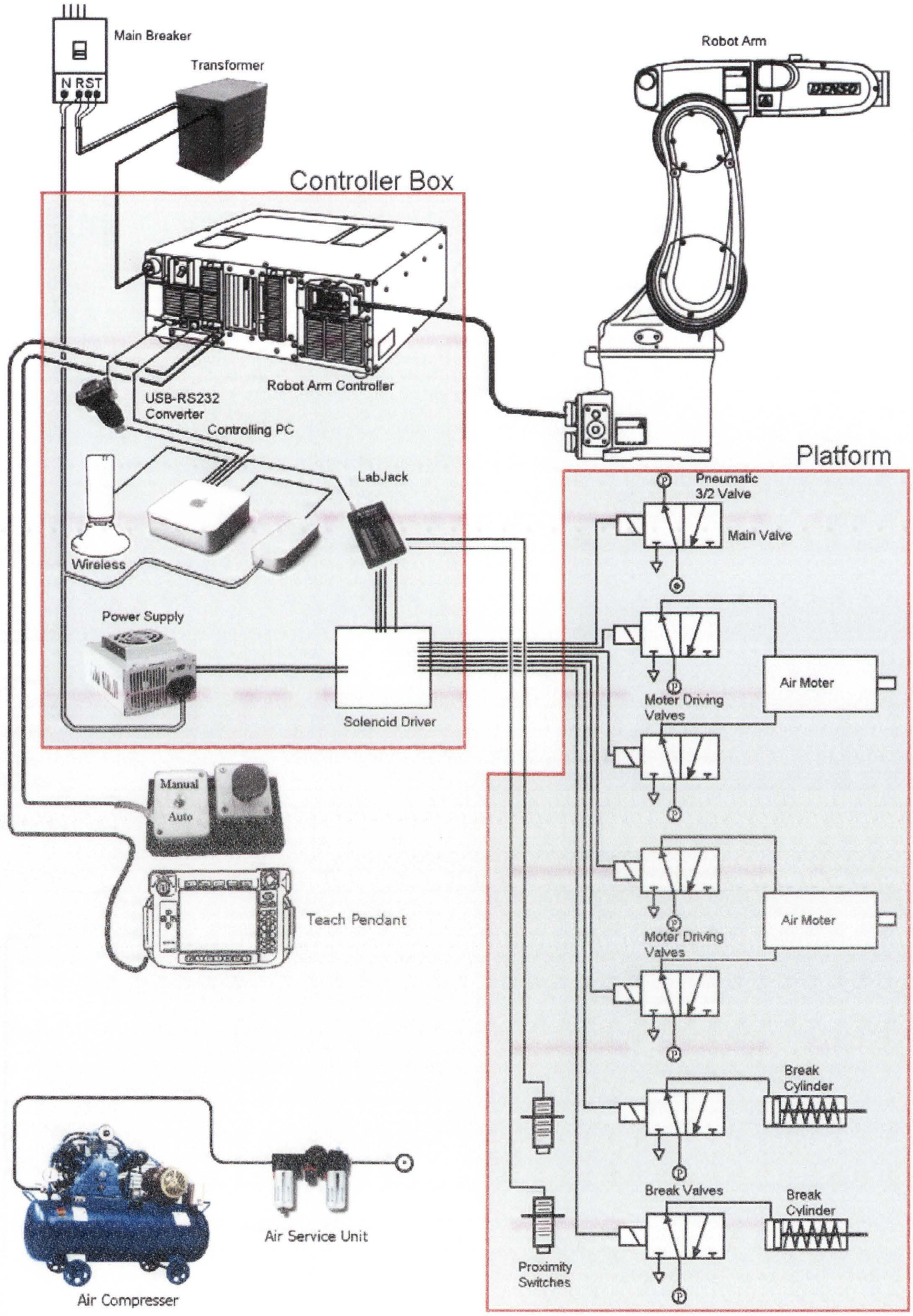

Figure A.1 Robot and Platform Controller Diagram

Sensor for Environment Mapping - A Hokuyo Laser Scanner (URG-04LX) is attached on the end-effecter of the manipulator. A 3D map is generated from exploration and mapping algorithms based on the sensor readings. Figure A.2a shows the scanner sweeping laser ray by tilting the stand and Figure A.2b shows an environment map of the laboratory setup for the autonomous steel bridge maintenance robot.

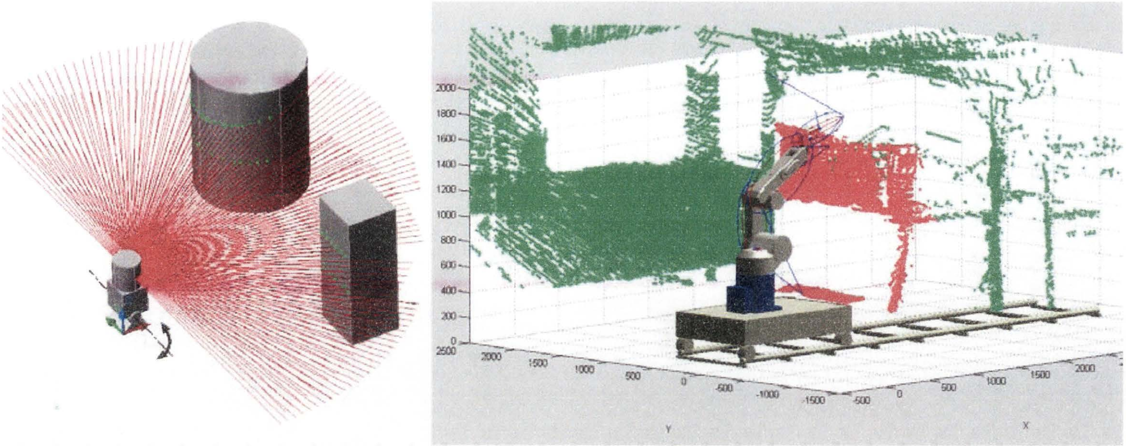

Figure A.2 A laser scanner (Left), an example environmental map (Right)

Sandblasting System-Grit-blasting or sandblasting process is a surface treatment process, which is used to clean surface of a work piece or a structure. The sandblasting system uses compressed air to blow sandblasting media through a nozzle. High-speed abrasive particle is blown across surface. Figure A.3 shows the diagram of a sandblasting system which includes a sand-pot, a hose, and two types of sandblasting nozzles.

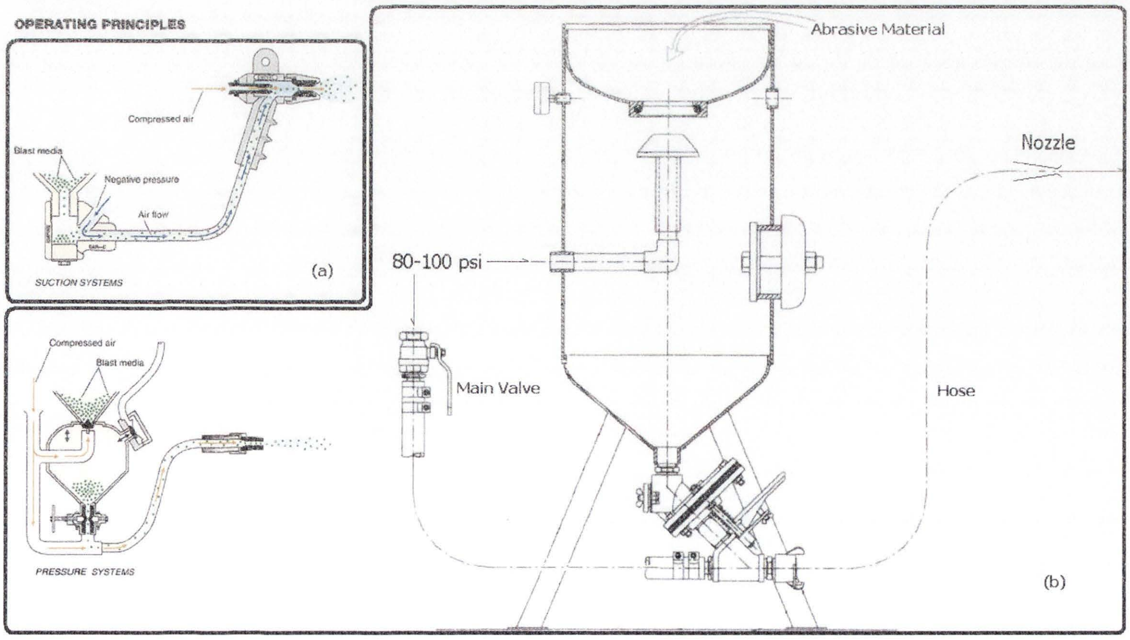

Figure A.3 A Sandblasting System, (a) A system for small-scale blasting using blasting gun, (b) A system for industrial scale blasting

Appendix B. Steering Test with Novint®Falcon Haptic Device

This steering test aims to get the start/stop time (*a*) and the speed of the operator (*b*) in the Steering law by an experiment. As shown in Figure B.1, the experiment requires participants to move a haptic cursor clockwise on within a circular path track an X-Y plane for one minute. The radius of the centreline between the inner and outer boundaries is set at 25.4 mm. In order to take the path-track width into consideration, four different widths of circular path track (ϕ) are used: 15.88 mm, 12.7 mm, 9.53 mm, and 6.35 mm. The control scale $G_x(G_x = G_e / G_h)$ is set at 1.

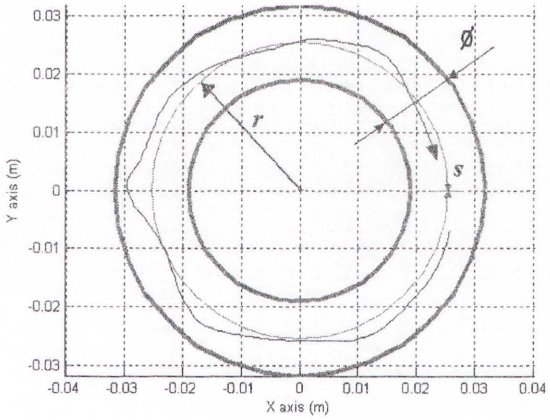

Figure B.1Hand movement testing in circular path track (unit: m)

In this experiment, the travel distance *s* and the path-track widthϕ are independent, thus the movement time equation (Steering law) is

$$MT = a + \frac{bs}{G_x \emptyset} \tag{B.1}$$

$G_e = 1/k_{sc}$ where k_{sc} is scaling factor of the workspace mapping method (Section 4.3).Four people participated in this test. The movement times from the four participants are recorded. Table B.1 gives the movement times of one participant. The graph in Figure B.2 shows the movement time of all the four participants.

Table B.1 Movement time of one participant in one cycle movement of difference path-track widths

No. of circles moved in 1min.	Path-track width (ϕ: mm)			
	15.88	12.7	9.53	6.35
1	3.6623	4.5366	3.6561	7.0838
2	3.9162	4.1375	3.7226	6.8583
3	3.5687	3.7384	4.281	7.2297
4	3.8628	3.3925	4.4804	7.4022
5	3.7959	3.4989	4.0815	7.9859
6	4.0232	3.8315	4.0948	7.7869
7	3.8227	3.6585	4.7729	7.1236
8	3.5153	3.6851	4.2012	
9	3.288	3.4856	4.8659	
10	3.1945	3.898	4.6266	
11	3.0074	3.8714	4.6798	
12	3.2346	3.6718	5.8099	
13	2.8202	3.6851		
14	2.8737	3.7251		
15	2.8336	3.8581		
16	2.7935			
17	2.9138			

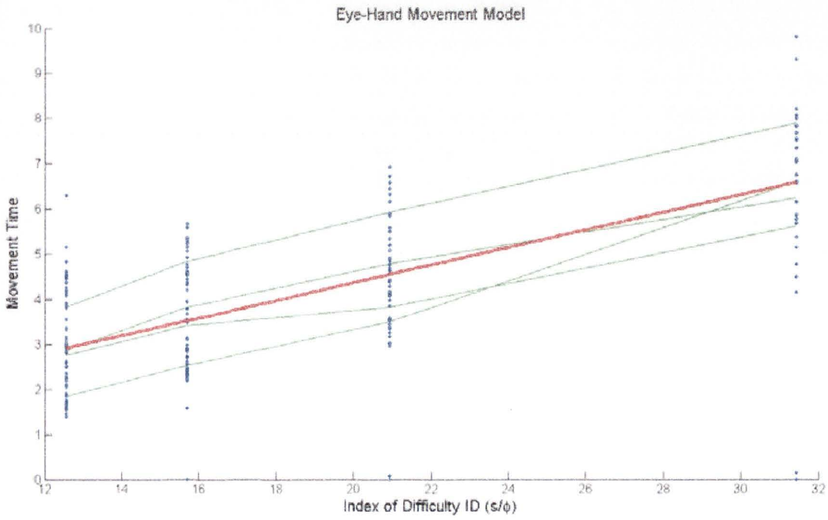

Figure B.2 Hand movement testing result of 4 participants

Based upon the results of these experiments conducted with the four participants, according to the Steering law, the hand movement model formulated by linear regression is given as:

$$MT = 0.4453 + \frac{0.1958s}{\emptyset} \text{ with } R^2{=}0.988 \quad \text{(B.2)}$$

Where the start/stop time (*a*) is found to be 0.4453 seconds and the speed of the operator *b* is found to be 0.1958 mm/sec. R^2 for the hand movement model based upon the results shown is found to be 0.988.

Appendix C. Table of Standard Normal Distribution

There are several ways to calculate probability density of the normal distribution and a lookup table as Table C.1 is one way to get the probability density.

Table C.1 Probability Density of Standard Normal Distribution

Z	0	0.01	0.02	0.03	0.04	0.05	0.06	0.07	0.08	0.09
0.0	0.5000	0.5040	0.5080	0.5120	0.5160	0.5199	0.5239	0.5279	0.5319	0.5359
0.1	0.5398	0.5438	0.5478	0.5517	0.5557	0.5596	0.5636	0.5675	0.5714	0.5753
0.2	0.5793	0.5832	0.5871	0.5910	0.5948	0.5987	0.6026	0.6064	0.6103	0.6141
0.3	0.6179	0.6217	0.6255	0.6293	0.6331	0.6368	0.6406	0.6443	0.648	0.6517
0.4	0.6554	0.6591	0.6628	0.6664	0.6700	0.6736	0.6772	0.6808	0.6844	0.6879
0.5	0.6915	0.6950	0.6985	0.7019	0.7054	0.7088	0.7123	0.7157	0.7190	0.7224
0.6	0.7257	0.7291	0.7324	0.7357	0.7389	0.7422	0.7454	0.7486	0.7517	0.7549
0.7	0.7580	0.7611	0.7642	0.7673	0.7704	0.7734	0.7764	0.7794	0.7823	0.7852
0.8	0.7881	0.7910	0.7939	0.7967	0.7995	0.8023	0.8051	0.8078	0.8106	0.8133
0.9	0.8159	0.8186	0.8212	0.8238	0.8264	0.8289	0.8315	0.834	0.8365	0.8389
1.0	0.8413	0.8438	0.8461	0.8485	0.8508	0.8531	0.8554	0.8577	0.8599	0.8621
1.1	0.8643	0.8665	0.8686	0.8708	0.8729	0.8749	0.8770	0.8790	0.8810	0.8830
1.2	0.8849	0.8869	0.8888	0.8907	0.8925	0.8944	0.8962	0.8980	0.8997	0.9015
1.3	0.9032	0.9049	0.9066	0.9082	0.9099	0.9115	0.9131	0.9147	0.9162	0.9177
1.4	0.9192	0.9207	0.9222	0.9236	0.9251	0.9265	0.9279	0.9292	0.9306	0.9319
1.5	0.9332	0.9345	0.9357	0.9370	0.9382	0.9394	0.9406	0.9418	0.9429	0.9441
1.6	0.9452	0.9463	0.9474	0.9484	0.9495	0.9505	0.9515	0.9525	0.9535	0.9545
1.7	0.9554	0.9564	0.9573	0.9582	0.9591	0.9599	0.9608	0.9616	0.9625	0.9633
1.8	0.9641	0.9649	0.9656	0.9664	0.9671	0.9678	0.9686	0.9693	0.9699	0.9706
1.9	0.9713	0.9719	0.9726	0.9732	0.9738	0.9744	0.9750	0.9756	0.9761	0.9767
2.0	0.9772	0.9778	0.9783	0.9788	0.9793	0.9798	0.9803	0.9808	0.9812	0.9817
2.1	0.9821	0.9826	0.9830	0.9834	0.9838	0.9842	0.9846	0.9850	0.9854	0.9857
2.2	0.9861	0.9864	0.9868	0.9871	0.9875	0.9878	0.9881	0.9884	0.9887	0.9890
2.3	0.9893	0.9896	0.9898	0.9901	0.9904	0.9906	0.9909	0.9911	0.9913	0.9916
2.4	0.9918	0.9920	0.9922	0.9925	0.9927	0.9929	0.9931	0.9932	0.9934	0.9936
2.5	0.9938	0.9940	0.9941	0.9943	0.9945	0.9946	0.9948	0.9949	0.9951	0.9952
2.6	0.9953	0.9955	0.9956	0.9957	0.9959	0.9960	0.9961	0.9962	0.9963	0.9964
2.7	0.9965	0.9966	0.9967	0.9968	0.9969	0.9970	0.9971	0.9972	0.9973	0.9974
2.8	0.9974	0.9975	0.9976	0.9977	0.9977	0.9978	0.9979	0.9979	0.998	0.9981
2.9	0.9981	0.9982	0.9982	0.9983	0.9984	0.9984	0.9985	0.9985	0.9986	0.9986
3.0	0.9987	0.9987	0.9987	0.9988	0.9988	0.9989	0.9989	0.9989	0.999	0.9990

Table C.1 is the probability density of the standard normal distribution which has a mean of 0 and a standard deviation of 1. To use this table, a normal distribution must be standardised before looking for the probability density in this table. If x is a random variable with normal distribution with mean μ and standard deviation σ, Z which is used to find the probability density can be calculated from

$$Z = \frac{x-\mu}{\sigma} \tag{C.1}$$

For the probability density function (*P*), there are three 3 different conventions in determination of probability density (φ) including cumulative, complementary cumulative, and cumulative point-to-point.

Cumulative:

$$\varphi = P(Z \leq a) \tag{C.2}$$

Complementary Cumulative:

$$\varphi = P(Z \geq a) = 1 - P(Z \leq a) \tag{C.3}$$

Cumulative Point-to-Point:

$$\varphi = P(b \leq Z \leq a) = P(Z \leq a) - P(Z \leq b) \tag{C.4}$$

The table provides only the probability density of cumulative (Equation C.2).

For example from section 5.1, Equation 5.2 is the probability density of normal distribution of x where $\mu = 0$.

$$\varphi = P\left(-\frac{\phi}{2\sigma} < Z < \frac{\phi}{2\sigma}\right) \tag{5.2}$$

And the Equation 5.2 can be re-written as

$$\varphi = P\left(Z \leq \frac{\phi}{2\sigma}\right) - P\left(Z \leq -\frac{\phi}{2\sigma}\right) \tag{C.5}$$

If $\frac{\phi}{2\sigma}$ is equal to 2, the probability density (φ) can be calculated from

$$\varphi = P(Z \leq 2) - P(Z \leq -2) \tag{C.6}$$

which is equal to

$$\varphi = P(Z \leq 2) - P(Z \geq 2) \tag{C.7}$$

$$\varphi = 0.9772 - (1 - 0.9772) \tag{C.8}$$

and then the probability density is

$$\varphi = 0.9544 \tag{C.9}$$

Bibliography

1. Lion Precision, *Capacitive Sensor Operation and Optimization*, Technical Note, http://www.lionprecision.com, accessed 10 February, 2009.
2. T. Lozano-Perez, 1983, 'Spatial Planning: A Configuration Space Approach', *IEEE Transactions on Computers,* vol. C-32, no.2, pp.108-119.
3. T. Lozano-Perez, 1987, 'A Simple Motion-Planning Algorithm for General Robot Manipulators', *IEEE Journal of Robotics and Automation,* vol. RA-3, no.3, pp. 224-238.
4. S. Quinlan and O. Khatib, 'Elastic Bands: Connecting Path Planning and Control', *Proceedings of the IEEE International Conference on Robotics and Automation*, pp. 802-807.
5. O.Khatib, 1985, 'Real-Time Obstacle Avoidance for Manipulators and Mobile Robots', *Proceedings of the IEEE International Conference on Robotics and Automation*, pp.500-505.
6. O. Khatib, 1986, 'Real-time Obstacle Avoidance for Manipulators and Mobile Robots', *International Journal of Robotics Research*, vol. 5, pp. 90-98.
7. O. Brock, 1999, Generating Robot Motion: The Integration of Planning and Execution, PhD Thesis, Stanford University.
8. J. G. Juang, 'Robot Collision Avoidance Control using Distance Computation', 1995, *Proceedings of the IEEE International Conference on Systems, Man and Cybernetics*. vol. 3, pp. 2564-2569.
9. D. Kulic and E. Croft, 2007, 'Pre-collision Safety Strategies for Human-Robot Interaction', *Autonomous Robots*, vol. 22, no. 2, pp. 149-164.
10. D. Wang, D.K. Liu, and G. Dissanayake, 2006, 'A Variable Speed Force Field Method for Multi-Robot Collaboration', *Proceedings of the 2006 IEEE/RSJ International Conference on Intelligent Robots and Systems*, pp. 2697-2702.
11. L. M. Munoz and A. Casals, 2009, 'Improving the Human-Robot Interface Through Adaptive Multispace Transformation', *IEEE Transactions on Robotics*, vol. 25, no. 5, pp. 1208-1213.
12. G. Casiez, D. Vogel, R. Balakrishnan, and A. Cockburn, 2008, 'The Impact of Control-Display Gain in User Performance in Pointing Tasks', *International*

Journal of Human-Computer Interaction, vol. 23, pp. 215-250

13. F. Conti and O. Khatib, 2005, 'Spanning Large Workspaces Using Small Haptic Devices', *Proceedings of the 1st Joint Euro haptics Conference and Symposium on Haptic Interfaces for Virtual Environment and Teleoperator Systems*, pp. 183-188.
14. P. M. Fitt, 1954, 'The Information Capacity of the Human Motor System in Controlling the Amplitude of Movement', *Journal of Experimental Psychology*, vol. 47, no. 6, pp. 381-391.
15. J. Accot and S. Zhai, 2003, 'Refining Fitts'Law Models for Bivariate Pointing', *Proceedings of the International Conference on Computer-Human Interaction 2003*, vol. 5, no. 1, pp. 193-200.
16. Occupational Safety and Health Administration (OSHA) http://www.osha.gov, accessed 26 June 2008.
17. R.Alami, A. Albu-Schaeffer, A. Bicchi, R. Bischoff, R. Chatila, A. De Luca, A. De Santis, G. Giralt, J. Guiochet, G. Hirzinger, F. Ingrand, V. Lippiello, R. Mattone, D. Powell, S. Sen, B. Siciliano, G. Tonietti and L. Villani,2006, 'Safe and Dependable Physical Human-Robot Interaction in Anthropic Domains: State of the Art and Challenges', *Proceedings of the IROS06 Workshop on pHRI - Physical Human-Robot Interaction in Anthropic Domains.*
18. ANSI/RIA R15.06 Industrial Robots and Robot Systems - Safety Requirements
19. ISO 10218-1:2006 Robots for Industrial Environments- Safety requirements -Part 1: Robot
20. EN775:1993 Manipulating Industrial Robots - Safety
21. AS2939-1987 Australian Standard, Industrial Robot Systems - Safe Design and Usage
22. EN954-1:1997 Safety of Machinery. Safety Related Parts of Control Systems.
23. Occupational Safety and Health Administration of U.S. Department of Labor, *OSHA Technical Manual*, Section IV: Chapter 4 Industrial Robots and Robot System Safety, http://63.234.227.130/dts/osta/otm/otm_iv/otm_iv_4.html, accessed 20 July 2008.
24. J. Park and O. Khatib, 2006, 'A Haptic Teleoperation Approach Based on Contact', *International Journal of Robotics Research*, vol. 25, no. 5-6, pp. 575-

591.

25. K. J. Kuchenbecker and G. Niemeyer, 2006, 'Improving Telerobotic Touch Via High-Frequency Acceleration Matching', *Proceedings of the 2006 IEEE International Conference on Robotics and Automation*, pp.3893-3898.
26. F. Nagata, Y. Kusumoto, Y. Fujimoto, and K. Watanabe, 2007,'Robotic Sanding System for New Designed Furniture', *Robotics and Computer-Integrated Manufacturing*, vol. 23, pp. 371-379.
27. H. Z. Tan, M. A. Srinivasan, B. Eberman, and B. Chang, 1994, 'Human Factors for the Design of Force-Reflecting Haptic Interfaces', *Dynamic Systems and Control*, vol. 55, no. 1, pp. 353-359.
28. J. T. Dennerlein and M. C. Yang, 2001, 'Haptic Force-Feedback Devices for Office Computers: Performance and Musculoskeletal Loading Issues', *Human Factors*, vol. 43, no. 2, pp. 278-286.
29. D. Natapov, S. J. Castellucci, and I. S. MacKenzie, 2009, 'ISO 9241-9: Evaluation of Video Game Controllers', *Proceedings of the ACM Graphic Interface Conference 2009*, pp. 223-230.
30. J. Accot and S. Zhai, 2001, 'Scale Effects in Steering Law Tasks', *Proceedings of the ACM Computer Human Interface Conference, Spatial Interest Group on Computer Human Interaction (SIGCHI)*, vol. 3, no. 1, pp. 1-8.
31. J. Accot and S. Zhai, 1997, 'Beyond Fitts'Law: Trajectory-Based HCI Tasks', *Proceedings of the ACM Computer Human Interface Conference, Spatial Interest Group on Computer Human Interaction (SIGCHI)*, pp. 295-302.
32. D. Ferguson, A. Morris, D. Haehnel, C. Baker, Z. Omohundro, C. Reverte, S. Thayer, W.Whittaker, W. Burgard, and S. Thrun, 2003, 'An Autonomous Robotic System for Mapping Abandoned Mines', *Proceedings of the Conference on Advances in Neural Information Processing Systems*, pp. 587-594.
33. S. Thrun, D. Haehnel, D. Ferguson, M Montemerlo, R. Triebel, W. Burgard, C. Baker, Z. Omohohundro, S. Thayer, and W. L. Whittaker,2003, 'A System for Volumetric Robotic Mapping of Abandoned Mines', *Proceedings of the IEEE International Conference on Robotics and Automation* (ICRA'03), pp. 1-6.
34. G. Paul, D.K. Liu, N. Kirchner, and G. Dissanayake, 2009, 'An Effective Exploration Approach to Simultaneous Mapping and Surface Material-type

Identification of Complex 3D Environments', *Journal of Field Robotics*, vol. 26, no. 11-12, pp. 915-933.

35. J. Popinga, N. Vaskevicius, A. Birk, and K. Pathak, 2008, 'Fast Plane Detection and Polygonalization in Noisy 3D Range Images', *International Conference on Intelligent Robots and Systems* (IROS'08), pp. 3378-3383.
36. N. Kirchner, D.K. Liu, and G. Dissanayake, 2009, 'Surface Type Classification with a Laser Range Finder', *Sensors Journal*, vol. 9, no. 9, pp. 1160-1168.
37. N. Kirchner, D. Hordern, D.K. Liu, and G. Dissanayake, 2008, 'Capacitive Sensor for Object Ranging and Material Type Identification', *Science Sensors and Actuators*, vol. 148, no. 1, pp. 96-104.
38. K. Weib and H. Worn, 'The Working Principle of Resistive Tactile Sensor Cells', *Proceedings of the 2005 IEEE International Conference on Mechatronics & Automation*, vol. 1, pp. 471-476.
39. H. Iwata and S. Sugano, 2005, 'Human-Robot-Contact-State Identification Based on Tactile Recognition', *IEEE Transactions on Industrial Electronics*, vol. 52, no. 6.
40. N. Kirchner, D.K. Liu, and G. Dissanayake, 2006, 'Bridge Maintenance Robotic Arm: Capacitive Sensor for Obstacle Ranging in Particle Laden Air', *Proceedings of the 23rd International Symposium on Automation and Robotics in Construction* (ISARC'06), pp. 596-601.
41. Vladimir J. Lumelsky, 2006, *Sensing, Intelligence, Motion*, John Wiley & Sons, New Jersey, USA, pp. 389-416.
42. L.E. Kavraki and S.M. LaValle, 2008, 'Motion Planning', in B. Siciliano and K. Oussama (Eds.), *Springer Handbook of Robotics*, Springer-Verlag, Berlin, pp. 109-128.
43. L. E. Kavraki, M. N. Kolountzakis, and J. C. Latombe, 1998, 'Analysis of Probabilistic Roadmaps for Path Planning', *IEEE Transactions on Robotics and Automation*, vol. 14, pp. 166-171.
44. C. Nissoux, T. Simeon, and J. P. Laumond, 1999, 'Visibility Based Probabilistic Roadmaps',*Proceedings of the IEEE/RSJ International Conference on Intelligent Robots and Systems*, pp. 1316-1321.

45. R.A. Brooks, 1990, 'Solving the Find-Path Problem by Good Representation of Free Space', *Autonomous Robot Vehicles*, pp. 290-297.

46. J. J. Kuffner, Jr. and S. M. LaValle, 2000, 'RRT-Connect: An Efficient Approach to Single-Query Path Planning', *Proceedings of the IEEE International Conference on Robotics and Automation*, pp. 995-1001.

47. J.-G. Juang, 1998, 'Collision Avoidance using Potential Fields', *Industrial Robot: An International Journal*, vol. 25,pp.408-415.

48. J.-G. Juang, 2004,'Application of Repulsive Force and Genetic Algorithm to Multi-manipulator Collision Avoidance', *Proceedings of the 5th Asian Control Conference*, vol. 2, pp.971-976.

49. C.-C. Lin and J. Chuang, 2003, 'Potential-Based Path Planning for Robot Manipulators in 3-D Workspace', *Proceedings of the International Conference on Robotics Automation*, pp.3353-3358.

50. H. P. Xie, R. V. Patel, S. Kalaycioglu, and H. Asmer, 1998, 'Real-Time Collision Avoidance for Redundant Manipulator in an Unstructured Environment', *Proceedings of the IEEE International Conference on Intelligent Robots and Systems,*vol. 3, 1925-1930.

51. K. Bouyarmane, A. Escande, F. Lamiraux, and A. Kheddar, 2009, 'Potential Field Guide for Humanoid Multi contacts Acrylic Motion Planning', *Proceedings of the IEEE International Conference Robotics and Automation* (ICRA'09), pp. 1165-1170.

52. M. Greenspan and N. Burtnyk, 1996, 'Obstacle Count Independent Real-Time Collision Avoidance', *Proceedings of the IEEE International Conference on Robotics and Automation*, pp.1073-1080.

53. M. Greenspan and N. Burtnyk, 1994, *Real Time Collision Detection*, US patent 5347459, filed 13 September 1994.

54. A. Dominique and G Bessonnet, 2000, 'Optimal Motion Planning of Robotic Manipulators Removing Mobile Objects Grasped in Motion', *Intelligent and Robotic Systems*, vol. 29, pp. 233-255.

55. L. Guangyu, S. Zengqi, and M. Chundi, 2006, 'Optimal Motion Planning Passing Through Kinematic Singularities of Manipulators', *Proceedings of the 2006 IEEE/RSJ International Conference on Intelligent Robots and Systems*, pp.4350-

4355.

56. K.Y. Lee, S. Y. Lee, J. H. Choi, S. H. Lee, and C. S. Han, 2006, 'The Application of the Human-Robot Cooperative System for Construction Robot Manipulating and Installing Heavy Materials', *Proceedings of the SICE-ICASE International Joint Conference*, pp. 4798-4802.
57. S. Y. Lee, Y. S. Lee, B. S. Park, S. H. Lee, and C. S. Han, 2007,'MFR (Multipurpose Field Robot) for Installing Construction Materials', *Autonomous Robots*, vol. 22, no. 3, 265-280.
58. R. D. Schraft, C. Meyer, C. Parlitz, and E. Helms, 2005, 'PowerMate - A Safe and Intuitive Robot Assistant for Handling and Assembly Tasks', *Proceedings of the IEEE International Conference on Robotics and Automation*, pp. 4074-4079.
59. Y. Fujisawa, T. Fukuda, K. Kosuge, F. Arai, E. Muro, H. Hoshino, T. Miyazaki, K. Ohtsubo, and K. Uehara, 1992, 'Control of Manipulator/Vehicle System for Man-Robot Cooperation Based on Human Intention', *Proceedings of the IEEE International Workshop on Robot and Human Communication*, pp. 188-193.
60. T. Fukuda, Y. Fujisawa, K. Kosuge, F. Arai, E. Muro, H. Hoshino, T. Miyazaki, K. Ohtsubo, and K. Uehara, 1991, 'Manipulator for Man-Robot Cooperation', *IEEE Proceedings of the International Conference on Industrial Electronics Control and Instrumentation* (IECON'91), vol. 2, pp. 996-1001.
61. Z. Wu, M. Meng and F. Shen, 2004, 'Interaction Force Measurement of Robotic Manipulator Based on 12DOF Force Sensor Compensation', *Proceedings of the IEEE International Conference on Information Acquisition*, pp. 240-243.
62. C. Esteves, G. Arechavaleta, and J.P. Laumond, 2005, 'Motion Planning for Human-Robot Interaction in Manipulation Tasks', *Proceedings of the IEEE International Conference on Mechatronics and Automation*, vol.4, pp.1766-1771.
63. S. Kobayashi, A. Muis, and K. Ohnishi, 2005, 'Sensorless Cooperation between Human and Mobile Manipulator', *Proceedings of the IEEE International Conference on Industrial Technology*, pp. 811-816.
64. The ABB Group, *RobotWare Assembly FC and RobotWare Machining FC*, http://www.abb.com, accessed 26 June, 2008
65. O. Khatib, 1987, 'A Unified Approach for Motion and Force Control of Robot Manipulators: The Operational Space Formulation', *Journal of Robotics and*

Automation, vol. RA-3, no. 1, p. 43-53.

66. C. I. Connolly, J. B. Burns and R. Weiss, 1990, 'Path Planning using Laplace's Equation', *Proceedings of the IEEE International Conference on Robotics and Automation*, pp. 2102-2106.
67. C. W. Warren, 1990, 'Multiple Robot Path Coordination using Artificial Potential Fields', *Proceedings of 1990 IEEE International Conference on Robotics and Automation*, pp. 500-505.
68. O. Brock and O. Khatib, 2000, 'Real-time Re-planning in High-Dimensional Configuration Spaces Using Sets of Homotopic Paths', *Proceedings of the IEEE International Conference on Robotics and Automation* (ICRA'00), pp. 550-555.
69. J. Barraquand, B. Langlois, and J. C. Latombe, 1991, 'Numerical Potential Field Techniques for Robot Path Planning', *Proceedings of the Fifth International Conference on Advanced Robotics* (ICAR'91), pp. 1012-1017.
70. L. Chien-Chou, P. Chi-Chun, and C. Jen-Hui, 2003, 'A Novel Potential-Based Path Planning of 3-D Articulated Robots with Moving Bases', *Proceedings of the IEEE International Conference on Robotics and Automation* (ICRA'03), vol. 3, pp. 3365-3370.
71. M. G. Park and M. C. Lee, 2003, 'Artificial Potential Field Based Path Planning for Mobile Robots using a Virtual Obstacle Concept', *Proceedings of the IEEE/ASME International Conference on Advanced Intelligent Mechatronics*, pp. 735 - 740.
72. M. T. Wolf and J. W. Burdick, 2008, 'Artificial Potential Functions for Highway Driving with Collision Avoidance', *Proceedings of the IEEE International Conference on Robotics and Automation*, pp. 3731-3736.
73. M. C. Mora and J. Tornero, 2008, 'Path Planning and Trajectory Generation using Multi-rate Predictive Artificial Potential Fields', *Proceedings of the IEEE/RSJ International Conference on Intelligent Robots and Systems*, pp. 2990-2995.
74. N. A. Scott and C. R. Carignan, 2008, 'A Line-Based Obstacle Avoidance Technique for Dexterous Manipulator Operations', *Proceedings of the IEEE International Conference on Robotics and Automation*, pp. 3353-3358.
75. G. Besseron, C. Grand, F. Ben Amar, and P. Bidaud, 2008, 'Decoupled Control of the High Mobility Robot Hylos Based on a Dynamic Stability Margin',

Proceedings of the IEEE/RSJ International Conference on Intelligent Robots and Systems, pp. 2435-2440.

76. G. C. Karras and K. J. Kyriakopoulos, 2008, 'Visual Servo Control of an Underwater Vehicle using a Laser Vision System', *Proceedings of the IEEE/RSJ International Conference on Intelligent Robots and Systems*, pp. 4116-4122.
77. R. Jing, K. A. McIsaac, and R. V. Patel, 2006, 'Modified Newton's Method Applied to Potential Field-Based Navigation for Mobile Robots,'*IEEE Transactions on Robotics*, vol. 22, pp. 384-391.
78. Di Xiao, B.K Ghosh, Ning Xi, and T.J. Tarn, 2000,'Sensor-Based Hybrid Position/Force Control of a Robot Manipulator in an Uncalibrated Environment', *IEEE Transactions on Control Systems Technology*, vol. 8, no. 4, pp. 635-645.
79. R. Tinos, M.H. Terra, and J.Y. Ishihara, 2006, 'Motion and Force Control of Cooperative Robotic Manipulators with Passive Joints', *IEEE Transactions on Control Systems Technology*, vol. 14 , no. 4, pp. 725-734.
80. D. Kulic and E. Croft, 2007, 'Affective State Estimation for Human-Robot Interaction', *IEEE Transactions on Robotics*, vol. 23, no. 5, pp. 991-1000.
81. D. Kulic and E. Croft, 2005, 'Real-Time Safety for Human-Robot Interaction', *Proceedings of the 11th IEEE International Conference on Advanced Robotics* (ICAR'05), pp. 719-724.
82. D. Kulic and E. Croft, 2003, 'Estimating Intent for Human Robot Interaction', *Proceedings of the IEEE International Conference on Advanced Robotics*, pp. 810-815.
83. D. Kulic and E. Croft, 2005, 'Anxiety Detection during Human-Robot Interaction', *Proceedings of the IEEE International Conference on Intelligent Robots and Systems* (IROS'05), pp. 616-621.
84. S. Oberer and R. D. Schraft, 2007, 'Robot-Dummy Crash Test for Robot Safety Assessment', *Proceedings of the IEEE International Conference on Robotics and Automation*, pp. 2934-2939.
85. S. Oberer, M. Malosio, and R. D. Schraft, 2006, 'Investigation of Robot-Human Impact', *Proceedings of the Joint Conference on Robotics ISR 2006*, vol. 120, pp. 212-218.
86. Barratt Technology, *The Barratt WAM™ Arm*, http://www.barrett.com, accessed

28 May 2009

87. S. Haddadin, A. Albu-Schäffer, and G. Hirzinger, 2007, 'Approaching Asimov's 1st Law: The Role of the Robot's Weight Class', paper presented at the Robotics: Science and Systems Conference, 27-30 June 2007, Atlanta, USA.
88. F. Conti and O. Khatib, 2009, 'A New Actuation Approach for Haptic Interface Design', *International Journal of Robotics Research*, vol. 28, no. 6, pp. 834-848.
89. D. Shin, I. Sardellitti and O. Khatib, 2008, 'A Hybrid Actuation Approach for Human-Friendly Robot Design', *Proceedings of the International Conference on Robotics and Automation*, pp. 1747-1752.
90. V. Hayward and K. E. MacLean, 2007, 'Do It Yourself Haptics Part I', *IEEE Robotics & Automation Magazine*, vol. 14, no. 4, pp. 88-104.
91. K. E. MacLean and V. Hayward, 2008, 'Do It Yourself Haptics Part II', *IEEE Robotics & Automation Magazine,* vol. 15, no. 1, pp. 104-119.
92. X. He and Y. Chen, 2009, 'Haptic-Aided Robot Path Planning based on Virtual Teleoperation', *Robotics and Computer-Integrated Manufacturing*, vol. 25, pp. 792-803.
93. O. Brock and O. Khatib, 1999, 'Real-Time Obstacle Avoidance and Motion Coordination in a Multi-Robot Workcell', *Proceedings of the IEEE International Symposium on Assembly and Task Planning*, Porto, Portugal, pp. 274-279.
94. Y.Y. Liao, L.R. Chou, T.J. Horng, Y. Y. Luo, K. Y. Young, and S. F. Su,2000, 'Force Reflection and Manipulation for a VR-based Telerobotic System', *Proceedings of the NSC Part A: Physical Science and Engineering*, vol. 24, no. 5, pp. 382-389.
95. J. Ueda and T. Yoshikawa, 2004, 'Force-Reflecting Bilateral Teleoperation with Time Delay by Signal Filtering', *IEEE Transactions on Robotics & Automation*, vol. 20, no. 3, pp. 613-619.
96. K. Salisbury, F. Conti, and F. Barbagli, 2004, 'Haptic Rendering: Introductory Concepts', *IEEE Computer Graphics and Applications*, vol. 24, no.2, pp.24-32.
97. K. Hashtrudi-Zaad and S. E. Salcudean, 2002, 'Transparency in Time-Delayed Systems and the Effect of Local Force Feedback for Transparent Teleoperation', *IEEE Transactions on Robotics and Automation*, vol. 18, no. 1, pp. 108-115.

98. D. Constantinescu, S. E. Salcudean, and E. A. Croft, 2003, ‘Haptic Feedback using Local Models of Interaction’, *Proceedings of the 11th Symposium on Haptic Interfaces for Virtual Environment and Teleoperator Systems* (HAPTICS’03), pp. 416- 421.

99. S. Macfarlane and E. A. Croft, 2003, ‘Jerk-Bounded Manipulator Trajectory Planning: Design for Real-Time Applications’, *IEEE Transactions on Robotics and Automation*, vol. 18, no. 1, pp. 42-52.

100. D. Constantinescu, S. E. Salcudean, and E. A. Croft, 2004, ‘Haptic Rendering of Rigid Body Collisions’, *Proceedings of the 12th International Symposium on Haptic Interfaces for Virtual Environment and Teleoperator Systems* (HAPTICS’04), pp. 2-8.

101. D. Constantinescu, S. E. Salcudean, and E. A. Croft, 2005, ‘Haptic Rendering of Rigid Contacts Using Impulsive and Penalty Forces’, *IEEE Transactions on Robotics*, vol. 21, no. 3, pp. 309-323.

102. O. Kerpa, D. Osswald, S. Yigit, C. Burghart, and H. Woern, 2003,‘Arm-Hand-Control by Tactile Sensing for Human Robot Co-operation’, *Proceedings of Humanoids 2003.*

103. M. Zinn,_O. Khatib, B. Roth, and J.K. Salisbury, 2008, ‘Large Workspace Haptic Devices: A New Actuation Approach’, *Proceedings of the IEEE Symposium on Haptic Interfaces for Virtual Environments and Teleoperator Systems*, pp. 185-193.

104. J. C. Perry, J. Rosen, and S. Burns, 2007, ‘Upper-Limb Powered Exoskeleton Design’, *IEEE/ASME Transactions on Mechatronics*, vol.12, no. 4, pp. 408-417.

105. Y. Hou and G. R. Luecke, 2005, ‘Time Delayed Teleoperation System Control, A Passivity-based Method’, *Proceedings of the 12th International Conference on Advanced Robotics* (ICAR’05), pp. 796-802.

106. S. Hirche, A. Bauer, and M. Buss, 2005, ‘Transparency of Haptic Telepresence Systems with Constant Time Delay’, *Proceedings of the IEEE Conference on Control Applications*, pp. 328-334.

107. Q. W. Deng, Q. Wie, and Z. X. Li, ‘Analysis of Absolute Stability for Time-Delay Teleoperation Systems’, *International Journal of Automation and Computing*, vol. 4, no. 2, pp. 203-207.

108. E. Slawinski, V. A. Mut, and J. F. Postigo, 2007, 'Teleoperation of Mobile Robots with Time-Varying Delay', *IEEE Transactions on Robotics*, vol. 23, no. 5, pp. 1071-1082.

109. G. Biegelbauer, A. Pichler, M. Vincze, C. L. Nielsen, H. J. Andersen and K. Haeusler, 2005, 'The Inverse Approach of FlexPaint', *IEEE Robotics & Automation Magazine*, vol. 12, issue 3, pp. 24-34.

110. H. Chaudhary and S. K. Saha, 2006, 'Constraint Force Formulation for Industrial Manipulators', *Proceedings of the 2006 IEEE/RSJ International Conference on Intelligent Robots and Systems*, pp. 1498-1503.

111. S. J. Lorenc, B. E. Handlon, and L. E. Bernold, 2000, 'Development of a Robotic Bridge Maintenance System, *Automation in Construction*, vol. 9, pp. 251-258.

112. B. Joode, C. Verspuy, and A. Burdorf, 2004, *Physical Workload in Ship Maintenance: Using the Observer to Solve Ergonomics Problems*, Technical report, Erasmus University of Rotterdam.

113. S. Lahiri, C. Levenstein, D. Nelson, and B. Rosenberg, 2005, 'The Cost Effectiveness of Occupational Health Interventions: Prevention of Silicosis', *American Journal of Industrial Medicine*, vol 48, no. 6, pp. 503-517.

114. B. Ross, J. Bares, and C. Fromme, 2003, 'A Semi-Autonomous Robot for Stripping Paint from Large Vessels', *International Journal of Robotics Research*, vol. 22, no. 7-8, pp. 617-626.

115. W. Schmitz, 2003, 'Robotic Paint Stripping of Large Aircraft: A Reality with the Air Jet Coatings Removal Process', paper presented at the Aerospace Coatings Removal and Coatings Conference, 19-22 May 2003, Colorado Springs, USA.

116. S. Moon and L. Bernold, 1997, 'Vision-Based Interactive Path Planning for Robotic Bridge Paint Removal', *Journal of Computing in Civil Engineering*, vol. 11, no. 2, pp. 113-120.

117. R. J. Teather, A. Pavlovych, and W. Stuerzlinger, 2009, 'Effect of Latency and Spatial Jitter on 2D and 3D Pointing', *Proceedings of the IEEE Virtual Reality Conference 2009*, pp 229-230.

118. Y. Guiard and M. Beaudouin-Lafon, 2004, 'Target Acquisition in Multiscale Electronic Worlds', *International Journal of Human-Computer Studies*, vol. 61, no. 6, pp. 875-905.

119. X. Ren, K. Shinomori, and Y. Kimura, 2006, 'S-H Model and Its Application in Human Interface Design', *Kochi University of Technology Research Bulletin*, vol. 3, no. 1, pp. 55-64.

120. G. S. Lee and B. Thuraisingham, 2008, 'Differences in Fitts'Law Task Performance Based on Environment Scaling', *Haptics: Perception, Devices and Scenarios: 6th International Conference EuroHaptic 2008*, Springer-Verlag, Berlin, pp. 295-300.

121. Mikell P. Groover, 2007, 'Automation, Production Systems, and Computer-Integrated Manufacturing System', Prentice Hall, pp.49-68.

122. R. Balakrisnan and S. MacKenzie, 1997, 'Performance Differences in the Fingers, Wrist, and Forearm in Computer Control', *Proceedings of the 1997 ACM Conference on Human Factors in Computing Systems* (CHI'97), pp. 303-310.

123. R. Arsenault and C. Ware, 2004, 'The Importance of Stereo and Eye-Coupled Perspective for Eye-Hand Coordination in Fish Tank VR', *Presence*, vol. 13, no. 5, pp. 549-559.

124. A. Murata and H. Iwase, 2001, 'Extending Fitts' Law to a Three-Dimensional Pointing Task', *International Journal of Human Movement Science*, vol. 20, pp. 791-805.

125. M. J. McGuffin and R. Balakrishnan, 2005, 'Fitts' Law and Expanding Target: Experimental Studies and Designs for User Interface', *ACM Transactions on Computer-Human Interaction,* vol. 12, no. 4, pp. 388-422.

126. J. Ding, T. Kesar, A. S. Wexler, and S. A. Binder-Macleod, 2005, 'A Mathematical Model that Incorporates the Force-Intensity Relationship of Human Skeletal Muscle', paper presented at the *10th Annual Conference of the International Functional Electrical Stimulation Society*, 5-8 July 2005, Montreal, Canada.

127. J. Z. Liu, R. W. Brown, and G. H. Yue, 2002, 'A Dynamical Model of Muscle Activation, Fatigue, and Recovery', *The Biophysical Journal*, vol. 82, pp. 2344-2359.

128. L. Ma, D.Chablat, F.Bennis, W. Zhang, and F. Guillaume, 2008, 'A New Muscle Fatigue and Recovery Model and Its Ergonomics Application in Human Simulation', *Proceedings of IDMME-Virtual Concept 2008,* pp. 1-10.

129. J. Ding, A. S. Wexler, and S. A. Binder-Macleod, 2003, 'Mathematical Models for Fatigue Minimization During Functional Electrical Stimulation', *Journal of Electromyography and Kinesiology*, vol. 13, pp. 575-588.
130. J. Ding, A. S. Wexler, and S. A. Binder-Macleod, 2002, 'A Mathematical Model that Predicts the Force-Frequency Relationship of Human Skeletal Muscle', *Journal of Muscle and Nerve*, vol. 26, pp. 477-485.
131. A. Edsinger and C. C. Kemp, 2006, 'Manipulation in Human Environments', *Proceedings of the IEEE-RAS International Conference on Humanoid Robots* (HUMANOID'06), pp. 102-109
132. C. C. Kemp, A. Edsinger, and E. Torres-Jara, 2007, 'Challenges for Robot Manipulation in Human Environments', *IEEE Robotics & Automation Magazine*, vol. 14, no. 1, pp. 20-29.
133. G. Paul, 2009, Autonomous Exploration and Mapping of Complex 3D Environments by Means of 6DOF Manipulator. PhD thesis, University of Technology, Sydney.
134. N. Kirchner, 2008, Exploiting Laser and Capacitive Ranging Sensors' Behaviour to Yield Mission-Critical Material Type Identifications in Real-World Environments. PhD thesis, University of Technology, Sydney.
135. D.K. Liu, G. Dissayanake, P. B. Manamperi, P. A. Brooks, G. Fang, G. Paul, S. Webb, N. Kirchner, P. Chotiprayanakul, N. M. Kwok, and T. R. Ren, 2008, 'A Robotic System for Steel Bridge Maintenance: Research Challenges and System Design', paper presented at the *2008 Australasian Conference on Robotics and Automation*, 3-5 December 2008, Canberra, Australia.
136. W. K. To, G. Paul, N.M. Kwok, and D.K. Liu, 2009, 'An Efficient Trajectory Planning Approach for Autonomous Robots in Complex Bridge Environments', *International Journal of Computer Aided Engineering and Technology*, vol. 1, no. 2, pp. 185-208.
137. P. Chotiprayanakul, D.K. Liu, D. Wang, and G. Dissanayake (2007), "Collision-free trajectory planning for manipulators using virtual force based approach", *in Proceeding of the International Conference on Engineering, Applied Sciences, and Technology*(ICEAST 2007), November 21-23, 2007, Swissôtel Le Concorde, Bangkok, Thailand,4 pp.

138. P. Chotiprayanakul, D.K. Liu, D. Wang and G. Dissanayake, 2007, 'A 3-Dimensional Force Field Method for Robot Collision Avoidance in Complex Environments', *Proceedings of the 24th International Symposium on Automation and Robotics in Construction* (ISARC'2007), pp. 139-145.
139. P. Chotiprayanakul, D. Wang, N.M. Kwok, and D.K. Liu, 2008, 'A Haptic Base Human Robot Interaction Approach for Robotic Grit Blasting', *Proceedings of the 25th International Symposium on Automation and Robotics in Construction* (ISARC'2008), pp. 148-154.
140. P. Chotiprayanakul and D.K. Liu, 2009, 'Workspace Mapping and Force Control for Small Haptic Device Based Robot Teleoperation', *Proceedings of the 2009 IEEE International Conference on Information and Automation* (ICIA'2009), pp. 1613-1618.
141. Novint Technologies, *Novint® Falcon Haptic Device*, http://www.novint.com, accessed 23 Oct 2010
142. Kevin M. Baird, Errol R. Hoffmann, and Colin G. Drury, 2002, 'The effects of probe length on Fitts' law', *Applied Ergonomics*, vol. 33, pp. 9-14.
143. Mesa Imaging AG, *SwissRanger 3D Camera*, http://www.mesa-imaging.ch, accessed 23 Oct 2010
144. Richard C. Simpson, 2009, 'Using the Speed-Accuracy Operating Characteristic to Visualize Performance with Pointing Device', *Journal of The Open Rehabilitation*, vol.2, pp. 58-63.
145. Jack T. Dennerlein and Maria C. Yang, 2001, 'Haptic Force-Feedback Devices for the Office Computer: Performance and Musculoskeletal Loading Issues', *Human Factors*, pp 278-286.
146. Point Gray Research, *Bumblebee® Stereo Vision*, http://www.ptgray.com, accessed 23 Oct 2010
147. Corrie I. Nichol and Milos Manic, 2009, 'Video Game Device Haptic Interface for Robotic Arc Welding', *Proceeding of IEEE Conference on Human System Interaction* (HSI 2009), Catania, Italy, 21-23 May, 2009, pp. 1-6.
148. Yisheng Guan and Hong Zhang, 2003, 'Kinematical Feasibility Analysis of 3D Multi-figured Grasps', *IEEE Transactions on Robotics and Automation*, vol. 19, no. 3, pp 507-513.

149. Yisheng Guan and Hong Zhang, 2000, 'Kinematical Graspability of a 2D Multi-figured Hand', *IEEE International Conference on Robotics and Automation (ICRA)*, pp. 3591-3596.

150. Carsten Moenning and Neil A. Dodgson, 'A New Point Cloud Simplification Algorithm', *3rd IASTED International Conference on Visualization, Imaging, and Image Processing* (VIIP2003), Benalmadena, Spain, 8-10, Sep 2003, 6 pp.